

APPLICATION OF RIGID BODY IMPACT MECHANICS AND
DISCRETE ELEMENT MODELING TO
ROCKFALL SIMULATION

by

Parham Ashayer

A thesis submitted in conformity with the requirements

for the degree of Doctor of Philosophy

Graduate Department of Civil Engineering

University of Toronto

© Copyright by Parham Ashayer 2007

Abstract

Application of Rigid Body Impact Mechanics and Discrete Element Modeling to Rockfall Simulation

Doctor of Philosophy 2007

PARHAM ASHAYER

Department of Civil Engineering

University of Toronto

Numerical modeling can assist in predicting falling rock trajectories and reducing the destruction caused by rockfalls. The majority of existing rockfall simulations are based on particle or lumped-mass models that consider the falling rock as an infinitesimal particle with a concentrated mass. Hybrid models usually find the rock-slope contact point using techniques similar to those used in particle models, while incorporating some aspects of the rigid body collisions for bouncing. There are also some rigid body models that employ simplified mathematical impact models. In the framework of this thesis, the applications of rigid body theory and discrete element modeling to rockfall simulation are investigated.

A modified version of the discrete element model (MDEM), which can model impacts using methods similar to low-compliance impact models, is offered. In this model, the normal linear dashpot is replaced by a nonlinear dashpot which dissipates the impact velocity based on the contact normal velocity. A mono-direction sliding unit is added to model low-compliance impacts and the tangential dashpot is removed. Several numerical tests strongly

indicate that if shape geometries can be sufficiently approximated by a group of particles, the proposed MDEM can replicate the rebound velocities that are predicted by the application of low compliance rigid body impact models.

Application of rigid body impact mechanics (RBIM), originally developed by Stronge, in rockfall simulation is studied and compared with other classical rockfall impact models. The effects of several parameters on widely-used coefficients of restitution are investigated including: rock geometry and slenderness, angle of impact, rock orientation, and slope material properties.

A new geometrical rockfall simulation program, *GeoRFS*, based on rigid body mechanics in two-dimensional space, is developed, where rock geometry can vary from prisms with a randomly generated polygonal cross section to superellipsoids.

The trajectories of different rock geometries (e.g., roll-out distances, bounce heights, velocities, and energies) during multiple impacts on flat and inclined impact surfaces are studied. The results strongly suggest that the provided simulation program can satisfactorily replicate the roll-out distances obtained from the in-situ tests performed by the Oregon Department of Transportation using different rock geometries.

It is expected that the geometrical simulation tools introduced in this work will replace the particle impact model currently used in rockfall programs.

ACKNOWLEDGMENTS

Myself when young did eagerly frequent
Doctor and Saint, and heard great Argument
About it and about: but evermore
Came out by the same Door as in I went.

Khayyam (11th century), translated by *Fitzgerald* (19th century)

My life is similar to a rolling stone moving down a slope. It is the slope which guides; there is no choice about when to start or how to stop. Even so, my imagination and endeavours have travelled far. This made the fall unique and beautiful, but, nevertheless, gloomy.

I could not have completed this thesis without the help of many individuals and organizations:

First, I would like to express my gratitude to my supervisor, Professor John Curran, who provided the initial idea for this research. His leadership, support, and vision had a major influence on this thesis. I could not have finished this work without his understanding of the nature of rockfalls, including its numerical simulation.

I would like to thank the other members of my defence committee: Prof. Jean Hutchinson, Prof. Will Bawden, Prof. Murray Grabinsky, and Prof. Evan Bentz. Their reviews helped improve the thesis.

I am grateful for the financial support for this research, which came from Professor Curran's NSERC Discovery Grant, the 'Digital Mine' project supported by the Keck Foundation and a Robert M. Smith scholarship.

I would especially like to thank Dr. Hossein Bidhendi for his continuous help and friendship in rainy days. Many thanks to Azadeh Riahi, whose friendship and suggestions were very rewarding over the last four years. Nonetheless, I thank Adam Coulson and Safdar Khan for their help and friendship.

I must also acknowledge Jeremy Smith, who helped me by providing interfaces for 3D particle modeling and the research version of RocFall[®]. I'd like to thank Dr. Jim Hazzard for his generous helps in writing the FISH programs for PFC^{2D}. In addition, Dr. Vijay Sinnathurai was always in the lab to help in programming, and Dr. Reginald Hammah provided guidance in improving my writing skills. Thanks to Jennifer Horkoff for her kind help in proofreading the thesis.

Finally, I should thank my patient parents, Shahin and Mohsen, and my brother, Amirreza, who endured me to be far from them during these last five years. This journey's main motivation came from my sister Ghazaleh, who encouraged me to come to Canada to study in summer 2000, and helped me greatly through the tough days; so I deeply thank her and dedicate this thesis to her.

At last, but not least, I thank my aunt, Shahla, and her family: Golnaz and Golriz and Ali Amooee who have been there for my family.

I would like to thank many people whose rewarding friendships were like a gift to me over these years, including: Daryoush Gharghi, Zhoobin Abbasi, Omid Saremi, Shakib Shakeri, Harpak Poorgan, Ali Nezhadi, Nazli Kamvari, Ben Thompson, Ehsan Foroughi, Kaveh Yekta, Djordje Stefanovic, Ulrich Kamp, Afshin Afsharzadeh, Siamak Mohammadi, Raha Abedi, Zohreh Khavandgar, Laili Soleimani, Azadeh Hatami, Saba Saneinezhad, Azadeh Zereshkian, Bahman Kalbasi, Afshin and Azadeh Ebtekar, Arash Zolghadri, Shahyad Morovatjoo, Amirreza Golpayegan, Pezhman Hassanpoor, Amir Mirshahi, Marmar Mehrabadi, Mr. Iraj Emad, Babak Mokaberinezhad, Amir Zand, Pooyan Mashayekh, Farzaneh Ashrafi, Azar Sanei, Farid Katirai, the Mougouies, and the Valizades.

TABLE OF CONTENTS	PAGE
ABSTRACT	ii
ACKNOWLEDGMENTS	iv
TABLE OF CONTENTS	v
LIST OF TABLES	x
LIST OF FIGURES	xi
LIST OF APPENDICES	xx
LIST OF SYMBOLS	xxi
CHAPTER 1: INTRODUCTION AND OUTLINE	1
CHAPTER 2: ROCKFALL STUDIES – PRELIMINARIES AND LITERATURE REVIEW	4
2.1 Introduction	4
2.2 Rockfall impact models	6
2.2.1 Coefficients of restitution (COR)	8
2.2.1.1 Kinematic coefficient of restitution	8
2.2.1.2 Kinetic coefficient of restitution	9
2.2.1.3 Energy coefficient of restitution	10
2.2.2 Values of coefficients of restitution in rockfall literature	11
2.3 Summary and contribution of thesis	12
CHAPTER 3: APPLICATION OF DISCRETE ELEMENT MODELING (DEM) TO ROCKFALL SIMULATION	15
3.1 Introduction	15

3.2	The normal direction in DEM	16
3.2.1	Viscoelasticity in the normal direction	16
3.2.2	Application of nonlinear viscoelasticity in rockfall modeling	22
3.3	The tangential direction in DEM	24
3.3.1	The discrete compliance model (DCM)	24
3.3.2	Collinear impacts in DCM	26
3.3.3	Tangential contact forces	29
3.3.4	Modifying the tangential module in DEM: introducing the mono-direction unit	32
3.3.5	Variation of tangential forces using modified discrete element modeling (MDEM)	34
3.3.5.1	Low impact angles ($v_I(0)/\mu v_3(0) < 1.21$)	35
3.3.5.2	Intermediate impact angles ($1.21 < v_I(0)/\mu v_3(0) < 7.0$)	36
3.3.5.3	Large impact angles ($7.0 < v_I(0)/\mu v_3(0)$)	38
3.3.6	Successive impacts using MDEM	38
3.3.7	The effect of impact angle on tangential COR when applying MDEM	40
3.4	Application of MDEM in rigid-body clumps	41
3.4.1	Ellipse representation	44
3.4.2	Rectangle representation	46
3.4.3	Square representation	47
3.4.4	Disk representation	49
3.5	The rotational module in MDEM	50
3.6	Summary	51
 CHAPTER 4: APPLICATION OF RIGID BODY MECHANICS TO ROCKFALL SIMULATION		 53
4.1	Introduction	53
4.2	Rigid body impact mechanics (RBIM)	54
4.2.1	Amontons-Coulomb law of dry friction	56
4.2.2	Energy coefficient of restitution	57
4.2.3	Implementation of equations	58
4.2.4	Collinear impacts in RBIM	63
4.3	Impact models in rockfall literature	65
4.3.1	Hybrid (stereomechanical) model by Pfeiffer and Bowen (1989)	66
4.3.2	Hybrid model by Bozzolo et al. (1986) and Azzoni et al. (1995)	68
4.3.3	Rigid body model by Descouedres et al. (1987)	70
4.3.3.1	No-sliding mode ($\gamma \leq \gamma_c$)	71
4.3.3.2	Sliding mode ($\gamma > \gamma_c$)	72
4.3.3.3	Rebound velocities	72

4.4	Effect of rock geometry on the COR in the application of RBIM in rockfall studies	73
4.4.1	Effect of the impact model on object rebound parameters	76
4.4.2	Effect of RBIM parameters on object rebound parameters	80
4.4.2.1	Rebound parameters versus friction coefficient	80
4.4.2.2	Rebound parameters versus energy coefficient of restitution	82
4.4.3	Effect of object geometry on rebound parameters	84
4.4.3.1	Effect of rock aspect ratio (or slenderness) on rebound values	85
4.4.3.2	Effect of rock shape on rebound values – 0° impact angle	87
4.4.3.3	Effect of rock shape on rebound values – 45° impact angle	90
4.4.4	Effect of impact angle on rebound parameters	93
4.5	Application of rigid body rolling in rockfall modeling	95
4.5.1	Rolling for non-circular objects	95
4.5.1.1	Rolling-sliding mode	97
4.5.2	Rolling for circular objects	97
4.5.3	Rigid body toppling	98
4.6	Summary	98
 CHAPTER 5: GEOMETRICAL ROCKFALL SIMULATION: <i>GEORFS</i>		100
5.1	Introduction: rockfall simulations in the literature	100
5.1.1	Hybrid versus geometrical modeling	103
5.1.1.1	Conventional hybrid models	104
5.1.1.2	Circumscribing hybrid models	105
5.2	Methodology for rigid body rockfall simulation program: <i>GeoRFS</i>	106
5.2.1	Basic assumptions	106
5.2.2	Slope decomposition	109
5.2.2.1	Slope roughness	109
5.2.3	Model rock geometries	110
5.2.4	Domain of analysis	112
5.2.5	Modes of motion	113
5.2.6	Mechanical models of contact	114
5.3	Contact search procedure	115
5.3.1	Contact search optimization	115
5.3.1.1	Circumscribing	115
5.3.2.1	Dynamic timestep refinement	116
5.3.2	Object-segment contact search procedure	116
5.3.2.1	Step 1 – constructing local coordinate system	117
5.3.2.2	Step 2 – geometry transformation	117
5.3.2.3	Object-segment contact	117
5.3.2.4	Object-corner contact	119
5.3.2.5	Back transformation	120

5.4	Miscellaneous simulation assumptions	120
5.4.1	Time domain formulation	120
5.4.2	Multiple contacts manipulation	121
5.4.2.1	Multiple contacts: all impact modes	122
5.4.2.2	Multiple contacts: rolling with impact	122
5.4.3	Defining contact mode: impact mode versus rolling-sliding mode	122
5.4.4	Overlap treatment in impact mode	123
5.4.5	Critical timestep criteria	123
5.4.6	Arrest (termination) criteria	124
5.4.7	Modeling pseudo-code	125
5.4.8	Programming language used	126
5.4.9	UML Diagram of the simulation implementation	126
5.5	Implementation of <i>GeoRFS</i> in RocFall® research version	128
5.5.1	Seeder Properties Window	129
5.5.2	Material Property Window	130
5.5.3	Rock Shape Editor Window	130
5.6	Summary	131
 CHAPTER 6: RIGID BODY IMPACT MECHANICS IN ROCKFALL ANALYSIS: APPLICATION AND VERIFICATION		 133
6.1	Introduction	133
6.2	Effect of rock geometry on multiple impacts	134
6.2.1	Equivalent object convention	134
6.2.2	Double-impact numerical test	135
6.2.2.1	Double impacts on a horizontal plane – 0° impact	136
6.2.2.2	Double impacts on a horizontal plane – 45° impact	138
6.2.2.3	Double impacts on an inclined plane – 0° impact angle	140
6.2.2.4	Double impacts on an inclined plane – 45° impact	142
6.2.3	Five-impact numerical test	144
6.2.3.1	5 impacts on a horizontal plane – 0° impact angle	145
6.2.3.2	5 impacts on a horizontal plane – 45° impact angle	147
6.2.3.3	Shape effect on roll-out distances on a plane with 15° of inclination – 45° impact angle	151
6.2.3.4	Aspect ratio effect on roll-out distances and total energies	152
6.2.3.5	Effect of friction and energy COR on rebound parameters of an ellipsoid	155
6.2.3.6	Effect of friction and energy COR on rebound parameters of a prism with a rectangular cross section	158
6.2.4	Multiple impact studies using random object generation	160
6.2.4.1	Effect of aspect ratio on trajectories during five impacts on a horizontal plane	161
6.2.4.2	Effect of rock shape on trajectories for the objects with a 1:2 aspect ratio	163
6.2.4.3	Effect of rock shape on trajectories for the unit objects	165

6.3	Rockfall case study	166
6.3.1	Output data analysis	169
6.4	Summary	174
 CHAPTER 7: CONCLUSIONS AND FUTURE WORK		 176
7.1	Conclusions	176
7.2	Future work	184
7.2.1	Three-dimensional simulation	184
7.2.1.1	3D eccentric collision of objects on rough half space	185
7.2.1.2	3D centric collision of objects on rough half space	187
7.2.2	Application of RBIM in hybrid modeling	188
7.2.3	Complementing the application of modified DEM in 2D and 3D rockfall modeling	189
7.2.4	Extending the application of <i>GeoRFS</i> to soft-soil slopes	190
 APPENDIX 1: VALUES OF RESTITUTION, FRICTION, AND ROLLING FRICTION COEFFICIENTS		 191
 APPENDIX 2: DEFINING RIGID BODY IMPACT MECHANICS (RBIM) PARAMETERS USING EXPERIMENTAL METHODS		 194
 APPENDIX 3: EFFECT OF ROCK SHAPE ON SINGLE ROCK TRAJECTORIES PERFORMING RANDOM OBJECT GENERATION		 197
 REFERENCES		 202

LIST OF TABLES

PAGE

Table 2.1:	Available theories for low speed impact, after Stronge (2000)	7
Table 3.1:	Slip processes during incidence of a circular object on a half space	26
Table 3.2:	Tangential and rotational rebound velocities for spheres and disks using Brach impact model for the case of sliding termination before separation	31
Table 3.3:	Different rigid body clumps representing geometrical shapes	42
Table 3.4:	Parameters needed in MDEM and the applied values	43
Table 4.1:	Impact parameters for different scenarios happening at planar impact, after Strong (2000)	60
Table 4.2:	Relative position of critical impact processes in eccentric impact	63
Table 4.3:	Minimum tangential COR for different geometrical objects	65
Table 4.4:	Statistical data for COR, rebound rotational velocity, and the ratio of retrieved energy to initial energy for different rocks, corresponding to Figure 4.17	92
Table 5.1:	Different computer simulation models for rockfalls categorized based on their main characteristics, after Guzzetti et al. (2002)	101
Table 5.2:	List of provided geometrical shapes in <i>GeoRFS</i> and the mechanical properties of motion	112
Table 5.3:	The simulation pseudo-code applied in the <i>GeoRFS</i> engine	125
Table 6.1:	The dimensions for different equivalent geometrical shapes	135
Table 6.2:	Variation in the rebound energies and roll-out distances for rocks with variable orientations and different geometries on a 30° inclined surface with an initial angle of 45°	144
Table 6.3:	The averages of height of bounces for different objects during the five impacts	150
Table 6.4:	The model parameters used to randomly generate objects	161
Table 6.5:	RocFall® research version parameters used in simulating the Oregon catchment field test	169
Table A.1.1:	Values of COR in the literature defined by various researchers as well as different types of coefficient and for different materials after Heidenreich (2004) and RocFall® 4.0 (2002)	191

LIST OF FIGURES

PAGE

Figure 2.1:	Rockfall trajectory in a mountain slope next to a highway.	5
Figure 2.2:	The range of variation for the coefficients of restitution in R_n - R_t space: (a) after Fornaro et al. (1990), and (b) after Chau et al. (2002).	12
Figure 3.1:	Kelvin-Voigt system of spring and dashpots in normal and tangential directions with a no-tension unit in normal direction and a slider in tangential direction.	16
Figure 3.2:	Variation of the contact's normal force in the linear viscoelastic system defined by Equation (3.2.1): (a) versus overlap, and (b) versus time.	17
Figure 3.3:	The ideal variation of normal contact force in a nonlinear viscoelastic system after Hunt et al. (1975): (a) versus overlap, and (b) versus time.	18
Figure 3.4:	The hysteresis loop of overlap-force caused by nonlinear viscoelasticity for: (a) Equation (3.2.6), in which the viscosity is relative to the velocity to a power of one, after Stronge (2000), and (b) Equation (3.2.9), in which the viscosity is relative to the velocity to a power of two.	20
Figure 3.5:	Descending coefficients of restitution as a function of initial contact velocity for the nonlinear viscoelastic models of Equations (3.2.4) and (3.2.9) (note: the dimensionless velocities differ for the two curves).	20
Figure 3.6:	Decaying COR resulting from inelastic fracturing at the point of impact for the Pfeiffer scaling (Equation (3.2.16)) and the variation of nonlinear viscoelastic models defined by Equations (3.2.8) and (3.2.15) for: (a) normal COR (R_n) = 1.0, and (b) normal COR (R_n) = 0.5.	23
Figure 3.7:	Impact of an object against a rigid half-space using the discrete compliant model (DCM) proposed by Stronge (1994b).	25
Figure 3.8:	Variation of contact forces versus time during small impact angle for centric impacts after Stronge (1994) (the values of the forces are dimensionless and are shown for CORs equal to 1.0 and 0.5 and for $\Omega_t/\Omega_n = 1.7$).	27
Figure 3.9:	Tangential velocity at the contact point at the instance of contact termination for collision of a spherical compliant object at a rigid half space, after Stronge (1994b) (the material has a Poisson ratio equal to 0.3 and $e_* = 1.0$).	28
Figure 3.10:	Collinear impact: free body diagram of a sphere impacting a solid half space at angle γ .	30
Figure 3.11:	Increasing sequence of tangential impulse versus the contact normal impulse which is constant, after Brach (1988).	32

Figure 3.12:	Mono-direction unit in the tangential direction along with a spring and a slider.	33
Figure 3.13:	Normal and tangential modules in Modified DEM (MDEM).	34
Figure 3.14:	Variation of dimensionless tangential forces and velocities at the contact point for the impact of a sphere with the initial settings of Figure 3.11 at different impact velocities using DEM and MDEM for low impact angles: (a) variation of forces using DEM, (b) variation of tangential velocities using DEM, (c) variation of forces using MDEM, and (d) variation of tangential velocities using MDEM.	36
Figure 3.15:	Variation of dimensionless tangential forces and velocities at the contact point for the impact of a sphere with the initial settings of Figure 3.11 at different impact velocities using DEM and MDEM for intermediate impact angles: (a) variation of forces using DEM, (b) variation of tangential velocities using DEM, (c) variation of forces using MDEM, and (d) variation of tangential velocities using MDEM.	37
Figure 3.16:	Variation of dimensionless tangential forces and velocities at the contact point for the impact of a sphere with the initial settings of Figure 3.11 at different impact velocities using DEM and MDEM for high impact angles: (a) variation of forces using DEM and MDEM, and (b) variation of tangential velocities using DEM and MDEM.	38
Figure 3.17:	Five successive impact of a discoidal object under gravity using both the DEM and MDEM models: (a) the settings for the test, (b) variation of the disk horizontal velocity using the DEM model, and (c) variation of the disk horizontal velocity using the MDEM model.	39
Figure 3.18:	(a) Variation of tangential COR (R_t) versus impact angle, ψ , at different friction coefficients applying MDEM, and (b) the variation of tangential coefficients of restitution versus impact angle after Chau et al. (2002) for spheres with different mass.	41
Figure 3.19:	Numerical test setup: the impact of different eccentric clumps (introduced in Table 3.4) on a rigid half space at variable impact orientations, under zero-gravity force using MDEM.	43
Figure 3.20:	Variation of rebound velocities versus the object orientation for vertical impact of an ellipse using RBIM and the represented clumps of Table 3.3 (three, five, seven, and nine-particle ellipse) and using MDEM: (a) typical impact of the three-particle ellipsoidal clump, (b) rebound normal COR at the clumps center, (c) rebound tangential velocity at the clumps center (m/s), and (d) rebound rotational velocity (rad/s).	44
Figure 3.21:	Variation of rebound velocities versus object orientation for the vertical impact of a rectangle, using RBIM, and the represented clump of Table 3.3 (eight-particle rectangle) using MDEM: (a) typical impact of the eight-particle rectangular clump, (b) rebound normal COR at the clump center, (c) rebound tangential velocity at the clump center (m/s), and (d) rebound rotational velocity (rad/s).	47

Figure 3.22:	Variation of rebound velocities versus object orientation for vertical impact of a rectangle and a superellipse power 4 using RBIM, and the represented clump of Table 3.3 (four-particle rectangle) using MDEM: (a) typical impact of the four-particle rectangular clump, (b) rebound normal COR at the clump center, (c) rebound tangential velocity at the clump center (m/s), and (d) rebound rotational velocity (rad/s).	48
Figure 3.23:	Variation of rebound velocities versus object orientation for vertical impact of the represented clump of Table 3.3 (seven-particle disk) using MDEM: (a) typical impact of the seven-particle discoidal clump, (b) rebound normal COR at the clump center, (c) rebound tangential velocity at the clump center (m/s), and (d) rebound rotational velocity (rad/s).	50
Figure 3.24:	Modified DEM consists of three modules: normal, tangential and rotational.	51
Figure 4.1:	Rigid body collision against a rigid surface (half space) where the contact point C is separated by an infinitesimal deformable body (the arrows show the positive signs).	54
Figure 4.2:	Typical variations of normal and tangential components of velocity, v_1 and v_3 , at the contact point versus normal impulse, after Stronge (2000) for: (a) slip-reversal and slip-stick in compression processes, and (b) continuous slip and continuous stick processes.	57
Figure 4.3:	Different impact angles defined in Table 4.1.	59
Figure 4.4:	Collinear impacts: (a) impact of spherical object, (b) impact of a rectangular shape, and (c) impact of an ellipsoidal object.	63
Figure 4.5:	Tangential coefficients versus impact velocity as defined by Pfeiffer et al. (1989): (a) Friction function versus tangential velocity, and (b) Friction scaling factor.	67
Figure 4.6:	Impact configuration for the application of Azzoni's model: (a) general eccentric impact, and (b) collinear impact (in Azzoni's model), any non-rotational collinear impact ends in zero normal rebound velocity and pure rolling.	69
Figure 4.7:	(a) The variation of contact forces versus time in two phases of compression and restitution, (b) the variation of normal impulse as a function of time.	71
Figure 4.8:	The impact of an eccentric object on a rigid half space at variable impact angles and different orientations, under zero gravity force.	73

Figure 4.9:	Variation of velocities and energies versus object orientation for planar impact of an ellipsoid at an impact angle of 45° ($V_{ini,hor} = 10$ m/s): (a) rebound normal velocity at the center, (b) rebound tangential velocity at the center (m/s), (c) rebound rotational velocity (rad/s), and (d) ratio of retrieved energies after impact to initial energies: the total retrieved energy consists of rotational and translational energies, the ratio of translational energy to total initial energy, and the ratio of rotational energy to total initial energy (in the above figures low, med., and large impact angles refer to the conventions defined in Table 4.1 and demonstrated in Figure 4.3).	75
Figure 4.10:	Variation of velocities and energies versus object orientation for planar impact of an ellipsoid at an impact angle of 45° , $V_{ini,hor} = 10$ m/s, using different impact models: (a) rebound central normal velocity (m/s), (b) rebound central tangential velocity (m/s), (c) rebound rotational velocity (rad/s), and (d) ratio of retrieved energies after impact to initial energies.	78
Figure 4.11:	Variation of the ratio of retrieved energies to initial energy versus object orientation for planar impact of an ellipsoid at an impact angle of 45° , $V_{ini,hor} = 10$ m/s, using different impact models: (a) Descouedres' model, and (b) Azzoni's model.	79
Figure 4.12:	Variation of the average velocities and retrieved energies versus the friction coefficient for the planar impact of an ellipsoid at an impact angle of 45° , $V_{ini,hor} = 10$ m/s, using RBIM at different energy COR, e_* : (a) averaged rebound normal velocity at the center, (b) averaged rebound tangential velocity at the center, (c) variation of the standard deviation of tangential rebound velocity, and (d) averaged ratio of retrieved total energy after impact to initial energy.	81
Figure 4.13:	Variation of the average velocities and retrieved energies versus the energy COR, e_* , for planar impact of an ellipsoid at an impact angle of 45° , $V_{ini,hor} = 10$ m/s, using RBIM at different friction coefficients: (a) averaged rebound normal velocity at the center (m/s), (b) averaged rebound tangential velocity at the center (m/s), (c) variation of standard deviation of normal rebound velocity (m/s), and (d) averaged ratio of retrieved total energies after impact to initial energies.	83
Figure 4.14:	Geometries used for rock representation: (a) spheres transferring to ellipsoid used in slenderness numerical experiment, aspect ratios from 1:1 to 3:1, and (b) Objects used in numerical shape experiment: rectangle, ellipsoid, and superellipsoid with ratio 2:1.	84
Figure 4.15:	Variation of the average velocities and retrieved energies versus aspect ratio for planar impact of an ellipsoid at an impact angle of 45° , $V_{ini,hor} = 10$ m/s, (average, maximum, and standard deviation values): (a) rebound normal velocity (m/s), (b) rebound tangential velocity (m/s), (c) ratio of total energy retrieved to initial energy, and (d) ratio of retrieved rotational energy to initial total energy.	86

Figure 4.16:	Variation of the rebound parameters versus object orientation for rocks with different geometries (shown in 4.14b) and with the configurations of Figure 4.8 with an impact angle of 0° ($V_{ini,hor} = 0$): (a) rebound normal velocity, (b) rebound tangential velocity, (c) rebound rotational velocity, and (d) ratio of retrieved total and rotational energies to initial energy.	89
Figure 4.17:	Variation of the rebound parameters versus object orientation for rocks with different geometries (shown in Figure 4.14b), with the configurations of Figure 4.8 at an impact angle of 45° and $V_{ini,hor} = 10$ m/s: (a) rebound normal velocity, (b) rebound tangential velocity, (c) rebound rotational velocity, and (d) ratio of the retrieved total and rotational energies to initial energy.	91
Figure 4.18:	Variation of the average rebound parameters versus impact angle for planar impact of an ellipsoid at $V_{ini,hor} = \text{var.}$ (from 0 to 30 m/s): (a) ratio of rebound normal velocity to initial normal velocity, (b) ratio of rebound tangential velocity to initial tangential velocity, (c) ratio of total retrieved energy to initial energy, and (d) ratio of retrieved rotational energy to initial rotational energy.	94
Figure 4.19:	Rigid body object rolling in the local Cartesian framework.	96
Figure 4.20:	Object vulnerable to toppling around corner.	98
Figure 5.1:	Hybrid contact search methods: (a) parabola-surface contact search method surface, and (b) error involved in estimation of the object orientation at contact for hybrid model.	105
Figure 5.2:	Hybrid contact search methods: circumscribing hybrid models: (a) Single-circle circumscribe hybrid method (SCCHM), (b) error involved in estimation of the object orientation at contact, (c) double-circle circumscribing hybrid method (DCCHM), and (d) error involved in estimation of the object orientation at contact in double circle method.	106
Figure 5.3:	Choosing two-dimensional slope profile from three-dimensional topography, after Bozzolo et al. (1986) and Azzoni et al. (1995).	108
Figure 5.4:	Slope modeling in <i>GeoRFS</i> : (a) slope made of straight rigid segments with node and segment numbering, and (b) segment rotation around middle point representing the uncertainties in geometrical modeling of slope.	109
Figure 5.5:	Rock shape representation in the <i>GeoRFS</i> simulation: (a) 3-D ellipsoids defined by Equation (5.2.1) for different values of n , after <i>mathworld.com</i> , (b) 2-D superellipse with different values of n , (c) prismatic 2-D objects with thickness, t and side number, s in addition to ellipse-extended shape, (d) circular cross section with radius r , (e) relative presentation of the rectangle, ellipse, and superellipse, and (f) n -sided polygonal section of prismatic object with the nodes P_1 to P_n .	111
Figure 5.6:	Different modes of motion: (a) freefall, (b) contact: impact, (c) contact: rolling-sliding, and (d) contact: arrest.	114

Figure 5.7:	(a) Body-based circular and rectangular cells, and (b) geometric transformation contact search method.	116
Figure 5.8:	The contact search procedure based on the intersection of the slope segment and the lines connecting the object's center and the potential contact points.	118
Figure 5.9:	Object segment contact points in the object's local coordinate system: (a) Superellipse-segment contact point, (b) polygon-segment contact, and (c) polygon-segment side contact when two contact points exist.	119
Figure 5.10:	(a) Polygon side contact happening at low angle of impact, (b) object-corner contact for superellipses, (c) object-corner contact for polygons.	120
Figure 5.11:	Multiple contact points in one time step: (a) multiple impact points, and (b) one rolling contact point and one impact contact point.	122
Figure 5.12:	<i>GeoRFS</i> graphical user interface (GUI): (a) typical input menu for a superellipsoid, and (b) typical output window showing the impact of the rock with a typical slope.	126
Figure 5.13:	UML representation of the main simulation classes used in <i>GeoRFS</i> in addition to the class relationship legend.	127
Figure 5.14:	The RocFall [®] research version graphical user interface simulating a highway slope.	129
Figure 5.15:	The seeder property window in RocFall [®] research version.	130
Figure 5.16:	The Material Property Window in RocFall [®] research version.	130
Figure 5.17:	The shape editor window in RocFall [®] research version showing the superellipse case.	131
Figure 6.1:	Double impact of different geometrical objects on a rigid half space at different orientations with $V_{ini,ver} = -10$ m/s located at a vertical distance equal to 3.0 m on: (a) horizontal plane, and (b) inclined plane, here 15° and 30°.	136
Figure 6.2:	Variation of the rebound parameters versus object initial orientation for planar impact of different geometrical objects with the configuration of Figure 6.1a and horizontal velocity equal to zero (impact angle of 0°): (a) ratio of the retrieved total energy to the initial total energy after the second impact, (b) ratio of the second normal rebound velocity to the initial normal velocity, (c) roll-out distances of object up to the second impact, and (d) maximum height of bounce after the first impact.	138
Figure 6.3:	Variation of the rebound energies and displacements versus object initial orientation for planar impact of different objects at the impact angle of 45° with the configuration of Figure 6.1: (a) ratio of the retrieved energy to the initial energy after the second impact, (b) ratio of the second normal rebound velocity to the initial normal velocity, (c) horizontal displacement of object until the second impact, and (d) maximum height of bounce after first impact.	140

Figure 6.4:	Variation of the rebound energies and displacements versus object initial orientation for planar impacts of different objects at the impact angle of 0° ($V_{ini,hor} = 0$ m/s) at a surface with an inclination angle of 30° with the configuration of Figure 6.1b: (a) ratio of the retrieved energies to the initial energy after the first impact, (b) ratio of the retrieved energies to the initial energy after the second impact, (c) horizontal displacements prior to the second impact, and (d) maximum height of bounce after the first impact (normal distance to the plane).	141
Figure 6.5:	Variation of the rebound energies and displacements versus object initial orientation for a planar impact of different objects at an impact angle of 45° ($V_{ini,hor} = 10$ m/s) on a 30° inclined surface with the configuration of Figure 6.1b: (a) ratio of the retrieved energies to the initial energy after the first impact, (b) ratio of the retrieved energies to the initial energy after the second impact, (c) central horizontal displacements prior to the second impact, and (d) maximum height of bounce after the first impact (normal distance to the plane).	143
Figure 6.6:	Variation of the rebound energies and roll-out distances versus object initial orientation occurring during five successive planar impacts of different objects (with an aspect ratio of 2:1) at an impact angle of 0° ($V_{ini,hor} = 0$) on a horizontal surface with the same configuration as in Figure 6.1a: (a) retrieved energies for the ellipsoid, (b) roll-out distances for the ellipsoid, (c) retrieved energies for the rectangle, (d) roll-out distances for the rectangle, (e) retrieved energies for ellipsoid-4, and (f) roll-out distances for ellipsoid-4.	146
Figure 6.7:	Variation of the rebound energies and roll-out distances versus object initial orientation occurred during five successive planar impacts of different objects (with an aspect ratio of 2:1) at an impact angle of 45° ($V_{ini,hor} = 10$ m/s) on a horizontal surface using the configuration of Figure 6.1a: (a) ratio of retrieved energies to initial energy for the ellipsoid, (b) roll-out distances for the ellipsoid, (c) ratio of retrieved energies to initial energy for the rectangle, (d) roll-out distances for the rectangle, (e) ratio of retrieved energies to initial energy for the ellipsoid-4, and (f) roll-out distances for the ellipsoid-4.	149
Figure 6.8:	Variation of bounce height versus object initial orientation occurring during five successive planar impacts of different objects (with ratio of 2:1) at an impact angle equal to 45° ($V_{ini,hor} = 10$ m/s) on a horizontal surface with the configuration as used in Figure 6.1a: (a) the ellipsoid-2, (b) the rectangle, and (c) the ellipsoid-4.	151
Figure 6.9:	Variation of the rebound parameters versus object initial orientation occurring during five successive planar impacts for different objects (with ratio of 2:1) at an impact angle of 45° ($V_{ini,hor} = 10$ m/s) on a surface with 15° of inclination and the configuration of Figure 6.1a: (a) roll-out distances after five impacts, and (b) bounce height envelope curve for five impacts.	152

Figure 6.10:	Average and maximum rebound parameters for different objects versus aspect ratio after five successive impacts at an impact angle of 45° ($V_{ini,hor} = 10$ m/s) on a horizontal surface with the configuration used in Figure 6.1a: (a) maximum roll-out distances, (b) average roll-out distances, (c) maximum retrieved energies, and (d) average retrieved energies.	154
Figure 6.11:	Variation of the average and maximum rebound parameters for ellipsoid-2 versus the friction coefficient for different energy COR after five successive impacts occurring with an impact angle of 45° ($V_{ini,hor} = 10$ m/s) on a horizontal surface with the same configuration as used in Figure 6.1a: (a) maximum roll-out distance, (b) the average roll-out distance, (c) maximum bounce height, (d) the average bounce height, (e) maximum ratio of retrieved total energy to initial total energy, and (f) the average ratio of total retrieved energy to initial total energy.	157
Figure 6.12:	Variation of the average rebound parameters for a rectangle versus the friction coefficient for different energy COR after five successive impacts occurring with an impact angle of 45° ($V_{ini,hor} = 10$ m/s) on a horizontal surface with the same configuration as used in Figure 6.1a: (a) the average of roll-out distances, (b) the average of bounce height, and (c) the average of the ratio of retrieved total energy to initial total energy.	160
Figure 6.13:	Rock trajectories during five successive impacts for different geometries and the configurations used in Figure 6.1a and the settings of Table 6.4 for rock aspect ratios of 1:1.05, 1:1.5, 1:2.0, 1:3.0: (a) ellipsoid-2, (b) prism with rectangular cross section, and (c) ellipsoid-4.	162
Figure 6.14:	Rock trajectories during several successive impacts for rock geometries including: ellipsoids 2 and 4 and a rectangle with the configurations of Figure 6.1a and settings of Figure 6.4 for a rock aspect ratio equal to 2:1: (a) 5 impacts, (b) 10 impacts, and (c) time limit of 10 seconds.	164
Figure 6.15:	Rock trajectories during successive impacts for rock geometries of a near sphere (ellipsoid with aspect ratio of 1:1.05) and prisms with square and polygon five and six-sided cross sections using the configurations of Figure 6.1a and the settings of Figure 6.4 for rock aspect ratio equal to 1:1: (a) 5 impacts, (b) 10 impacts, and (c) 10 seconds.	165
Figure 6.16:	Typical rockfall test performed by Pierson et al. (2001) where the slope is 12.0 m height and the circles denote the rocks.	167
Figure 6.17:	Slope configurations used in numerical tests with inclination of 1H:4V and catchment areas of flat and 6H:1V.	168

Figure 6.18:	Variation of roll-out parameters versus slope height for different geometrical shapes and for the slopes with the same configuration as used in Figure 6.17 and the setup of Table 6.4: (a) roll-out distance for 90% caught, flat catchment area, (b) roll-out distance for 90% caught, 6H:1V catchment area, (c) average roll-out distance, flat catchment area, (d) average roll-out distance, 6H:1V catchment area, (e) roll-out standard deviation, flat catchment area, and (f) roll-out standard deviation, 6H:1V catchment area.	171
Figure 6.19:	Rockfall roll-out distance histograms for different geometrical shapes and for the 24 m slope using the configuration of Figure 6.17 and flat catchment area: (a) frequency curve for different geometries, (b) cumulative frequencies for different geometries, (c) frequency for five and six-sided polygonal shapes, (d) frequency for ellipsoidal and prism with a rectangular cross section, and (e) frequency and cumulative histogram for field observation after Pierson et al. (2001).	173
Figure 7.1:	3D rigid body collision on a rigid half space: (a) eccentric impact of an arbitrary object, and (b) collinear impact of a sphere.	185
Figure 7.2:	Histogram of the variation of the coefficients of restitution for an ellipsoid with different aspect ratios for an impact angle of 45° and the settings of Figure 4.8: (a) tangential COR, and (b) normal COR.	189
Figure A.2.1:	Defining rebound height, h_r , using collinear drop test.	195
Figure A.2.2:	Calculating the friction coefficients: (a) using the sliding test on an inclined surface for the friction coefficient, μ , and (b) using rolling test on an inclined surface to define the rolling friction coefficient, μ_r .	196
Figure A.3.1	Rock trajectories during successive impacts for rock geometries with the configurations of Figure 6.1a and settings of Figure 6.4 for different rock geometries with aspect ratio equal to 2:1 after 5 impacts: (a) an ellipsoid-2, (b) an ellipsoid-4, and (c) a rectangle.	199
Figure A.3.2	Rock trajectories during successive impacts for rock geometries with the configurations of Figure 6.1a and settings of Figure 6.4 for different rock geometries with aspect ratio equal to 2:1 after 10 impacts: (a) an ellipsoid-2, (b) an ellipsoid-4, and (c) a rectangle.	200
Figure A.3.3	Rock trajectories during successive impacts for rock geometries with the configurations of Figure 6.1a and settings of Figure 6.4 for different rock geometries with aspect ratio equal to 2:1 after 10 seconds: (a) an ellipsoid-2, (b) an ellipsoid-4, and (c) a rectangle.	201

LIST OF APPENDICES	PAGE
APPENDIX 1: VALUES OF RESTITUTION, FRICTION, AND ROLLING FRICTION COEFFICIENTS	191
APPENDIX 2: DEFINING RIGID BODY IMPACT MECHANICS (RBIM) PARAMETERS USING EXPERIMENTAL METHODS	194
APPENDIX 3: EFFECT OF ROCK SHAPE ON SINGLE ROCK TRAJECTORIES PERFORMING RANDOM OBJECT GENERATION	197

LIST OF SYMBOLS

Roman symbols

a, b, c	ellipsoids and prisms dimensions in three perpendicular directions
a_1, a_3	the acceleration components of the object's center of gravity
a_i	translational acceleration
A	cross sectional area
c	viscosity coefficient
C_n, C_s	normal and tangential damping coefficients
COR	coefficient of restitution
D_{max}	object's maximum dimension
e	normal coefficient of restitution
e_n	kinetic coefficient of restitution
e_*	energy coefficient of restitution
E	modulus of elasticity
E_r, E_i	translational energies after and before impact
F	contact force
F	contact friction force
F_n, F_t	normal and tangential contact forces
$F(x, y)$	object closed-form equation
\hat{f}	friction force direction
G	gravitational acceleration
\hat{g}	gravity vector
I	moment of inertia around the axis perpendicular to the surface
\hat{I}	rotation matrix
I_{kl}	inertial tensor
k	spring stiffness in the system of one degree of freedom
k_r	polar radius of gyration
K_n, K_s, K_r	normal, tangential, and rotational stiffness of the springs
K_0	the total initial kinetic energy
M	object's mass
n	ellipsoid power
$n_{fractions}$	the number of secondary timestep refinements

n_x, n_y	contact normal vector components in two perpendicular directions
\hat{n}	contact normal vector
N	contact normal force
p_i	i^{th} component of impulse
p_c, p_f, p_s	termination impulses for: normal velocity, contact, tangential velocity
$p_{c,crit}, p_{f,crit}, p_{s,crit}$	critical termination impulses for: normal velocity, contact, tangential velocity
p_1, p_3	tangential and normal impulses at the contact
\hat{p}	impulse vector
\bar{P}_n	polygon nodal vector
P_n	polygon nodal coordinate
r_1, r_3	contact vector components
r_n	the modified tangential contact vector in tangential direction
r_i	i^{th} component of contact vector
\hat{r}	object position vector
R	circle (sphere) radius
R_n	normal coefficient of restitution
R_t	tangential coefficient of restitution
$R_{t,min}$	minimum tangential coefficient of restitution
$R_{Kinematic} (R_v)$	kinematic (velocity) coefficient of restitution
R_{Kin}	kinetic coefficient of restitution
$R_{Energy} (R_E)$	energy coefficient of restitution
$R_{E,trans}$	translation energy coefficient of restitution
$R_{E,tot}$	total energy coefficient of restitution
\bar{R}_E	average total retrieved energy
\hat{s}	slip direction
s	sliding speed
t	time
t_c	contact time
T_R, T_S, T_T	transformation matrices of rotation, scaling, and translation
v_1, v_3	contact velocities in the tangential and normal directions
v_i	i^{th} component of contact velocity vector
V	object volume
$V_{I,min}$	minimum value of rebound tangential velocity
V_{arrest}	the threshold cut-off velocity
V_i	i^{th} component of object velocity vector
$V_{ini,ver}, V_{ini,hor}$	initial object velocity in vertical and horizontal directions

V_{n1}, V_{n2}	approaching and rebound normal velocities
V_{t1}, V_{t2}	approaching and rebound tangential velocities
v_n, V_n	normal velocities at the object center before and after impact
\hat{V}, \hat{v}	incoming and outgoing object's velocities
v_t, V_t	tangential velocities at the object center before and after the impact
$v_{roll,tr}$	rolling threshold velocity
\hat{V}	object velocity vector
$\bar{V}_{r,n}, \bar{V}_{r,t}$	average rebound normal and tangential velocities
W_c	work done by normal component of impulse during compression
W_r	work done by normal component of impulse during restitution
x	overlap in oscillating systems
x, x_0	object global coordinate in x axis, its initial value in x direction
y, y_0	object global coordinate in y axis, its initial value in y direction
z, z_0	object global coordinate in z axis, its initial value in z direction

Greek symbols

α	rotational acceleration
α_c	angle at which the stick situation changes to sliding
$\beta_a, \beta_b, \beta_c, \beta_d$	indexes helping in defining the rebound velocities applying Stronge impact theory
β_1, β_2	toppling angles
$\bar{\beta}_c$	index helping in defining the rebound velocities applying Stronge impact theory
β_i	configuration matrix components
β_{snd}	percentage of the diameter which results in the maximum acceptable overlap
γ	angle of incidence (impact)
Δt	time step
Δt_{max}	maximum time step
ε_{ijk}	permutation number
ε_{max}^e	energy coefficient of restitution
Z, Z_0, Z_f	dimensionless velocity, its initial and final values
η	ratio of tangential and normal springs stiffness at a contact
θ	object orientation around the axis perpendicular to the plane
λ	ratio of the natural frequencies of tangential to normal direction
μ	friction coefficient
μ_c	critical friction coefficient

μ_s	sliding (friction) coefficient in Voigt-Kelvin module
μ_r	rotational friction coefficient
$\bar{\mu}$	friction coefficient used as stick condition
ν	Poisson ratio
ϕ	sliding direction
$\hat{\phi}_i$	in-plane sliding direction for spheres in 3D impacts
X, X_0	dimensionless displacement and its initial value
ψ	slope (segment or line) inclination
ω	the rotational velocity
ω_i	rotational velocity vector
ω_0	initial rotational velocity
$\hat{\omega}$	rotation matrix
Ω_n, Ω_t	natural frequencies of the system in the tangential and normal directions

CHAPTER 1

INTRODUCTION AND OUTLINE

Rockfalls occur when rocks or boulders detach from mountains or hills and tumble down. Rockfalls can pose significant hazards to infrastructures next to mountainous areas, and they are one of the events triggered by earthquakes which cause fatalities. Slopes that are at risk of rockfall have highly variable geometries. The location, mass, and shape of the rocks that might dislodge and fall are uncertain. Moreover, the materials that make up a slope can vary considerably from one section of a slope to another. Furthermore, the relevant material properties for the slopes are usually not well known. Performing probabilistic simulations of rockfalls, combined with proper statistical analyses, has proven to be an effective and acceptable method for predicting the rock path trajectories. A rockfall model is evaluated based on its ability to efficiently predict the velocity, frequency, bounce height, and run-out distance of falling rocks. With this information, the engineer can design remedial measures such as restraining nets and ditches. The movements of a falling rock can be classified as freefall, bouncing, sliding, toppling, or rolling. The falling trajectory is controlled mainly by the geometry of the slope, the rock shape, and the energy dissipated at each contact of the rock with the slope.

Most of the existing rockfall simulation programs are based on particle models that consider the falling rock as an infinitesimal particle with a mass, called the lumped mass (stereomechanical) models. Other models involve hybrid methods relying on simplified assumptions. The most common hybrid methods are based on contact searching for the movement of a dimensionless object, and incorporating some aspects of rigid body impact

mechanics for bouncing. The literature also describes simulations which use simplified rigid body models. The work in this thesis applies a more sophisticated rigid body theory based on rigid body impact mechanics (RBIM) developed by Stronge (1994). Stronge's theory captures all modes of rigid body movement. Due to the importance of rock geometry, in this work, single and multiple impacts of different rock geometries are investigated. The effects of rock slenderness, angle of impact, rock orientation at impact, and slope material properties on rebound velocities and energies are investigated. The correspondence between the model parameters and data from rockfall literature will be discussed and an in-situ rockfall test will be replicated.

This thesis is structured in 7 chapters:

Chapter 2 is devoted to providing the preliminaries needed in creating and understanding a rockfall simulation. The available theories in impact modeling are presented with the limitations and advantages of each theory. The essential definitions of the coefficients of restitution are presented along with the parameter values in the rockfall literature.

In Chapter 3 the application of discrete element modeling (DEM) in rockfall simulation is investigated. This chapter introduces a modified version of discrete element modeling in which the normal linear dashpot is replaced with a nonlinear module. In this modified version, in the tangential direction, a mono-direction spring replaces the spring where the tangential dashpot is eliminated. The results of the impact of rigid body clumps using the modified module are compared with the impact results of similar objects using rigid body impact mechanics.

Chapter 4 reviews rigid body impact mechanics, introduced by Stronge (1994), and offers a method for defining the slipping process in two-dimensional space. This model is compared with several available rigid body models in the rockfall literature. The classical definition of coefficients of restitution (COR) is challenged by introducing rock geometries. The effects of several parameters on the variation of COR are studied. The essential equations for rigid body rolling and toppling are also presented in this chapter.

In Chapter 5 the developed geometrical rockfall simulation program, *GeoRFS*, is introduced. Several basic assumptions and procedures used in the program are introduced including: modes of motion definition, rock geometries, contact search procedures, and time step criteria. In addition to a description of the application of class structure, the simulation pseudo-code is provided. Finally the application of the simulation in the new version of RocFall[®] is illustrated.

In Chapter 6, the simulations created in this code are utilized to study the trajectories of different rock geometries during multiple impacts on flat and inclined impact surfaces. Several rock trajectory parameters including roll-out distances, bounce heights, velocities, and energies are studied during different stages of impact. The effect of rock orientation, impact angle, slope material parameters, and rock slenderness on the roll-out distances and energy levels after multiple impacts are investigated. As a case study, the in-situ experiments of Pierson et al. (2001), performed to develop design charts for dimensioning rockfall catchment areas adjacent to highways, were replicated using the new version of RocFall[®].

Conclusions and suggestions for further research work are summarized and outlined in Chapter 7.

CHAPTER 2

ROCKFALL STUDIES – PRELIMINARIES AND LITERATURE REVIEW

2.1 INTRODUCTION

Rockfalls occur when rocks or boulders detach from mountains, hills, or rock cuts and tumble down. They can pose significant hazards to infrastructure such as highways, buildings, and open pit mines, and they can sometimes result in injury or death. Rockfalls can cause the same number of fatalities as all other forms of rock slope instability combined, Hoek (2007). Badger and Lowell (1992) stated that 45% of rock slope instabilities are related to rockfall phenomena. Hunger and Evans (1989) stated that 13 deaths were caused by rockfalls during the last 87 years prior to 1989 in Canada, all of them in British Columbia.

Understanding rockfalls involves investigating two main stages: the triggering and the post-failure stages. Researchers have pursued one or other of these directions. This research studies the post-failure procedure, disregarding the triggering process.

Usually, rockfalls are initiated by some climatic, biological or mechanical events making a change in the active and passive forces on a piece of rock, as stated by Hoek (2007). These events may include: pore water pressure increase due to rain, freeze-thaw process in the cold climate, wind and sand erosion in dry climates, climate degradation or weathering of the rocks, earthquake vibrations, and mechanical disturbances from active construction zones.

The movements of a falling rock can be classified as freefall, bouncing, sliding, toppling, or rolling. Figure 2.1 demonstrates a rockfall trajectory next to a mountain slope. Recently, computer programs have become popular for modeling the trajectory of a falling rock. The most important, and yet very complicated, mode of motion is the impact mode. The most common models used in rockfall simulations are lumped-mass (or stereomechanical) models which are based on particle methods that concentrate the mass of a rock at an infinitesimal particle (Wu (1985), Fornaro et al. (1990), Evans et al. (1993), Giani et al. (1992), Hoek (1986), and Spagn et al. (1988)).

Other models involve hybrid methods that utilize simplified impact models at the time of the impact of a particle and a surface such as the models offered by: Pfeiffer et al. (1989), Bozzolo et al. (1988), Azzoni et al. (1995), Stevens (1989) and Jones et al. (2000).

A few rigid body models are offered in the rockfall literature which consider simplified rock geometries and use specific impact model such as: Descouedres et al. (1987) and Kobayashi et al. (1990). The different categories of impact models which potentially can be used in rockfall simulations are studied in the following section.

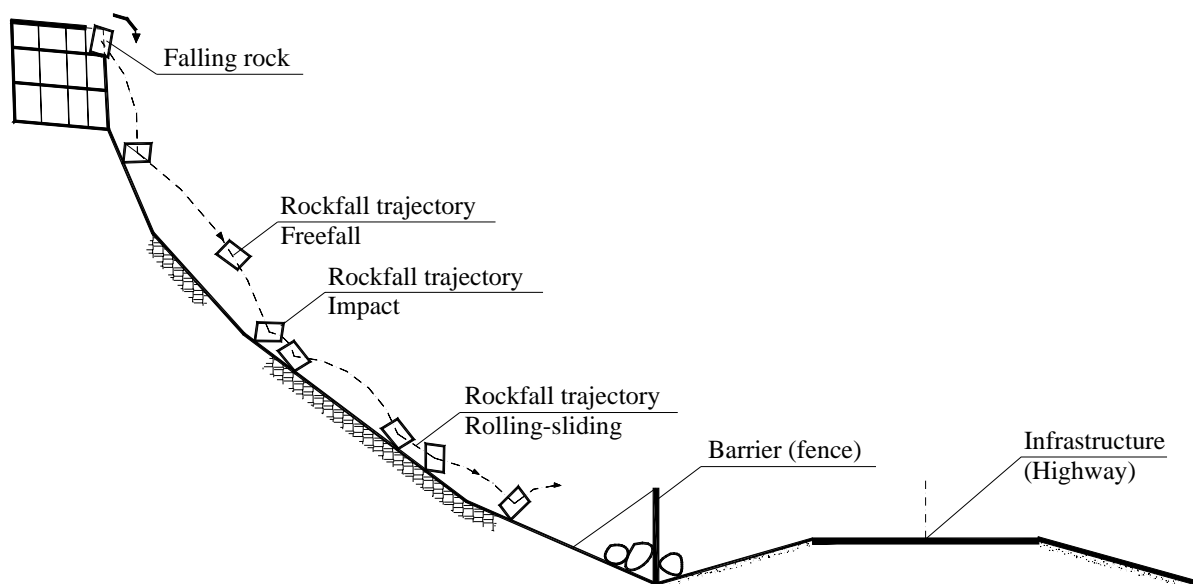


Figure 2.1: Rockfall trajectory in a mountain slope next to a highway.

2.2 ROCKFALL IMPACT MODELS

The collision of two approaching objects, or one object and an infinite surface, occurs at a surface referred to as the collision surface or impact area. For an infinitesimal time step, the relative velocities of some close parts of the two objects are negative, indicating that, for that brief point in time, the objects are in contact with each other. The mobilized contact forces, brought on by collision, push the two objects to separate from each other, causing the relative contact velocities to become positive. Any numerical model which tries to replicate the generation of the impulses at the contact point and predict the rebounding velocities is known as an impact model.

The majority of the existing impact models study collisions which occur at low impact velocities. The deformations caused by this type of impact are imperceptible; impacts for which this is not the case are out of the scope of these types of models. Stronge (2000) has produced a list of the existing impact theories, reproduced here in Table 2.1.

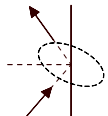
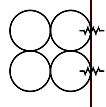
In stereomechanical or lumped-mass models the rebound velocities are a discontinuous function of the incident velocities, while in the other models the velocities are usually a function of either time or impulse. The computational cost of finding the contact point is usually higher in rigid body models in comparison to lumped-mass models; however, the computational effort needed for lumped-mass and rigid body models is significantly lower than the effort needed in discrete element and continuum models. As a result, the rigid body models are an important candidate for rockfall probabilistic modeling, which is repetitive in nature. The application of rigid body mechanics in rockfall modeling is the main subject of this study, explored in Chapters 4 through 6.

Hybrid models use the contact search procedures similar to lumped-mass models, while they use mathematical impulse models to calculate the rebound velocities. For hybrid models, both the contact search procedure and applying the impact equations are computationally effective. The first hybrid model was offered by Bozzolo et al. (1982) followed by several researchers such as Azzoni et al. (1995), and Pfeiffer et al. (1989). Hybrid impact models

will be studied in Chapter 4 and their application in rockfall simulation are discussed in Chapter 5.

Cundall and Hart (1992) identify four different classes of simulations which are part of the general definition of discrete element modeling (in UDEC, 2000): distinct element methods, modal methods, discontinuous deformation analysis (DDA), and momentum-exchange methods. The distinct element method, which is the numerical model studied in Chapter 3, applies explicit time-driven methods to solve equations of motion. The main representatives of these models are UDEC (2000) and PFC (2002). These models have the potential of modeling rock fragmentation as shown by Potyondy et al. (2004).

Table 2.1: Available theories for low speed impact, after Stronge (2000)

<i>Impact theory</i>	<i>Independent variable</i>	<i>Independent parameters</i>	<i>Computational effort</i>	<i>Illustration</i>
<i>Lumped-mass (Stereomechanical)</i>	None	R_n, R_t ^a	Contact search: low ^b Application: low ^c	
<i>Hybrid</i>	None	R_{Kin} or R_{Energy} ^d μ	Contact search: low Application: low	
<i>Rigid body</i>	Impulse (p)	R_{Kin} or R_{Energy} μ	Contact search: medium Application: low	
<i>Discrete element (compliant contact)</i>	Time (t)	Combination of ^e springs, dashpots, and sliders	Contact search: medium Application: medium	
<i>Continuum</i>	Time (t)	Elastic moduli	Contact search: high Application: high	

^a normal and tangential coefficients of restitution

^b computational effort needed for contact search procedure

^c computational effort needed for calculating the rebound velocities

^d kinetic or energy coefficient of restitution in addition to friction coefficient

^e tangential and normal (even rotational) springs and dashpots along with sliders

DDA, developed by Shi (1985), assumes the contacts as rigid bodies; however, the blocks can be rigid or deformable. The impenetrability condition is achieved by performing iterative methods, while the deformability comes from the superposition of strain modes. Continuum models, like finite element methods (FEM), are also out of the scope of this work, due to their high computational cost (for the application of FEM in impact mechanics refer to Belytschko (2000) and Wriggers (2002)).

Lumped-mass and rigid body models use different definitions of the coefficients of restitution. Discrete element modeling also uses a combination of dashpots and sliders as the source of energy dissipation, as will be discussed in Chapter 3. In addition, most of the data in rockfall literature is expressed in the terms of the coefficients of restitution. It is not practical to utilize various definitions for energy dissipation in each theory if there is an intention to compare the energy dissipations in different theories and use the rockfall literature values. As a result the parameters in rigid body or discrete element models are calibrated and compared according to the definitions used for coefficients of restitution defined in lumped-mass model.

Due to the importance of these coefficients, different categories of coefficients of restitutions are studied in the following section.

2.2.1 Coefficients of restitution (COR)

Coefficients of restitution characterize the amount of energy lost due to the inelastic deformation during the collision of two objects or an object and a surface. Different definitions have been suggested for the coefficients of restitution (COR), but there is no consensus among researchers. There are three groups of definitions for defining the coefficients of restitution, as described by Stronge (2000): kinematic, kinetic, and energy coefficients of restitution.

2.2.1.1 Kinematic coefficient of restitution

The kinematic coefficient of restitution was originally identified and named by Newton (1686) to describe the amount of energy lost during the impact of identical spheres. A

popular definition for the COR in this category is the ratio of the particle rebounding velocity, V_r , to the incoming velocity (the velocity prior to impact), V_i . This ratio is known as velocity COR:

$$R_v = \frac{V_r}{V_i} \quad (2.2.1)$$

The most widely accepted definition for the COR is derived by projecting the velocity vector into two perpendicular directions, normal and tangential to the impact surface. The two coefficients are described by the ratios of the velocities before and after the impact:

$$R_n = \frac{V_m}{V_{in}} \quad , \quad R_t = \frac{V_{rt}}{V_{it}} \quad (2.2.2)$$

where V_m and V_{rt} are the components of the rebounding velocity normal and tangential to the impact surface, respectively. V_{in} and V_{it} are the equivalent components of the incoming velocity of the object. This type of model, which applies the tangential and normal COR, is known as a lumped-mass or stereomechanical model and is the most common model used in rockfall studies. Such models have been applied by several researches such as: Wu (1985), Fornaro et al. (1990), Pfeiffer et al. (1989), Evans et al. (1993), Giani et al. (1992), Hoek (1986), and Spagn et al. (1988).

2.2.1.2 Kinetic coefficient of restitution

The kinetic coefficient of restitution describes the ratio between the tangential and normal impulses during impact, and can be defined for rough objects which have friction. This definition was initially introduced by Poisson (1811) with later work demonstrating that the kinetic coefficient is related to the friction coefficient, Stronge (2000). Despite the wide usage of kinematic coefficients in rockfall studies, kinetic coefficient is not widely used, with a few exceptions (Descouedres (1987)), and will be discussed in detail in Section 4.3.3. The coefficient is as follows:

$$R_{kin} = \frac{p_t}{p_n} \quad (2.2.3)$$

where p_t and p_n are the tangential and normal impulses and R_{Kin} is the kinetic coefficient of restitution.

2.2.1.3 Energy coefficient of restitution

The energy coefficient of restitution defines the ratio of the retrieved energy after the impact to the initial energy. The most common definition utilized for this purpose is the ratio between the translational energies:

$$R_{E,Trans} = \frac{E_{r,tr}}{E_{i,tr}} = \frac{1/2 MV_r^2}{1/2 MV_i^2} = \frac{V_r^2}{V_i^2} \quad (2.2.4)$$

In the above equation $E_{r,tr}$ and $E_{i,tr}$ are the translational energies before and after the impact, and M is the particle mass. This definition is not robust as it does not consider the effect of the rotational component of the energy. A more robust definition, for two dimensional impacts, is as follows:

$$R_{E,Kin} = \frac{E_{r,kin}}{E_{i,kin}} = \frac{1/2(MV_r^2 + I\omega^2)}{1/2(MV_i^2 + I\Omega^2)} = \frac{V_r^2 + k_r^2\omega^2}{V_i^2 + k_r^2\Omega^2} \quad (2.2.5)$$

where I and k_r are the moment of inertia and polar radius of gyration, respectively, ω and Ω are the rotational velocities after and before the impact, and $E_{r,kin}$ and $E_{i,kin}$ are kinetic energies before and after impact. Bozzolo et al. (1988) and Azzoni et al (1955) employ this definition of COR for their proposed impact models. This definition of COR, defined by Equation (2.2.5), incorporates the effect of rotational velocities to the values of COR and as a result, this definition is widely used in this thesis to compare the ratio of retrieved energy to initial energy for different impact setups. In Section 4.2.2 another definition for the energy COR, defined by Stronge (1994a), will be introduced.

Another definition for the energy coefficient of restitution, which is used in Chapter 6, is the ratio of total energy after the impact to total energy before the impact. This definition of COR is used for comparing the retrieved energies for different objects when, at the time of impact, they have equal total energies while they have different kinetic energy. Total energy coefficient of restitution can be defined as follows:

$$R_{E,Tot} = \frac{E_{r,Kin} + E_{pot}}{E_{i,Kin} + E_{pot}} = \frac{1/2(MV_r^2 + I\omega^2) + Mgz}{1/2(MV_i^2 + I\Omega^2) + Mgz} = \frac{0.5(V_r^2 + k_r^2\omega^2) + gz_c}{0.5(V_i^2 + k_r^2\Omega^2) + gz_c} \quad (2.2.6)$$

In the equation above, E_{pot} is the object's potential energy, z_c is the level of center of gravity, and g is gravitational acceleration. It should be mentioned that in the framework of rigid body impact mechanics the object does not displace during the impact, therefore the object's elevation is constant.

2.2.2 Values of coefficients of restitution in rockfall literature

In order to acquire precise data to use during different modes of motion in rockfall simulation programs, several approaches can be used, as defined by Heidenreich (2004). These methods are as follows: back analysis of natural rockfall events, in-situ tests, and laboratory experiments. The values of the resulting coefficients used in each numerical model are entirely dependent on the type of experiment performed to derive the coefficients. Figure 2.2 shows the variability of the tangential and normal coefficients of restitution for different slope materials as reported by Fornaro et al. (1990), Wu (1985), and Chau et al. (2002). The Figure reveals the high range of variability for both the tangential and normal coefficients of restitution. This variability should be attributed to factors other than the slope material. As will be discussed in this thesis, several parameters in addition to the slope material affect the values of the coefficients of restitution, including: rock shape, rock slenderness, impact angle, and mass distribution around the contact point. Several researchers have gathered information on different coefficients of restitution, such as Stevens (1998), Azzoni et al. (1995), and Jones et al. (2000). Heidenreich (2004) categorized these coefficients based on the group of COR discussed in Section 2.2.1. These coefficients are presented in Appendix 1 based on the tables provided by Heidenreich (2004) and RocFall (2002).

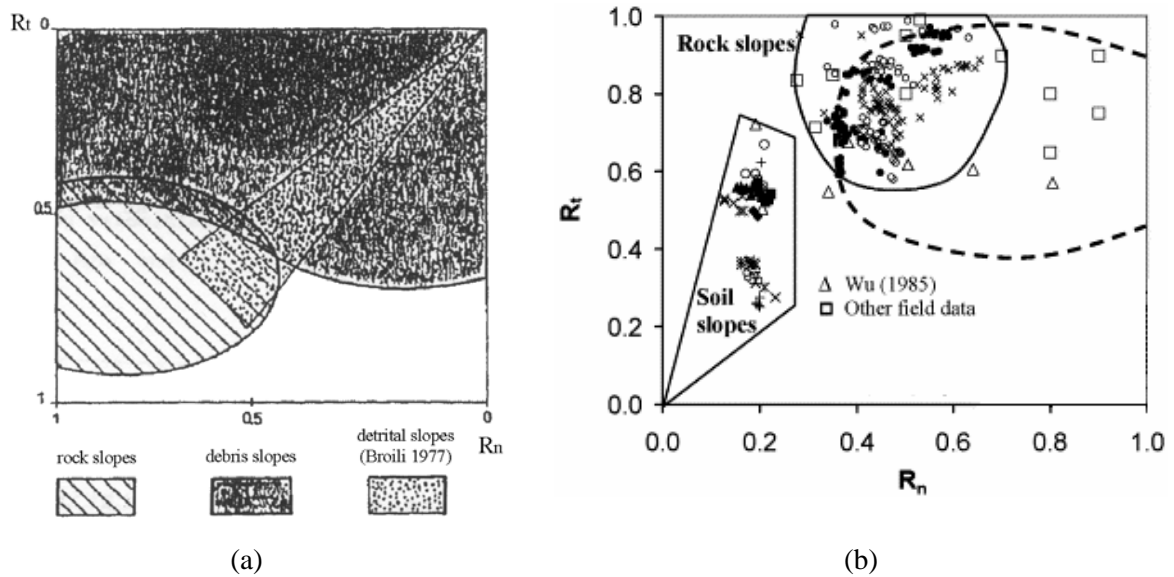


Figure 2.2: The range of variation for the coefficients of restitution in R_n - R_t space: (a) after Fornaro et al. (1990), and (b) after Chau et al. (2002).

2.3 SUMMARY AND CONTRIBUTION OF THESIS

As stated in Section 2.2.1.1, the majority of rockfall simulations deploy kinematic definition for the coefficient of restitution, as these models assume that the coefficients of restitution are intrinsic material parameters. The conventional definition of the normal coefficient of restitution has a physical interpretation when the object impacts a surface collinearly. However, when the impact configurations are eccentric, no physical interpretation exists. There is also no practical way in the literature to define a value for the tangential coefficient of restitution, especially when the rock has non-circular geometry.

In this research, the application of two numerical models to rockfall simulation is investigated: discrete element modeling (DEM), and rigid body impact mechanics (RBIM). In both RBIM and DEM, the models' parameters have a physical interpretation and are measurable. RBIM uses an energy coefficient of restitution which is compatible with the normal coefficient of restitution, when the impact configuration is centric, and can be derived through experiments. It is shown that the normal dashpot in DEM, as the main source of impact energy dissipation, can be calibrated with the normal coefficient of restitution.

Additionally, both models use the friction coefficient, which also has a physical interpretation.

To apply DEM to rockfall simulation, the author proposes a modified version of DEM (MDEM). In MDEM, the normal dashpot is replaced with a nonlinear dashpot. This dashpot eliminates the shock force at impact initiation, eliminates the tensile force at impact termination, and correlates the amount of energy dissipation (normal coefficient of restitution) with the impact velocity. As a result of the application of the nonlinear dashpot, the no-tension unit can be detached. This work proposes to remove the dashpot in the tangential direction, while a mono-direction mechanical unit is added. This unit releases the strain energy stored in the tangential direction when the direction of tangential slip reverses. As a result, the mono-direction unit eliminates the inconsistent variation of the tangential contact velocity for low compliance impacts. To demonstrate that the modified model can sufficiently capture low compliance impacts, the author has compared the rebound velocities of rigid assemblies of particles, known as clumps, with equivalent geometrical shapes when using RBIM. As predicted, the trends of variation of rebound velocities are compatible with the variations predicted by RBIM whenever the clump geometry satisfactorily represents the equivalent geometries.

In the application of RBIM to rockfall simulation, a practical method is offered in this work to accurately define the tangential slipping process and the rebound velocities. The author completed the rebound velocities equation table, originally offered by Stronge (2000), to incorporate all modes of impact, rebound velocities, and slip direction in two-dimensional space. In this work, the rebound velocities and energies predicted by RBIM are compared with selected impact models previously offered in the rockfall literature (Descouedres (1987) and Azzoni (1995)). In addition, the effects of the different parameters on the rebound velocities and retrieved energies at different impact configurations are investigated, including: rock shape and slenderness, impact angle, material parameters, and rock orientation. The author showed that the conventional definitions of coefficients of restitution are not applicable to geometrical shapes, where the geometries allow for eccentric impacts.

In the framework of this research a deterministic simulation program, *GeoRFS*, is developed by the author based on rigid body mechanics. RBIM is used as the main impact model and rigid body rolling is used for rolling modeling. This simulation considers rock geometry ranging from ellipsoidal shapes to prisms with a concave polygonal cross section, and considers the slope as a polyline consisting of rigid line segments. In addition to RBIM, the author has offered closed-form solutions for two-dimensional impact models offered by Azzoni (1995) and Descouedres (1987), implemented in the *GeoRFS* application. It is demonstrated that by using Object-Oriented programming techniques, any other impact model can be applied to the simulation by implementing a new impact model class. Because the falling rock initial configurations can not be predicted in rockfall simulation, the probabilistic analysis is provided by transferring the *GeoRFS* engine to the graphical user interface (GUI) of the research version of the program RocFall[®] from RocScience Company.

By applying the developed applications, *GeoRFS* and the RocFall[®] research version, this research studies successive impacts of different rock geometries on horizontal and inclined surfaces under different impact configurations. It is shown that rock geometry strongly affects trajectories, bounce heights, and velocities (kinetic energy) during successive impacts.

In this work the field experiments performed by Pierson et al. (2001) are modeled using the proposed simulation programs. The author demonstrates that the developed programs can satisfactorily capture the roll-out distances observed in the field tests. However, for some geometrical objects, as it is expected from a two-dimensional simulation, the predicted roll-out distances are rather conservative where the trend of variation has a high standard deviation. For future work, it is suggested that a three dimensional simulation program based on RBIM be developed in order to more accurately model roll-out distances.

CHAPTER 3

APPLICATION OF DISCRETE ELEMENT MODELING (DEM) TO ROCKFALL SIMULATION

3.1 INTRODUCTION

Discrete element modeling (DEM) was originally introduced by Cundall et al. (1979) to define the interaction of an assembly of disks or spheres. The authors demonstrated that this theory is capable of defining the chain of contact forces between the assemblies of particles. In this section, the applicability of this theory to impact mechanics is investigated. In the DEM, the forces are mobilized as the disks overlap. The contact forces developed in DEM can represent the viscous nature of the impact; in other words, they are especially suitable for impacts where the contact response is velocity dependent. Figure 3.1 shows the system of the linear Kelvin-Voigt model in which one spring and one dashpot act in parallel. When the contact occurs, to represent the interaction of overlapping objects, a Kelvin-Voigt model is used in both the tangential and normal directions. It should be emphasized that, in this simple DEM module, five coefficients are needed to define the model: two stiffness moduli, K_n and K_s ; two damping coefficients, C_n and C_s ; and one sliding (friction) coefficient, μ_s .

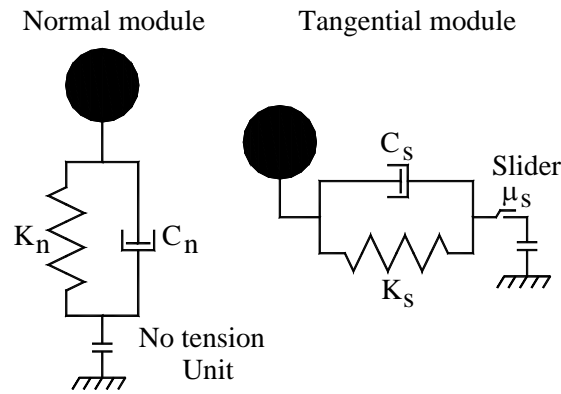


Figure 3.1: Kelvin-Voigt system of spring and dashpots in normal and tangential directions with a no-tension unit in normal direction and a slider in tangential direction.

3.2 THE NORMAL DIRECTION IN DEM

3.2.1 Viscoelasticity in the normal direction

In the DEM proposed by Cundall et al. (1979), the viscosity is caused by a linear dashpot which acts in parallel to a linear spring. In this model the variation of the normal component of the contact force versus time is typically half sinusoidal. In a typical collision, during the first period of the impact, the normal force develops in compression and during the restitution phase, this force decreases until the contact terminates. As a result, the resultant normal force is purely compressive during the contact period.

Figure 3.2 demonstrates the variation of normal force versus time as well as its variation versus contact overlap for a linear viscoelastic system. The variation of this system in the absence of any other external forces can be described by Equation (3.2.1), which is the differential equation of the system with one degree of freedom, vibrating without the exertion of external forces. The equation is as follows:

$$m\ddot{x} + c\dot{x} + kx = 0 \quad (3.2.1)$$

where m is the mass, c is the viscosity coefficient, and k is the linear stiffness of the system while x represents the overlap between either two particles or a particle and a rigid half space.

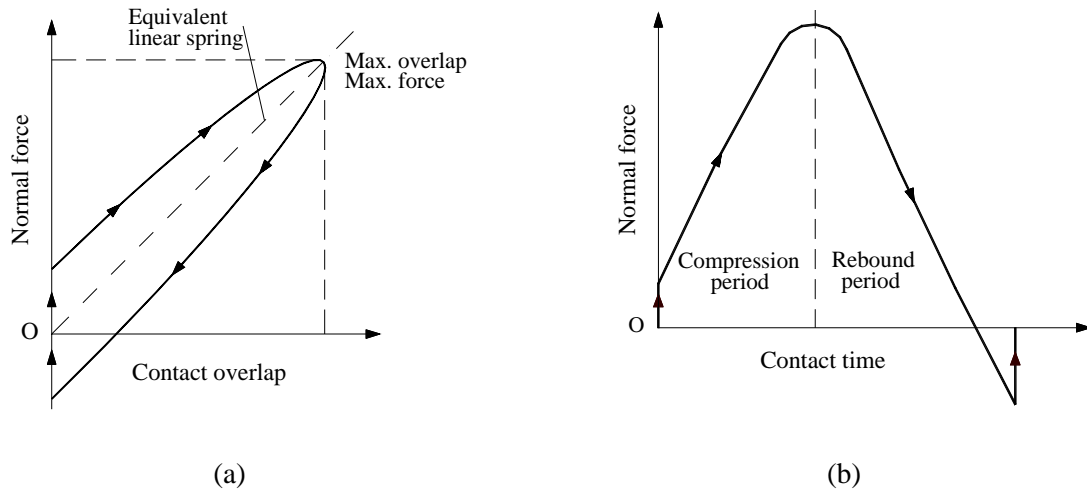


Figure 3.2: Variation of the contact's normal force in the linear viscoelastic system defined by Equation (3.2.1): (a) versus overlap, and (b) versus time.

Figure 3.2a shows the variation of contact normal force versus contact overlap for the Kelvin-Voigt module described by Equation (3.2.1). Hunt et al. (1975) demonstrated that the half elliptical curve shows a hysteresis behavior with the maximum damping force at the origin. This behavior is related to the term $c\dot{x}$, which has its maximum value at the beginning of impact. This is in contrast with the general expectation that the applied external force is zero at the beginning of an impact, and that there should be no shock at that moment. The variation of contact normal force versus time is represented in Figure 3.2b which shows that the contact force is tensile close to the contact termination time. This is incorrect because a zero contact force is expected at the end of contact. As shown in Figure 3.2b, this tensile force extends to the contact termination time and this effect dissipates some extra energy, leading to a reduced velocity at the instance of separation.

The correct hysteresis contact force should have the general response of the Figure 3.3, with the contact forces equal to zero at the origin. The main deficiency of applying the linear viscoelasticity theory is that, against the expectations and observations, the amount of energy dissipation from the linear Kelvin-Voigt model, Equation (3.2.1), is independent of the

impact velocity and as a result, the coefficient of restitution is constant. It is observed that at higher impact velocities, an increased amount of local crushing and plastic deformation occurs; therefore, smaller rebound velocities, or smaller coefficients of restitution, are anticipated.

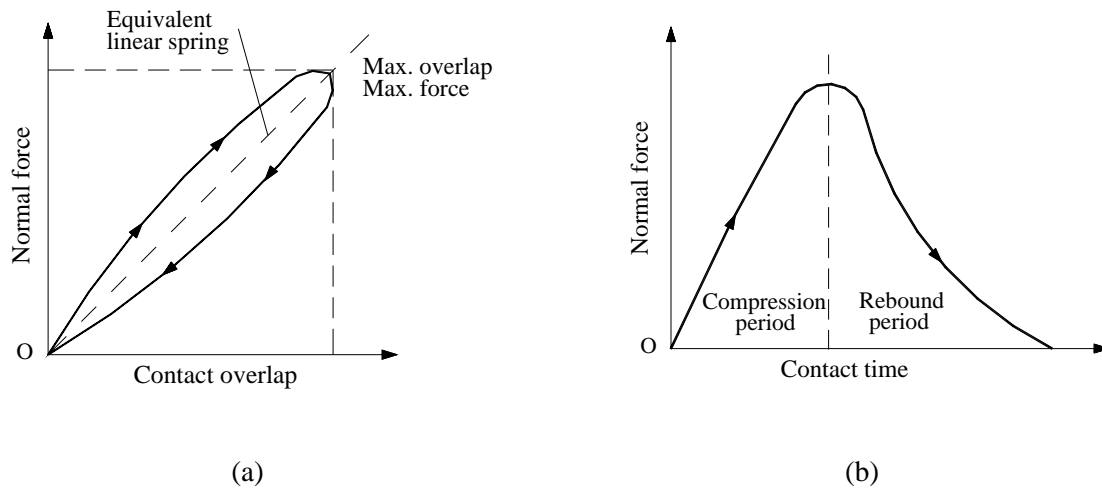


Figure 3.3: The ideal variation of normal contact force in a nonlinear viscoelastic system after Hunt et al. (1975): (a) versus overlap, and (b) versus time.

All the missing factors mentioned above can be compensated by putting a nonlinear dashpot in parallel with a linear spring, a solution offered by Hunt et al. (1975). As a result of this change, Equation (3.2.1) changes to Equation (3.2.2). The loading-unloading trend of variation in this equation, at low damping coefficients, is shown in Figure 3.3 versus indentation (or overlap) and time. The damping force resulting from this equation can be presented as: $c(x)^p (\dot{x})^q$, which is equal to zero both at the origin and at the instance of maximum penetration. The equation of motion in this case is as follows (the absolute value of overlap, $|x|$, is used not to change the force direction):

$$m\ddot{x} + c|x|^p (\dot{x})^q + kx = 0 \tag{3.2.2}$$

In the above equation, the external normal force on the colliding object can be defined as:

$$F_n = -c|x|^p (\dot{x})^q - kx \tag{3.2.3}$$

The absolute value of overlap in the above equations is used to prevent a change in the force direction. Walton (1992) offered a simplified version of the above equation, with the assumption that $p = q = 1$. Stoianovici and Hurmuzlu (1996) and Chatterjee (1997) adopted the same linear system which is shown by Equation (3.2.4).

$$m\ddot{x} - c\dot{x} + kx = 0 \quad \dot{x}(0) \equiv -v(0) < 0 \quad (3.2.4)$$

In the above equation, because the displacement has a negative sign, the absolute value can be removed. Chatterjee (1997) offered a closed-form solution for this nonlinear differential equation by introducing a new set of dimensionless parameters (X and Z represent dimensionless velocity and displacement):

$$X \equiv \frac{c\dot{x}}{\sqrt{mk}} = \frac{c\omega x}{k}, \quad Z \equiv \frac{cx}{k}, \quad \omega^2 = \frac{k}{m} \quad (3.2.5)$$

Substituting the above parameters into Equation (3.2.4) and integrating, results in displacement and force equations which simplify to the following:

$$Z - Z_0 + \ln\left(\frac{1-Z}{1-Z_0}\right) = \frac{X^2}{2} \quad (3.2.6)$$

$$c(mk^3)^{-1/2} F = -X(1-Z) \quad (3.2.7)$$

where F is the contact force and Z_0 is the initial velocity. The force displacement curve is plotted in Figure 3.4a for two different values of initial impact velocity. This figure has the general shape of a force-overlap curve similar to Figure 3.3a.

The enclosed areas between the loading and unloading curves define the amount of energy dissipated during the impact. As we can see from the curves, more energy is lost when the impacts occur with higher initial normal velocities. COR can be derived for these types of impacts directly as the ratio of final to initial velocity, Z_f/Z_0 . The coefficient of restitution for this nonlinear viscoelasticity is shown in Figure 3.5. Chatterjee (1997) offered an approximation for the coefficient of restitution resulting from Equation (3.2.4) as follows:

$$R_n \approx (-Z_0 + e^{0.4Z_0})^{-1} \quad (3.2.8)$$

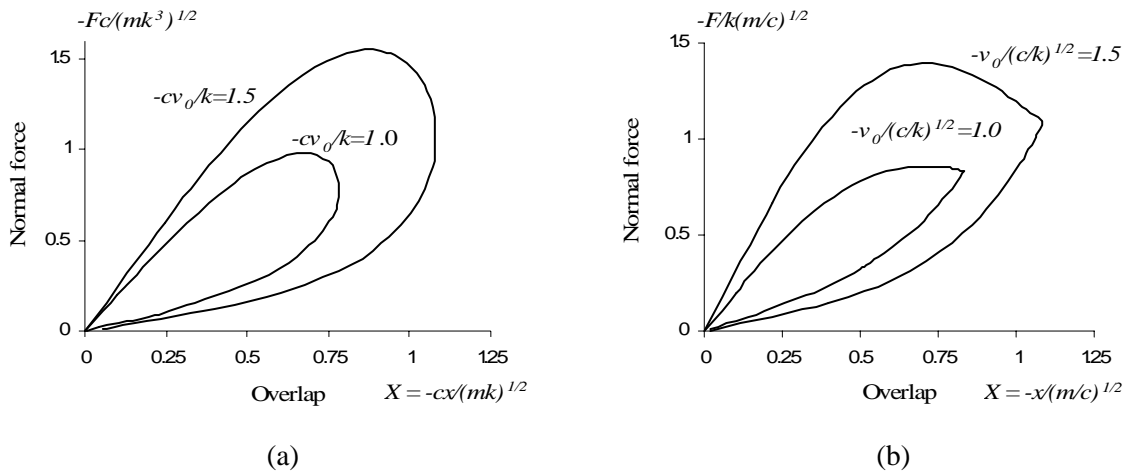


Figure 3.4: The hysteresis loop of overlap-force caused by nonlinear viscoelasticity for: (a) Equation (3.2.6), in which the viscosity is relative to the velocity to a power of one, after Stronge (2000), and (b) Equation (3.2.9), in which the viscosity is relative to the velocity to a power of two.

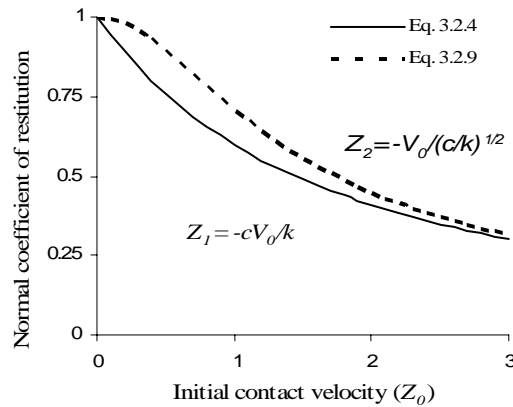


Figure 3.5: Descending coefficients of restitution as a function of initial contact velocity for the nonlinear viscoelastic models of Equations (3.2.4) and (3.2.9) (note: the dimensionless velocities differ for the two curves).

Rocks impacting the slopes crush around the impact area. This effect occurs more extensively at higher velocities; therefore the actual decreasing trend of COR is greater than what Equation (3.2.4) predicts. Moreover, the shape of the damping curve at low impact velocity is concave, as shown by the solid line in Figure 3.5, indicating a gradual variation in energy dissipation. However, taking into account the items considered previously, a convex

shape for energy dissipation is anticipated, emphasizing the velocity related nonlinearities in energy dissipation. Because of these observations, it is proposed to change Equation (3.2.2) with the values $p=1$ and $q=2$. This change results in the following equation:

$$m\ddot{x} - c x |\dot{x}| \dot{x} + kx = 0 \quad \dot{x}(0) \equiv -v_n(0) < 0 \quad (3.2.9)$$

where $v_n(0)$ is the contact normal velocity. In this equation, the external forces acting on the colliding object can be added and shown in the following equation:

$$F_n = c x |\dot{x}| \dot{x} - kx \quad (3.2.10)$$

In this case the new dimensionless overlap and velocities are defined as follows:

$$X \equiv \frac{x}{\sqrt{m/c}}, \quad Z \equiv \frac{\dot{x}}{\sqrt{k/c}} \quad (3.2.11)$$

Substituting the above values into Equation (3.2.9) results in new differential equations for the compression and rebounding periods:

$$\begin{aligned} Z \frac{dZ}{dX} + XZ^2 + X &= 0 \quad \dot{x}(0) \equiv -v_n(0) < 0 \quad (\text{compression period}) \\ Z \frac{dZ}{dX} - XZ^2 + X &= 0 \quad \dot{x}(0) \equiv -v_n(0) > 0 \quad (\text{rebounding period}) \end{aligned} \quad (3.2.12)$$

Integrating the above differential equations and applying the boundary condition of $x = 0$ and $v = v_n(0)$ to the equation of motion results in Equations (3.2.13). The impact compression force is given by the two equations defined in Equations (3.2.14).

$$\ln(1 + Z^2) \mp \ln(1 + Z_0^2) = -X^2 \quad (3.2.13)$$

$$F / (k\sqrt{m/c}) = \mp XZ^2 - X \quad (3.2.14)$$

The variation of the contact force is shown in Figure 3.4b. These forces can be compared with the forces in Figure 3.4a. In Figure 3.4b, it can be observed that the contact force reaches its maximum long before the highest penetration, due to presence of a squared

velocity term in the viscous force equation, described by Equation (3.2.10). This figure also shows a relatively larger hysteresis loop, compared to Figure 3.4a, resulting from a larger normal contact force in compression and a smaller force in restitution.

The motion differential introduced by Equation (3.2.13) can be solved explicitly for the contact overlap and the rebound termination velocity. Equation (3.2.15) shows the closed-form relationship between the coefficient of restitution and the impact velocity:

$$R_n = 1/\sqrt{1+Z_0^2} \quad (3.2.15)$$

3.2.2 Application of nonlinear viscoelasticity in rockfall modeling

For each contact material, the normal coefficient of restitution is not a constant value. Theoretically, at impacts with zero velocity the normal coefficient of restitution is equal to the magnitude of the normal COR defined by Equation (2.2.2). More local crushing occurs on both the rock and the impact surface during higher impact velocities. This results in a reduced amount of COR, according to Habib (1976). Pfeiffer et al. (1989) proposed a scaling factor to incorporate the effect of velocity, defined by Equation (3.2.16), on the normal COR. The scaling factor halves the normal COR at the velocities equal to 9.8 *m/s*; assuming the normal restitution coefficient is equal to one. This property is used to define the nonlinear viscous coefficient; *c*. Pfeiffer et al.'s velocity equation is as follows:

$$R_n \approx \frac{R_n}{1+(V_n/9.8)^2} \quad (3.2.16)$$

where V_n is the normal impact velocity and is measured in (m/s). Figures 3.6a and 3.6b show the variation of normal COR versus impact velocity assuming $R_n=1.0$ and 0.5, respectively. Figure 3.6a shows that the nonlinear dashpot properly reproduces the value of coefficients when $R_n=1.0$. Furthermore, this figure shows that the power-2 nonlinear viscosity is a better approximation for the nonlinearities involved in the normal coefficient of restitution.

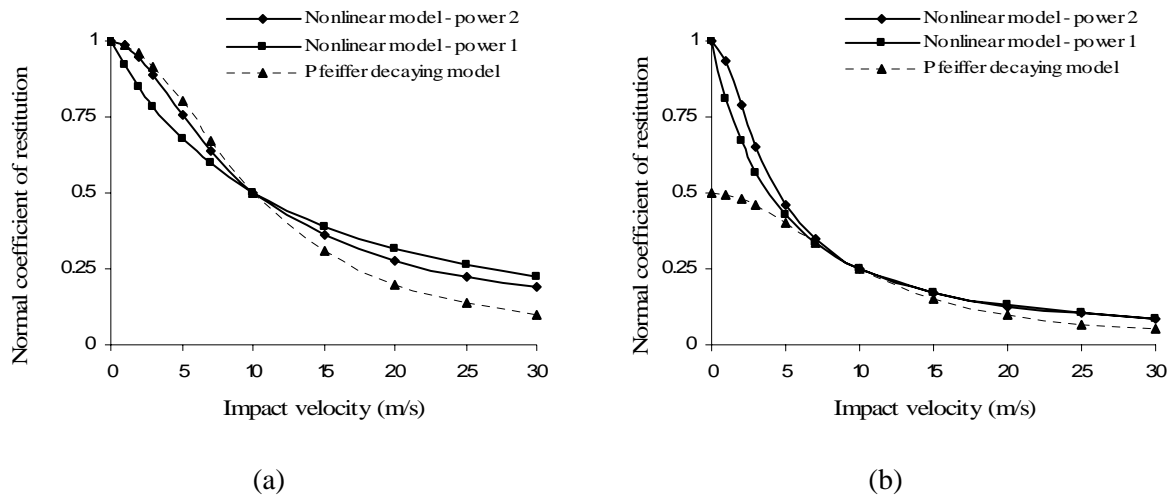


Figure 3.6: Decaying COR resulting from inelastic fracturing at the point of impact for the Pfeiffer scaling (Equation (3.2.16)) and the variation of nonlinear viscoelastic models defined by Equations (3.2.8) and (3.2.15) for: (a) normal COR (R_n) = 1.0, and (b) normal COR (R_n) = 0.5.

Figure 3.6b, shows the variation of Equation (3.2.16) with $R_n = 0.5$. In this figure, the values of the nonlinear viscoelastic Equations (3.2.5) and (3.2.11) are defined so that all the viscoelastic equations produce the same normal COR at the normal impact velocity of 9.8 m/s. This figure shows that the energy dissipations derived from viscoelastic formulations are not close to the values derived from the scaling factor defined by Equation (3.2.16) for velocities less than 5 m/s. However, this difference is not considered as a limitation of the viscoelastic model, as the two groups of energy dissipation models have different fundamental assumptions. The nonlinear dashpots dissipate the energy according to the value of the velocity; therefore dissipation does not occur when the impact velocity is zero. In contrast, Equation (3.2.16) is a scaling equation which decreases the value of R_n according to the magnitude of the contact normal velocity. At velocities greater than 5 m/s, both nonlinear viscoelastic models predict a variation of COR close to the scaling factor.

3.3 THE TANGENTIAL DIRECTION IN DEM

The available definitions for COR are usually applied to dimensionless objects where the whole object geometry experiences an equal translational velocity. As a result of rotational velocity, the translational velocities in two perpendicular directions are variable within an object. Conventionally, for geometrical objects, the velocities at the center of gravity are used for defining the coefficients of restitution in Equations (2.2.2). However, applying DEM to define the rebound velocities, it has been observed that the variation of tangential COR, using the conventional Kelvin-Voigt module in addition to a slider, is inconsistent. This inconsistency indicates that the variation of rebound tangential velocity is not well predicted by the model tangential parameters, including: the friction coefficient, spring stiffness, and the dashpot viscosity coefficient. Further literature review for similar models to DEM, has led to the development of a new constitutive model in the tangential direction, presented in the following sections.

3.3.1 The discrete compliance model (DCM)

Similar to DEM, Stronge (1994b) offered a new rigid body impact model for compliant rough bodies, known as the discrete compliant model (DCM). In this model all of the deformations and forces are concentrated in an infinitesimal object at the interface of two colliding objects, or at the interface of an object and a rigid half space, as shown in Figure 3.7. In this system a combination of tangential and normal springs are used at the contact point, with a slider in the tangential direction. In this model it is assumed that the ratio of normal to tangential stiffness is equal to η^2 . Despite the fact that overlap occurs during the collision, the impenetrability condition is observed in DCM by accumulating the elastoplastic deformations in the deformable particle at the contact point.

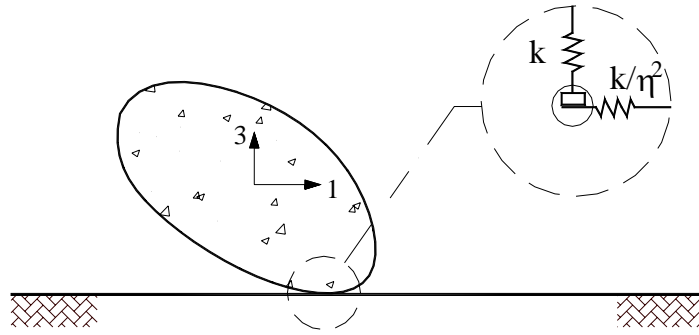


Figure 3.7: Impact of an object against a rigid half-space using the discrete compliant model (DCM) proposed by Stronge (1994b).

In DEM, the contact forces are mobilized based on the overlap between two objects or between an object and an impact surface. In DCM, the displacements are calculated based on a group of closed-form equations with the time as the input variable. The contact forces are defined upon mobilization of the displacements in the springs. The equations of motion are illustrated in Equations (3.3.1) and (3.3.2) for the perpendicular, normal and tangential directions.

$$\begin{aligned}
 v_3(t) &= v_3(0) \cos \Omega_n t & 0 \leq t \leq t_c \\
 v_3(t) &= e_* v_3(0) \cos \left(\frac{\Omega_n t}{e_*} + \frac{\pi}{2} (1 - e_*) \right) & t_c \leq t \leq t_f
 \end{aligned} \tag{3.3.1}$$

$$v_1(t) = \Omega_t u_1(t_2) \sin \Omega_t (t - t_2) + v_1(t_2) \cos \Omega_t (t - t_2) \tag{3.3.2}$$

In the above equations, Ω_t and Ω_n are the natural frequencies of the system in the tangential and normal directions; v_t and v_n are the contact velocities in the tangential and normal directions; e_* is the energy coefficient of restitution and is defined as the ratio of energy released in restitution to the amount of energy adsorbed during the compression phase; and $v_t(0)$ and $v_n(0)$ are the contact velocities at the time of impact. From the second equation of the Equations (3.3.1), it can be concluded that the energy dissipation is assumed to occur during the second half of the impact, the restitution phase.

3.3.2 Collinear impacts in DCM

An impact is called collinear (or centric) when the contact normal vector passes through the object's center of gravity. Clearly, the impacts of circular disks or spheres are always collinear; however, collinear impacts might occur with other objects. In collinear impacts the natural frequencies of the system simplify to: $\Omega_n = \pi/2t_c$ and $\Omega_t = \sqrt{3.5}\pi/2\eta t_c$, where t_c is the time when the normal component of the velocity terminates. It should be mentioned that in collinear impacts, the equations of motion for tangential and normal directions are decoupled. Stronge (1994b) categorized the centric collisions into three main groups based on the impact angle: small, intermediate, and large. The division is based on three parameters: the ratio of springs' stiffness, η^2 ; the friction coefficient, μ ; and the energy coefficient of restitution, e_* . In eccentric impacts, the geometry of the object, or mass distribution around the contact point, is also effective in defining the categories. Table 3.1 shows the three slip processes occurring during the impact of a circular object against the half-space.

Table 3.1: Slip processes during incidence of a circular object on a half space

<i>Angle of incidence</i> ($v_1(0)/v_3(0)$)	<i>Velocity criteria</i>	<i>Slip Process</i>
Small	$v_1(0)/v_3(0) < \mu\eta^2$	stick-slip
Intermediate	$\mu\eta^2 < v_1(0)/v_3(0) < 3.5\mu(1+e_*)$	slip-stick-slip
Large	$3.5\mu(1+e_*) < v_1(0)/v_3(0)$	pure slip

Johnson (1985) gives the expressions for the normal and tangential spring stiffness coefficients for the case of a rigid circular punch on an elastic half space: $k = Ea/(1-\nu^2)$, $k/\eta^2 = 2Ea/(2-\nu)(1+\nu)$, where E and ν are modulus of elasticity and Poisson ratio; and a is the punch ratio. From these relationships, η^2 can be calculated as:

$$\eta^2 = (2-\nu)/2(1-\nu) \quad (3.3.3)$$

It will be shown in the following sections that the inconsistency between DEM (and DCM), in comparison with the low compliant models, occurs at small and intermediate angles of

The termination velocities for the tangential velocity can be derived for the three proposed impact angles using the DCM, as shown in the Figure 3.9. This figure demonstrates the termination velocity at the contact point for a compliant material versus the normalized impact angle of, $\gamma = \tan^{-1}(v_1(0)/v_3(0))$, as proposed by Stronge (1994b). The final velocities for a rubber sphere ($\nu = 0.5$) striking a heavy steel plate are compared with the elastic solutions given by Maw et al. (1976) and the experimental results by Johnson (1983). The figure shows that the termination velocities are the same for the compliant model and elastic continuum model. The results for the impact of the spherical rubber are also consistent with the rebound velocities predicted by the DCM. Stronge (1994) explains Figure 3.9 as follows:

“The elastic solution and the discrete parameter model each have similar processes that develop at the contact point in three parts of the range of angle of incidence. The predictions of these two models are most different for small and intermediate angles of incidence where the discrete parameter model has a final period of slip that is prolonged by elastic strain energy stored in the tangential compliant element. Throughout most of the range of small to intermediate angles of incidence, both the elastic continuum and the discrete parameter models of sphere impact have a tangential relative velocity at separation that is in the opposite direction to the incident tangential velocity. For a collinear collision this velocity reversal at contact point is entirely due to tangential compliance.”

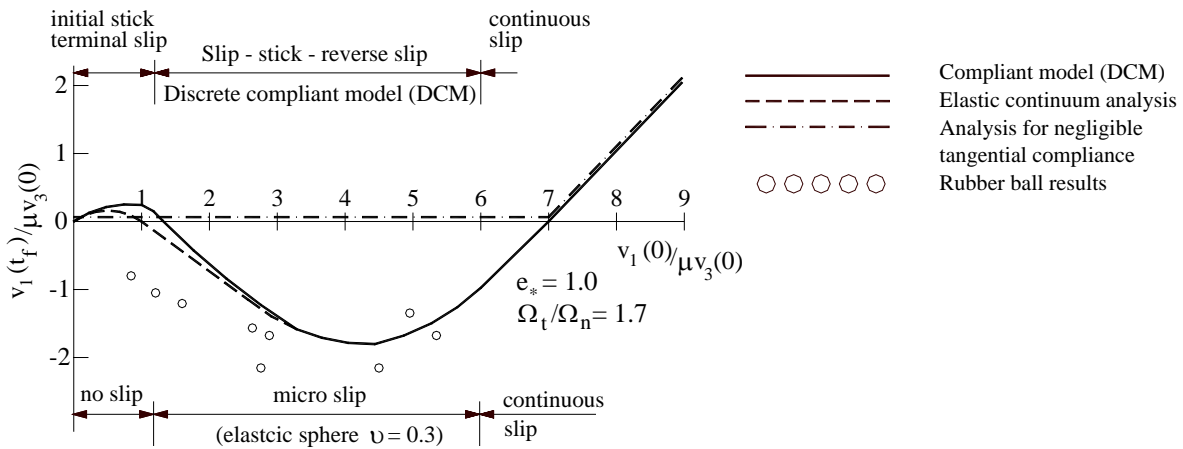


Figure 3.9: Tangential velocity at the contact point at the instance of contact termination for collision of a spherical compliant object at a rigid half space, after Stronge (1994b) (the material has a Poisson ratio equal to 0.3 and $e_* = 1.0$).

3.3.3 Tangential contact forces

Defining the internal forces during impact is a common problem in wear science. Frequently, coefficients of restitution are used to define the ratios of the velocities or energies after to the values before the impacts, but this does not describe the variation of normal and tangential forces or moments. In these methods, coefficients of restitution are considered constant to simplify the calculations. However, several researchers have reported that these coefficients vary due to the impact specifications, including: Pfeiffer et al. (1989) and Azzoni et al. (1995). Brach (1988) proposed a constitutive model for defining the rebound velocities based on the ratio of tangential to normal impulses; however, he showed that assuming a tangential coefficient of restitution to be constant is not realistic or necessary.

For two-dimensional problems, Brach (1988) utilized three assumptions to define the velocities after impact: using a COR for normal velocity, applying the conservation of angular momentum about the impact point, and introducing the coefficient of limiting friction (μ) as the ratio of tangential to normal impulses. The third assumption can be expressed as follows:

$$\mu = p_1 / p_3 \quad (3.3.5)$$

where p_3 and p_1 are the normal and tangential impulses as shown in Figure 3.10. This model is not restricted to circular objects; however, in the following presentation the equations are simplified for the impact of spherical and discoidal objects. For a centric impact, based on the presence of sliding at the instance of separation, two different scenarios can occur: total sliding or pure rolling.

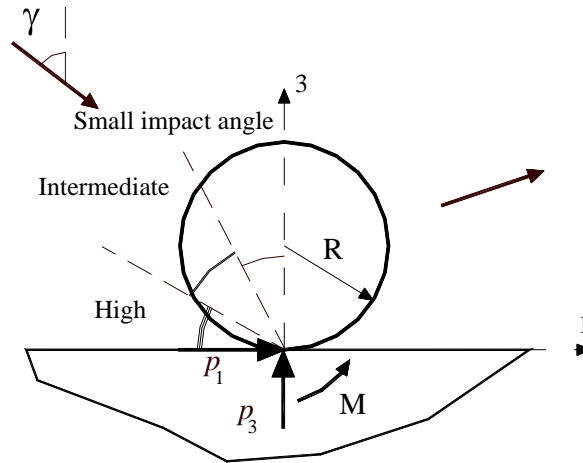


Figure 3.10: Collinear impact: free body diagram of a sphere impacting a solid half space at angle γ .

In this theory, the normal velocity is calculated applying the conventional definition of normal coefficient of restitution:

$$V_3(f) = -e_n V_3(0) \tag{3.3.6}$$

where $V_3(f)$ and $V_3(0)$ are the normal velocities at the object center before and after the impact, and e_n is the normal coefficient of restitution equivalent to R_n . In the tangential direction, if the sliding at the contact point continues until the contact termination, the tangential and rotational velocities are defined based on the following equations:

$$\begin{aligned} V_t(f) &= V_t(0) - \mu(1 + e_n)V_n(0) \\ \omega(f) &= \omega(0) + \mu(1 + e_n)\lambda V_n(0) / R \end{aligned} \tag{3.3.7}$$

In Equation (3.3.7), $V_t(0)$ and $V_t(f)$ are the tangential velocities at the object center before and after the impact, $\omega(0)$ and $\omega(f)$ are the rotational velocities before and after impact and $\lambda = R^2 / k_r^2$ where R is sphere radius and k_r is polar radius of gyration. For spheres λ is equal to 5/2 and for disks it is equal to 2.0.

If sliding finishes prior to separation the equation (3.3.7) reduces to the Equations described in Table 3.2, by assuming that $V_t = R\omega(f)$. This equation means that if sliding ceases prior

to separation, the circular object starts to roll till the time of contact termination. During this period of time the tangential and rotational velocities do not change.

Table 3.2: Tangential and rotational rebound velocities for spheres and disks using Brach impact model for the case of sliding termination before separation

<i>Spherical objects</i>	<i>Discoidal objects</i>
$V_t(f) = 5/7 V_t(0) + 2/7 R\omega(0)$	$V_t(f) = 2/3 V_t(0) + 1/3 R\omega(0)$
$\omega(f) = 5/7 R V_t(0) + 2/7 \omega(0)$	$\omega(f) = 2/3 R V_t(0) + 1/3 \omega(0)$

Brach (1988) introduced the definition of critical friction, which is the lowest friction that can stop the rotational velocity prior to separation. For the case of development of friction force, it can be assumed that: $F_1(t) = f F_3(t)$, where t is the time, f is a constant, and F_3 and F_1 are the developed contact forces in the normal and tangential directions, respectively. Figure 3.11 shows the gradual increase of tangential impulse versus the constant normal impulse. By increasing the friction coefficient, the tangential impulse curve starts to increase. In one stage, where f_2 is equal to the critical friction coefficient, the tangential velocity is halted. Any further increase in the value of f will diminish the frictional force before the end of the contact. As a result, the friction force drops to a small value. In this case the disk will roll without sliding. Brach (1988) states this situation as:

“For all coefficients of friction which are greater than f_2 , the tangential impulse will never be larger than $f_2 p_3$. Thus a limiting or critical value of p_1/p_3 exists and denoted by μ_c . Under all conditions the value of tangential impulses can never exceed $\mu_c p_3$. The limiting condition occurs when the solution equations for sliding are identical to the solution equations for rolling. It is important to note that μ_c is the value of μ that maximizes the energy loss.”

For centric impacts, the critical friction coefficient, μ_c , is equal to:

$$\mu_c = r_v / (1 + e_n)(1 + \lambda) \quad (3.3.8)$$

where r_v is the ratio of contact velocities at the contact point: $(V_t(0) - R\omega(0))/V_n(0)$.

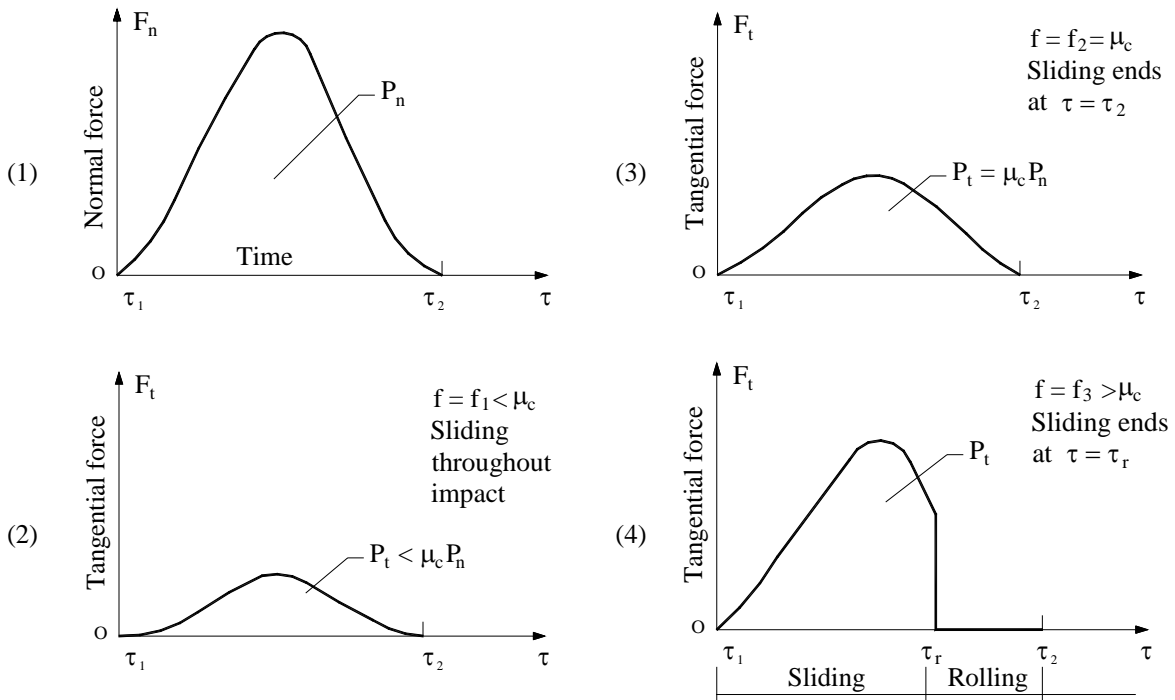


Figure 3.11: Increasing sequence of tangential impulse versus the contact normal impulse which is constant, after Brach (1988).

3.3.4 Modifying the tangential module in DEM: introducing the mono-direction unit

The definitions proposed by Brach (1994) clarify that the direction of the tangential force does not reverse in collinear impacts for natural materials. In DEM, the tangential spring stores energy during compression. This strain energy is released during the tangential restitution phase. This results in reverse sliding in the tangential direction. Stronge (1994b) showed that the frequency of the variation of tangential force is higher than the frequency in the normal direction, as shown in Figure 3.8. As a result, tangential contact force reversal occurs for most impact angles. The only exception is the pure sliding case that occurs during low impact angles.

Similar to DEM, the discrete compliant model shows the same tangential force reversal, the only difference being that the overlap is zero in the DCM. The penetration causes a variable contact vector and as a result the values of rebound tangential and rotational velocities might be different for the two models.

To modify the inconsistent reversal of the tangential force, a new unit is introduced in the tangential direction for the spherical particles experiencing centric impact. This unit modifies the inconsistent variation of the tangential force and releases the strain energy at the time of tangential reverse in the direction of sliding. This new unit is named the mono-direction unit, as shown in Figure 3.12. Mathematically, for spheres, this behavior can be expressed by Equation (3.3.9). This equation explains that every time the sliding direction reverses the spring force releases, respectively. The sliding reversal can be captured when the rate of the tangential sliding becomes zero as shown here:

$$\text{If } \dot{s} = V_t - R_{overlap} \omega = 0 \Rightarrow F_{spring} = F_{fric} = 0 \quad (3.3.9)$$

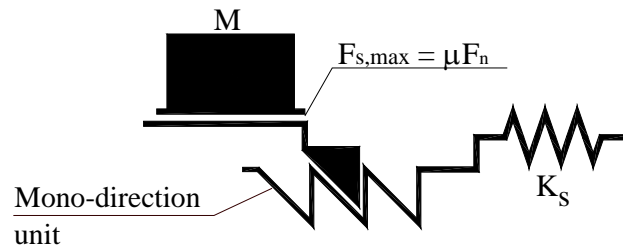


Figure 3.12: Mono-direction unit in the tangential direction along with a spring and a slider.

As the slip direction is arbitrary, for the purpose of clarification, two sets of springs are used, along with the new mono-direction unit as shown in Figure 3.13. This new model is called the modified discrete element model (MDEM). In the newly proposed module, the tangential dashpot is omitted for the following reasons:

- to decrease the constitutive model's total number of parameters
- negligible effect of the tangential dashpot, which is due to a fast energy release as a result of the presence of the slider
- lack of data and evidence on the viscous nature of the tangential force, based on the available experimental data that the tangential force is frictional.

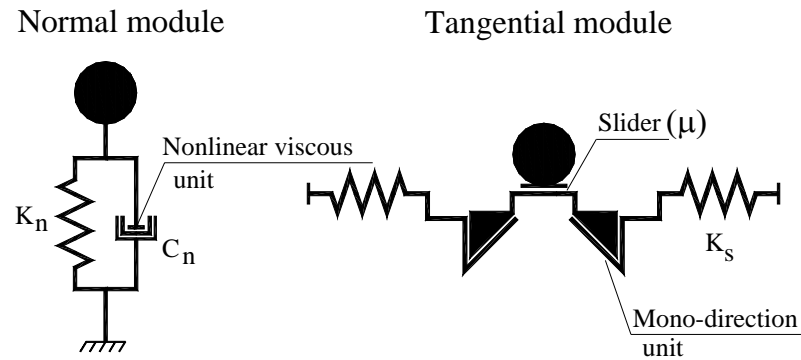


Figure 3.13: Normal and tangential modules in Modified DEM (MDEM).

3.3.5 Variation of tangential forces using modified discrete element modeling (MDEM)

The application of MDEM is tested using the impact of a circular object against a rigid half space, as shown in Figure 3.10. Here, rigidity means that the impact surface neither displaces nor deforms during impact; however, in contrast with the DCM, the object overlaps with the wall. This causes minor differences between the two models in the evaluation of the contact and also in the values of rebound velocities, but the trend of variations are generally the same.

For this test K_n is assumed equal to 5×10^5 kg/m and, K_s is chosen as 4.1×10^5 kg/m for a material with a Poisson ratio of 0.3, as shown in Equation (3.3.3). The radius of the sphere is assumed to be 3 cm and the normal impact velocity, V_3 , is considered constant equal to -10 m/s while the horizontal velocity, V_1 , is variable. Furthermore, $\mu = 0.3$ and $e_* = 1.0$ (c in Equation (3.2.9) is set equal to zero). The collision is studied at different impact angles, by varying the value of $V_1/\mu V_3$, as described in Table 3.2, to include the three ranges of impact angles. The time step is considered constant, equal to $1e-5$ sec.

In the following sections the variation of contact forces in addition to the variation of tangential velocity is studied applying both discrete element modeling (DEM) and the proposed modified version, MDEM.

3.3.5.1 Low impact angles ($v_1(0)/\mu v_3(0) < 1.21$)

Figure 3.14 shows the variation of dimensionless tangential forces and contact velocities for the impact of a sphere with the initial settings of Figure 3.10 at different impact velocities and low impact angle configurations. In this case, the contact point sticks prior to the final stage of sliding, which occurs at a time ratio equal to 0.63, as shown in Figure 3.14a. In this curve the variation of normal contact force is sinusoidal where its natural frequency is smaller than natural frequency in the tangential direction. In Figure 3.14b, the variation of the tangential velocities versus time is demonstrated for different initial tangential velocities. As shown, the directions of these velocities are reversed at a time ratio equal to 0.31; however, the velocity directions do not reverse until the contact terminates. As described before, this sliding reversal is not realistic for low compliance impacts.

In Figure 3.14c the force variations are plotted when a mono-direction unit is added in the tangential direction in comparison to the configurations of Figure 3.14a. The tangential force drops to zero when the direction of sliding reverses, as shown in Figure 3.14d, occurring when the ratio of passed time to initial time is equal to 0.31. After this state, the tangential forces and velocities are expected to stay at zero constant value; however, as a result of the variation of the overlap between the object and the surface, there are minor perturbations in the velocities and forces.

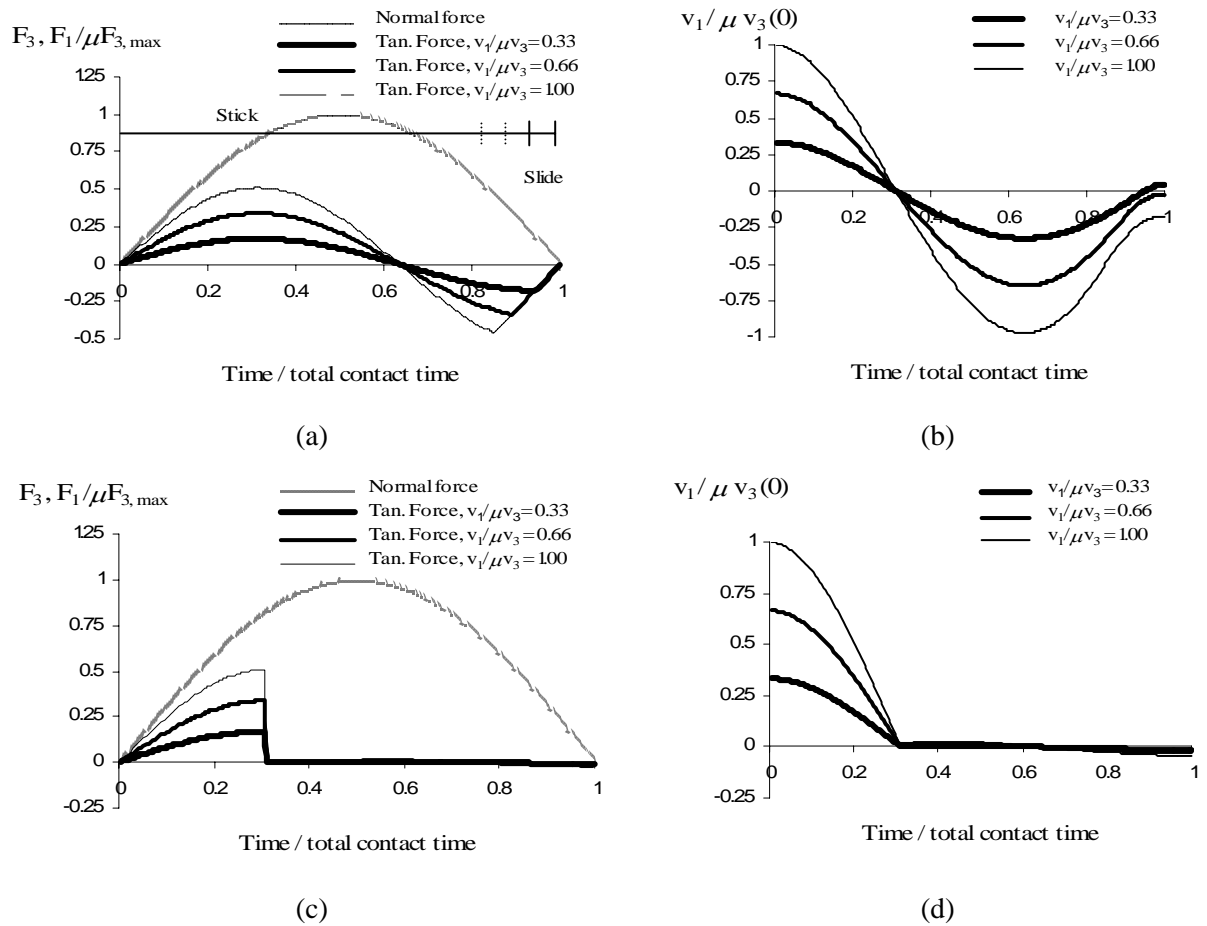


Figure 3.14: Variation of dimensionless tangential forces and velocities at the contact point for the impact of a sphere with the initial settings of Figure 3.11 at different impact velocities using DEM and MDEM for low impact angles: (a) variation of forces using DEM, (b) variation of tangential velocities using DEM, (c) variation of forces using MDEM, and (d) variation of tangential velocities using MDEM.

3.3.5.2 Intermediate impact angles ($1.21 < v_1(0)/\mu v_3(0) < 7.0$)

Figure 3.15 depicts the variation of dimensionless tangential forces and contact velocities for the configurations of Figure 3.10 at variable intermediate impact velocities. In Figure 3.15a, for those parts where the tangential force is equal to the multiplication of μ by the normal force, the contact point experiences sliding, before the stick case occurs. For the sliding case, the variations of normalized normal and tangential force curves are identical, as shown in Figure 3.15a. As the tangential velocity grows, the range of occurrence of sliding grows. This range is set by the upper boundary of the velocity ratio, stated in Table 3.2 as: $v_1(0)/\mu v_3(0) = 3.5\mu(1+e^*) = 7.0$. In Figure 3.15b the variation of the tangential contact velocity versus the

time ratio is plotted. This Figure shows that, similar to low impact angles, the direction of v_3 reverses, but for this case at different incidence times.

Figure 3.15c plots the variation of tangential force at different tangential velocities within the range of intermediate impact angles when a mono-direction unit is added to the DEM module. In this figure, the tangential forces drop to zero when the directions of velocities reverse in the tangential direction, as is shown in Figure 3.15d. Similar to Figures 3.14c and 3.14d, due to the variation of the contact vector caused by the sphere-surface overlap, the tangential contact forces and velocities are not constant and oscillate around the zero value.

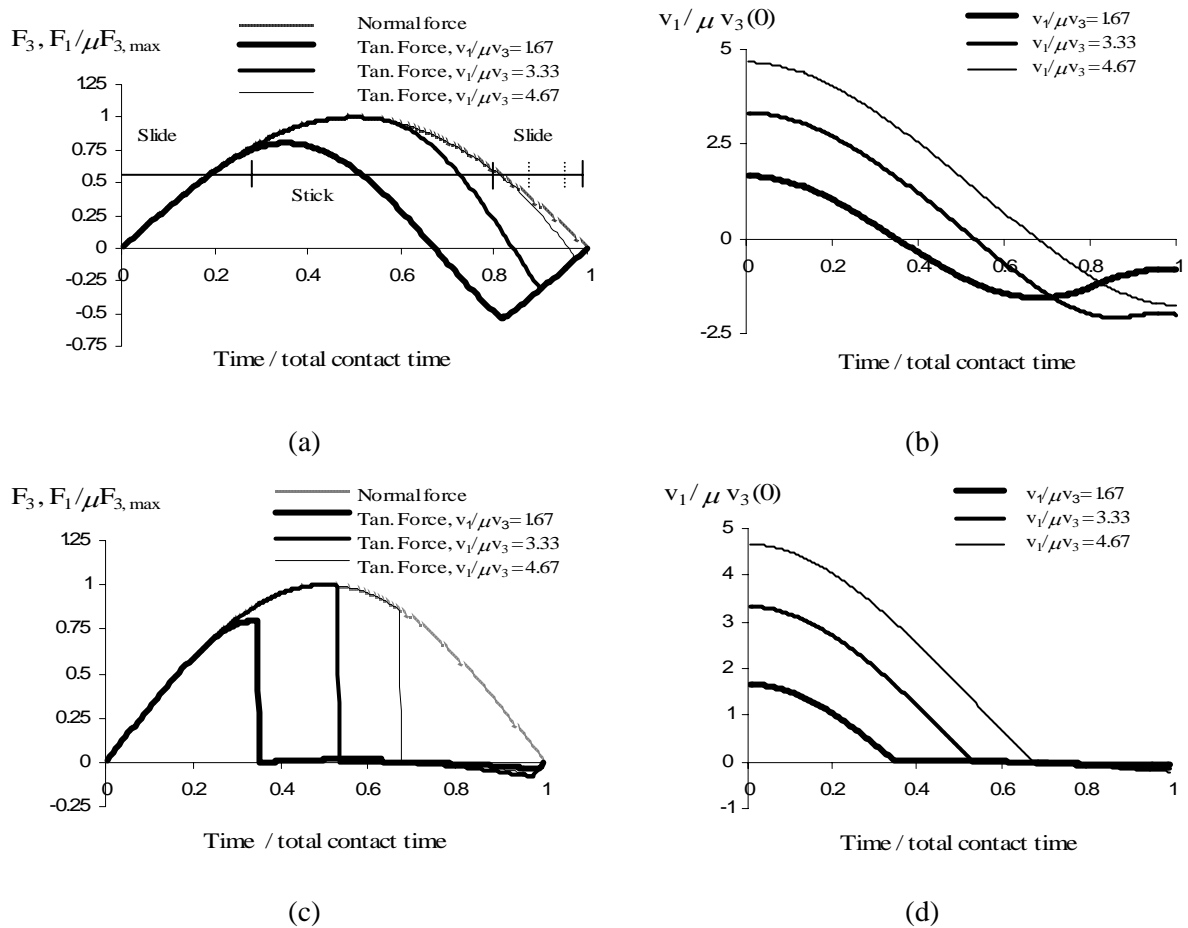


Figure 3.15: Variation of dimensionless tangential forces and velocities at the contact point for the impact of a sphere with the initial settings of Figure 3.11 at different impact velocities using DEM and MDEM for intermediate impact angles: (a) variation of forces using DEM, (b) variation of tangential velocities using DEM, (c) variation of forces using MDEM, and (d) variation of tangential velocities using MDEM.

3.3.5.3 Large impact angles ($7.0 < v_1(0)/\mu v_3(0)$)

Figure 3.16 depicts the variation of dimensionless tangential forces and contact velocities for the configurations of Figure 3.10 at variable high impact velocities. Figure 3.16a shows that the object experiences sliding through the whole impact period. Figure 3.16b confirms the continuous sliding, as the contact velocity does not reverse during the contact. In other words, in high impact angles the tangential mono-direction unit does not activate and, as a result, the rebound velocities derived from MDEM are the same as the velocities predicted by DEM or DCM.

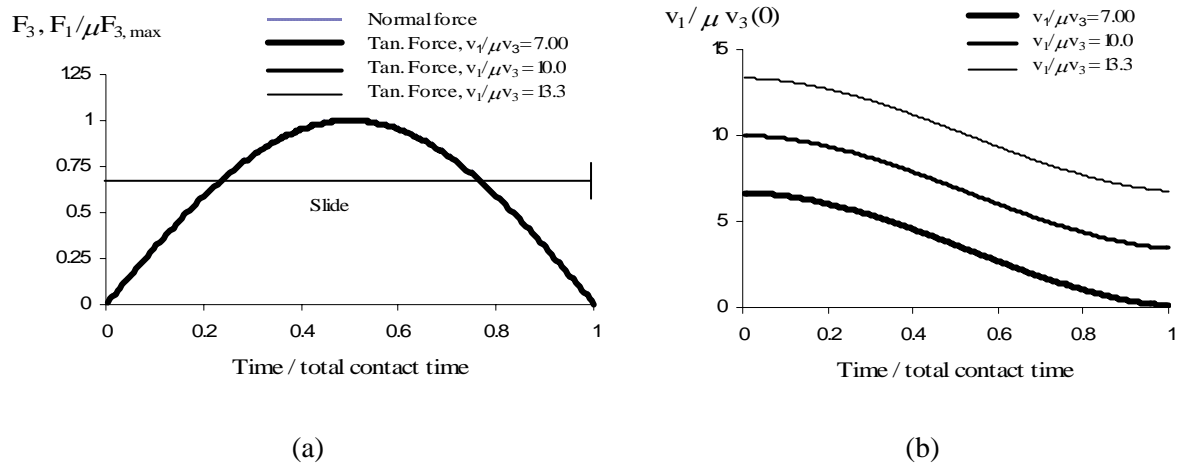


Figure 3.16: Variation of dimensionless tangential forces and velocities at the contact point for the impact of a sphere with the initial settings of Figure 3.11 at different impact velocities using DEM and MDEM for high impact angles: (a) variation of forces using DEM and MDEM, and (b) variation of tangential velocities using DEM and MDEM.

3.3.6 Successive impacts using MDEM

In this section, five successive impacts of a disk on a horizontal rigid half space are studied using DEM and MDEM, as described by Figure 3.17a. In this example, the disk radius is equal to 0.5 m, and the contact, K_n is equal to K_s which is equal to 1.0×10^7 kg/m, and $e_* = 1.0$, which indicates that the normal spring viscosity is equal to zero. The friction, μ , is considered variable from 0.05 to 0.3 and the object initial horizontal velocity, $V_{ini,hor}$, is assumed to be 3.0 m/s.

Figure 3.17b plots the variation of the horizontal velocity at the disk center versus time, applying DEM. As described by Stronge (1994b) in Figure 3.9, after the first impact, the rebound tangential velocity may vary from 1.4 to 2.7 m/s for different values of contact friction. After the second impact, this range is limited, and after the third impact all values approach 1.97 m/s, which is equal to 65.7% of the initial velocity.

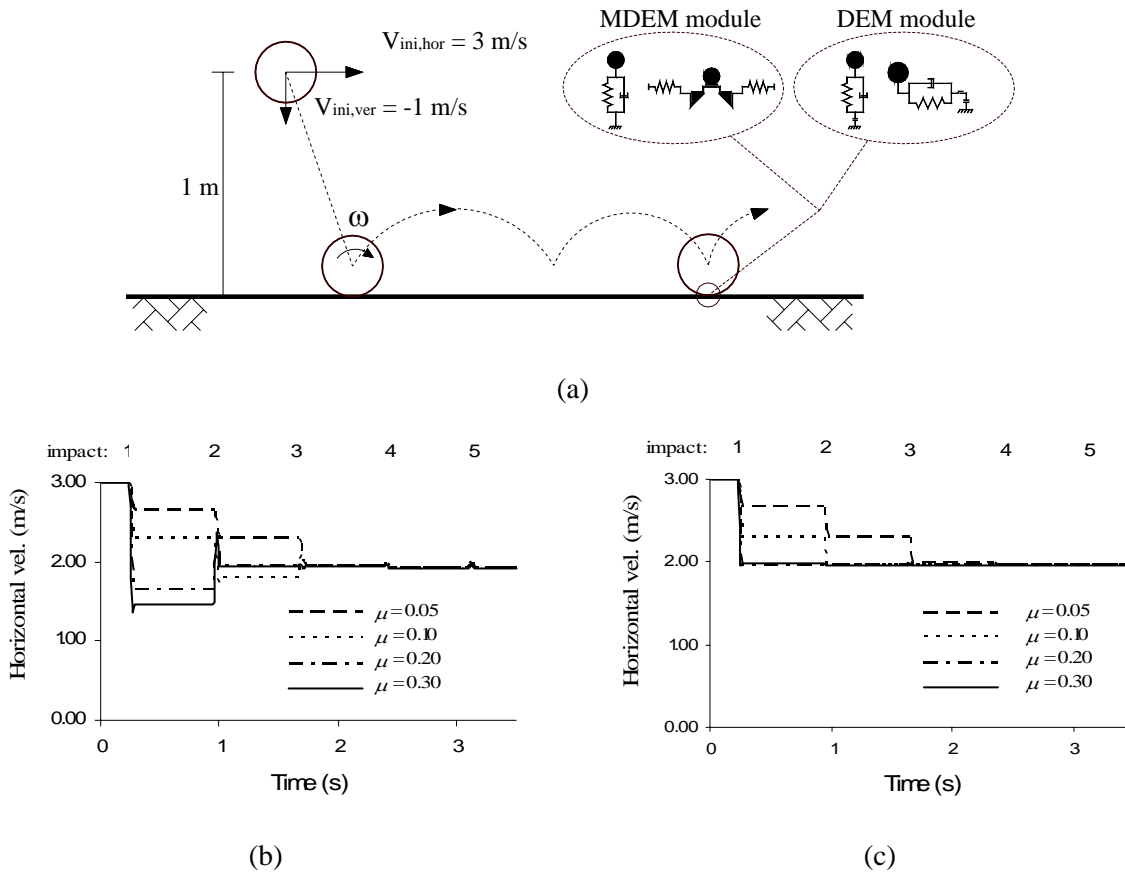


Figure 3.17: Five successive impact of a discoidal object under gravity using both the DEM and MDEM models: (a) the settings for the test, (b) variation of the disk horizontal velocity using the DEM model, and (c) variation of the disk horizontal velocity using the MDEM model.

Figure 3.17c depicts the variation of tangential velocity versus time using MDEM. At the time of contact the disk normal velocity is 3.28 m/s due to gravity. Using Equation (3.3.8), the critical friction, μ_c , is equal to 0.15. For friction coefficients greater than this value, after the first impact the rebound disk velocity approaches the final value of 1.97 m/s. For friction coefficients smaller than the critical friction, the tangential velocity approaches the final

value after one or two impacts. However, the final tangential velocity is also predictable using the disk equation in Table 3.2. These velocities differ by less than 1% from the tangential velocities predicted by the rigid body model proposed by Brach (1988), discussed previously. Due to the disk indentation, the disk horizontal velocity experiences small perturbations after the fourth and fifth impacts. This is due to the contact tangential velocity being almost zero.

3.3.7 The effect of impact angle on tangential COR when applying MDEM

In this section, the variations of tangential COR versus impact angle with different friction coefficients are investigated. Figure 3.18a shows the variation of tangential COR derived from the inclined impact of a discoidal object using MDEM with different friction coefficients. This test is performed by throwing a disk vertically on an inclined surface. For this impact setup, if the energy dissipation in the normal direction is negligible the rebound velocities are independent of the initial velocity. The presented results are comparable with the impact model offered by Brach (1988).

Figure 3.18a shows that by decreasing the impact angle the tangential COR decreases and stays constant around the value 0.69, the lower limit of tangential COR for a disk. This decrease of tangential COR is due to an increase in the normal impulse in addition to a decrease in the tangential impulse. It can be observed that for the friction coefficient equal to 0.3, the contact velocity halts earlier than friction coefficients equal to 0.1 or 0.2, resulting in a faster approach to the lower limit velocity.

Figure 3.18b illustrates the experimental results of the variation of tangential COR (R_t) performed by Chau et al. (2002) for different spherical objects with variable mass. Although they could not define any conclusion explaining the variation of tangential coefficient of restitution, there are some similarities between their results and Figure 3.18a. These similarities are: both values have a minimum tangential COR around 0.65 and the coefficients of restitution generally increase when the slope angle increases. It should be mentioned that there is no reference to the values of friction coefficient by Chau et al. (2002).

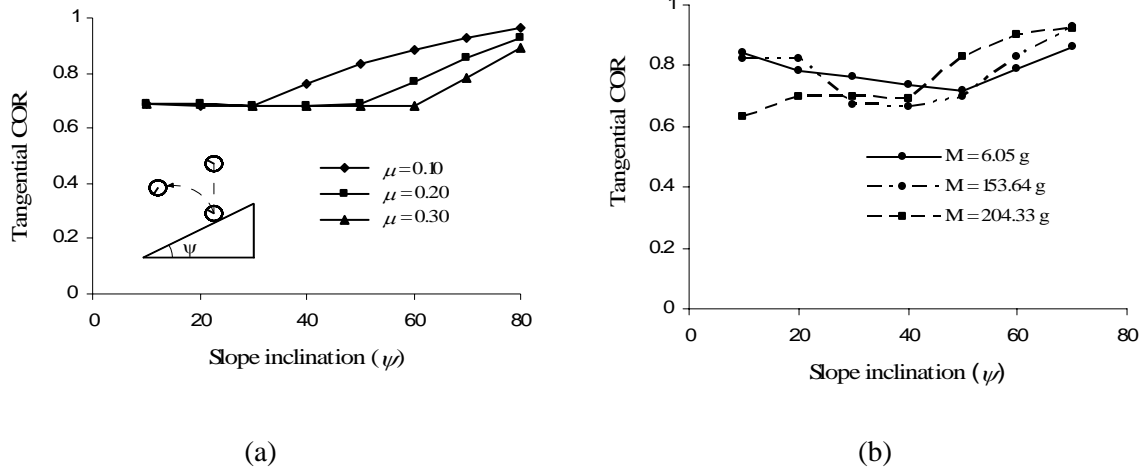


Figure 3.18: (a) Variation of tangential COR (R_t) versus impact angle, ψ , at different friction coefficients applying MDEM, and (b) the variation of tangential coefficients of restitution versus impact angle after Chau et al. (2002) for spheres with different mass.

3.4 APPLICATION OF MDEM IN RIGID-BODY CLUMPS

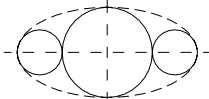
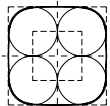
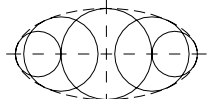
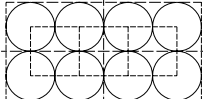
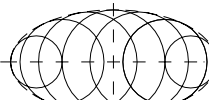
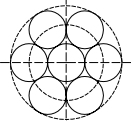
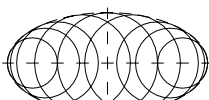
A clump is an assembly of particles which behaves as a rigid body, with the particles remaining at a fixed distance relative to each other, regardless of the external forces (PFC^{2D} theory and background). As a result, these particles cannot overlap and mobilize the forces internally; however, they can interact with the particles that are not part of the clump or other surfaces. The total developed external forces in addition to the gravitational force exert collectively on the rigid clump mass center which results in the motion of the clump.

Building complicated shapes from an assembly of particles is relatively easy. Fortunately, the contact search procedure is robust for this assembly. Studying the impact behavior of a clump is essential before utilizing more complicated discrete element capacities like constructing synthetic materials using bonded particles. In other words, if clumped particles do not simulate the collision correctly, more complicated materials, like bonded materials, bring extra complications into the simulation without addressing the impact behavior properly. DEM approaches have been used to simulate dynamic problems like: collision tests of an assembly of particles, and granular flow through a hopper. What is missing from these studies is whether the constitutive model used in DEM can represent the collisions properly.

The DEM constitutive model consisting of a Kelvin-Voigt system of springs and dashpots might be applicable for quasistatic problems without further investigation, as developed by Potyondy et al. (2004). In these types of simulations, only the final stage of equilibrium is of interest.

The falling rocks can acquire complicated geometry, underlining the importance of studying the coefficients of restitution for complicated shapes made of an assembly of particles e.g. clumps. Table 3.3 shows several clumps which are proposed to be approximations of squares, rectangles, circles, and ellipses. These geometries were chosen as their rebound parameters can be compared with the results from rigid body impact mechanics, which will be introduced in the next chapter.

Table 3.3: Different rigid body clumps representing geometrical shapes

<i>Three-particle ellipse</i>		<i>Four-particle square</i>	
<i>Five-particle ellipse</i>		<i>Eight-particle rectangle, 2:1</i>	
<i>Seven-particle ellipse</i>		<i>Seven-particle disk</i>	
<i>Nine-particle ellipse</i>			

To simulate the clump, the PFC^{2D} (particle flow code) *Version 3.0* (2002) software created by Itasca Consulting Group Inc. was used. For implementation of the MDEM model, the capability of the program to allow the creation of user-defined constitutive models was used. For this purpose, simple C++ code was written using the provided base classes. This code was compiled, and the *DLL* file was transferred into the PFC^{2D} environment. The model parameters were used within the special programming language provided in the software, known as *FISH* language.

To illustrate the application of the new model in impact mechanics a numerical test is introduced in Figure 3.19. In this figure, different proposed clump geometries, shown in Table 3.3, impact on a rigid half space at different orientation angles, θ , under a zero gravity force. The clump vertical velocity is -1 m/s while the tangential velocity is zero, simplifying the motion to a vertical impact. The viscosity of the normal dashpot, C_n , is considered to be zero, assigning a zero-energy dissipation in the normal direction. The friction coefficient is assumed to be 0.58, equal to $\tan(30^\circ)$. The other model properties are defined in Table 3.4. The impact rebound velocities are recorded every 5 degrees of orientation from 0° to 90° . These values are compared with the rebound velocities derived from the impact of geometries having closed-form equation using RBIM, which will be introduced in Chapter 4.

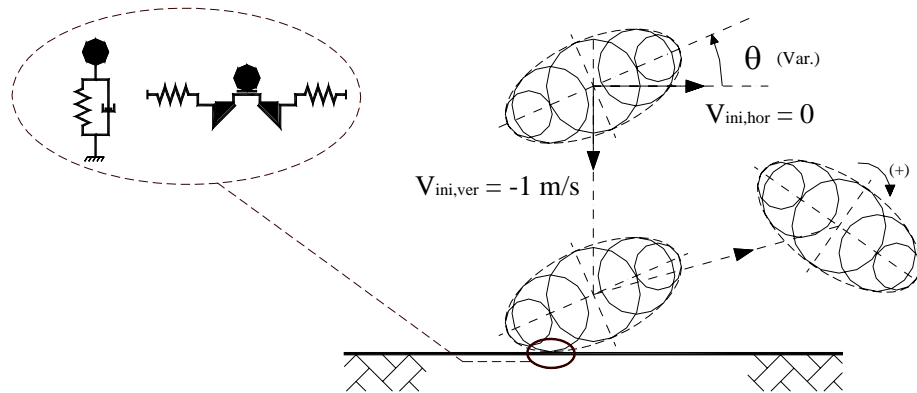


Figure 3.19: Numerical test setup: the impact of different eccentric clumps (introduced in Table 3.4) on a rigid half space at variable impact orientations, under zero-gravity force using MDEM.

Table 3.4: Parameters needed in MDEM and the applied values

<i>Property (Coefficient)</i>	<i>Effect on COR</i>	<i>Value in the simulation</i>
K_n , <i>Nor. spring</i>	No	1e7 (kg/m)
C_n , <i>Nor. viscosity</i>	Yes	0 (no damping)
K_s , <i>Tan. spring</i>	No	1e7 (kg/m)
μ_s , <i>Tan. friction</i>	Yes	$\tan(30^\circ) = 0.58$
K_r , <i>Rot. spring</i>	No	0 (no rotational module)
μ_r , <i>Rot. friction</i>	Yes	0 (no rotational module)

3.4.1 Ellipse representation

In this section, an ellipsoidal shape object is represented by clumps consisting of 3, 5, 7, and 9 particles, as shown in Table 3.3 and Figure 3.19. The normal COR and the rebound tangential and rotational velocities resulting from the impact of these particles are shown in Figure 3.20 versus the impact orientation.

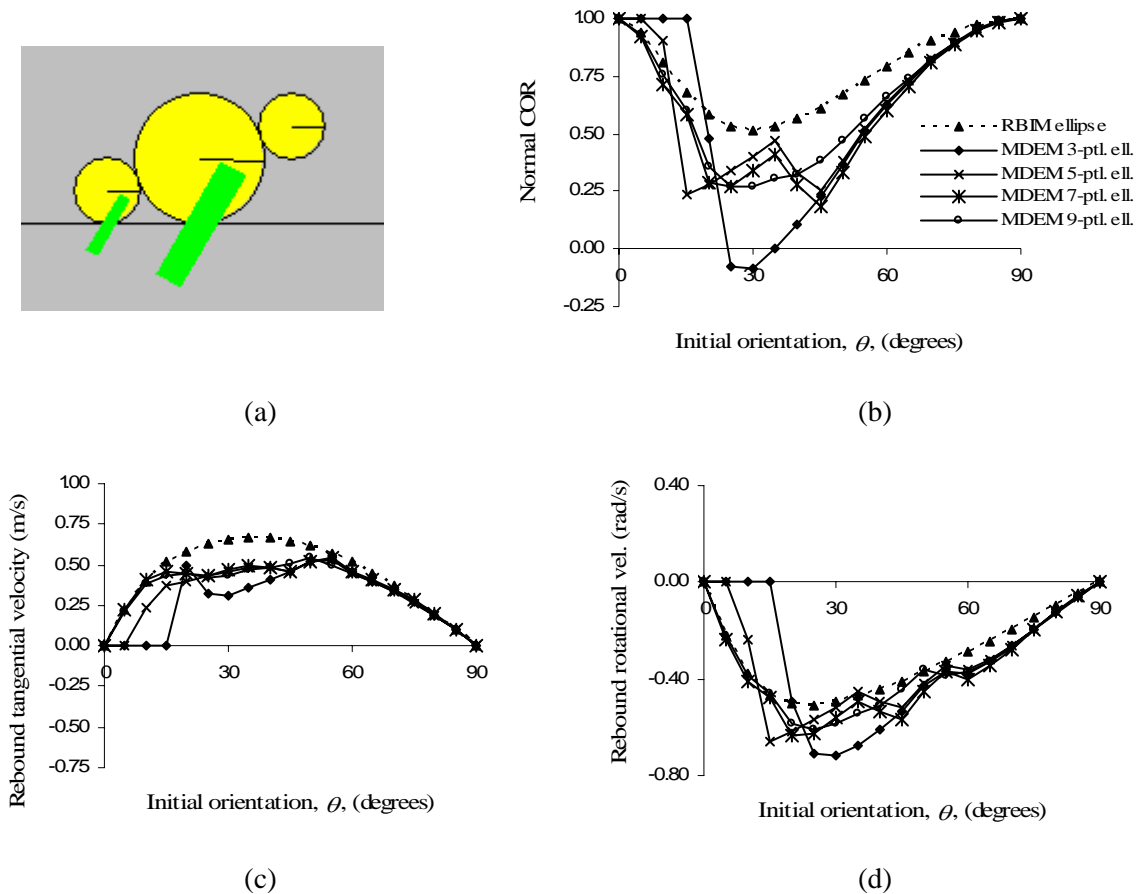


Figure 3.20: Variation of rebound velocities versus the object orientation for vertical impact of an ellipse using RBIM and the represented clumps of Table 3.3 (three, five, seven, and nine-particle ellipse) and using MDEM: (a) typical impact of the three-particle ellipsoidal clump, (b) rebound normal COR at the clumps center, (c) rebound tangential velocity at the clumps center (m/s), and (d) rebound rotational velocity (rad/s).

In Figure 3.20b the normal COR is plotted for the clumps and prism with elliptical cross section. For the three-particle clump, at orientation angles between 5° and 15° , a normal coefficient of restitution equal to 1.0 is derived. The effect is caused by the contact force

passing through the center of the middle particle, producing no tangential energy dissipation. In addition, in this case normal dissipation does not occur as the viscosity is set equal to zero. However, these results are limited to five-particle clumps at orientation angles between 0° to 5° , and do not occur for seven and nine-particle clumps. Generally, the three-particle clump inadequately simulates the normal COR between angles 10° to 45° ; although, these results improve significantly using clumps with more particles. The results for five and seven-particle clumps vary discontinuously at certain impact angles. For example, the trend of variation for the normal COR for a 5-particle clump changes at 15° , 35° , and 45° . This is due to one of two reasons: either the contact point at these angles transfers from one particle to another, or two particles contact the surface at the same time. This variation for normal COR for nine-particle clumps is smooth, showing that this number of particles is enough to geometrically represent the ellipse. The normal COR predicted by a nine-particle clump with the application of MDEM is generally lower than the values predicted by RBIM.

In modeling the ellipse by a nine-particle clump, approximations occur in three cases: when finding the contact point, in defining the contact vector, and in applying the contact forces. It is observed that, over the impact period, a second particle usually enters into the contact. This results in a shift in the contact point which would not occur if the impact occurred between two rigid objects. Moreover, during the impact period as the contact forces are mobilized, the object rotates slightly, and this results in a reduced rebound normal velocity in comparison to the rigid impacts. This situation is similar to rigid impacts when the friction coefficient is lower than the value used in the application of RBIM. Overall, these results produced a reduced normal COR in comparison to the application of RBIM.

Figures 3.20c and 3.20d depict the variations in the rebound tangential and rotational velocities for the objects. These figures show that most of the clumps adequately predict the rebound tangential and rotational velocities for an elliptical shape object. Between 50° and 90° orientation the rebound parameters for the clumps and the ellipse are almost identical. The five-particle clump has a satisfactory result for orientations between 10° and 45° , in contrast with the poor results of three-particle clump for this range. The results for seven and nine-particle clumps are significantly improved because of a better geometrical representation.

It can be concluded from this test that representing an ellipse with the seven and nine-particle clumps is satisfactory. In addition, MDEM represents the RBIM adequately. More investigations can determine if the approximations are primarily caused by the clump geometries or the impact model.

3.4.2 Rectangle representation

In this example, a 2:1 prism with a rectangular cross section is represented by eight particles as shown in Table 3.3 and Figure 3.21a. Figure 3.21 shows the normal COR in addition to the rebound tangential and rotational velocities resulting from the impact of the objects versus orientation.

Figure 3.21b shows the variation of normal COR for the two objects with the impact configurations of Figure 3.19. The proposed clump can replicate the variation of the rectangular section in different impact orientations with very good accuracy. The clump can capture the negative values of COR and the reverses in the trend of variations around 0° and 5° and between 85° and 90° . In Figure 3.21c the variation of rebound tangential velocity is plotted versus the object orientation angle. Generally, the clump does not replicate the exact values because of the corners in the rectangle which are approximated by an arc with radius 0.5 (particle radii). This clump is a better approximation for abraded rocks. The variation of the rebound rotational velocity by a clump strongly follows the same variation for a rectangular prism using RBIM theory, as shown in Figure 3.21d.

It is concluded from this modeling that applying MDEM, and using the concept of a clump model, the object's COR trends of variations are nearly the same as the results of RBIM theory.

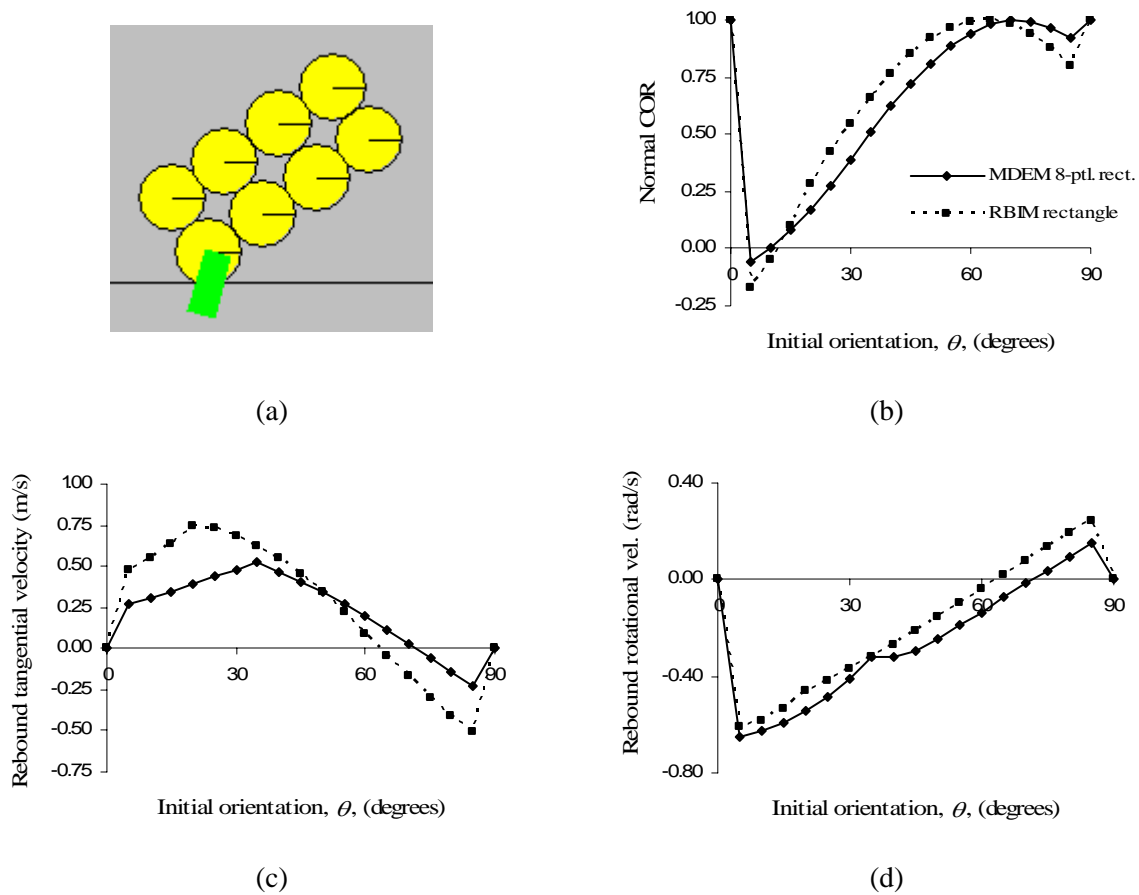


Figure 3.21: Variation of rebound velocities versus object orientation for the vertical impact of a rectangle, using RBIM, and the represented clump of Table 3.3 (eight-particle rectangle) using MDEM: (a) typical impact of the eight-particle rectangular clump, (b) rebound normal COR at the clump center, (c) rebound tangential velocity at the clump center (m/s), and (d) rebound rotational velocity (rad/s).

3.4.3 Square representation

In this section, a square is represented with a four-particle clump as shown in Table 3.3 and Figure 3.22a. The resulted variation of normal COR and the rebound tangential and rotational velocities versus impact orientation are plotted in Figure 3.22. These figures also show the variation of rebound parameters of a square and a unit superellipse power 4 derived by applying the RBIM theory.

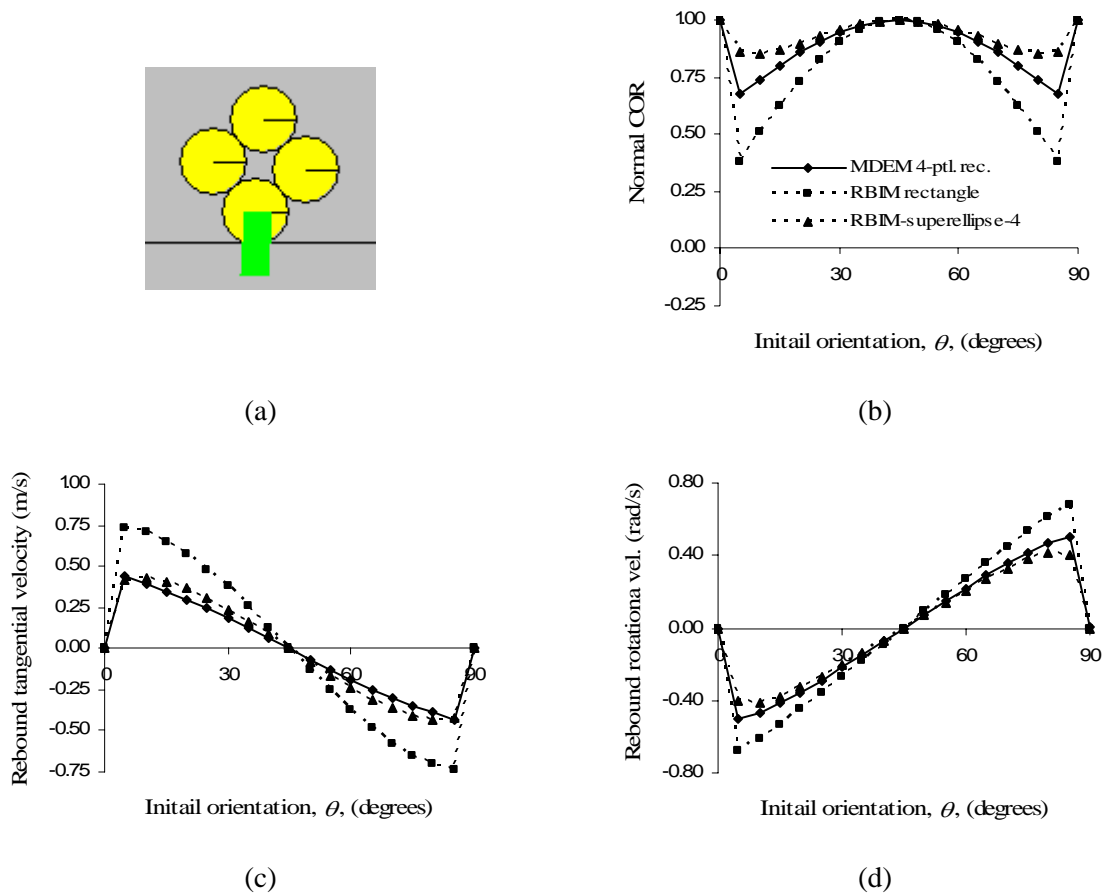


Figure 3.22: Variation of rebound velocities versus object orientation for vertical impact of a rectangle and a superellipse power 4 using RBIM, and the represented clump of Table 3.3 (four-particle rectangle) using MDEM: (a) typical impact of the four-particle rectangular clump, (b) rebound normal COR at the clump center, (c) rebound tangential velocity at the clump center (m/s), and (d) rebound rotational velocity (rad/s).

Figure 3.22b plots the derived normal COR for the clump and the two objects. The variation of the clump normal COR is between the variations of the square and the superellipse for orientation angles between 5° to 30° ; however, between 30° and 45° all objects predict almost the same normal COR. It is also apparent that the curves are symmetric around the angle of 45° . This trend of variation is comparable with the expectations that the rebound values should be between the rebound values resulting from the impact of a rigid body square and a superellipse, as the clump geometry can be considered as an approximation of both geometries.

The variation for the clump tangential COR closely matches the variation for the superellipse, underlining the significance of the curvilinear corners. This can be observed in Figure 3.22c where the variation of both the clump and superellipse rebound tangential velocity is shown to be far from the variation of the rectangular section. For the rotational rebound velocity, as shown in the Figure 3.22d, the variation of the clump is between the variations of the prisms with rectangular and superellipsoidal cross sections; however, the velocity is similar to the variation of the superellipse.

These figures strongly suggest that if shape geometries can be sufficiently approximated by clumps, the proposed MDEM can accurately replicate the rebound velocities predicted by the application of rigid body impact mechanics.

3.4.4 Disk representation

In this section, a circular object is approximated by an assembly of seven particles as shown in Table 3.3 and Figure 3.23a. Figure 3.23 shows the normal COR and the rebound tangential and rotational velocities resulting from a series of impacts, as described in Figure 3.19.

In Figure 3.23a the variation of the normal COR versus impact orientation is plotted. For a discoidal object, a constant COR of 1.0 should result. As a result of the eccentric impact of the boundary particles, values different from 1.0 are derived with a minimum of 0.82 occurring at 5° , 55° , and 65° of orientation. In Figure 3.23b the variation of rebound tangential velocity is plotted for the proposed clump versus the orientation. In discoidal objects, because of the vertical impact, zero tangential velocity is expected. However, because of local eccentric impact of the disks, the clump moves sideways resulting in a value of tangential COR between -0.33 to 0.33. Similar to the normal COR, whenever the clump centric impact occurs, the value of rebound tangential velocity is the same as the impact of the disk.

Figure 3.23c plots the variation of rotational velocity resulting from the impact of the clump at different orientation angles. Despite the zero rotational velocity resulting from the impact

of a disk on a solid half space, the rebound rotational velocity varies between -0.32 to 0.32 rad/s. This trend is similar to the tangential velocity but with opposite sign.

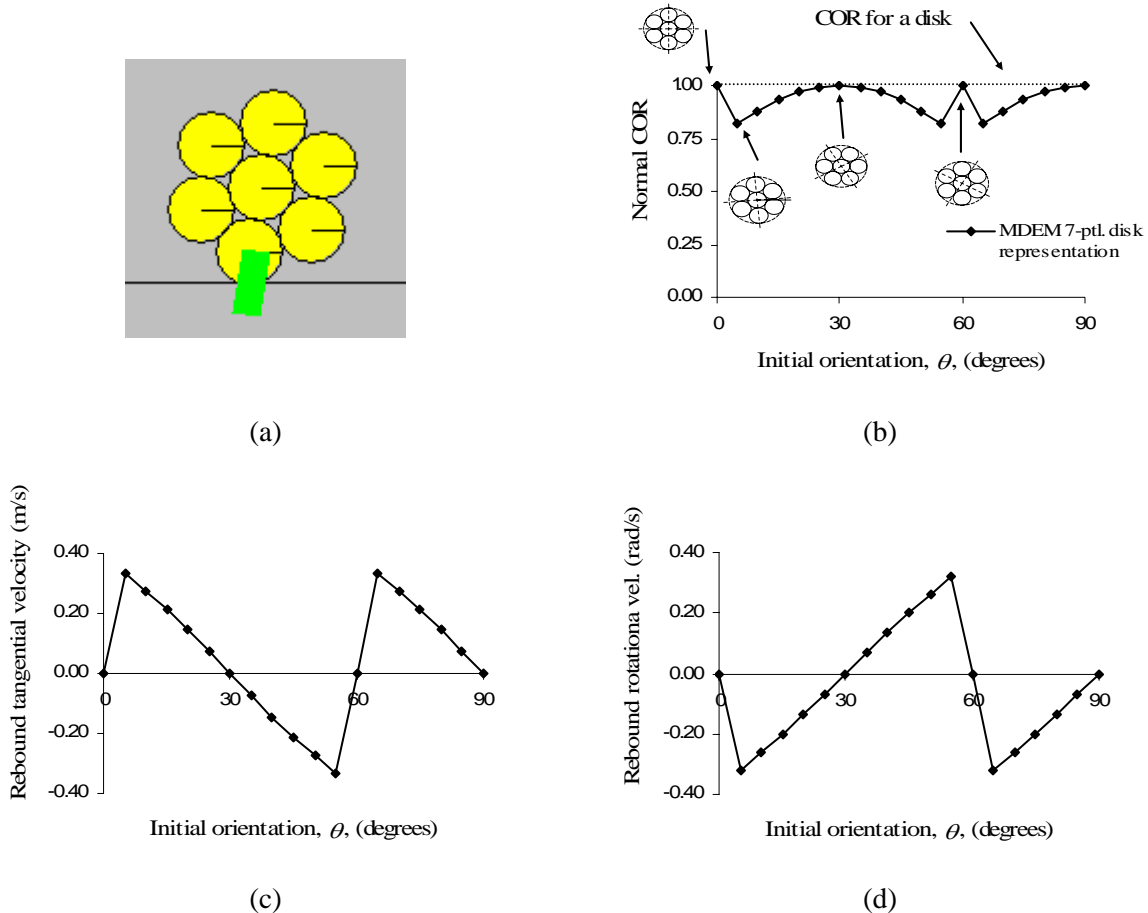


Figure 3.23: Variation of rebound velocities versus object orientation for vertical impact of the represented clump of Table 3.3 (seven-particle disk) using MDEM: (a) typical impact of the seven-particle discoidal clump, (b) rebound normal COR at the clump center, (c) rebound tangential velocity at the clump center (m/s), and (d) rebound rotational velocity (rad/s).

3.5 THE ROTATIONAL MODULE IN MDEM

The last modification needed in DEM is to add a rotational module to the model. Rotating circular objects continue their rotation with a constant rotational velocity after reaching the zero contact point velocity. Figure 3.24 shows the modified DEM with the addition of rotational module. As shown in this figure, the rotational slider is kept as the only source of

rotational energy lost, and the dashpot in this direction is removed in comparison to the classical DEM models in the literature. This dashpot is eliminated for the same reasons used to justify removing the tangential dashpot, as discussed in Section 3.3.4. Researchers such as Bardet et al. (1993) and Iwashita et al. (1998) have used this rotational module to control extensive rotations.

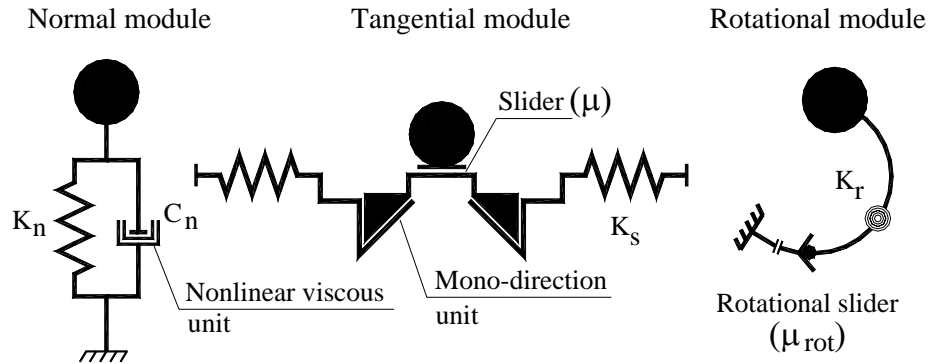


Figure 3.24: Modified DEM consists of three modules: normal, tangential and rotational.

The modified discrete element model (MDEM) consists of six parameters, three springs, two sliders and one dashpot which in total make six unknown parameters. The set of parameters should be chosen in such a way that they resemble the impact, rolling and sliding of a rock. There are several relationships, empirical or theoretical, to relate the stiffness coefficients as described by Equation (3.3.3) or by Iwashita et al. (1998). The three coefficients which control the rebound velocities, or in other words CORs, are: C_n , the viscosity in normal direction; μ the friction coefficient; and μ_{rot} the rotational friction coefficient.

3.6 SUMMARY

- In the proposed MDEM, the linear dashpot in the normal direction is replaced with a nonlinear module. This nonlinear dashpot improves the deficiencies caused by the linear dashpot in three ways: it eliminates the shocking force at the time of impact initiation;

removes the tensile force at the time of contact termination; and causes the normal COR to be a velocity dependent coefficient.

- A mono-direction unit is added in the tangential direction. This releases the strain energy stored in the tangential spring at the time of the tangential reversal. It is shown that the behavior of MDEM in the tangential direction is similar to its behavior in impacts with low tangential compliance (i.e. RBIM).
- Several numerical tests indicate that if shape geometries can be sufficiently approximated by clumps, the proposed MDEM can replicate the rebound velocities that are predicted by the application of RBIM. This approximation needs to resemble both the object's geometry and its mass distribution.
- Numerical investigations by the author showed that the contact search procedure and the calculation of rebound velocities for discrete element modeling are computationally expensive. Due to the probabilistic nature of rockfall modeling, the application of DEM to rockfalls remains restricted to research applications.

CHAPTER 4

APPLICATION OF RIGID BODY MECHANICS TO ROCKFALL SIMULATION

4.1 INTRODUCTION

Rigid body impact results from the collision of two relatively stiff objects over a small area relative to the size of the objects. In rigid body impact the contact stress does not distribute around the contact area, due to the high normal stiffness of the colliding objects. In an ideal case of rigid body impact the contact time is extremely short. This time depends on stiffness, mass, and the velocities of the colliding objects. A large force is developed during this short period of time, and this force terminates the contact by reversing the velocities at the contact point. The developing forces, possibly passing the yield point of the materials, results in high stress. Consequently, the two objects experience irreversible strains around the contact point. These irreversible strains dissipate energy during collision. In rigid body impact mechanics, it is assumed that the colliding objects exhibit high stiffness and the deformed area remains small and does not spread much beyond the contact point.

In rigid body impact mechanics, the contact time is infinitesimally small. As a result the colliding objects do not move during the impact; therefore impact occurs in an invariable framework. The rebounding velocities are assumed to change in a discontinuous trend from an approaching negative velocity to a departing positive one.

In this chapter the collision of a single rock or boulder with an infinite half-space, is investigated. The contact surface is usually considered rigid, referring to an unlimited rigid surface which does not displace, deform, or crush during the impact.

4.2 RIGID BODY IMPACT MECHANICS (RBIM)

Rigid body impact mechanics (RBIM) were originally proposed by Stronge (1994a through 2000). The key assumption in this theory is that all the deformations and energy dissipation is lumped in a small deformable body at the contact point (see Figure 4.1); therefore the rigid bodies neither displace nor deform during the impact. This definition of the deformable body is equivalent to Keller's (1986) asymptotic method of integration with respect to time of the equations for relative acceleration of deformable bodies as the contact time becomes vanishingly small, as explained by Stronge (2000). Consider an object impacting a surface with the local coordinate system at the contact point, as shown in Figure 4.1. The moment the object collides with the surface, resisting forces F_i , develop at the contact point. This results in normal and tangential impulse components, p_n, p_t .

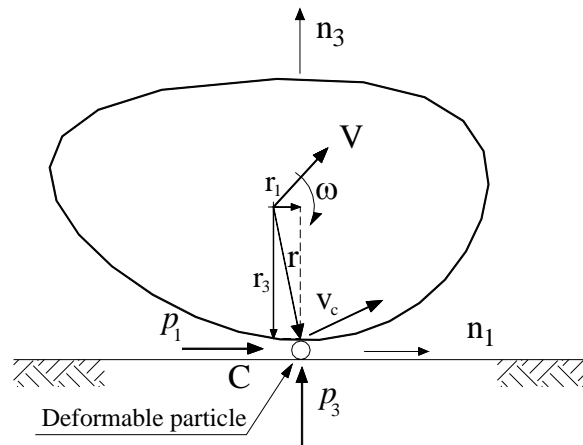


Figure 4.1: Rigid body collision against a rigid surface (half space) where the contact point C is separated by an infinitesimal deformable body (the arrows show the positive signs).

Using Newton's second law of motion for planar displacements, incremental variations of the velocities result in:

$$dp_i = F_i dt \quad i = 1, 3 \quad (4.2.1)$$

$$dV_i = M^{-1} dp_i \quad i = 1, 3 \quad (4.2.2)$$

$$d\omega_i = (Mk_r^2)^{-1} \varepsilon_{ijk} r_j dp_k \quad i = 2 \quad (4.2.3)$$

where ε_{ijk} is permutation number, j and k are dummy indices, M the object mass, dp_k the impulse variation, and k_r the polar radius of gyration. In the above equations, $i=1$ and 3 show the direction tangential and perpendicular to the surface and $i=2$ shows the direction perpendicular to the paper. Using the diagram in Figure 4.1, the contact velocities are calculated as follows:

$$v_i = V_i + \varepsilon_{ijk} \omega_j r_k \quad i = 1, 3 \quad j = 2 \quad (4.2.4)$$

By differentiating the above equation and substituting Equations (4.2.2) and (4.2.3) into this equation, the variations of the planar velocities reduce to:

$$\begin{Bmatrix} dv_1 \\ dv_3 \end{Bmatrix} = M^{-1} \begin{bmatrix} \beta_1 & -\beta_2 \\ -\beta_2 & \beta_3 \end{bmatrix} \begin{Bmatrix} dp_1 \\ dp_3 \end{Bmatrix} \quad (4.2.5)$$

The matrix in Equation (4.2.5) is known as the configuration matrix in which the β s can be described as:

$$\beta_1 = 1 + r_3^2 k_r^2, \beta_2 = r_1 r_3 k_r^2, \beta_3 = 1 + r_1^2 k_r^2 \quad (4.2.6)$$

For eccentric impacts $\beta_2 \neq 0$, this indicates that the variations of the normal and tangential velocities are dependent. In centric or collinear impacts, the contact normal vector passes through the object's center so that $r_1 = 0$. Consequently impacts of circular objects are always centric.

4.2.1 Amontons-Coulomb law of dry friction

The normal and tangential components of impulses can be related to each other using the coefficient of limiting friction, μ , which is applicable to sliding of rough surfaces (Johnson 1985). In planar impacts the relationships between normal and tangential impulses are:

$$\text{if } v_1 = 0 \text{ then } dp_1 < \mu dp \quad (4.2.7)$$

$$\text{if } |v_1| > 0 \text{ then } dp_1 = -\hat{s}\mu dp \quad (4.2.8)$$

where \hat{s} denotes the direction of slip and $dp = dp_3$. Equation (4.2.8) describes the sliding situation, whereas Equation (4.2.7) defines the situation where the contact point sticks. Stronge (1994a) demonstrated that to maintain the sticking situation at the contact point after the tangential velocity reaches zero, the friction should be greater than the stick coefficient: $\mu > |\bar{\mu}| = |\beta_2 / \beta_1|$. Equation (4.2.6) shows that this coefficient exclusively depends on the mass distribution around the contact point. For collinear impact, $\bar{\mu} = 0$; therefore for rough collinear impacts, if the tangential velocity reaches zero the contact point sticks. This fact has also been proposed by Brach (1988), derived from the study of contact forces during impact.

Stronge (1994a) has shown that by substituting Equation (4.2.8) into Equation (4.2.5) and integrating, the relationships between normal and tangential velocities at the contact point simplify to:

$$\begin{aligned} v_1(p) &= v_1(0) - M^{-1}[\beta_2 + \hat{s}\mu\beta_1]p \\ v_3(p) &= v_3(0) + M^{-1}[\beta_3 + \hat{s}\mu\beta_2]p \end{aligned} \quad (4.2.9)$$

These equations state that the variations of the velocities with respect to the normal impulse are linear. Figure 4.2 shows four typical variations of the tangential and normal velocities versus the normal impulse as will be discussed in Section 4.2.3. There are three benchmark impulses in these figures: p_s , the impulse at which the tangential velocity becomes zero; p_c ,

the impulse for zero normal velocity, at which the impulse transforms from compression to restitution; and p_f , at which the contact terminates.

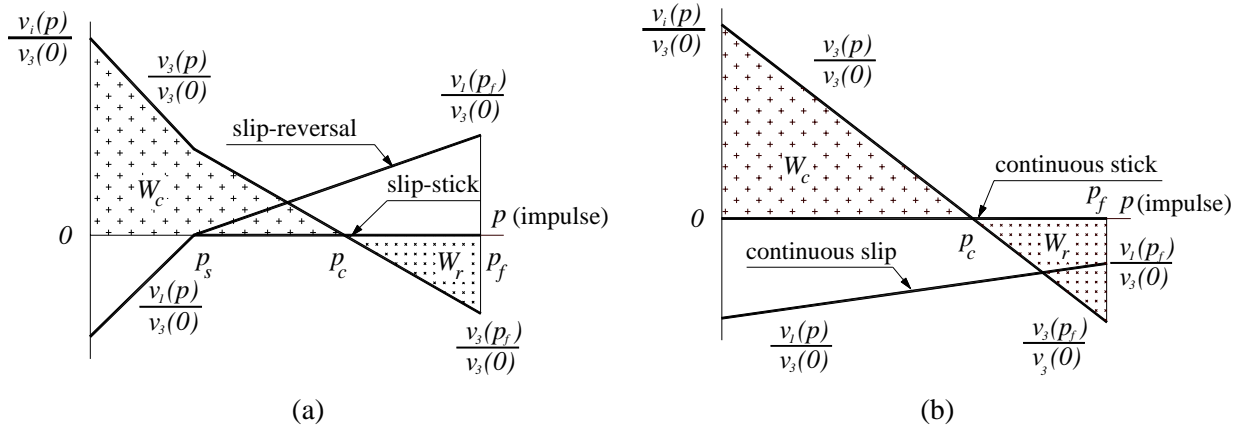


Figure 4.2: Typical variations of normal and tangential components of velocity, v_1 and v_3 , at the contact point versus normal impulse, after Stronge (2000) for: (a) slip-reversal and slip-stick in compression processes, and (b) continuous slip and continuous stick processes.

4.2.2 Energy coefficient of restitution

Dividing the impact process into two phases, compression and restitution, Stronge (1994a) assumed that all the energy dissipation occurs during the period of restitution. Under this assumption, the negative of the value of the ratio of the elastic energy released during restitution to the amount of energy adsorbed during compression is equal to the square of the energy coefficient of restitution, as defined in Equation (4.2.10). This coefficient concentrates all the energy dissipation due to the plastic deformation and hysteretic behavior of the normal force at the contact point. Another source of contact energy loss, not considered by Equation (4.2.10), is due to frictional force.

$$e_*^2 = -\frac{W_c}{W_r} = \frac{-\int_{p_c}^{p_f} v_3(p) dp}{\int_0^{p_c} v_3(p) dp} \quad (4.2.10)$$

The friction coefficient, μ , and the energy coefficient of restitution, e_* , are experimentally measurable, as explained in Appendix 2.

4.2.3 Implementation of equations

The last three equations can be solved to define the rebound velocities. Stronge (2000) showed that the termination velocities depend on the slip process at the contact point, and, based on the impact configuration, five different scenarios may occur:

- Continuous stick
- Continuous slip
- Slip-stick
- Slip-reversal
- Jam-stick.

It should be mentioned that the slip-stick and stick-reversal processes may occur either in compression or restitution. These depend on the relative position of p_s and p_c . If p_s terminates prior to p_c , the process is considered as “in compression”, otherwise it will be “in restitution”. Stronge (2000) showed that the following parameters affect the rebound velocities:

- mass distribution of the object around the impact point,
- contact vector and polar radius of gyration,
- friction coefficient,
- energy coefficient of restitution, e_* ,
- velocity trajectory at the contact point.

Table 4.1 categorizes the impact terminal impulses and velocities for the different impact scenarios. The most important criterion in categorizing the impact is the impact angle, which is represented by the contact velocity ratio shown in Figure 4.3. Table 4.1 demonstrates that defining the impact angle is not only dependent on the ratio of normal to tangential velocities but also on the other four main parameters mentioned above.

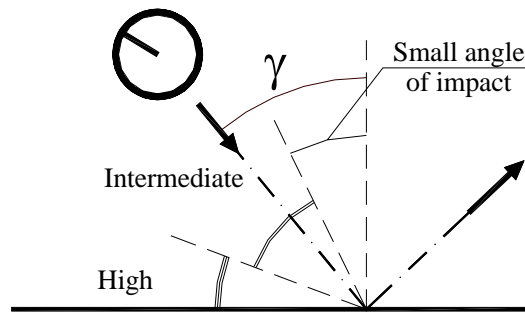


Figure 4.3: Different impact angles defined in Table 4.1.

Theoretically, there is no difficulty in finding the rebound velocities using RBIM if the following three variables are defined for an object in contact:

- object's radius of gyration
- contact point (contact vector)
- normal contact vector.

Table 4.1: Impact parameters for different scenarios happening at planar impact, after Strong (2000)

Angle of impact	Process	Velocity ratio $-v_1(0)/v_3(0)$	Friction ratio $\frac{\mu}{ \bar{\mu} }$	Halting impulse $\frac{p_s}{Mv_1(0)}$	Normal comp. impulse $-\frac{p_c}{Mv_3(0)}$	Ratio of normal terminal impulse to tangential one $\frac{p_f}{p_c}$
Low	Slip-stick in comp.	$-\frac{v_1(0)}{v_3(0)} \leq \frac{\beta_a}{\beta_b}$	≥ 1	β_a^{-1}	$\bar{\beta}_c^{-1} \left(1 + \frac{(\hat{s}\mu + \bar{\mu})\beta_2}{\beta_a} \frac{v_1(0)}{v_3(0)} \right)$	$1 + e_* \left(1 + \frac{(\hat{s}\mu + \bar{\mu})\beta_2}{\bar{\beta}_c} \frac{p_s^2}{p_c^2} \right)^{1/2}$
Low	Slip reversal in rest.	$-\frac{v_1(0)}{v_3(0)} \leq \frac{\beta_a}{\beta_b}$	< 1	β_a^{-1}	$\beta_c^{-1} \left(1 + \frac{2\hat{s}\mu\beta_2}{\beta_a} \frac{v_1(0)}{v_3(0)} \right)$	$1 + e_* \left(1 + \frac{2\hat{s}\mu\beta_2}{\beta_c} \frac{p_s^2}{p_c^2} \right)^{1/2}$
Med.	Slip-stick in comp.	$\frac{\beta_a}{\beta_b} < -\frac{v_1(0)}{v_3(0)}$ $\leq (1 + e_*) \frac{\beta_a}{\beta_b}$	≥ 1	β_a^{-1}	β_b^{-1}	$\frac{p_s}{p_c} + \frac{\beta_b}{\beta_c} \left(\frac{p_s}{p_c} - 1 \right) \left(\left[\frac{(\hat{s}\mu + \bar{\mu})\beta_2}{\beta_b} + \frac{p_c^2 e_*^2}{(p_s - p_c)^2} \frac{\bar{\beta}_c}{\beta_b} \right]^{1/2} - 1 \right)$
Med.	Slip reversal in rest.	$\frac{\beta_a}{\beta_b} < -\frac{v_1(0)}{v_3(0)}$ $\leq (1 + e_*) \frac{\beta_a}{\beta_b}$	< 1	β_a^{-1}	β_b^{-1}	$\frac{p_s}{p_c} + \frac{\beta_b}{\beta_c} \left(\frac{p_s}{p_c} - 1 \right) \left(\left[\frac{2\hat{s}\mu\beta_2}{\beta_b} + \frac{p_c^2 e_*^2}{(p_s - p_c)^2} \frac{\beta_c}{\beta_b} \right]^{1/2} - 1 \right)$
High	Continuous slip	$-\frac{v_1(0)}{v_3(0)} < \frac{\beta_a}{\beta_b}$	≥ 1	-	β_b^{-1}	$1 + e_*$
All	Continuous stick	0	-	-	$\bar{\beta}_c^{-1}$	$1 + e_*$
All	Jam-stick	$\hat{s}\beta_2 < 0$	$\mu \geq -\frac{\beta_3}{\hat{s}\beta_2}$	β_a^{-1}	$\bar{\beta}_c^{-1} \left(1 + \frac{(\hat{s}\mu + \bar{\mu})\beta_2}{\beta_a} \frac{v_1(0)}{v_3(0)} \right)$	^a

Table 4.1: (Continued) Impact parameters for different scenarios happening at planar impact, after Strong (2000)

Angle of impact	Process	Tangential termination Impulse $p_1(p_f)$	Variation in rotational velocity $\Delta\omega$	Tangential termination velocity $v_1(p_f)$	normal termination velocity $v_3(p_f)$
Low	Slip-stick in compression	$-\hat{s}\mu p_s + \bar{\mu}(p_f - p_s)$	$(-r_1 p_f + r_3 p_1(p_f))/k_r^2$	0	$(p_f - p_c)\bar{\beta}_c$
Low	Slip reversal in restitution	$-\hat{s}\mu p_s + \mu\hat{s}(p_f - p_s)$	$(-r_1 p_f + r_3 p_1(p_f))/k_r^2$	$-\beta_d(p_f - p_s)$	$(p_f - p_c)\beta_c$
Med.	Slip-stick in compression	$-\hat{s}\mu p_s + \bar{\mu}(p_f - p_s)$	$(-r_1 p_f + r_3 p_1(p_f))/k_r^2$	0	$\beta_b(p_s - p_c) + \bar{\beta}_c(p_f - p_s)$
Med.	Slip reversal in restitution	$-\hat{s}\mu p_s + \mu\hat{s}(p_f - p_s)$	$(-r_1 p_f + r_3 p_1(p_f))/k_r^2$	$-\beta_d(p_f - p_s)$	$\beta_b(p_s - p_c) + \beta_c(p_f - p_s)$
High	Continuous slip	$-\hat{s}\mu p_f$	$(-r_1 p_f + r_3 p_1(p_f))/k_r^2$	$v_1(0) - \beta_a(p_f)$	$-e_* v_y(0)$
All	Continuous stick	0	$(-r_1 + r_3 \bar{\mu})p_f / k_r^2$	0	$-e_* v_y(0)$
All	Jam-stick	$-\hat{s}\mu p_s + \bar{\mu}(p_f - p_s)$	$(-r_1 p_f + r_3 p_1(p_f))/k_r^2$	0	$(p_f - p_c)\bar{\beta}_c$

$$\beta_a = \beta_2 + \hat{s}\mu\beta_1 \quad \beta_b = \beta_3 + \hat{s}\mu\beta_2 \quad \beta_c = \beta_3 - \hat{s}\mu\beta_2 \quad \beta_d = \beta_2 - \hat{s}\mu\beta_1 \quad \bar{\beta}_c = \beta_3 - \bar{\mu}\beta_2$$

$$\bar{\mu} = \beta_2/\beta_1 \quad \hat{s} = \text{sgn}(v_1) = v_1/|v_1| \quad |\bar{\mu}| = |\beta_2/\beta_1|$$

$$^a p_f = p_c - \frac{e_* m v_3(0)}{\bar{\beta}_c} \left(1 + \frac{(\hat{s}\mu + \bar{\mu})\beta_2 v_1(0)}{\beta_a v_3(0)} + \frac{(\hat{s}\mu + \bar{\mu})\beta_2 \beta_b v_1^2(0)}{\beta_a^2 v_3^2(0)} \right)^{1/2}$$

In order to find the rebound velocities, the impact should be categorized based on the processes in Table 4.1. On the other hand, basing the impact process on the impact angle is not a feasible approach, as the velocity ratios overlap with each other. In order to categorize the impact process based on the processes in Table 4.1, three critical impulse ratios are defined. Theoretically, the tangential impulse, p_s , terminates the tangential velocity, the normal impulse, p_c , terminates the normal velocity, and at the impulse, p_f , the contact terminates. To define these impulses Equations (4.2.9) are set to zero and it is assumed that the termination normal impulse varies linearly, proportional to $(1 + e_*)$, resulting in:

$$p_{f,crit} = (1 + e_*)p_{c,crit} \quad (4.2.11)$$

The impact process can be defined uniquely, based on the relative position of these impulses:

$$p_{s,crit} = -v_1(0)/(\beta_2 + \hat{s}\mu\beta_1) \quad (4.2.12)$$

$$p_{c,crit} = -v_3(0)/(\beta_3 + \hat{s}\mu\beta_2) \quad (4.2.13)$$

$$p_{f,crit} = -v_3(0)(1 + e_*)/(\beta_3 + \hat{s}\mu\beta_2) \quad (4.2.14)$$

The jam-stick process cannot be defined using the above equations, due to its simultaneous dependence on the β values and the friction coefficient, rather than the impact angle. As a result the occurrence of the jam-stick process should be checked separately. Table 4.2 defines the slip modes based on the relative values of the critical impulses.

The tangential and normal rebound velocities at the object's center of gravity and in the local frame work are calculated based on the contact velocities and the rebound rotational velocity as follows:

$$\begin{aligned} V_x(p_f) &= v_x(p_f) - r_3\omega(p_f) \\ V_y(p_f) &= v_y(p_f) + r_1\omega(p_f) \end{aligned} \quad (4.2.15)$$

Table 4.2: Relative position of critical impact processes in eccentric impact

<i>Process</i>	<i>Critical impulses</i>	<i>Friction</i>
<i>Continuous stick</i>	$p_s = 0$	$\mu > \bar{\mu}$
<i>Continuous slip</i>	$p_s > p_f$	-
<i>Slip-stick in compression</i>	$p_s < p_f$ and $p_s < p_c$	$\mu > \bar{\mu}$
<i>Slip-stick in restitution</i>	$p_s < p_f$ and $p_s > p_c$	$\mu > \bar{\mu}$
<i>Slip-reversal in compression</i>	$p_s < p_f$ and $p_s < p_c$	$\mu < \bar{\mu}$
<i>Slip-reversal in restitution</i>	$p_s < p_f$ and $p_s > p_c$	$\mu < \bar{\mu}$

4.2.4 Collinear impacts in RBIM

A collinear or centric impact occurs when the contact vector passes through the object's center of gravity, when $r_I = 0$ in Figure 4.1. In this situation, for spherical objects, the contact configuration simplifies to Figure 4.4a. The centric impact case does not exclusively occur for spheres, but can also occur for other geometries, such as prisms and ellipsoids at particular orientations (0° and 90°) as shown by Figures 4.4b and 4.4c. As a result, the following relationships can be applied to the centric impact for any type of geometries, as far as the impact is centric.

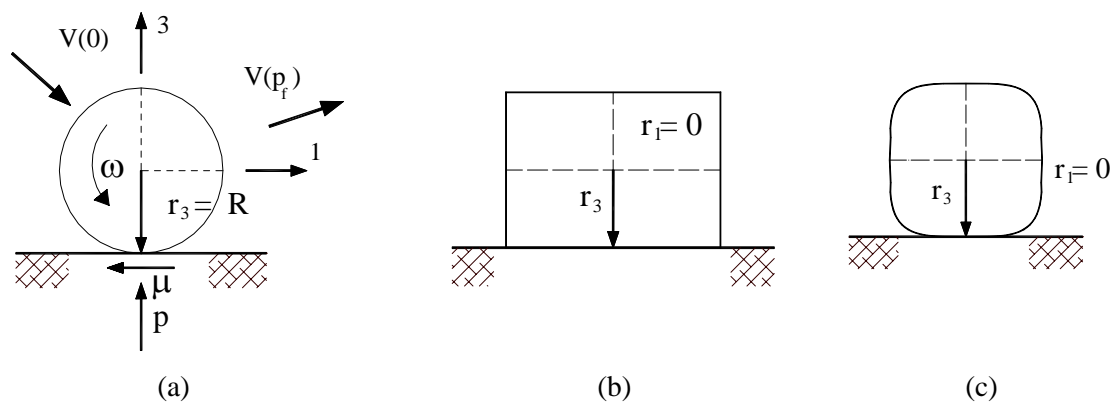


Figure 4.4: Collinear impacts: (a) impact of spherical object, (b) impact of a rectangular shape, and (c) impact of an ellipsoidal object.

In centric collisions $\beta_2 = 0$ and $\beta_3 = 1$, and, as a result, the complicated equations shown in Table 4.1, for the case of pure sliding, simplify to the following three equations:

$$V_3(p_f) = -e_* V_3(0) \quad (4.2.16)$$

$$V_1(p_f) = V_1(0) - \hat{s}\mu(1 + e_*)V_3(0) \quad (4.2.17)$$

$$\omega(p_f) = \omega(0) - \hat{s}\mu R / k_r^2 (1 + e_*)V_3(0) \quad (4.2.18)$$

In collinear impacts there is no contact velocity reversal in the tangential direction. This means that, if the tangential contact velocity reaches zero, the contact point does not slide in the reverse direction, but instead sticks. As a result the tangential mechanism for collinear impacts can be one of these mechanisms: continuous stick, pure sliding, or slip-stick. The minimum rebound velocity, or the minimum tangential COR, occurs in the sliding-stick situation. In order to define these minimum values, the pure rolling constraint of $V_1 = r_3\omega$ is used to relate the velocity values in the Equations (4.2.17) and (4.2.18) which results in the minimum value of the rebound tangential velocity as follows:

$$V_{1,\min}(p_f) = V_1(0) - \frac{V_1(0) - r_3\omega(0)}{(1 + r_3^2 / k_r^2)} \quad (4.2.19)$$

Brach (1998) defined the critical friction, μ_{crit} , needed to bring the tangential contact velocity to a halt. This value can be defined by equating Equations (4.2.17) and (4.2.19):

$$\mu_{crit} = \frac{[V_1(0) - r_3\omega(0)]}{(1 + r_3^2 / k_r^2)(1 + e_*)V_3(0)} \quad (4.2.20)$$

The minimum tangential COR for non-rotating objects in a centric impact may be defined by setting $\omega = 0$ in Equation (4.2.19), producing:

$$R_{t,\min} = \frac{1}{1 + k_r^2 / r_3^2} \quad (4.2.21)$$

Table 4.3: Minimum tangential COR for different geometrical objects

<i>Object</i>	<i>2-D object</i>	<i>3-D object</i>
Circles (spheres)	0.67	0.71
Square	0.61	0.61
Superellipse (ellipsoid) III	0.64	0.67
Superellipse (ellipsoid) IV	0.62	0.64
Rectangle with aspect ratio 2:1	0.625	0.625

Equation (4.2.21) shows the dependence of $R_{t,min}$ on k_r , the object geometry represented by radius of gyration, or, in other words, mass distribution around the contact point. Table 4.3 illustrates this value for different two-dimensional and three-dimensional geometries. The values derived in this table are compatible with the data shown in Figure 2.2 for tangential COR, with the minimum observed value around 0.6. It should be noted that these values are prepared for lumped-mass models which consider the rock shape as an infinitesimal sphere. It will be shown later that R_t for non-spherical objects has a wider range of variation, from negative values to values greater than 1.0.

4.3 IMPACT MODELS IN ROCKFALL LITERATURE

Rigid body impact models have been utilized in rockfall studies by either direct application to define the rebound parameters, or with the use of simplifying assumptions. These assumptions might occur by the usage of a simplified version of the impact model or by the usage of a simplified contact search procedure. The simulators which apply these simplifying assumptions are known as hybrid models. Rockfall simulations are categorized by Guzzetti et al. (2002) as: rigid body, hybrid, or lumped-mass models. Properties used to categorize these models include: rock geometry, model dimension (2D or 3D), impact model, and the consideration of probabilistic analysis. These simulation properties are covered in the next chapter. In this section, the properties of some hybrid and rigid body models are investigated, mentioning the limitations and advantages of each, along with a study of the effects of geometrical shapes in COR.

4.3.1 Hybrid (stereomechanical) model by Pfeiffer and Bowen (1989)

Pfeiffer and Bowen (1989) proposed the best-known and widely-used rockfall model, implemented in the CRSP computer simulation. This model was later used by Stevens (1998) in RocFall[®] and by Jones et al. (2000) in CRSP 4.0 simulations. These models consider the falling rock as a dimensionless, circular, rigid object with the mass concentrated at the center. The authors considered these assumptions as conservative as the circular object has the highest weight and energy with the least area in comparison with the other geometries, and they expected that the circular object should have the greatest roll-out distance.

There are three major assumptions used to determine the rebound translational and rotational velocities. First, the normal velocity is reduced using scaled normal COR (SI units), demonstrated in Equation (4.3.1). This factor considers the inelastic deformation mechanism happening at the contact point, concentrating all rock crushing and fracturing at this point (Habib, 1976):

$$V_3(f) = \frac{R_n}{1 + (V_3(0)/9.8)^2} V_3(0) \quad (4.3.1)$$

In the above equation $V_3(0)$ and $V_3(f)$ are the approaching and rebound normal velocities, and R_n is the normal coefficient of restitution. Second, it is assumed that sliding is terminated at the end of contact; therefore, the contact ceases in pure rolling (or slip-stick as explained earlier):

$$\omega(f) = V_1(f)/R \quad (4.3.2)$$

Finally the combination of tangential and rotational impact energy is reduced using two factors: scaling and friction. As a result, the tangential velocity is defined as follows:

$$V_1(f) = \sqrt{\frac{R^2(I\omega^2(0) + MV_1^2(f))\tilde{f}(F)SF}{I + MR^2}} \quad (4.3.3)$$

and this reduces to the following equation for spheres in planar impacts:

$$V_1(f) = \sqrt{\left(2/7 R^2 \omega^2(0) + 5/7 V_1^2(0)\right) \tilde{f}(F) SF} \quad (4.3.4)$$

where R , I , M , are radius, moment of inertia, and the mass of the object, respectively. In these equations ω and V_1 represent the rotational and tangential velocities. The friction function, $\tilde{f}(F)$, adjusts the tangential COR according to the tangential velocity at the contact and incorporates the reduction in the friction coefficient at higher velocities. The scaling factor integrates the effect of the normal velocity on tangential COR. As the normal velocity increases, the tangential compliance increases, leading to reduced tangential and rotational velocities. Figure 4.5 shows the variations of these factors versus velocity. The friction and scaling factors are defined as (SI units):

$$\tilde{f}(F) = R_t + \frac{1 - R_t}{\left((V_1(0) - R\omega(0))/3.0\right)^2 + 1.5} \quad (4.3.5)$$

$$SF = R_t / \left(1 + (V_3(0)/15.2)^2\right) \quad (4.3.6)$$

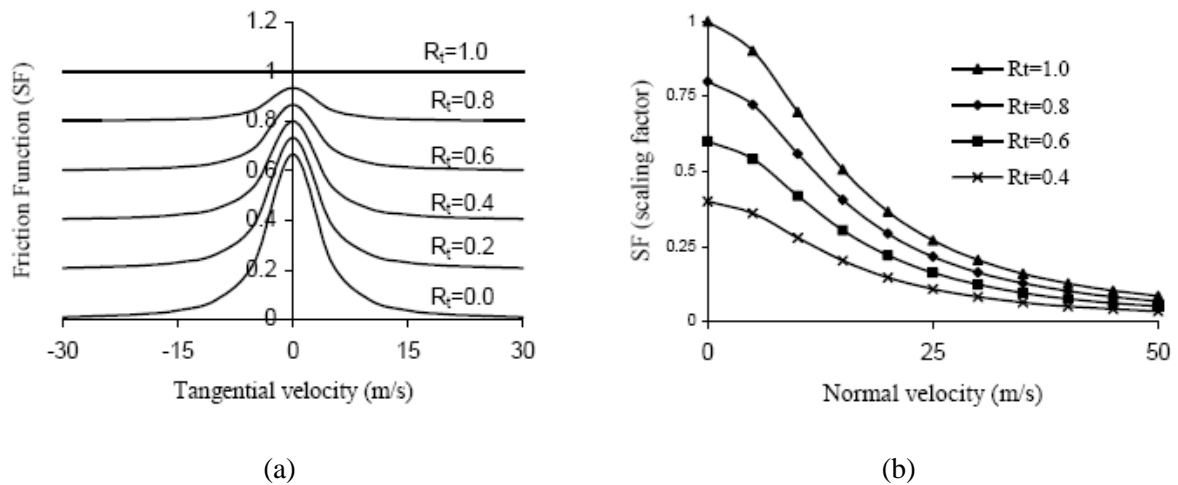


Figure 4.5: Tangential coefficients versus impact velocity as defined by Pfeiffer et al. (1989): (a) Friction function versus tangential velocity, and (b) Friction scaling factor.

The main deficiency of this model is that it does not incorporate the geometry effect, either rock geometry or the effects of corners. The other major deficiency of this model is the assumption of a pure rolling process, which does not always occur in the tangential direction.

It has been shown in Section 4.2.4 that the pure sliding assumption results in the minimum tangential COR which is not a conservative assumption.

4.3.2 Hybrid model by Bozzolo et al. (1986) and Azzoni et al. (1995)

Azzoni et al. (1995) proposed a hybrid mathematical model for rockfall impact modeling and implemented it in the CADMA application. The impact model was originally introduced by Bozzolo et al. (1988) and implemented in the simulation programs SASS and MASSI. Azzoni introduced new algorithms to solve the impact equations and generalized the rolling of circular objects for different geometrical shapes. In CADMA, the impact is defined when the parabolic object path intersects with the contact surface. This model is defined for special types of non-circular objects, mainly ellipses. In CADMA, the hybrid impact model is based on three assumptions: conservation of angular momentum, no-sliding at the contact point (pure rolling at the time of contact termination), and the energy coefficient of restitution accounts for energy losses. By applying the above assumptions, the rebound rotational velocity is calculated as:

$$\omega(f) = \frac{I\omega(0) + V_1(0)r_3 - V_3(0)r_1}{I + r_1^2 + r_3^2} \quad (4.3.7)$$

$$V_1(f) = \omega(f)r_3, \quad V_3(f) = -\omega(f)r_1$$

where 1 and 3 denote the tangential and normal directions, and r_1 and r_3 are the contact vectors as defined in Figure 4.6a. The remaining variables are as defined in Equations (4.3.3) and (4.3.4).

The rebound velocities are defined using Equations (4.3.7), however, the rebound energy might be greater than the energy constraint defined as the maximum energy COR, ε_{\max}^e . In this case the rotational velocity, and consequently the translational velocities, is reduced according to the following equation:

$$\omega = \sqrt{\frac{2\varepsilon_{\max}^e K_0}{(I + R^2)}} \quad (4.3.8)$$

where K_0 is the total initial kinetic energy and ε_{\max}^e is the maximum energy COR, which acts as an upper bound for the rebound energy. This hybrid model incorporates the ellipsoid's geometry at the time of contact; therefore, when the normal rebound velocity is negative, the object can not separate. As a result, to assure separation, the authors introduced the occurrence of a second impact with a symmetric object configuration.

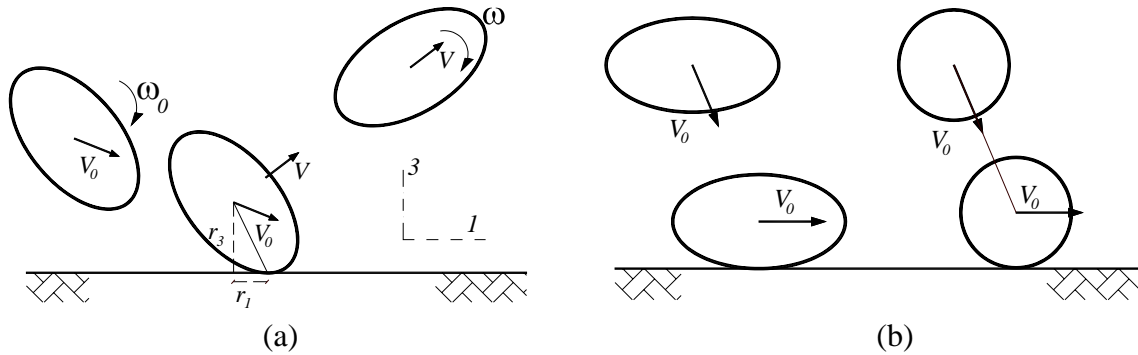


Figure 4.6: Impact configuration for the application of Azzoni's model: (a) general eccentric impact, and (b) collinear impact (in Azzoni's model), any non-rotational collinear impact ends in zero normal rebound velocity and pure rolling.

Figure 4.6b shows the special case of centric impact in which $r_l = 0$. In this case the equations for rebound velocities for spheres reduce to Equation (4.3.9).

$$\begin{aligned} \omega(f) &= \frac{2}{7} \omega(0) + \frac{5}{7} \frac{V_1(0)}{R} \\ V_1(f) &= \frac{2}{7} \omega(0)R + \frac{5}{7} V_1(0), \quad V_3(f) = 0 \end{aligned} \quad (4.3.9)$$

The derived equations for tangential and rotational velocities are compatible with most rigid body models when the impact stops in pure rolling. However, the model incorrectly considers the normal rebound velocity as equal to zero, which makes it impractical to model rock geometry. It should be mentioned that the tangential COR for a non-rotating sphere is derived as a constant equal to $5/7$ ($= 0.71$). This value is the same for the other rigid body models in the case where the sliding terminates before separation. Further investigation of the variations in COR in Azzoni's impact model is performed in the following sections.

4.3.3 Rigid body model by Descouedres et al. (1987)

Descouedres et al. (1987) proposed a three-dimensional kinetic impact model in which the reflected velocities are functions of the normal and tangential impulses. In this model, the normal and tangential impulses are divided into two portions, as defined in Figure 4.7a, according to the normal impulse. The first portion of the impulse occurs before the maximum of impulse, while the second portion occurs after, but before separation. By definition, at the time of maximum impulse, t_c , the contact velocities are equal to zero and the following equations can be applied:

$$\begin{aligned} M(\hat{V}(p_c) - \hat{V}(0)) &= \hat{p}_c \\ \hat{I}(\hat{\omega}(p_c) - \hat{\omega}(0)) &= \hat{r} \times \hat{p}_c \\ \hat{V}(p_c) + \hat{\omega}(p_c) \times \hat{r} &= 0 \end{aligned} \quad (4.3.10)$$

In these equations \hat{p} is the impulse vector, the index c represents the time of maximum impulse, 0 denotes the pre-impact situation, \hat{r} is the contact vector, M is the object's vector, \hat{V} is the object velocity vector, \hat{I} is the rotary inertia, and $\hat{\omega}$ is the rotation matrix. By introducing the kinetic coefficient of restitution, e_n , (similar to the definition provided in Section 2.2.1.2) and assuming that the variation of normal impulse is linear, the termination normal impulse is defined as (the real non-linear variation of normal impulse versus contact time is illustrated in Figure 4.7b):

$$p_f = (1 + e_n)p_c \quad (4.3.11)$$

Based on the variation of tangential impulses, two modes of impact are defined: no-sliding and sliding. Descouedres et al. (1987) suggested an iterative 3D method for solving the Equation-set (4.3.10), motivated by the nonlinear variation of the tangential impulse in the contact plane. In 2D, the sliding direction is invariable; therefore, a closed-form solution can be derived, similar to RBIM, saving computational time and effort. In the next section, it is shown that for impact angles smaller than a certain value γ_c , similar to the impact angle shown in Figure 4.3, sliding does not occur at the contact.

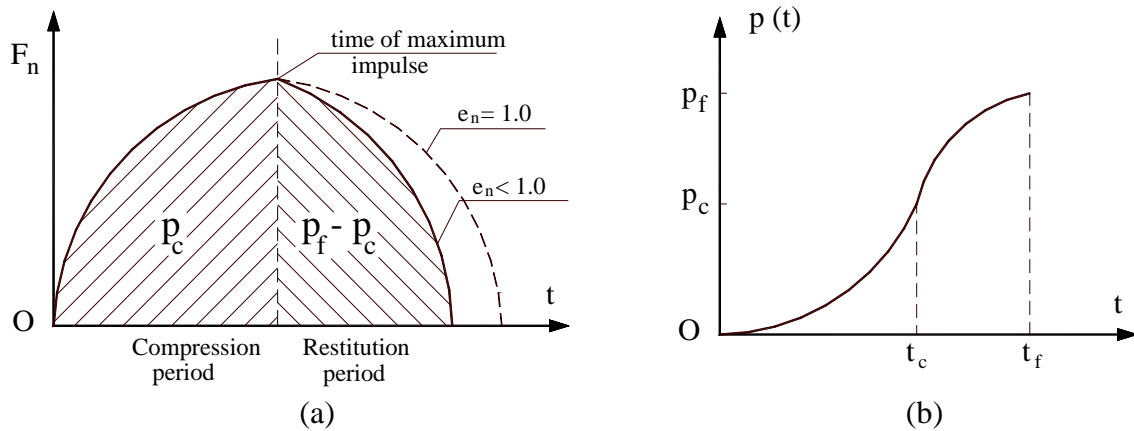


Figure 4.7: (a) The variation of contact forces versus time in two phases of compression and restitution, (b) the variation of normal impulse as a function of time.

4.3.3.1 No-sliding mode ($\gamma \leq \gamma_c$)

By simultaneously solving Equations (4.3.10), (4.2.3), and (4.2.4), tangential and normal impulses can be derived as follows:

$$p_1(p_c) = -\frac{\beta_3 v_1(0) + \beta_2 v_3(0)}{\beta_1 \beta_3 - \beta_2^2} \quad (4.3.12)$$

$$p_c = -\frac{\beta_2 v_1(0) + \beta_1 v_3(0)}{\beta_1 \beta_3 - \beta_2^2} \quad (4.3.13)$$

where the β s are defined in Equation (4.2.6), and $v_1(0)$ and $v_3(0)$ are the contact velocities before impact. In this case, the normal impulse variation is independent of the tangential impulse variation, as defined in Equation (4.3.11). The necessary condition for the object to remain in no-sliding condition is defined as:

$$p_1(p_f) = 2p_1(p_c) \quad \text{if} \quad p_1(p_f) \leq \mu p_f \quad (4.3.14)$$

where μ is the friction coefficient and is usually assumed to be constant. In this theory, when the impulse is maximum, both the tangential and normal contact velocities are equal to zero. However this assumption may not be realistic since the two impulses usually vary differently. If the no-sliding condition, defined in Equation (4.3.14), is not valid, the object undergoes sliding.

In order to find the impact angle in which the impact mode transfers from no-sliding to sliding, γ_c , Equations (4.3.11) to (4.3.13) are substituted into Equation (4.3.14). By simplifying the resulting equations, the velocity ratio, or the critical angle, is defined as:

$$-\frac{V_1(0)}{V_3(0)} = \frac{\mu\beta_1(1+e_n)-2\beta_2}{\mu(1+e_n)\beta_2+2\beta_3} \Rightarrow \gamma_c = \tan^{-1}\left(\frac{\mu\beta_1(1+e_n)-2\beta_2}{\mu(1+e_n)\beta_2+2\beta_3}\right) \quad (4.3.15)$$

In collinear impacts, where $\beta_2=0$, this angle reduces to $\gamma_c = \tan^{-1}(\mu\beta_1(1+e_n)/2\beta_3)$ and for spheres can be reduced to $-V_1(0)/V_3(0) = 7/4 \mu(1+e_n)$. This angle is twice the value derived by Brach (1988) and Stronge (2000): $-V_1(0)/V_3(0) = 7/2 \mu(1+e_n)$.

4.3.3.2 Sliding mode ($\gamma > \gamma_c$)

In the sliding case $p_1(p_f) > \mu p_f$, implying that either the friction coefficient or the normal impulse are not high enough to hold the tangential direction in sticking mode. Therefore, when the tangential impulse is large relative to the normal one, sliding occurs at either a low friction coefficient or a high impact angle. The tangential impulse at the time of maximum normal impulse, Equation (4.3.12), becomes:

$$p_1(p_c) = 1/2(-\hat{s})\mu p_f = 1/2(-\hat{s})\mu(p_c + e_n p_c) = 1/2(-\hat{s})\mu p_c(1+e_n) \quad (4.3.16)$$

This equation replaces the last equation of Equations (4.3.10). Simultaneous solving of these equations produces the normal impulse for sliding:

$$p_c = -\frac{v_3(0)}{\hat{s}\beta_2\mu(1+e_n)/2 - \beta_3} \quad (4.3.17)$$

4.3.3.3 Rebound velocities

The rebound velocities can be derived using the following equations:

$$\omega(p_f) = \omega(0) + (-p_f r_1 + p_1(p_f) r_3) / k_r^2 \quad (4.3.18)$$

$$V_3(p_f) = V_3(0) + p_f / M \quad (4.3.19)$$

$$V_1(p_f) = V_1(0) + p_1(p_f)/M \quad (4.3.20)$$

4.4 EFFECT OF ROCK GEOMETRY ON THE COR IN THE APPLICATION OF RBIM IN ROCKFALL STUDIES

In addition to the contact material properties, the object geometry and the distribution of mass around the contact point affect rebound velocities and energies. This causes the kinetic energy to transfer between modes of motion, between rotational and translational energies. As a result, it is not practical to use the definition of tangential and normal COR to define the rebound velocities of non-circular objects.

To illustrate the effect of impact geometry on rebound velocities and energies, the planar impact of an ellipsoidal object on a surface is studied as a numerical experiment. Figure 4.8 shows the impact of an ellipsoid on a flat surface at different impact angles, γ , and different initial orientations, θ , with a constant initial normal velocity equal to -10 (m/s). This ellipsoid has the minor and major axes of 1 and 2 meters, respectively.

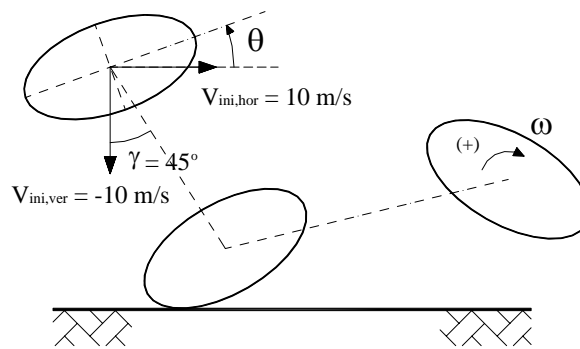


Figure 4.8: The impact of an eccentric object on a rigid half space at variable impact angles and different orientations, under zero gravity force.

For the first example of RBIM application, values for the impact properties, considered to be typical values in rockfalls, are used: $e_* = 0.5$, and $\mu = \tan(30) = 0.58$ for a friction angle of 30° . The ellipsoid is projected at the half-space (ground) at an angle of 45° , $V_{ini,hor} = 10$ m/s, and with different initial orientation angles, θ , under zero gravitational force. Figure 4.9

shows the object rebound velocities and energies resulting from the RBIM application. The impact rebounds are recorded every 5 degrees of orientation from 0° to 180° . The plots show that although the object is impacting the surface at an angle continually changing by 5° , the rebound velocities are highly dependent on the mass distribution around the contact point, and not solely on the angle of impact. The definition of high, medium, or low impact angle, as discussed in Section 4.2.3, is also dependent on this distribution. A similar sphere with the same contact properties experiences constant coefficients of restitution of $R_t = 0.71$ and $R_n = 0.5$. In contrast, the variation of these values for an eccentric object like an ellipsoid is highly nonlinear.

Figure 4.9a shows the variation of normal rebound velocity versus impact orientation. Normal rebound velocity varies between -3.5 and 7.0 (m/s), resulting in a normal coefficient of restitution, R_n , between -0.35 and 0.70. The average normal velocity is 2.5 m/s showing a normal COR equal to 0.25; if, however, the object were a sphere, the normal COR would be constant and equal to 0.5. The definitions of low, medium, and large modes of impact are used to categorize the variations in tangential direction. As a result, less sharp effects are apparent in this curve when compared, for example, to a tangential velocity variation curve. Sharper variations in the curve occur when the mode of contact varies, for example, from a large to a medium impact angle. The increasing trend of the curve reverses at the angle of 125° , when the angle of impact changes from a low impact angle to a medium and finally to a large impact angle, which occurs in a pure sliding case.

Figure 4.9b plots the variation of tangential rebound velocity against initial orientation, θ . Again, the variation is highly nonlinear. In this plot, the rebound tangential velocity varies between 1.1 and 10.6 m/s with an average of 6.2 m/s. These values indicate a variation in tangential COR between 0.11 and 1.06. This range of variation is significantly different from the range of variation for a sphere: $R_t = 0.71$ -1.0. At an angle of 135° , the slip-reverse mode in the tangential direction ceases and the contact experiences pure rolling, i.e. the decreasing trend of tangential velocity reverses to an increasing trend.

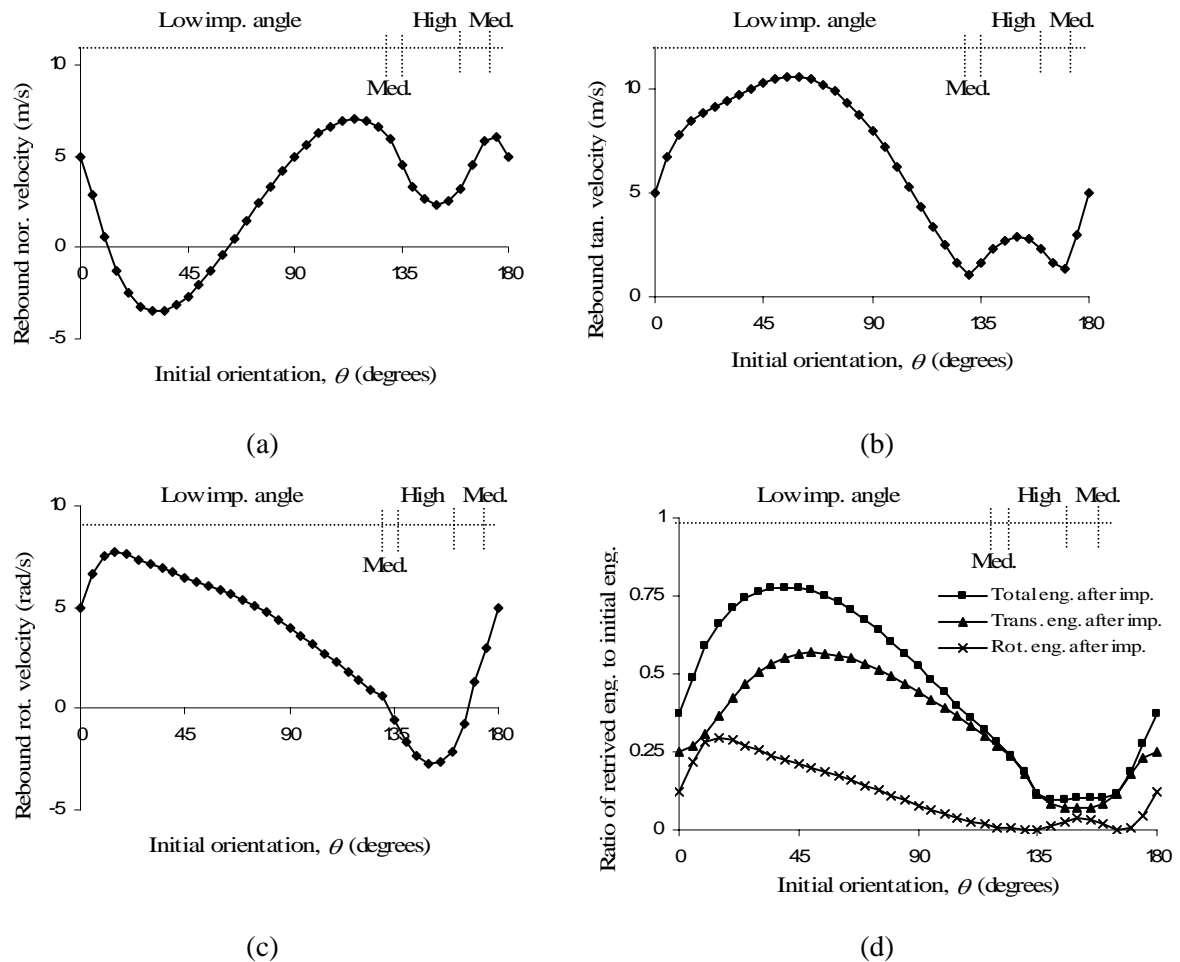


Figure 4.9: Variation of velocities and energies versus object orientation for planar impact of an ellipsoid at an impact angle of 45° ($V_{ini,hor} = 10$ m/s): (a) rebound normal velocity at the center, (b) rebound tangential velocity at the center (m/s), (c) rebound rotational velocity (rad/s), and (d) ratio of retrieved energies after impact to initial energies: the total retrieved energy consists of rotational and translational energies, the ratio of translational energy to total initial energy, and the ratio of rotational energy to total initial energy (in the above figures low, med., and large impact angles refer to the conventions defined in Table 4.1 and demonstrated in Figure 4.3).

Figure 4.9c shows the variation of rebound rotational velocity between -2.7 and 7.7 (rad/s), which follows the variation of rebound tangential velocity, except in the case of large angle impact, where its trend of variation is opposite to the trend of tangential velocity.

Figure 4.9d depicts the ratios of retrieved rotational, translational, and total energies after impact to the initial kinetic energy. The highest retained energy occurs at an orientation angle of 40° and is approximately 77% of the initial total energy. This is despite the constant value

of $e_* = 0.5$, which should result in a constant value of retrieved energy, e_*^2 , equal to 25% of initial energy. The lowest retrieved energy occurs at an orientation of 140° , and is equal to 10% of initial energy. This low energy point occurs when the velocity and orientation vectors coincide, occurring during the pure slipping mode, when the sliding energy dissipation is also significant.

When using numerical models, a series of parameters and settings affect the calculation of rebound values. In other words, the coefficients of restitution are not constant values. These parameters can be grouped into the following categories:

- impact model
- impact parameters
- rock geometry and the rock aspect ratio
- impact angle (or the ratio of tangential to normal contact velocity)
- object orientation at the contact instance (or mass distribution around the contact point).

In the following sections the effect of each category is studied in detail. It should be mentioned that θ , the object orientation at time of impact, is the primary variable of interest in the following chapters, varying from 0° to 180° , according to symmetry, with results calculated every 5° . θ is chosen as the main variable, as the mass distribution around the contact point has the most significant effect on the rebound parameters, when compared to other input parameters.

4.4.1 Effect of the impact model on object rebound parameters

The impact model significantly affects the rebound velocities. In this section the RBIM is compared with the models proposed by Descouedres et al. (1988) and Azzoni et al. (1995). In this comparison, the set-up of Figure 4.8 is utilized, with an impact angle of $\gamma = 45^\circ$. Figure 4.10 plots comparisons between the rebound velocities and energies which result from the application of the different models.

Figure 4.10a shows the variation of normal rebound velocity at the center of the ellipsoid. The Stronge and Descouedres models predict almost identical rebound normal velocities between angles 0° and 120° ; in these orientations the stick process is the dominant tangential process for both theories. From an angle of 120° , when pure sliding starts in Descouedres, the two variations diverge. The close variation of the two theories is only limited to normal direction, as both theories assume impulsive behavior for the variation of the normal direction. Both theories consider the energy dissipation in the restitution phase, as defined by the two Equations (4.2.11) and (4.3.11). Azzoni's model predicts the rebound negative velocity for the first 90° of the orientation, where $r_t > 0$, and the object is supposed to experience the second impact. In an orientation between 90° and 180° , Azzoni derives positive, relatively small, rebound velocities with $R_n < 0.2$. Here, it is found that using this theory to model the rock in full geometry is not feasible, as the object loses the normal velocity rapidly. Also as a result of rotation, after a few bounces, the rock reaches an early arrest when compared to the other models. This behavior has also been noticed when simulating several other shapes in different impact settings.

Figure 4.10b shows the tangential rebound velocities. In the tangential direction the rebound velocities derived from Stronge's theory are significantly different from those derived from Descouedres' model. This is because the criterion for sliding-stick mode differs between the two models. RBIM employs Amontons-Coulomb's dry friction law for impulse increments, while in Descouedres' model, the sliding criteria are checked based on the final impulses. In Descouedres' model, sliding occurs if the ratio of tangential termination impulse to the normal impulse is smaller than the friction coefficient. In addition, Descouedres' model is not capable of predicting the stick situation that occurs when the initial sliding halts on rough surfaces. When the stick situation occurs for angles between 0° and 90° , such as in Figure 4.10b, Azzoni's model predicts tangential velocity values which are closer to the values predicted by RBIM. However, for the cases of centric impact, the responses of the two models are exactly equal. This equality is due to Azzoni's assumption that sticking on the contact point always represents a pivot point; an assumption shared by RBIM model in this specific impact configuration.

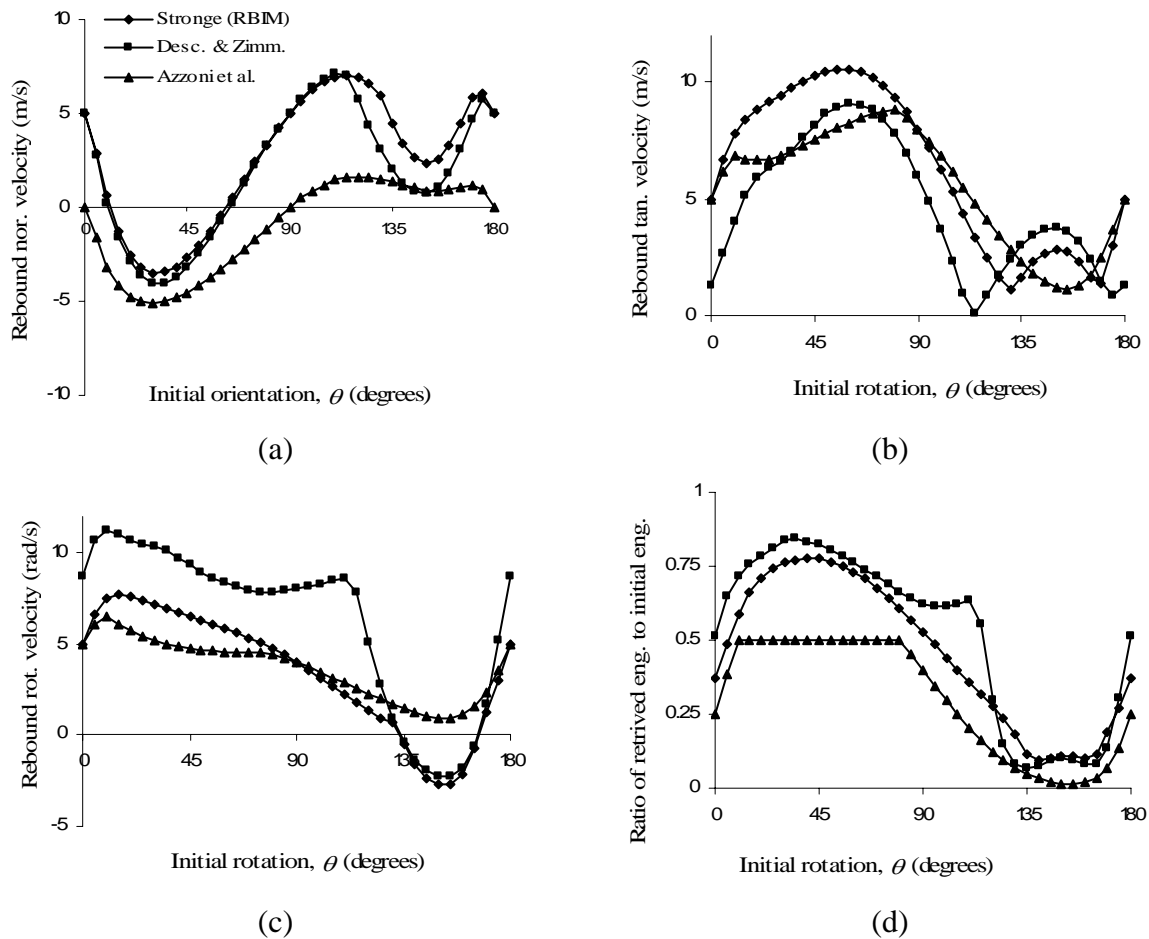


Figure 4.10: Variation of velocities and energies versus object orientation for planar impact of an ellipsoid at an impact angle of 45° , $V_{ini,hor} = 10$ m/s, using different impact models: (a) rebound central normal velocity (m/s), (b) rebound central tangential velocity (m/s), (c) rebound rotational velocity (rad/s), and (d) ratio of retrieved energies after impact to initial energies.

Figure 4.10c shows the rebound rotational velocities. Because of the aforementioned differences in tangential impulse, the Descouedres model predicts different rotational velocities than RBIM for stick situations (other than the continuous sliding case). In contrast, for the sliding range, between 130° and 170° , the values are almost the same. On average, Descouedres' model predicts considerably higher rotational velocities, 6.2 rad/s, in comparison to RBIM, with an average of 3.4 rad/s. The results from Azzoni's model differ significantly from the other two models in the continuous-sliding range, although the results are much closer in other ranges. Furthermore, the results from Azzoni's model are able to predict exact values for centric impacts at 0° and 90° .

Figure 4.10d shows the ratio of retrieved kinetic energies to the initial energy for different models. Descouedres' model predicts the highest retrieved energy, while Azzoni's model predicts the lowest. At zero orientation, RBIM predicts that 37.5% of the energy will be retained, while Descouedres' model predicts 51% retention. When sliding occurs, the results for the Descouedres' and RBIM methods are close. As both models predict similar normal rebound behavior, the difference in energy prediction is mainly a function of their tangential rebound velocity.

Figure 4.11 plots the variation of the ratio of retrieved energies to initial energy for the models offered by Descouedres and Azzoni. As explained earlier, in Descouedres' model, for impact angles of 0° to 45° , most of the energy transfers to rotational energy when the object is in continuous sliding mode. This is in contrast with RBIM, where, generally, the translational energy is the dominant retaining energy mode. For orientation angles of 45° to 110° , almost equal portions of energy are retained in translational and rotational energies. In Azzoni's model, Figure 4.11b, translational energy is the dominant mode of retrieved energy. However, during the energy check situation, for an impact angle of 10° to 80° and as can be seen in Figure 4.11b, Azzoni scales both translational and rotational energies in order to keep the maximum retrieved energy equal to 0.5.

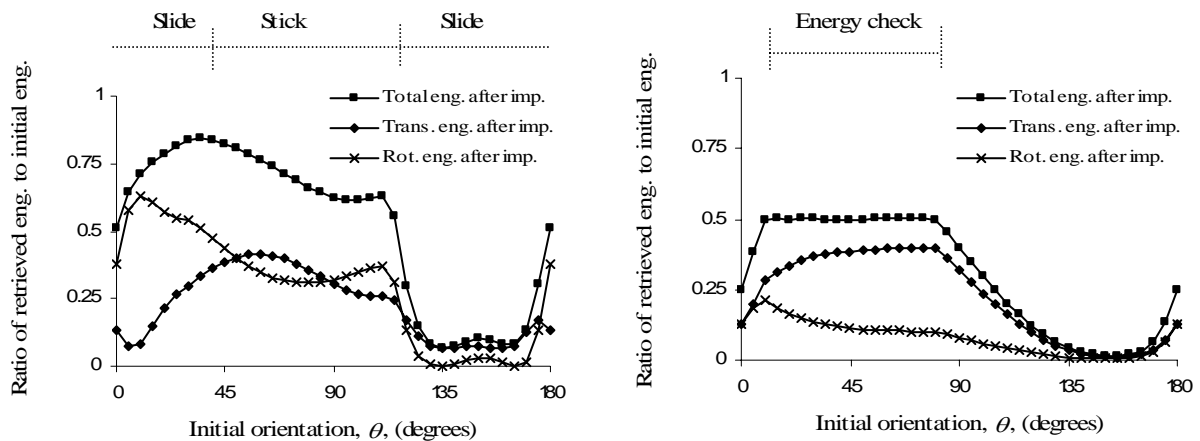


Figure 4.11: Variation of the ratio of retrieved energies to initial energy versus object orientation for planar impact of an ellipsoid at an impact angle of 45° , $V_{ini,hor} = 10$ m/s, using different impact models: (a) Descouedres' model, and (b) Azzoni's model.

4.4.2 Effect of RBIM parameters on object rebound parameters

The two impact parameters, e_* and μ , have a direct effect on the restitution values. The impact setup of Figure 4.8 is reapplied here with the tangential velocity, V_t , equal to 10 (m/s) at an angle of 45° . The numerical investigation is performed twice: the first time using different energy CORs, with the rebound values plotted versus the friction coefficient; and the second time using different friction coefficients, with the variations of rebound parameters plotted versus energy COR. Figure 4.12 shows the plots of rebound parameters against friction coefficient at different constant energy CORs. Figure 4.13 provides the same data at different friction coefficients versus energy COR.

Figures 4.12 and 4.13 are plotted using the average rebound values versus friction coefficient and energy COR. To acquire data for each point on the figures, the rock is shot 36 times against the rigid half space at an angle of orientation varying each time by 5° . This number of impacts is sufficient to produce a smooth variation of the rebound parameters. Equations (4.4.1) show the formulas used for calculating the average total retrieved energy and the average rebound normal and tangential velocities.

$$\bar{R}_E = \frac{\sum_{\alpha=0}^{180} R_E}{36} \quad \bar{V}_{r,n} = \frac{\sum_{\alpha=0}^{180} \bar{V}_{r,n}}{36} \quad \bar{V}_{r,t} = \frac{\sum_{\alpha=0}^{180} \bar{V}_{r,t}}{36} \quad (4.4.1)$$

4.4.2.1 Rebound parameters versus friction coefficient

Figure 4.12a plots the variation of the average normal rebound velocity versus the friction coefficient. At zero friction, and with $e_* = 1$, when there is no energy dissipation, the object geometry effect sets the average rebound velocity equal to 4.1 m/s, resulting in $R_{n,ave} = 0.41$. Increasing the friction angle increases this value, and also $R_{n,ave}$, as the governing mode of sliding changes from continuous-sliding to sliding-stick or sliding-reverse. The figure shows that friction values greater than 0.7 have almost no effect on the average values. This is further supported by the other three graphs in Figure 4.12. As expected, e_* has a direct uniform effect in decreasing the average normal rebound velocity.

Figure 4.12b plots the variation of the average tangential rebound velocity versus the friction coefficient. It illustrates the minor effect of e_* on the average tangential velocity. The friction coefficient has a direct effect on the decrease of the average tangential velocity to a minimum of 5.8 m/s at $\mu = 0.7$; however, this value stays constant after μ rises. This is due to assumptions in RBIM model, which is applicable to impacts with low tangential compliance. This means that the high values of friction coefficients can not decrease the tangential rebound velocity, significantly.

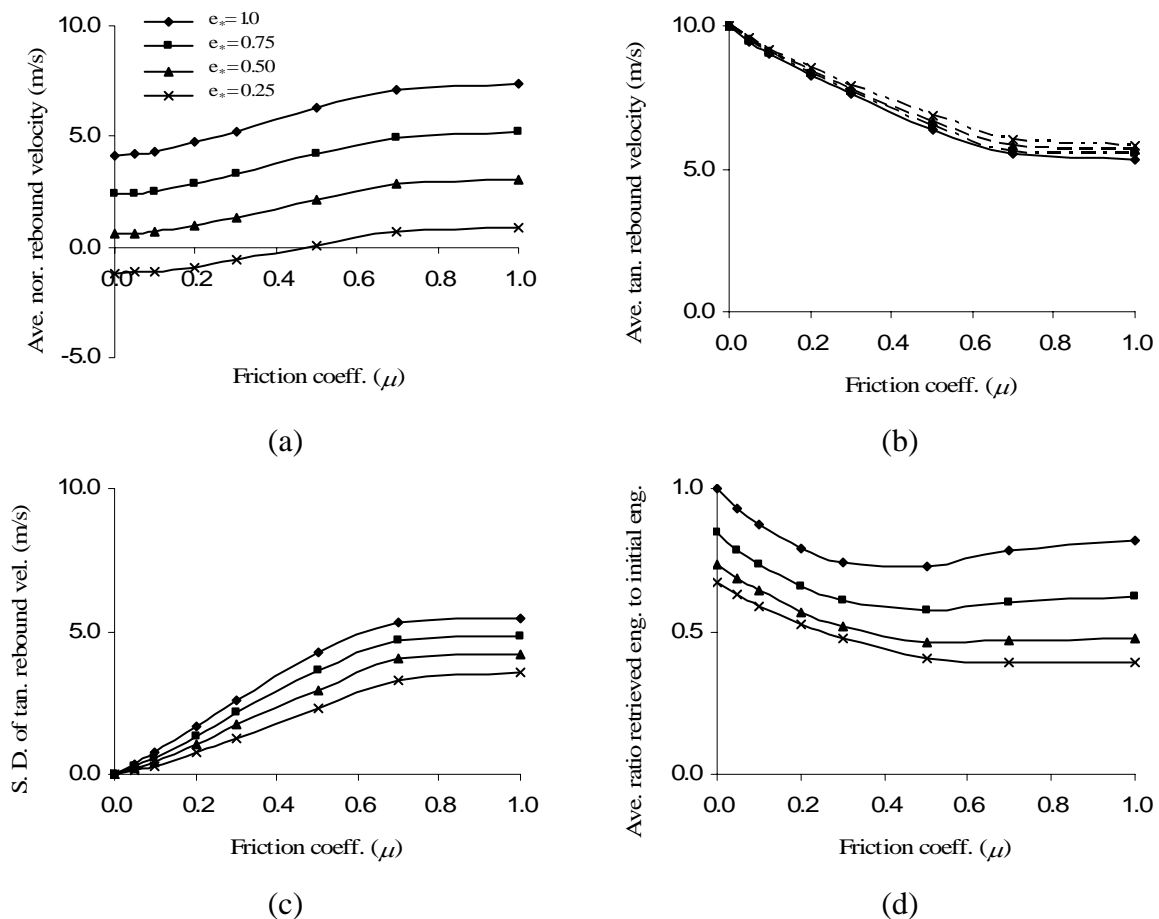


Figure 4.12: Variation of the average velocities and retrieved energies versus the friction coefficient for the planar impact of an ellipsoid at an impact angle of 45° , $V_{ini,hor} = 10$ m/s, using RBIM at different energy COR, e_* : (a) averaged rebound normal velocity at the center, (b) averaged rebound tangential velocity at the center, (c) variation of the standard deviation of tangential rebound velocity, and (d) averaged ratio of retrieved total energy after impact to initial energy.

Figure 4.12c plots the variation of the standard deviation of tangential rebound velocity versus the friction coefficient. The standard deviation increases to approximately half of the object's initial velocity at $\mu = 0.7$, showing an increase in tangential velocity dispersion at higher friction coefficients. This effect is caused by object shape and impact orientation. The increase in standard deviation suggests that the friction angle increases the highest roll-out distance during rockfall.

Figure 4.12d plots the variation of the ratio of retrieved energy to the initial energy versus the friction coefficient. Energy COR has a direct effect on this ratio, as a decrease in energy COR decreases the average ratio of retrieved energy to the initial energy; however, this trend is diminishing, as by decreasing the e_* , the ratio plots parallel curves that are close together. The friction coefficient decreases the energy ratio, and the lowest average of retrieved energy occurs at around $\mu = 0.5$ for all energy COR.

4.4.2.2 Rebound parameters versus energy coefficient of restitution

In Figure 4.13, the graphs are modified to depict the average velocities and energies for different friction coefficient versus the energy COR.

Figure 4.13a plots the variation of the average normal rebound velocity versus the energy COR, e_* . This figure shows the linear variation of average, R_n , versus the energy COR for all values of friction coefficients. A negative COR average means a higher chance of an immediate second impact, which occurs more frequently at lower values of μ and e_* . The friction coefficient appears to have a minor effect on the average normal COR in contrast to the major influence of e_* .

Figure 4.13b plots the variation of tangential rebound velocity versus e_* . This figure strongly shows that e_* has only a minor effect on the average tangential rebound velocity, in contrast to the direct effect of the friction coefficient. However, lower e_* has an indirect effect on the distance by changing the motion mode from impact to rolling more quickly than higher values of e_* .

Figure 4.13c shows the variation of standard deviation of the average normal rebound velocity versus e_* . An increase in both the friction coefficient and the energy COR increases the standard deviation considerably, with a linear trend. At a typical value of $e_* = 0.5$, the standard deviation is equal to 2.5 m/s. This value is half of the normal COR that occurs during a centric impact, which confirms the results indicating the dispersion of the distribution caused by the rock shape when there is an ellipsoid with a ratio of 2:1.

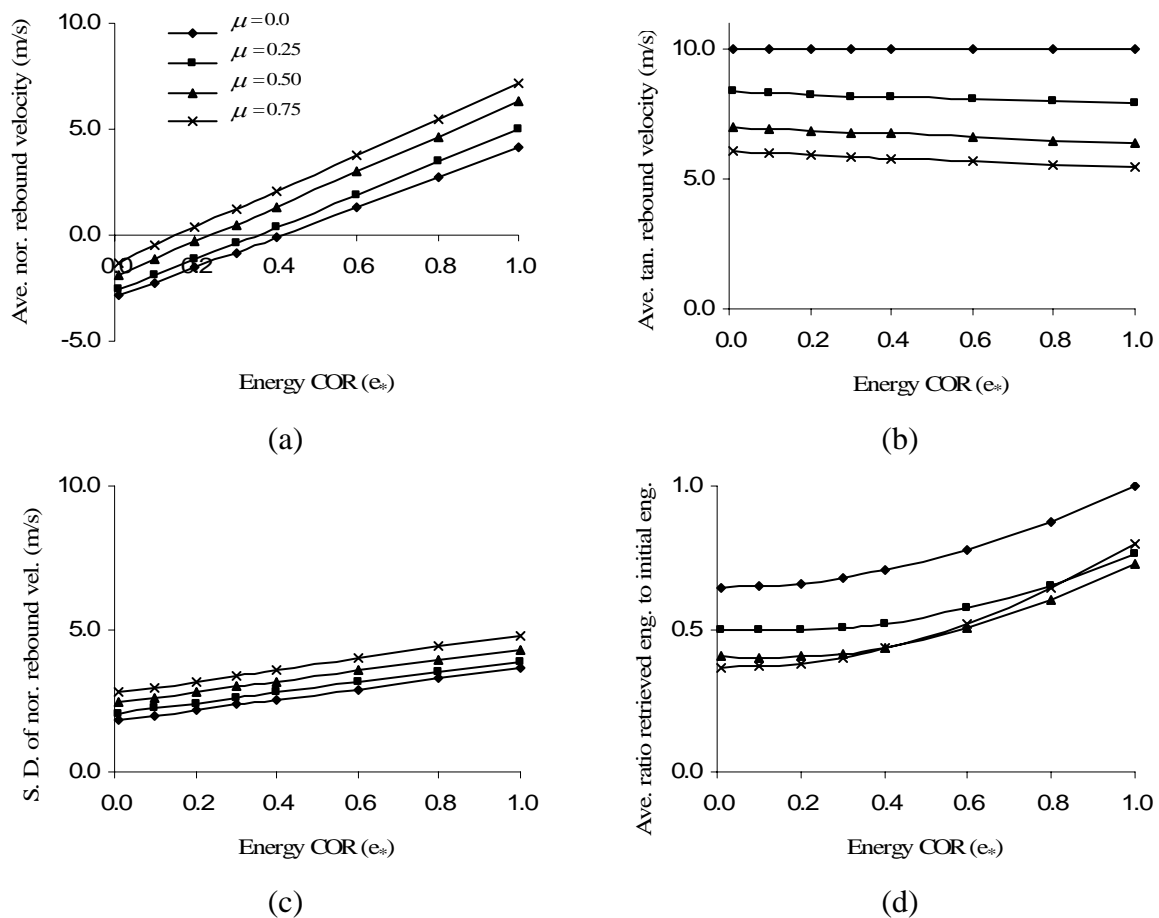


Figure 4.13: Variation of the average velocities and retrieved energies versus the energy COR, e_* , for planar impact of an ellipsoid at an impact angle of 45° , $V_{ini,hor} = 10$ m/s, using RBIM at different friction coefficients: (a) averaged rebound normal velocity at the center (m/s), (b) averaged rebound tangential velocity at the center (m/s), (c) variation of standard deviation of normal rebound velocity (m/s), and (d) averaged ratio of retrieved total energies after impact to initial energies.

Figure 4.13d shows the variation of the average ratio of retrieved energy to the initial energy for different friction coefficients. This graph depicts the direct effect of e_* and μ on the

average retrieved energy; however, this effect is not obvious for energy COR lower than 0.3 and friction coefficients greater than 0.5. For the usual parameters used in rockfall modeling, e_* between 0.2 and 0.5 and μ between 0.3 and 0.7, on average, for this specific configuration, 35% to 50% of the energy is retrieved during a single impact. The increasing trend at $\mu = 0.75$ can also be seen in Figure 4.12d due to an impact mode change in higher friction coefficients at some orientation angles.

4.4.3 Effect of object geometry on rebound parameters

Rock geometry affects the rebound velocities and energies. Both the rock shape and its aspect ratio, the ratio of maximum to minimum dimension, significantly affect the coefficients of restitution and the roll-out distances of the rock during rockfall. To investigate the effect of each geometry parameter, the numerical experiment in Figure 4.8 is repeated with impact angles, γ , of 0° and 45° . The object orientation, θ , remains as the main variable. The statistical parameters of 36 rock impacts against a rigid half space are presented in the following section. Figure 4.14 shows the geometries used in these studies. It should be mentioned that the objects are three-dimensional, but their impacts are essentially planar. These shapes are the most common geometries considered in the literature to represent the falling rock.

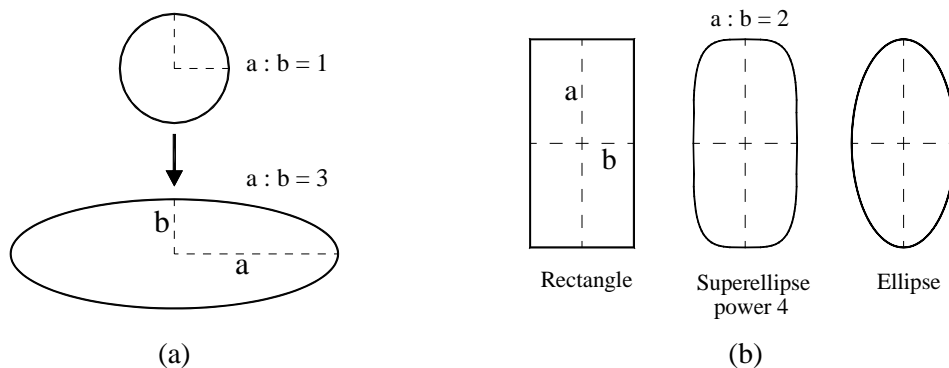


Figure 4.14: Geometries used for rock representation: (a) spheres transferring to ellipsoid used in slenderness numerical experiment, aspect ratios from 1:1 to 3:1, and (b) Objects used in numerical shape experiment: rectangle, ellipsoid, and superellipsoid with ratio 2:1.

4.4.3.1 Effect of rock aspect ratio (or slenderness) on rebound values

Figure 4.14a shows rock geometry modeled as an ellipsoid with aspect ratios of 1:1 to 3:1. Objects with aspect ratios higher than 3:1 are not of interest here, since more slender rocks tend to break on impact and for high slenderness ratios the source of energy dissipation is by wave propagation which is not captured by RBIM.

Figure 4.15a shows the variation of the average, maximum, and standard deviation results for the impact of ellipsoids at an angle, γ , of 45° with different aspect ratios. For an aspect ratio of 1.0, i.e., circular impact, the normal rebound velocity is constant and equal to 5.0 m/s which results in a value of $R_n = 0.5$. As the aspect ratio increases, the average of the values of the normal rebound velocity decreases significantly, along with a rapid increase in the standard deviation. The maximum normal velocity increases to 7.0 m/s at a ratio of 2.0 and stays constant, which results in an increase of 40% in the maximum rebound velocity. The large increase in the standard deviation indicates that the normal rebound velocities disperse due to an increase in the aspect ratio of the ellipsoid.

Figure 4.15b plots the restitution parameters for tangential rebound velocity. The average tangential velocity decreases slightly to its minimum of 6.3 m/s at an aspect ratio of 2.0, a 12% decrease in comparison to the value at the ratio of 1.0. In contrast, the maximum rebound velocity increases to 10.9 m/s at an aspect ratio of 3.0, an increase of 52% from the aspect ratio of 1.0, while the standard deviation increases to 3.43 from zero. These results suggest that the stop-point distribution for rockfalls caused by slender rocks should be more scattered than rockfalls caused by spherical rocks, while the average roll-out distance for single impact does not change significantly.

Figure 4.15c plots the restitution parameters for the ratio of kinetic rebound energy to initial energy versus the aspect ratio. It shows that the average retrieved energies remain approximately constant with a range of variation from 0.46 to 0.50. As a result of the presence of tangential velocity, the maximum retrieved energy grows considerably, to 83% of the initial energy, demonstrating that rockfall modeling based on spherical rock geometry underestimates the possibility of high impact energy retention during a fall. This might result in significantly greater roll-out distances. Figure 4.15c also shows that the standard deviation

increases to 25% of the initial impact energy, suggesting a scattered distribution of the rebound energy for slender ellipsoids.

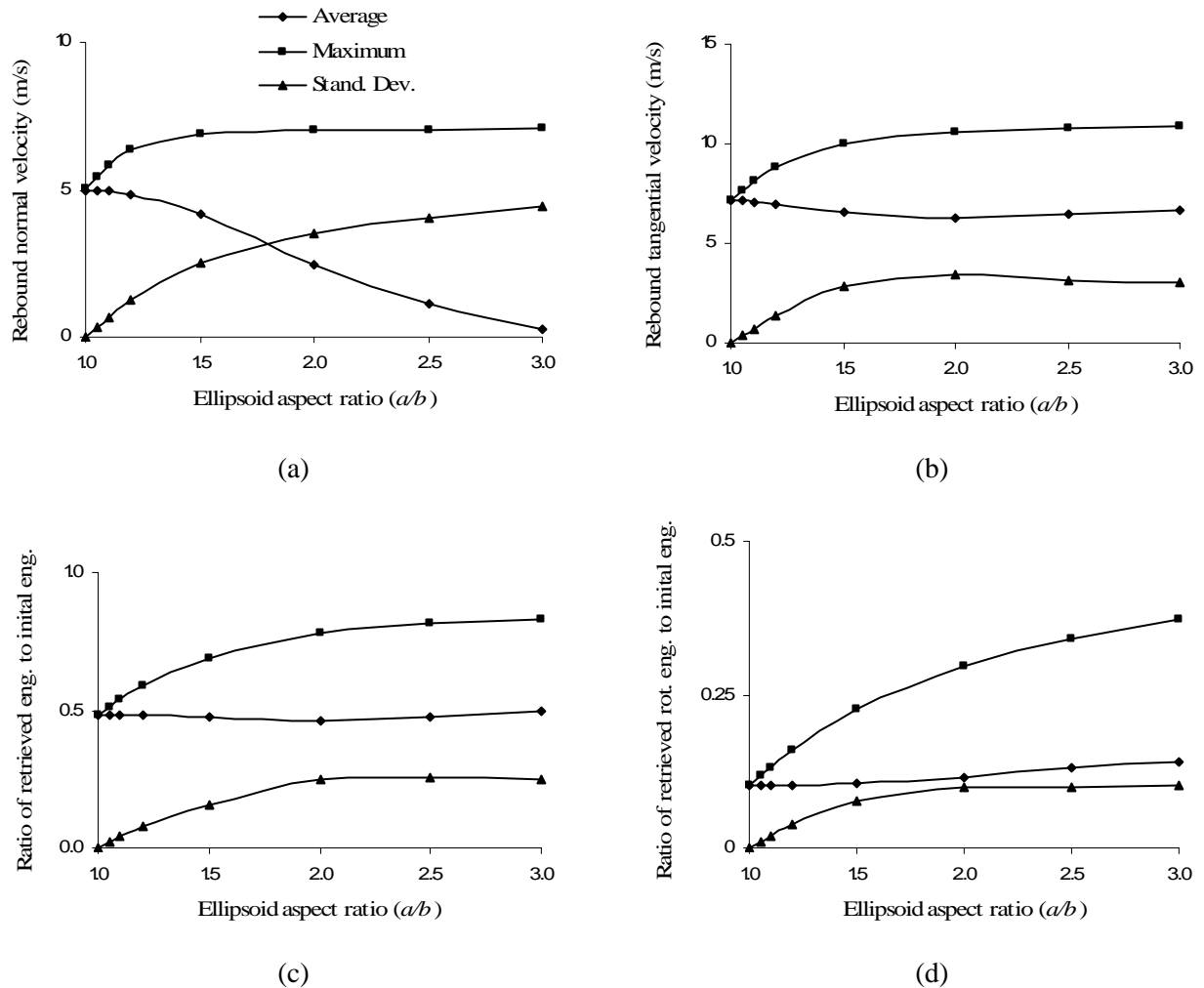


Figure 4.15: Variation of the average velocities and retrieved energies versus aspect ratio for planar impact of an ellipsoid at an impact angle of 45° , $V_{ini,hor} = 10$ m/s, (average, maximum, and standard deviation values): (a) rebound normal velocity (m/s), (b) rebound tangential velocity (m/s), (c) ratio of total energy retrieved to initial energy, and (d) ratio of retrieved rotational energy to initial total energy.

Figure 4.15d plots the restitution parameters for the ratio of retrieved rotational energy to initial energy versus the aspect ratio. The average ratio of the retrieved rotational energy increases from 10% at an aspect ratio of 1.0 to 14% at a ratio of 3.0. This slight increase occurs despite the fast growth of the maximums, from 10% to 37% at the same ratios, respectively, due to the slenderness of the rock.

4.4.3.2 Effect of rock shape on rebound values – 0° impact angle

The object rebound velocities depend on the mass distribution around the contact point. As a result, it is expected that different rebound velocities will be derived for different shapes at different orientations. In this section the rebound parameters of four different geometrical shapes are investigated as resulting from the numerical test, described in Figure 4.8. In this test, the impact angle, γ , is equal to 0, resulting from $V_{ini,hor}$ having a value of 0. The investigated objects are: an ellipsoid, a superellipsoid power 4, a superellipsoid power 10, and prism with a rectangular cross section, with cross sections as shown in Figure 4.14b. Here, superellipsoids with powers 4 and 10 are referred to as ellipsoid- n , where n shows the object's power, as shown in Equation (4.4.2) and in the object's local coordinate system. The prism is sometimes referred as a rectangular section, or simply rectangle. The geometrical properties of the objects used here are presented in Chapter 5.

$$F(x, y) = |x|^n + |y|^n + |z|^n - 1 = 0 \quad (4.4.2)$$

Figure 4.16a shows the variation of the normal rebound velocities versus the impact orientation. For ellipsoidal objects, the normal rebound velocity varies between 1.1 and 5.0 m/s, resulting in a normal coefficient of restitution, R_n , between 0.11 and 0.50. For rectangular objects, the domain of variation of the normal COR is even wider, due to the corner impact effect, which can result in a negative normal COR with the values as low as -0.38. The COR is negative when the object impacts the surface at a corner adjacent to the longer side having a low angle with respect to the surface. In this case, the object has a tendency to experience a second impact. This effect highlights the importance of corner modeling for polygonal objects, identified by some researchers like Giani et al. (2004) and Azzoni et al. (1995) as having an important influence on rockfall trajectories. The normal velocity for superellipsoid-4 varies between 0.09 and 5.0 m/s, resulting in R_n values between 0.09 and 0.50. Superellipsoid-10 can result in a normal velocity as low as -1.9 m/s. Both these values and the shapes of the variations show that superellipsoids are suitable representatives of rectangular objects; however, the results show that higher powers produce improved results for this representation.

Figure 4.16b plots the variation of tangential rebound velocities versus object initial orientation, θ . For ellipsoids, although the incoming tangential velocity is zero, the variation of the tangential COR is highly nonlinear, ranging from -5.6 to 5.6. Even without any initial tangential or rotational velocity the object may be thrown to either side. For rectangular objects, in addition to the features described above, there are sharp variations at impact angles near 0° and 90° , reflecting the sensitivity of the rebound to the impact angle. Similar to normal velocity variations, both superellipsoids have ranges of variation between those of the other shapes considered. Similar to rectangles, superellipsoid behavior changes rapidly near 0° and 90° orientation angles.

Figure 4.16c shows the rebound rotational velocities for ellipsoids which vary between approximately -4.1 and 4.1 rad/s, where the shape of variation is similar to the variation of the rebound tangential velocity. Rectangular rocks have a greater range of variability in comparison with ellipsoidal rocks, from -4.6 to 4.6 rad/s, because of the larger impact vectors which outweigh the effect of the object's higher radius of gyration. The variation of superellipsoids tends to be a stretched variation of an ellipsoid close to the variation of a rectangular object. Discontinuities are seen around the orientation angles of 0° and 90° for prisms and superellipsoids.

Fig. 4.15d depicts the ratios of retrieved kinetic and rotational energies after impact, to the initial kinetic energy for different geometrical objects. The lowest retained energy is equal to e_*^2 which is 25% of the initial kinetic energy, occurring at the centric impact, at angles of 0° and 90° . For ellipsoidal objects, this value increases to 44% at an angle of 30° , while for rectangular objects, the highest value, 63% of the initial energy, occurs at an angle close to zero. This value is almost 2.5 times the minimum value of 25%. The results show that, due to the geometrical impact setup, ratios of retrieved energy higher than e_*^2 are observed. These results conflict with the common belief in lumped-mass models that e_*^2 is highest value of retrieved energy, in the case of zero-tangential velocity. This may be also due to the expected dissipations of additional energy due to frictional forces. It is also expected that further energy dissipation occurs due to frictional forces. The maximum ratio of retrieved energy for

superellipsoids-4 and -10 are 50% and 58% of the initial energy, respectively. The average retrieved energy is almost the same for all three objects between the values of 34% to 36%.

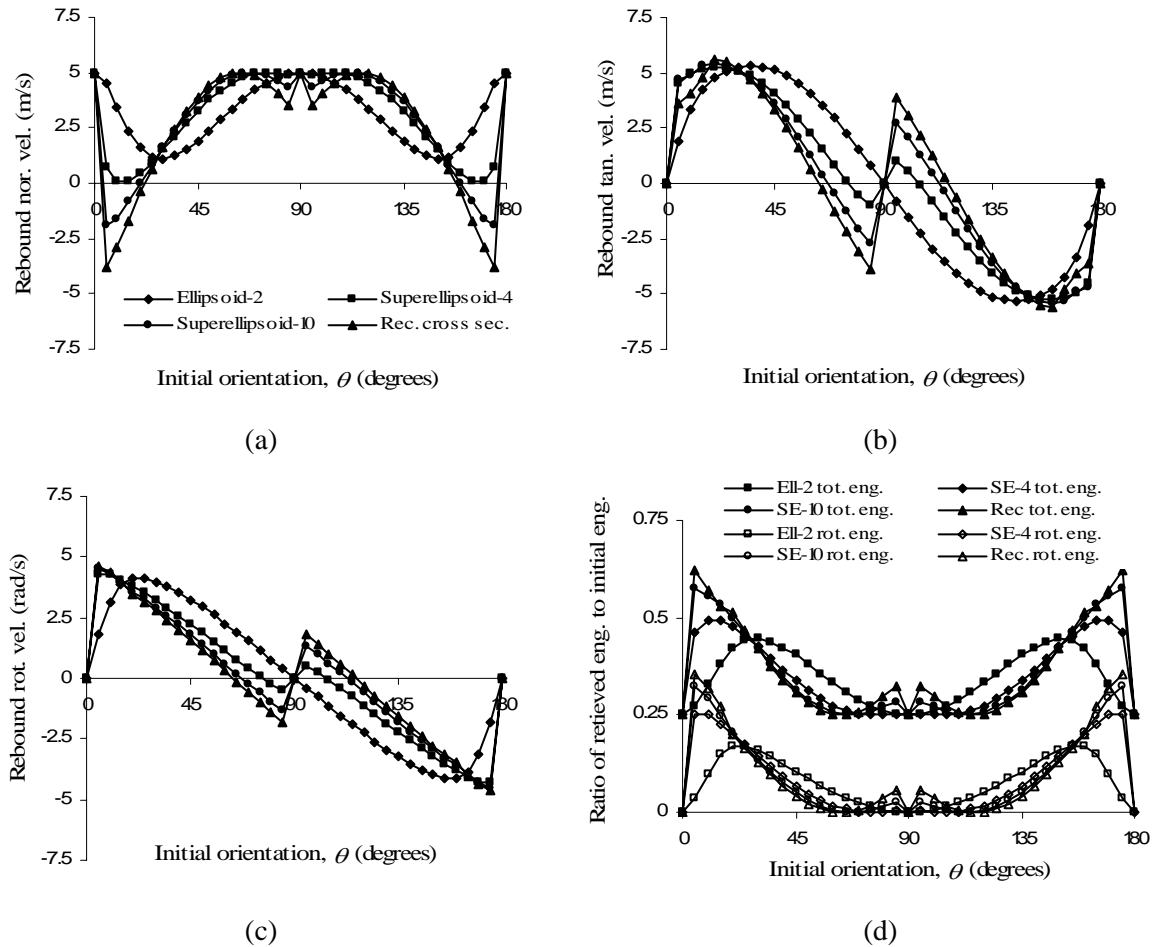


Figure 4.16: Variation of the rebound parameters versus object orientation for rocks with different geometries (shown in 4.14b) and with the configurations of Figure 4.8 with an impact angle of 0° ($V_{ini,hor} = 0$): (a) rebound normal velocity, (b) rebound tangential velocity, (c) rebound rotational velocity, and (d) ratio of retrieved total and rotational energies to initial energy.

Fig. 4.15d also plots the ratio of the energy transferred into rotational energy mode to the initial kinetic energy versus orientation angles. The highest value of rotational energy for ellipsoids occurs at an angle of 35° , and is equal to 17% of the initial energy. For the prismatic object, the highest value occurs at an angle of 5° , equal to 36% of the initial kinetic energy. The figures show that the amount of energy transferred to rotation mode is the highest for the rectangle.

Substituting spheres for these objects reduces the normal rebound velocity to a constant value equal to 50% of the initial velocity, with a retention of 25% of the initial energy. Incorporating the rock shape into the model results in an increase in retrieved energy. Therefore, simplifying the rock shape to spheres is not a conservative assumption, because it can seriously underestimate the amount of retrieved energy, which might lead to catastrophic rockfall events. Capturing the variation of object geometry is the main motivation for the introduction of the roughness angle to the models proposed by Pfeiffer et al. (1989).

4.4.3.3 Effect of rock shape on rebound values – 45° impact angle

Similar to the previous section, the impact of four different geometrical shapes are investigated as part of the numerical test described in Figure 4.8. In this study the objects are shot at an impact angle, γ , equal to 45° resulted from a horizontal velocity of 10 m/s, with the object's initial orientation varying from 0° to 180°. Figure 4.17 plots the variation of rebound velocities and energies. The statistical parameters for the variations of the rebound parameters for the objects are presented in Table 4.4.

Figure 4.17a shows the variation of the normal rebound velocity versus the impact orientation. For all four objects, the domain of variation in comparison to a 0° impact angle increases significantly without a change in the material property or the rock shapes. Similar to the rectangular section, the ellipsoids normal COR extends to negative values, causing immediate second impacts for initial orientations from 15° to 60°. Ellipsoidal objects have both the maximum and highest average of R_n , as shown in Table 4.4. However, the lowest normal rebound velocity, -6.2 m/s, occurs after the impact of the rectangular object. This value is 2.8 m/s lower than the minimum rebound velocity for ellipsoids, -3.4 m/s. Discontinuous variation in rebound normal velocity occurs for rectangular sections around impact angles of 0° and 90°. The same discontinuous variations can be also observed for superellipsoids; however, higher order superellipsoids capture this behavior closer to rectangular sections.

Figure 4.17b depicts the variation of the tangential rebound velocity versus the impact orientation. No negative R_t is observed. However, for this impact angle the range of variation for tangential COR becomes wider when compared to an impact angle of 0°. R_t for the

rectangular objects, varies from 0.1 to 1.01 and from 0.11 to 1.06 for the ellipsoidal objects. These values show a COR larger than 1.0, which cannot be explained by lumped-mass models. On average, the rectangular section has the highest tangential COR, as shown in Table 4.4. Again, the variations for tangential velocity for superellipsoids are between the variations of the other two objects.

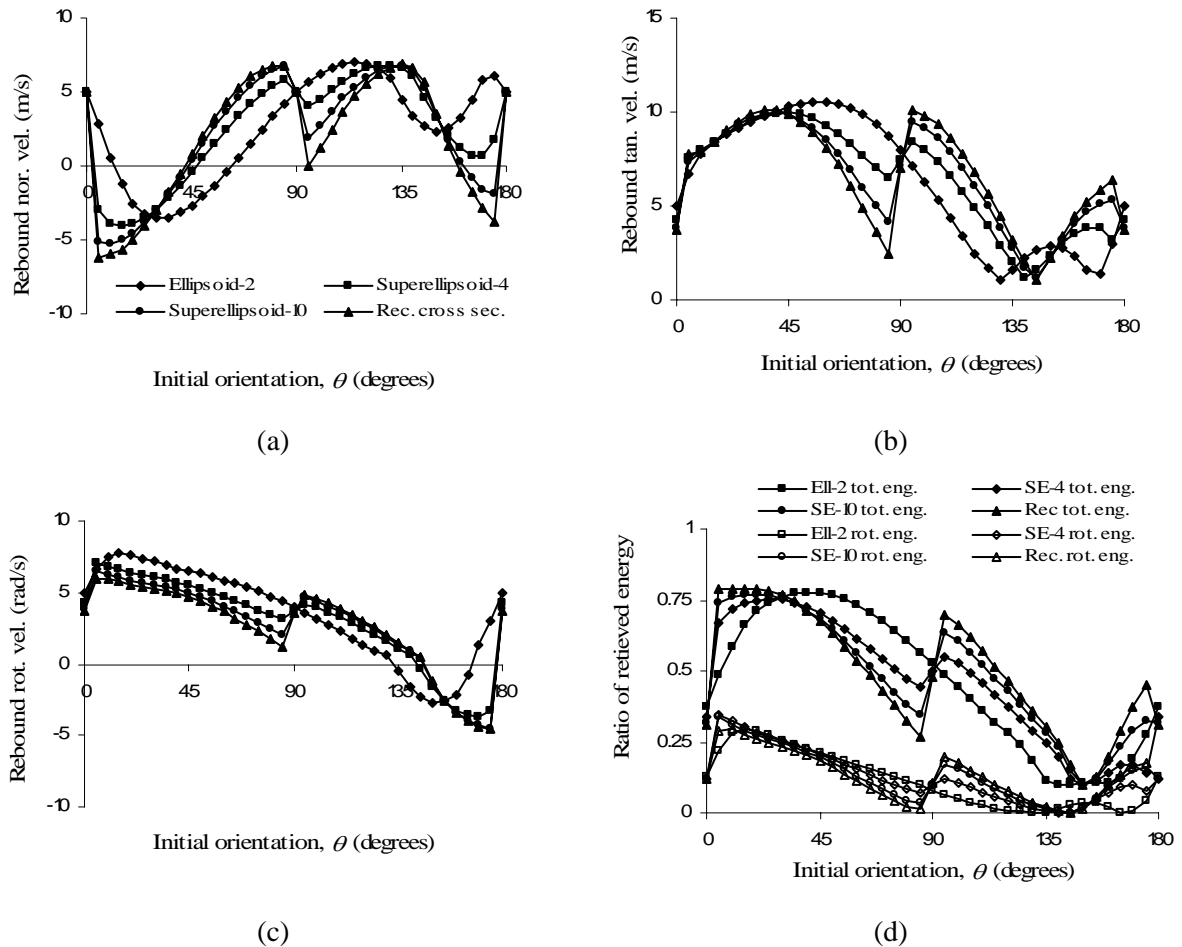


Figure 4.17: Variation of the rebound parameters versus object orientation for rocks with different geometries (shown in Figure 4.14b), with the configurations of Figure 4.8 at an impact angle of 45° and $V_{ini,hor} = 10$ m/s: (a) rebound normal velocity, (b) rebound tangential velocity, (c) rebound rotational velocity, and (d) ratio of the retrieved total and rotational energies to initial energy.

Figure 4.17c plots the variation of rebound rotational velocity versus the orientation. Other than the highly nonlinear variations around the 0° and 90° impact angles, the four objects have the same trend of variation between initial orientations of 0° and 135° . The negative

rotational velocity occurs between impact angles of 135° and 180° ; again, this behavior can neither be predicted nor modeled by lumped-mass models and constant COR. The ellipsoid has both the highest rotational velocity and the highest average, as shown in Table 4.4.

Figure 4.17d shows the ratios of retrieved energies and the energy transferred to rotational mode to initial energy for the different objects versus initial orientation. The rectangular object experiences the second impact at an initial orientation angle of 5° . In this impact angle, up to 79% of the initial energy may be retrieved with 30% of the kinetic energy being rotational energy. In this scenario, 77% of the initial energy can be retrieved in the ellipsoidal object and 29% of the initial energy can transfer to rotational energy. These values for superellipsoid-10 are 77% and 34%, respectively. These values demonstrate that corner abrasion can completely change the rebound energy values. On average, rectangular sections have the highest retrieved energy.

In order for these comparisons to be complete, multiple impacts must be studied to investigate whether or not the object can depart from the contact surface after the first impact. This investigation is performed in Chapter 6.

Table 4.4: Statistical data for COR, rebound rotational velocity, and the ratio of retrieved energy to initial energy for different rocks, corresponding to Figure 4.17

	Ellipsoidal			Superellipsoidal power 4			Superellipsoidal power 10			Prismatic with rectangular cross section		
	mean	max	min	mean	max	min	mean	max	min	mean	max	min
R_n	0.25	0.70	-.34	0.24	.068	-.41	0.22	0.68	-.53	0.18	0.68	-.62
R_t	0.62	1.06	0.11	0.64	1.00	0.12	0.64	1.00	0.12	0.67	1.01	0.10
ω , Rot. vel.	3.5	7.7	-2.7	3.0	7.1	-3.7	2.7	6.5	-4.5	2.5	0.60	-4.6
Ratio retrieved eng.*	0.46	0.77	0.10	0.46	0.75	0.10	0.48	0.77	0.10	0.50	0.79	0.10
Eng. ratio transferred to rot. eng.	0.11	0.29	0.00	0.13	0.34	0.00	0.13	0.34	0.00	0.13	0.30	0.00

* As the impact configuration does not change, the total energy is equal to the kinetic energy

4.4.4 Effect of impact angle on rebound parameters

To define the effect of the impact angle on the restitution parameters, the numerical experiment described by Figure 4.8 is repeated, and this time the impact angle, γ , is the resulting variable. Therefore, the horizontal impact velocity, $V_{int,hor}$ varies from 0 to 30 m/s resulting in the variation of impact angle between 0° and 72° . For every impact angle, the average rebound velocities and energy ratios are calculated and plotted versus impact angle, as shown in Figure 4.18. The ellipsoid aspect ratio is kept constant at 2:1.

Figure 4.18a shows the variation of the average, maximum, and standard deviation for normal COR resulting from the impact of an ellipsoid at varying impact angles, using the same configuration as described in Figure 4.8. Figure 4.18a shows a slight decrease in the average normal rebound velocity, despite the dramatic increase in the standard deviation. The standard deviation is greater than the mean values of normal rebound velocity, showing a highly dispersed distribution for higher impact angles. Also, the maximum value of the normal COR increases rapidly versus the impact angle.

Figure 4.18b shows the variation of the average, maximum, and standard deviation for tangential COR versus the impact angle. This figure shows an increase in the average of tangential COR in higher angles; here it increases from 0.56 to 0.78 units. This increase is mainly due to a change in the sliding process in the tangential direction, from a sliding-stick mode to a continuous-sliding mode, occurring at higher impact angles. At lower impact angles due to energy transfer from the normal direction, the maximum velocity is considerably higher than the value of normal velocity prior to impact.

Figure 4.18c depicts the variation of the average ratio of retrieved rotational energy parameters to initial energy versus the impact angle. As this figure shows, the ratio of energy transferred to rotational energy increases until the peak value at an impact angle of 56° . After this point, the average retrieved rotational energy decreases to approximately the initial value at 0° impact angle. This trend of variation also occurs for the maximum and the standard deviation of the rotational energy.

Figure 4.18d plots the variation of the average ratio of retrieved restitution energy parameters to initial energy versus the impact angle. It shows that the average ratio of retrieved energy to initial energy increases versus the impact angle. This figure shows that at impact angles greater than 50° , on average, 50% of the initial energy can be retrieved. High impact angles usually occur during the impact of a rock with highly inclined slope surfaces. Furthermore, such angles may occur during the impact of rocks on horizontal surfaces when the normal contact velocity is dissipated and the motion of the rock is a combination of small jumps and rolling-sliding. In this case the rocks may travel a long distance, much further than the pure rolling-sliding case.

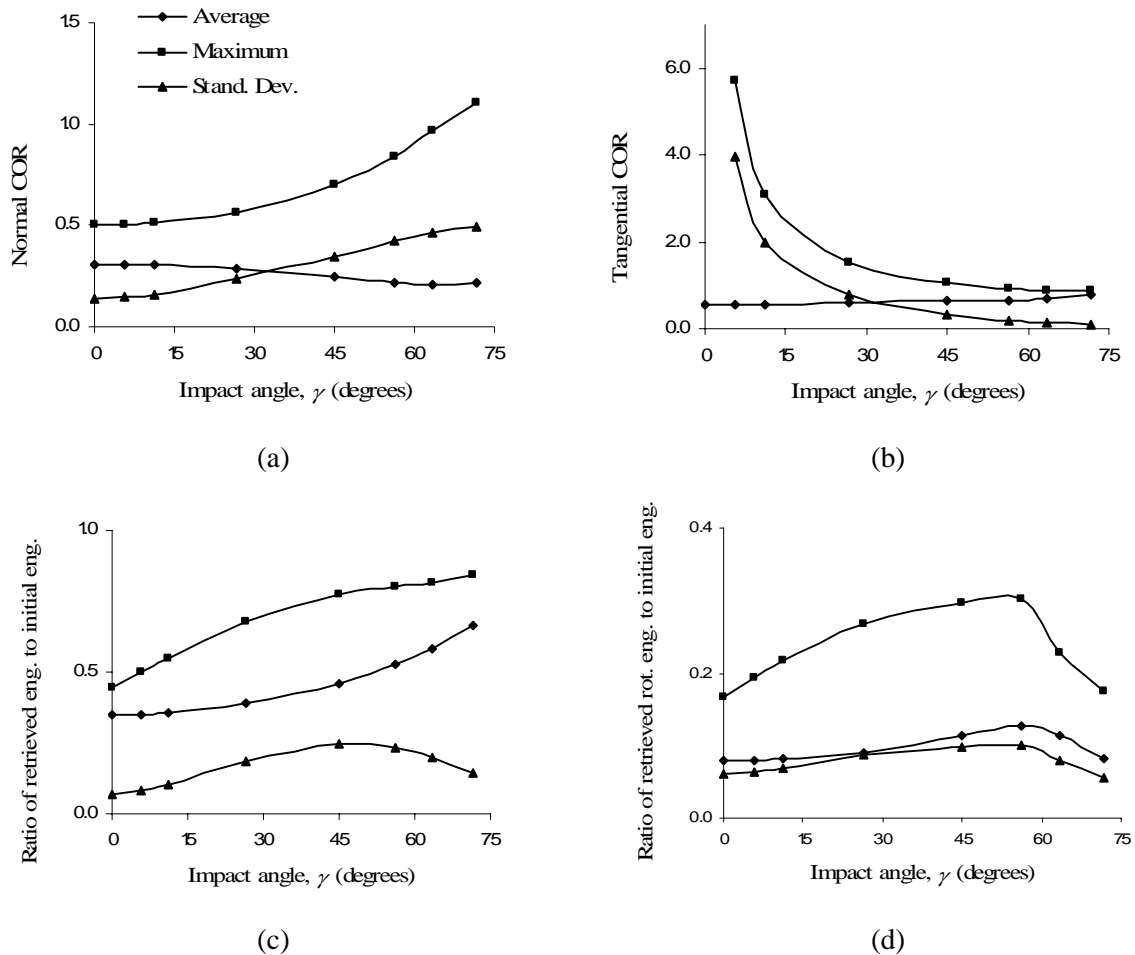


Figure 4.18: Variation of the average rebound parameters versus impact angle for planar impact of an ellipsoid at $V_{ini,hor} = \text{var.}$ (from 0 to 30 m/s): (a) ratio of rebound normal velocity to initial normal velocity, (b) ratio of rebound tangential velocity to initial tangential velocity, (c) ratio of total retrieved energy to initial energy, and (d) ratio of retrieved rotational energy to initial rotational energy.

4.5 APPLICATION OF RIGID BODY ROLLING IN ROCKFALL SIMULATION

When the contact normal velocity approaches zero, the object stays in contact with the surface. In this case the rock undergoes a complex rolling-sliding motion that is totally dependent on the geometry of the rock, the slope angle, and the contact material properties. Therefore, it is very rare to see an object experience pure rolling or sliding; the mode of motion is usually a combination of rolling, sliding, and small jumps.

Hybrid dimensionless rockfall simulators such as Pfeiffer et al. (1989), Stevens (1998), Guzzetti et al. (2002) usually ignore the rolling mode and merely consider sliding. Descouedres et al. (1987) suggested solving the simultaneous equations of motion for rolling at each time step. Azzoni et al. (1995) solved the rigid body equations of rolling motion for two-dimensional circular disks undergoing pure rolling, deriving simplified closed-form equations as a function of distance. They extended these simplified equations for more complicated shapes.

Here, the two-dimensional equations for the rolling-sliding motion for circular and noncircular objects are derived from the application of rigid body mechanics and the friction and rolling friction coefficients.

4.5.1 Rolling for non-circular objects

In rolling mode, an eccentric object experiences two perpendicular accelerations: normal and parallel to the rolling surface. Initially, assuming that pure rolling occurs at the contact point, the equations of motion, in the assumed framework of Figure 4.19, are written as follows:

$$\begin{aligned}
 1) & Mg \sin \psi + F = Ma_1 \\
 2) & N - Mg \cos \psi = Ma_3 \\
 3) & -F(-r_3) + (-r_n)N = (Mk_r^2)\alpha \\
 4) & a_1 = (-r_3)\alpha \\
 5) & a_3 = (r_1)\alpha
 \end{aligned} \tag{4.5.1}$$

where μ is Coulomb friction and μ_r is the rolling friction coefficient. This value has a length dimension and is described by Azzoni et al. (1995) and Bozzolo et al. (1988). In Equation (4.5.1) F and N are the surface and reaction forces of the contact, α is the angular acceleration, a_1 and a_3 are the oscillatory accelerations of the object's center of gravity, ψ is inclination of the contact surface, g is the gravitational acceleration, k_r is the polar radius of gyration, r_1 and r_3 are the contact vector components, and r_n is the modified tangential contact vector in tangential direction defined in Equation (4.5.3). Simultaneously solving Equation (4.5.1) leads to an expression for the angular acceleration:

$$\alpha = -\frac{r_3 \sin \psi + r_n \cos \psi}{k_r^2 + (r_n r_1 + r_3^2)} g \quad (4.5.2)$$

$$r_n = r_1 + \mu_r \cdot \hat{n}_r \quad (4.5.3)$$

where \hat{n}_r shows the direction of rotation and is equal to $\omega/|\omega|$.

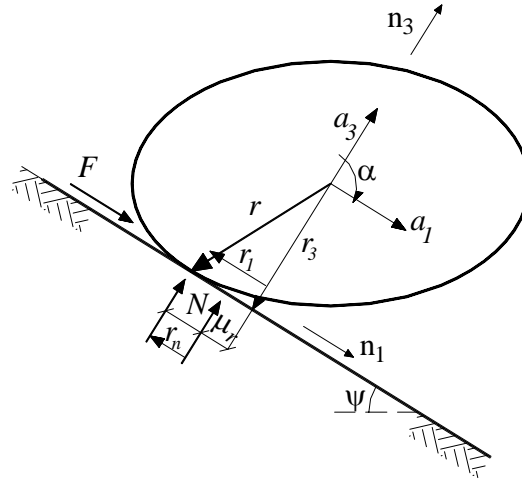


Figure 4.19: Rigid body object rolling in the local Cartesian framework.

Equation (4.5.2) is only valid if certain conditions hold. First, the friction force must be large enough to prevent the object from sliding on the surface, expressed by: $|F| \leq \mu \cdot N$. Second, the tangential contact velocity must be small enough, smaller than the tolerance level.

4.5.1.1 Rolling-sliding mode

If one of the two mentioned conditions does not hold, the objects start sliding during rolling. During sliding, the friction force, F , is constant and is opposite to the sliding direction:

$$F = \hat{f} \mu N \quad (4.5.4)$$

where \hat{f} shows the friction force direction (or the opposite direction of slip), and can be defined as: $\hat{f} = v_i / |v_i|$, (when there is no slip, the direction of friction force is against the inclination). Replacing the fourth equation of Equations (4.5.1), with Equation (4.5.4), the rotational acceleration changes to:

$$\alpha = -\frac{\mu r_3 \hat{f} \cos \psi - r_n \cos \psi}{k_r^2 + (r_n r_1 - \hat{f} r_1 r_3 \mu)} g \quad (4.5.5)$$

4.5.2 Rolling for circular objects

For circular disks or spheres the normal acceleration of the object center, a_3 , in Equation (4.5.1), is equal to zero; therefore there is no oscillation in the normal local direction. As a result, the angular momentum of a spherical object using Equation (4.5.2) and substituting the value of $k_r^2 = 2/5 R^2$, reduces to:

$$\alpha = -5/2 (\hat{f} \mu R - \hat{n}_r \mu_r) g \cos \psi / R^2 \quad (4.5.6)$$

A sphere undergoing sliding has an angular acceleration equal to:

$$\alpha = -5/7 (R \sin \psi + \hat{n}_r \cos \psi \mu_r) g / R^2 \quad (4.5.7)$$

4.5.3 Rigid body toppling

Any polygonal object in side contact with the surface, whether stationary or sliding, may experience toppling. According to Equation (4.5.2), toppling happens when the rotational acceleration α , is greater than zero. This causes the object to rotate on one of the contact corners. In other words, toppling occurs when the direction of the gravity vector passes the corner. Referring to Figure 4.20, toppling takes place if either of β_1 or β_2 is smaller than the inclination of the slope. Considering β_1 , this can be expressed by:

$$\beta_1 = \tan^{-1}(|r_1/r_3|) < \psi \Rightarrow \text{toppling occurs} \quad (4.5.8)$$

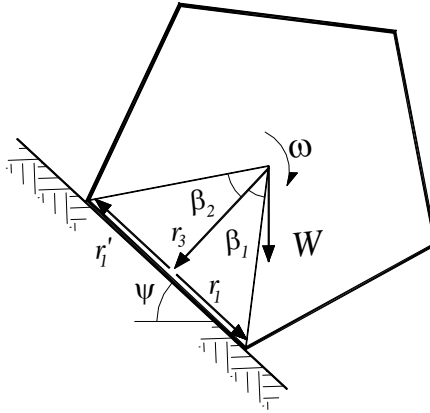


Figure 4.20: Object vulnerable to toppling around corner.

4.6 SUMMARY

- In the application of RBIM, offered by Stronge (1994), it is shown that by using RBIM, the rebound velocities can be calculated explicitly in a two-dimensional analyses, reducing computational cost to the lowest possible level, which is not significantly higher than that of lumped-mass models. When the contact configurations are defined, the rebound velocities can be calculated for any geometrical object.
- It is shown that an object's coefficients of restitution are strongly affected by its geometry and configuration at the instant of impact.

- Several parameters other than the impact model affect the coefficients of restitution including: rock slenderness, impact angle, impact orientation, and material parameters (friction coefficient, μ , and energy COR, e_*). These make field investigation of the rock shape, slope geometry, and rock-slope material parameters a vital step in the estimation of mitigation distances. Infrastructure might be in the safe zone for the fall of spherical rock but in the danger zone for an ellipsoidal rock.
- It is the author's opinion that rigid body impact mechanics should eventually replace the existing particle models currently used in most rockfall simulations.

CHAPTER 5

GEOMETRICAL ROCKFALL SIMULATION: *GeoRFS*

5.1 INTRODUCTION: ROCKFALL SIMULATIONS IN THE LITERATURE

Understanding the rockfall phenomenon involves investigating two main mechanisms: triggering and post-failure. Historically, researchers have pursued only one of these directions at one time. The current work studies the post-failure procedures which predict the rock trajectory during a fall from the detachment point on the slope. Guzzetti et al. (2002) described different rockfall models developed in the last three decades, and based on the impact model, categorized the models in three main groups: lumped mass, hybrid, and rigid body, as described in Table 5.1. In addition to the impact model, which was addressed in the last chapter, two additional assumptions affect modeling and computation cost: model dimensions, and the availability of probabilistic analyses. Table 5.1 illustrates that, due to dramatic computational cost, hardly any of the rockfall programs address all the important characteristics of rockfall simulation simultaneously. This means that there is no three-dimensional rigid body probabilistic model. Any computer simulation program incorporating all these aspects loses the ability to be run as a routine engineering application, its execution will be limited to the powerful supercomputers in research labs.

Lumped mass or stereomechanical models benefit from high computational efficiency but suffer significantly from a loss of accuracy. These models consider the impact point as a result of the intersection of the freefall parabola with the impact surface. The impact model is simplified by applying only two coefficients of restitution, one in each normal and tangential direction. Accordingly, the rolling phase is simplified to a sliding phase. Lumped-mass models are widely used in two and three-dimensional rockfall analyses. Approximately, 40% of the existing rockfall models are of this type; however, as these models do not incorporate rock shape, they are outside the scope of this study.

To improve the lumped mass models, hybrid models, which utilize simplified mathematical impact models for calculating the rebound velocities, were developed by Bozzolo et al. (1982). The contact search procedure for these models is similar to the lumped-mass models. These models can incorporate some aspects of the rigid body impact models, including: rock shape effect, rotational velocity, and energy loss mechanisms. Both the lumped-mass and hybrid models perform their intensive calculations, due to the presence of repetitive probabilistic analyses, in a highly cost-effective manner.

Table 5.1: Different computer simulation models for rockfalls categorized based on their main characteristics, after Guzzetti et al. (2002)

Year	Author(s)	Program name	Dimensions	Approach	Probabilistic
1976	Piteau and Clayton	Computer Rockfall Model	2-D	Lumped-mass	Partly
1982-86	Bozzolo and Pamini	SASS-MASSI	2-D	Hybrid	Yes
1985	Bassato et al.	Rotolamento Salto Massi	2-D	Lumped-mass	No
1987	Descouedres and Zimmermann	Eboul	3-D	Rigid body	No
1989-91	Pfeiffer and Bowen Pfeiffer et al.	CRSP	2-D	Hybrid	Yes
1990	Kobayashi et al.	-	2-D	Rigid body	No
1991-95	Azzoni et al.	CADAMA	2-D	Hybrid	Yes
1991	Scioldo	Rotomap	3-D	Lumped-mass	No
1998	Stevens	RocFall ver. 4.0	2-D	Hybrid	Yes
1999	Paronuzzi and Artini	Mobyrock	2-D	Lumped-mass	Yes
2000	Jones et al.	CRSP 4.0	2-D	Hybrid	Yes
2002	Guzzetti et al.	STONE	3-D	Lumped-mass	Yes
This work	Ashayer and Curran	<i>GeoRFS</i>	2-D	Rigid body	Yes *

* Probabilistic analysis is achieved in the research version of RocFall®

Introducing the third dimension into the two-dimension rockfall simulation will increase the system's degrees of freedom from three to six, making the contact search computation cost prohibitive. Consequently only a small fraction of commercial software tools are three-dimensional, although, the general trend seems to indicate an increase in such applications.

In rockfall modeling, the rock initial position and its motion characteristics are not known. As a result, any successful model should consider probabilistic analysis to compensate for these unknown values in the following stages: initial rock position and orientation, initial translational and rotational velocities, rock shape and geometry, and slope geometry and material. A more precise look at these variations and their applicability to rockfall modeling are considered in Chapters 4 and 6.

Bozzolo et al. (1982-86) proposed the first hybrid model SASS in which the contact search process is based on the parabola-line intersection and the impact model considers the impact of an ellipse with the impact surface. Later, they proposed a modified version of their simulation, MASSI, which finds the geometry-surface contact point. However, the rolling in MASSI utilizes simplified assumptions, causing the simulation to be considered a hybrid model. Azzoni et al. (1995) later developed their impact model, a specific mathematical model discussed in detail in Chapter 4.

Pfeiffer et al. (1989) proposed the most well-known and widely-used rockfall model, CRSP, adopted in other simulations such as Stevens (1998) and Jones et al. (2000). The most important limitation of this model is the simplicity of the rock shape geometry, which is considered to be circular, and the lack of proper definition for the tangential coefficient of restitution. Defining this coefficient of restitution for geometrical objects is not applicable in Pfeiffer's model because the size of the circle is shrunk to a dimensionless circular object. This model is briefly studied in Chapter 4, in comparison to other rigid body models. This model and its implementations can entirely incorporate probabilistic analysis, and may be applied in three-dimensional space.

Kobayashi (1990) proposed a two-dimensional rigid body model, limited to circular rock geometry, where the deployed impact constitutive model is a modified version of the impact

model developed by Bozzolo et al. (1986). In this model, it is assumed that the components of the reactive forces are proportional to the tangential and perpendicular trajectories of the velocity in reference to the contact surface. In rolling mode, the simulation determines the velocities and accelerations of a rock at the end of a segment when the rolling ends. The rolling constitutive model consists of three coefficients: viscosity, friction, and rolling friction, where the viscous resistance is proportional to the velocity of the rock and is higher at higher velocities, and the rolling friction is constant and dependent on the slope material.

Azzoni et al. (1995) proposed a two-dimensional hybrid model for ellipsoidal rock shapes where the impact model is a modified version of the model offered by Bozzolo et al. (1986). This model is thoroughly investigated in Chapter 4, with comparison to other impact models. The contact search algorithm in this model is based on parabola-line intersection and the applied rolling model is based on the pure rolling of a circular object where no sliding occurs.

Descouedres and Zimmermann (1987) offered a three-dimensional rigid body model where the rock geometry may be considered either ellipsoidal or polygonal for both the impact and the rolling modes of motion. A detailed study on the kinetic impact model is presented in Chapter 4, where it is compared to the other models. In addition, the closed-form equations are derived for two-dimensional space, while in three dimensions the iterative solution is needed. This model is the most sophisticated rigid body model offered in rockfall literature; however, the proposed simulation does not support probabilistic analyses and does not properly consider the tangential impact sliding modes.

5.1.1 Hybrid versus geometrical modeling

In this work, it is necessary to justify the application of rigid body models, versus the application of hybrid models, as the contact search procedures in rigid body models are much more computationally intensive. On the other hand, it is practical to pursue the other hybrid models and, based on the improved impact model, RBIM, create another hybrid simulation model. Hybrid models are far more efficient than rigid body models due to their straightforward contact search procedure in contrast to rigid body models which need the

exact contact point and the object position at the time of contact. The hybrid model users might argue that because there are a lot of uncertainties in rockfall simulations, such as rock dimensions, initial rock configurations, or slope material prosperities, any additional attempts to find precise contact configurations are unwarranted.

5.1.1.1 Conventional hybrid models

To underline some deficiencies involved in hybrid modeling, a numerical investigation is proposed in Figure 5.1a, which shows the typical contact search method used in most hybrid models. This test tries to highlight the errors involved in the calculation of the impact angle. It should be noted that, incorporating the rebound situation in addition to the incoming situation doubles the amount of error involved in the calculations. For the ellipse shown in Figure 5.1a, the following assumptions are made: $V_{in,hor} = 0$, $\omega_0 = 5$ (*rad/s*), $a:b = 2$, $\theta_0 = 90^\circ$, and $V_{ini,ver}$ is variable. These values illustrate a typical impact configuration when the rock initial orientation is vertical.

Figure 5.1b plots the variation of the ellipse impact orientation angle versus the size of the ellipse major axis, a , at variable impact normal velocities. This figure shows that the object is subjected to extensive over-rotation between two situations: the orientation angle at the time of intersection and the orientation at the time of the imaginary intersection of the trajectory parabola and the impact surface. The figure shows that at normal velocities lower than 5 m/s, with the size of boulder equal to 1 m, an over-rotation of 45° might occur. In the previous chapter, Figure 4.8, it was demonstrated that a variation in the object orientation, for example from an angle of 0 to 45° , may change the normal coefficient of restitution from 0.5 to -0.27 and the tangential coefficient from 0.5 to 1.03. Meanwhile, the retrieved energy varies from 38% to 77%, a 103% increase, demonstrating that the contact situation entirely changes to a new contact configuration.

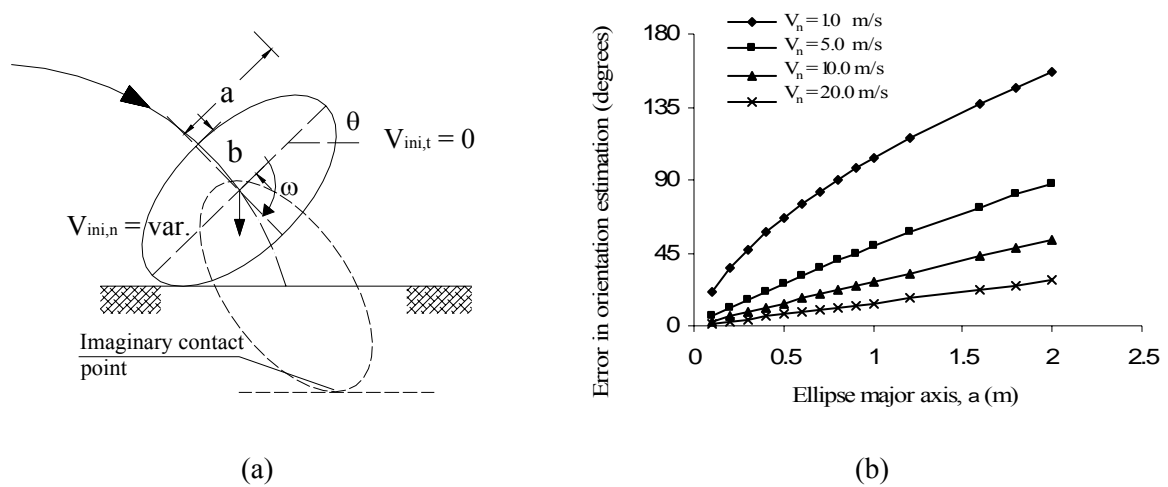


Figure 5.1: Hybrid contact search methods: (a) parabola-surface contact search method surface, and (b) error involved in estimation of the object orientation at contact for hybrid model.

Spherical objects are the only shapes for which the rebound parameters are not affected by their orientation at the time of impact. Therefore introducing a hybrid model for spherical rocks is reasonable if the rock geometry is similar to spherical shapes, which is not always correct.

5.1.1.2 Circumscribing hybrid models

In order to improve the proposed hybrid contact search method, a modified version of the model, which is called single-circle circumscribing hybrid model (SCCHM), is offered. This improvement is due to the high computational efficiency of the circle-line contact search procedure. In this method the object is circumscribed by a circle. The contact point between the circle and the imaginary line is considered to be the impact contact point, as shown in Figure 5.2a. Therefore, the object orientation at the time of contact is different from the actual impact orientation.

This procedure still suffers from over-rotation. To demonstrate the highest possible over-rotation, an ellipse with the major and minor axes of a and b is dropped at an initial orientation of 0° , an initial normal velocity of 1 m/s, and a is considered constant equal to 1.0 m while b is assumed to be variable. Figure 5.2b shows the error involved in the evaluation of the angle of impact when the object rotates at different rotational velocities against the

ellipsoid aspect ratio. The amount of the over-rotation angle for higher rotational velocities is significant regardless of the aspect ratio of the rock. If the acceptable amount of error in the estimation of the orientation angle is considered to be approximately 5° to 10° , then this method is unacceptable due to the inaccuracy in the calculation of the impact orientation angle.

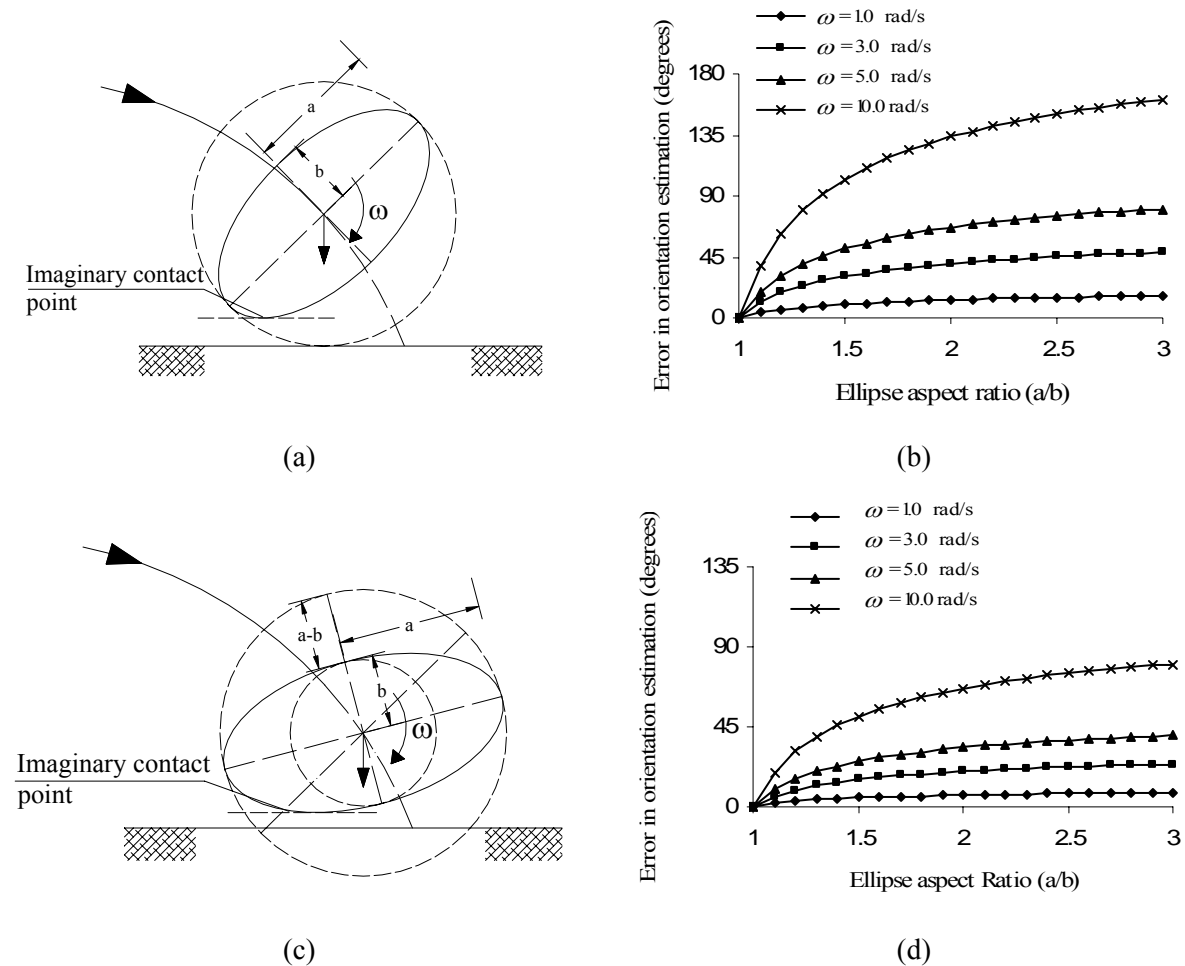


Figure 5.2: Hybrid contact search methods: circumscribing hybrid models: (a) Single-circle circumscribe hybrid method (SCCHM), (b) error involved in estimation of the object orientation at contact, (c) double-circle circumscribing hybrid method (DCCHM), and (d) error involved in estimation of the object orientation at contact in double circle method.

To improve the contact point search procedure, the double-circle circumscribing hybrid model (DCCHM) is suggested. In this method the impact position of the object is the average position of two circles: one circumscribing the ellipse (or any other eccentric object) and the

other circumscribed by the object, as shown in Figure 5.2c. The impact point is the imaginary contact point of the object and a line parallel with the surface. Using this method, the maximum amount of error reduces to half of the error of the SCCHM method, while the computational cost of the contact search doubles. Figure 5.2d shows the error occurring in the estimation of the object orientation angle using this method, in comparison with the actual geometry based contact search scheme. Even though the amount of error involved in this procedure is half of the SCCHM, it is still quite significant.

Although the hybrid models significantly reduce the search efforts, the previous numerical tests show they are not suitable for noncircular rocks with a high aspect ratio. This is due to extensive error involved in calculating the object impact orientation, which significantly affects the rebound parameters. Therefore, it can be said that the suggested model precision would be as low as if choosing the impact rebound parameters randomly.

5.2 METHODOLOGY FOR RIGID BODY ROCKFALL SIMULATION PROGRAM: *GeoRFS*

The first two-dimensional rigid body rockfall model was offered by Bozzolo et al. in the 1982. These rigid body models were later adopted and developed by some other researchers including: Descouedres et al. (1987), Kobayashi et al. (1990), and Azzoni et al. (1995). The present simulation, *GeoRFS*, follows some of the conventions made by Bozzolo; however, it is capable of implementing the former rigid body impact models in addition to RBIM for a wide range of rock shapes, as will be shown in Section 5.4.9. In the following sections, the primary assumptions made by the *GeoRFS* model are presented.

5.2.1 Basic assumptions

Rock fracturing and deformation: Most of the existing models, including Bozzolo et al. (1986), Azzoni et al. (1995), and Descouedres et al. (1986) ignore rock fragmentation, as they consider ignoring this factor to be more conservative for energy calculation. This

research accepts this reasoning and assumes that neither fragmentation nor extensive deformation occurs in the rock during the collision.

Multiple-rock impact: The *GeoRFS* model does not take into account the impact of the falling rock with the other rocks. However, there is no theoretical limitation in the consideration of the impact of a group of different rock geometries in the application of rigid body impact mechanics. It is likely that the lack of data for constructing such a model in addition to the different complications of implementation cause the modelers to ignore the modeling of multiple rocks.

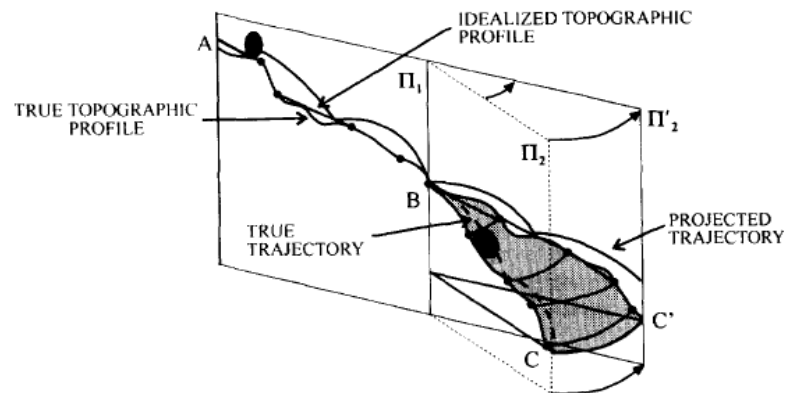


Figure 5.3: Choosing two-dimensional slope profile from three-dimensional topography, after Bozzolo et al. (1986) and Azzoni et al. (1995).

Two-dimensional model: The movement of the falling rock is constrained to two-dimensional space, reducing the system degrees of freedom to three: two translational and one rotational on an axis perpendicular to the plane passing through the object center of gravity. Figure 5.3 shows the two possible two-dimensional slopes selected from a real three-dimensional slope. It is the user's task to decompose and test the most hazardous planes from the slope topography, like the Π_2 and Π_2' planes in Figure 5.3. There are many successful reports concerning the combination of two and three-dimensional simulations such as Giani et al. (2004). These show that a simplified three-dimensional method may define the most critical planes and a more sophisticated two-dimensional model can analyze the planar rockfall.

5.2.2 Slope decomposition

The slope topographic profile, shown in Figure 5.3, is idealized as a series of rigid segments intersecting at nodes, depicted in Figure 5.4a. To take the uncertainties in the slope geometry once the polyline is introduced into account, each definite segment may rotate around its midpoint at an angle derived from a distribution defined by the user, depicted in Figure 5.4b. The new slope is then created by trimming the rotated segments. In this model, barriers can be defined in the geometry by introducing multiple line segments with limited or indefinite energy capacity. Figure 5.4 shows the slope numbering and the altered slope due to the rotation of the segments.

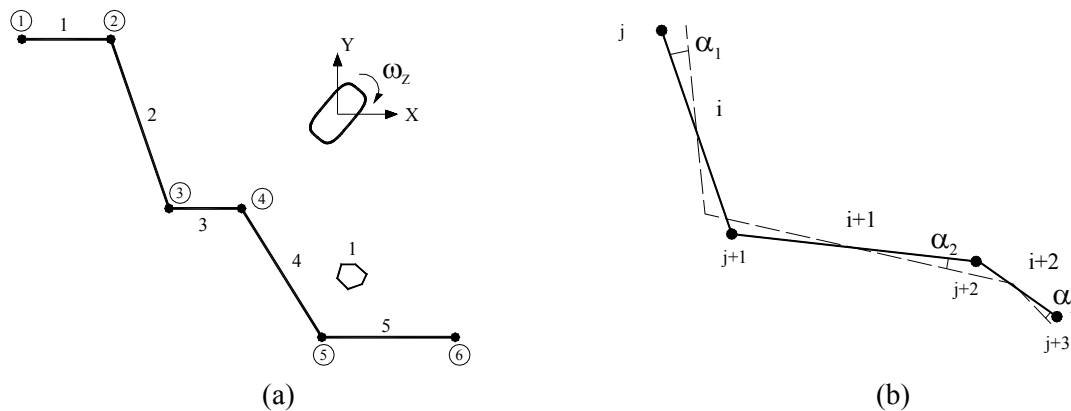


Figure 5.4: Slope modeling in *GeoRFS*: (a) slope made of straight rigid segments with node and segment numbering, and (b) segment rotation around middle point representing the uncertainties in geometrical modeling of slope.

5.2.2.1 Slope roughness

The slope roughness parameter was originally introduced by Pfeiffer et al. (1989) to consider the local variation in the impact angle due to the slope unevenness with respect to the scale of the rock diameter. This parameter was later adopted by other researchers (Stevens (1998) and Jones et al. (2000)).

Slope roughness parameter was introduced due to the necessity of having an appropriate statistical distribution representing the variation in the slope geometry. In contrast to lumped-mass models, as shown in Chapter 4, many parameters perturb the rebound values in rigid body models, including: impact angle, the rock geometry, and the impact orientation. In

Chapter 6, it will be shown that, without introducing the slope roughness to the model, spherical objects do not exhibit the correct roll-out distribution. The slope roughness in rigid body modeling can be introduced by altering the slope inclination in the beginning of each simulation as explained in Figure 5.4b.

5.2.3 Model rock geometries

It is shown in Chapter 4 that rock geometry dramatically affects rebound velocities and energies. The computer model *GeoRFS* allows the user to choose the appropriate rock geometry from a list of a wide range of available shapes. Not only may a rock shape be randomly chosen from a seeder consisting of several shapes but also its dimensions can be specified using a statistical distribution. The provided geometries can be divided into two major groups: polygonal (prismatic) or ellipsoidal (ellipse-extended). There is also the option of choosing either two- or three-dimensional objects; however, the three-dimensional objects are restrained to move in a plane even though they have three dimensional geometrical properties.

The ellipsoidal objects are derived from the three-dimensional superellipsoids general formula, described in Equation (5.2.1), where the center is located at $\{x_0, y_0, z_0\}^T$ in the Cartesian coordinate system. Figure 5.6a shows the available three-dimensional shapes using values for the ellipsoid power, n , equal to 1, 2, 3, and 4 in Equation (5.2.1). This figure shows that these shapes are suitable for the three-dimensional representation of rocks.

$$F(x, y, z) = \left| \frac{x - x_0}{a} \right|^n + \left| \frac{y - y_0}{b} \right|^n + \left| \frac{z - z_0}{c} \right|^n - 1 = 0 \quad (5.2.1)$$

The general two-dimensional formula is derived by eliminating the z term from Equation (5.2.1). Similar shapes, for different values of n , are plotted in Figure 5.5b. Two-dimensional objects are considered to have a third dimension, a thickness t , required for energy calculation, shown in Figure 5.5c. In the special case of $n = 2$ and $a = b = r$, the ellipsoid reduces to a circle, as shown in Figure 5.5d. In two-dimensional space, the superellipsoids are called superellipses, shown in Figure 5.5e. The regular polygonal objects are defined by

introducing side dimensions, while the irregular ones are defined by setting nodal local coordinates, shown in Figures 5.5c and 5.5f, respectively. As shown in Equation (5.2.1), the ellipsoid geometry approaches a rectangular shape for higher values of n .

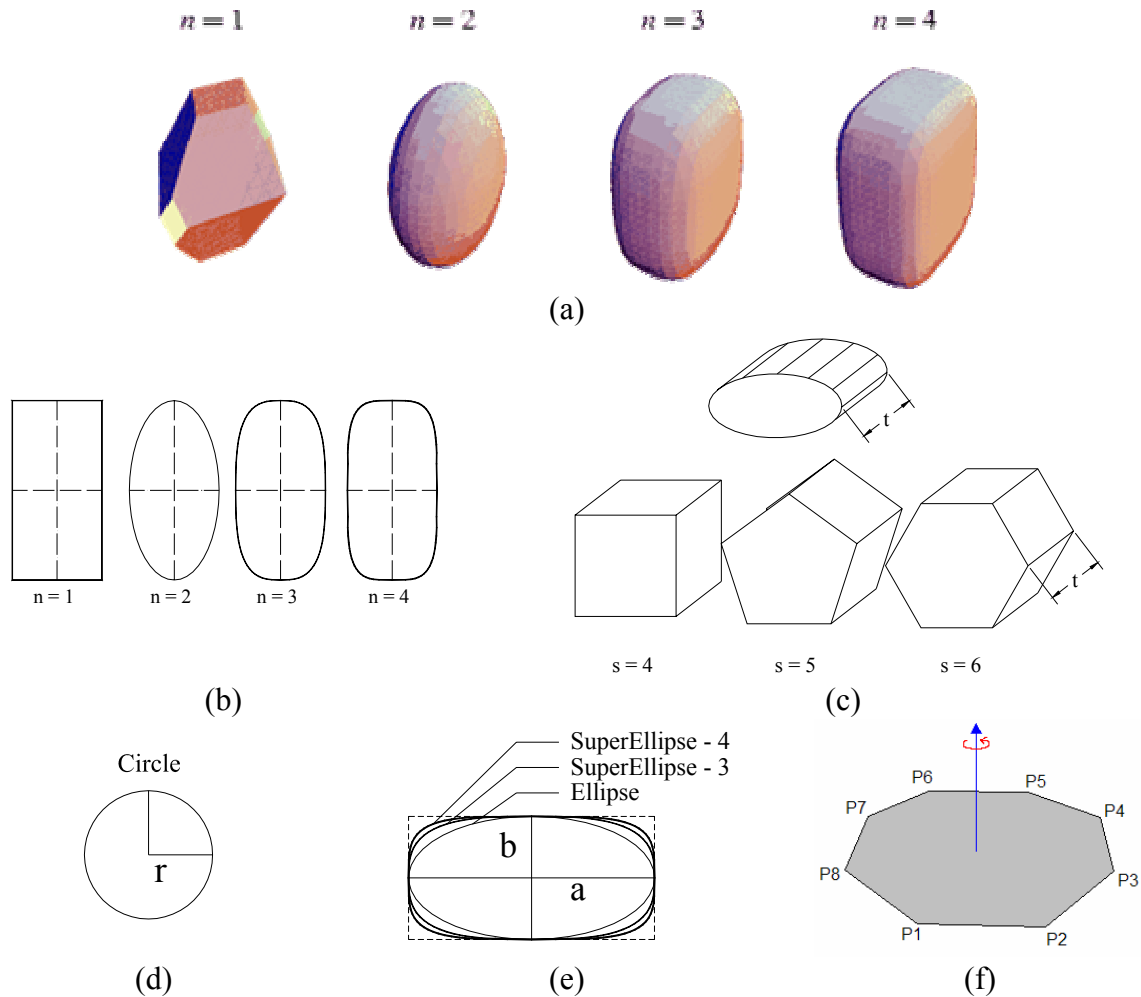


Figure 5.5: Rock shape representation in the *GeoRFS* simulation: (a) 3-D ellipsoids defined by Equation (5.2.1) for different values of n , after *mathworld.com*, (b) 2-D superellipse with different values of n , (c) prismatic 2-D objects with thickness, t and side number, s in addition to ellipse-extended shape, (d) circular cross section with radius r , (e) relative presentation of the rectangle, ellipse, and superellipse, and (f) n -sided polygonal section of prismatic object with the nodes P_1 to P_n .

Table 5.2 shows the geometrical properties for different two- and three-dimensional objects. In the application of rigid body mechanics, to define the rebound velocities, in addition to the contact vector, the polar radius of gyration, k_r , is needed. The geometrical properties of superellipsoids are calculated using the closed-form equations offered by Jaklić (2000).

In Figure 5.5f, an arbitrary polygon is demonstrated. This could be defined in the simulation by defining the nodal points in the local coordinate system. The mechanical properties are presented in Table 5.2.

Table 5.2: List of provided geometrical shapes in *GeoRFS* and the mechanical properties of motion

Geometrical shape	2D		3D	
	Cross sectional area (A)	Polar radius of gyration (k_r)	Volume (V)	Polar radius of gyration (k_r)
Circular (Spherical)	πr^2	$r/\sqrt{2}$	$4/3\pi r^3$	$\sqrt{2/5}r$
Ellipsoid	πab	$\sqrt{a^2 + b^2}/2$	$4/3\pi abc$	$\sqrt{(a^2 + b^2)}/\sqrt{5}$
Superellipsoid-3	$3.5338ab$	$\sqrt{a^2 + b^2}/1.8797$	$5.6966abc$	$\sqrt{a^2 + b^2}/2.0077$
Superellipsoid-4	$3.7081ab$	$\sqrt{a^2 + b^2}/1.8220$	$6.4558abc$	$\sqrt{a^2 + b^2}/1.9060$
Superellipsoid-10	$3.9424ab$	$\sqrt{a^2 + b^2}/1.7530$	$7.6752abc$	$\sqrt{a^2 + b^2}/1.7721$
Rectangular- (Cubic)	$4ab$	$\sqrt{a^2 + b^2}/\sqrt{3}$	$8abc$	$\sqrt{a^2 + b^2}/\sqrt{3}$
Prismatic	$\sum_{i=0}^{n-1} (x_i y_{i+1} - x_{i+1} y_i)/2$ ^a	$\sqrt{I/A}$ ^b	Same as 2D	Same as 2D

^a x_i and y_i are the nodal coordinates, and n is the total number of nodes

^b I is the polar moment of inertia of the polygonal cross section of the prismatic object. Considering the polygonal cross section of the Figure 5.5f and \vec{P}_n as the nodal vector in the local coordinate system, the polar moment of inertia is derived based on Equation (5.2.2):

$$I = \frac{1}{6} \frac{\sum_{n=1}^N \|\vec{P}_{n+1} \times \vec{P}_n\| (\vec{P}_{n+1}^2 + \vec{P}_{n+1} \cdot \vec{P}_{n+1} + \vec{P}_n^2)}{\sum_{n=1}^N \|\vec{P}_{n+1} \times \vec{P}_n\|} \quad (5.2.2)$$

5.2.4 Domain of analysis

The classical models, as a combination of one or several particles, use Newton's classical laws for defining motion. To define the interaction of particles, these models are divided into two major groups: event-driven methods (EDMs) and time-driven methods (TDMs), as described by Peters et al. (2002). In EDMs the situation of the particles is updated when a "collision" event occurs, and between these events the object moves based on the equations

of motion. In rockfall studies, this method is widely used in lumped-mass and hybrid models. The TDMs are used when the dynamic system is a combination of several particles or when the time of the event is smaller than the real time of the collisions. The latter condition occurs in geometrical modeling of the rockfall during the rolling phase. In this mode the object is in continuous contact with the surface, resulting in continuous variation of the contact forces and, consequently, in velocities and accelerations for non-circular objects.

In the *GeoRFS* model, time domain analysis is chosen instead of event based analysis. In the literature, the only rockfall rigid body model which applies a similar TDM, is the model offered by Descouedres et al. (1987). To make the model efficient and reduce the computation cost, an efficient optimization method which incorporates some aspects of EDMs is used. This optimization method is explained in Section 5.3.2.

5.2.5 Modes of motion

A detached rock, either from a cliff or from a loose spot, may acquire the following modes of motion: freefall, impact, rolling, and sliding until it finally reaches the equilibrium state called arrest. Other than freefall, the rock-surface contact is usually a combination of impact, rolling, and sliding modes. Rolling and sliding usually occur simultaneously, while pure sliding occurs after side contact of the polygonal objects where the rock may not experience toppling. Pure rolling may also occur during rolling on the slopes with a low inclination angle, or when the friction coefficient is relatively high. In impact mode, the object may experience sliding at the contact point, while a circular object may experience spin without any translational motion. Numerically, there are only two modes of motion: freefall and contact. Figure 5.6 shows the different modes of motion as the following:

- Freefall
- Contact
 - Impact (combined with sliding, rolling, and stick)
 - Rolling-sliding or low normal contact velocity
 - Arrest or low contact velocity

In freefall mode the object moves freely based on the gravitational force. If a falling rock contacts a surface with a velocity greater than a threshold velocity, the mode of contact is considered impact, otherwise the mode of motion is considered rolling. Theoretically, if an object's rebound velocity is smaller than the threshold velocity it cannot separate from the contact surface. The magnitude of this threshold velocity may be defined by the user; however, in time-domain analyses, it has a minimum value based on time step which will be discussed in the following sections.

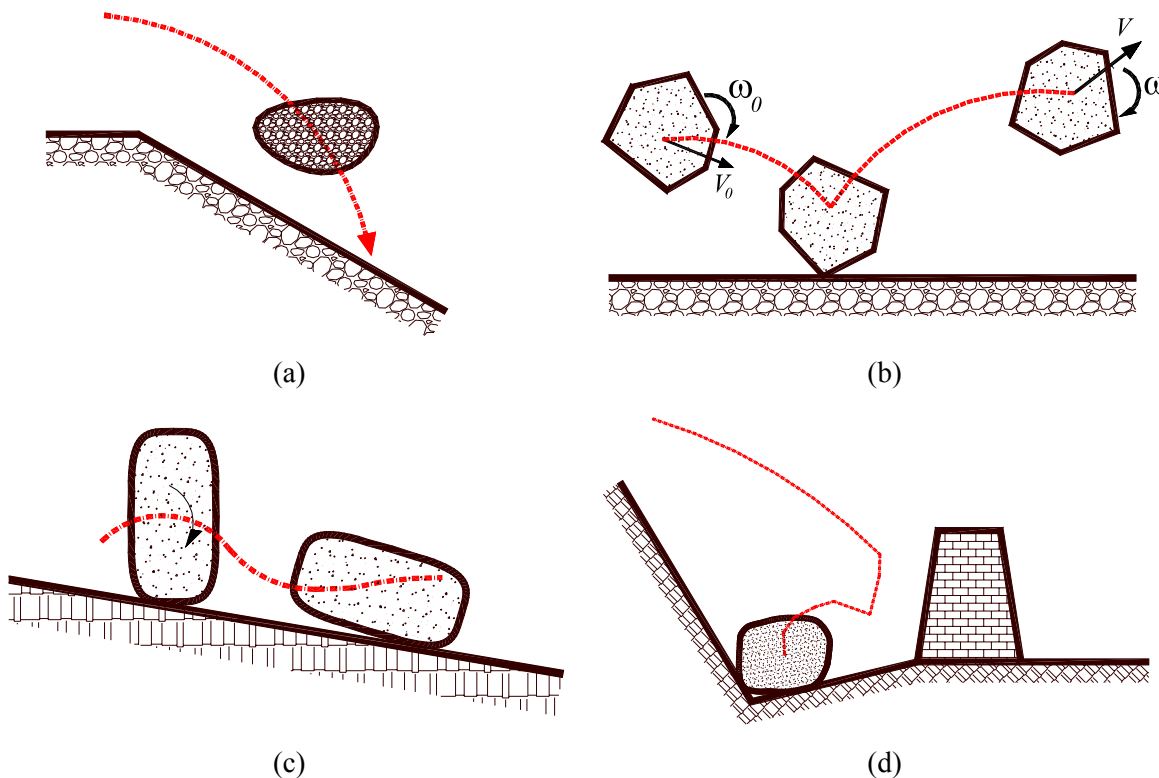


Figure 5.6: Different modes of motion: (a) freefall, (b) contact: impact, (c) contact: rolling-sliding, and (d) contact: arrest.

5.2.6 Mechanical models of contact

Rigid body impact mechanics (RBIM) offered by Stronge (1994a) is adopted here for modeling the impact mode in *GeoRFS* program. However, *GeoRFS* is designed in such a way that most of the well known rockfall impact models can be implemented in its structure. Already, the impact models offered by Descouedres et al. (1986) and Azzoni et al. (1995) are implemented in the *GeoRFS* simulation for research purposes. The Kobayashi (1990) impact

model is also implemented in this simulation for spherical, cylindrical, and discoidal rock shapes. Moreover, rigid body rolling is utilized for rolling mode, as described in Section 4.5.

5.3 CONTACT SEARCH PROCEDURE

Contact search procedures are needed to accurately identify the rock-surface contact point. Any error involved in defining the contact time or the object impact configuration affects the rebound velocity calculation and consequently the rock trajectory. In contrast, spending excessive computational efforts on contact search procedure is not practical in probabilistic rockfall simulation. This is because it is necessary to throw hundreds of rocks from any single location to determine the statistical distribution for rebound parameters. As the rebound velocities are defined explicitly in two-dimensional problems, the computational efforts needed to calculate rebound velocities are much lower than the efforts needed for contact search procedures. In this simulation, the rock-slope contact search reduces to the repetition of the rock-segment contact search. To establish a robust and efficient contact search algorithm, the following steps are suggested: circumscribing, optimization, and an object-line contact search.

5.3.1 Contact search optimization

In a single rockfall scenario, with a rigid slope, there is only one object having variable coordinates. However in a probabilistic analysis, the whole geometry can be reset at the beginning of each run. As a result, a combination of two optimization procedures is suggested for this simulation: timestep refinement and the gridding method.

5.3.1.1 Circumscribing

The contact search procedure for circles has the least computation cost among all other geometries. Ellipses and rectangles have the next lowest computational cost. As a result, it is common in contact mechanics to surround the complicated objects with either circles or rectangles. Uniform objects, like superellipses, are appropriate to be surrounded by both of

these shapes, while it is practical to circumscribe polygons only by circles. These conventions are followed in this simulation, as shown in Figure 5.7a.

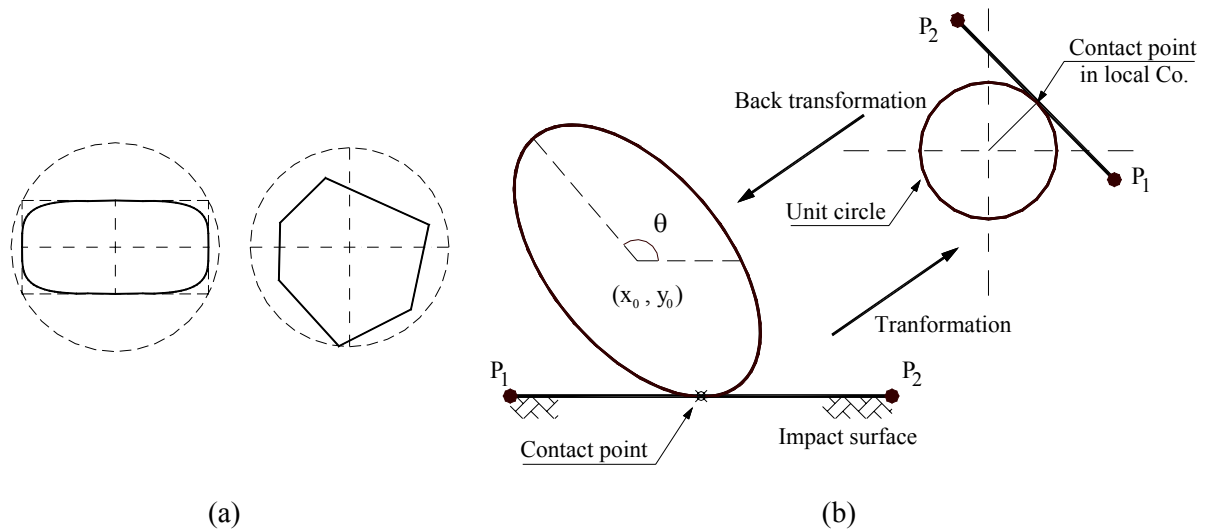


Figure 5.7: (a) Body-based circular and rectangular cells, and (b) geometric transformation contact search method.

5.3.1.2 Dynamic timestep refinement

Timestep refinement, or splitting the current timestep to n equal fractions, is used prior to impact in the simulation procedure. This is performed, when the current timestep is greater than the critical timestep. Usually, the discretization number, $n_{fraction}$, is a natural positive value between 10 and 100.

5.3.2 Object-segment contact search procedure

An object may contact a segment either at a corner or within a line segment. However, if an object contacts a segment with its nodes, the contact type is considered to be a corner contact. In this simulation, the contact search procedure is based on the geometrical transformation method, (GTM), introduced by Ting (1990), as shown in Figure 5.7b. This method was originally developed for ellipse based contact search procedures for application in discrete element modeling, but here it is generalized for superellipses and polygons.

5.3.2.1 Step 1 – constructing local coordinate system

In GTM, the contact search procedure is performed in the unit object's local coordinate system. It is necessary to transfer the slope geometry to this local coordinate system which is located at the object's center of gravity. In the unit object's coordinate system, the ellipse is represented by a circle, while higher order superellipse simplify to a unit superellipse given in explicit form in Equation (5.3.1). Consequently, rectangles reduce to unit squares while randomly generated polygons keep their size.

$$F(x, y) = |x|^n + |y|^n - 1 = 0 \quad (5.3.1)$$

5.3.2.2 Step 2 – geometry transformation

The slope geometry transformation is achieved by transferring the slope nodal points to the object's local coordinate system. Using the transformation matrices of rotation, scaling, and translation (in Hill (2001)), T_R , T_S , and T_T ; any definite point, P , in the global coordinate system will be translated to point P' in the object's local coordinate system by the following successive matrix productions: $P' = T_S(1/a, 1/b)T_R(-\theta)T_T(-x_0, -y_0)P$. The details of these matrices are presented in Equation (5.3.2):

$$T_S(a, b) = \begin{bmatrix} a & 0 & 0 \\ 0 & b & 0 \\ 0 & 0 & 1 \end{bmatrix} \quad T_R(\theta) = \begin{bmatrix} \cos(\theta) & -\sin(\theta) & 0 \\ \sin(\theta) & \cos(\theta) & 0 \\ 0 & 0 & 1 \end{bmatrix} \quad T_T(x_0, y_0) = \begin{bmatrix} 1 & 0 & x_0 \\ 0 & 1 & y_0 \\ 0 & 0 & 1 \end{bmatrix} \quad (5.3.2)$$

where θ is the object orientation, a and b are the object major and minor axes, and x_0 and y_0 are the object's center. It should be noted that by applying the geometric transformation any straight line remains a straight line.

5.3.2.3 Object-segment contact

Originally, for the search procedure, the penetration of the object points into the slope segments was checked. For example, for polygonal objects, the penetration of nodal points into the slope surface was tested. However, it was observed that when the contact event is

based on the penetration of the nodal points into the segment, sometimes, an incorrect contact event might be found. This occurs when two adjacent segments form a small angle. As a result, all the contact search methods, except when they are applied to circles, are based on the intersection of the slope segment and another segment which connects the object's center and some potential contact points as demonstrated in Figure 5.8. The procedures of deriving the potential points are explained in the following. Using this procedure is more computationally expensive than checking the nodal penetration; however, the new procedure can resolve the ambiguity of contact search procedures.

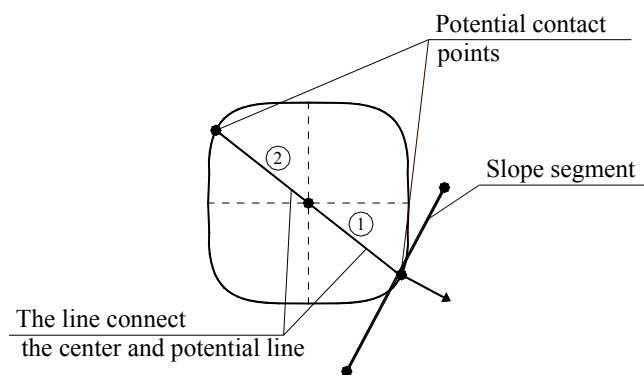


Figure 5.8: The contact search procedure based on the intersection of the slope segment and the lines connecting the object's center and the potential contact points.

After transferring the segment nodal points into the object local coordinate system, each geometrical shape has its own unique contact search procedure:

Circle (ellipse) - segment: The contact point is: $P_c = P_{center} - R \cdot \hat{n}$, where P_c is the contact point, P_{center} is the object center coordinate, here the origin, and R is the radius of circle, here a unit value, and \hat{n} is line normal vector.

Superellipse - segment: For superellipses the potential contact points are defined based on the common normal vector between the superellipse and the slope segment, as shown in Figure 5.9a. Defining x_c and y_c by Equation (5.3.3), the potential contact points can be derived as: (x_c, y_c) and $(-x_c, -y_c)$. One of these two potential contact points can be the object-segment contact point as demonstrated in Figure 5.8.

$$x_c = \frac{Sgn(n_1)}{\sqrt[n]{1 + |n_2/n_1|^{n/(n-1)}}} \quad y_c = \frac{Sgn(n_2)}{\sqrt[n]{1 + |n_1/n_2|^{n/(n-1)}}} \quad (5.3.3)$$

In the above equation $\hat{n} = (n_1, n_2)$ is the contact (segment) normal vector.

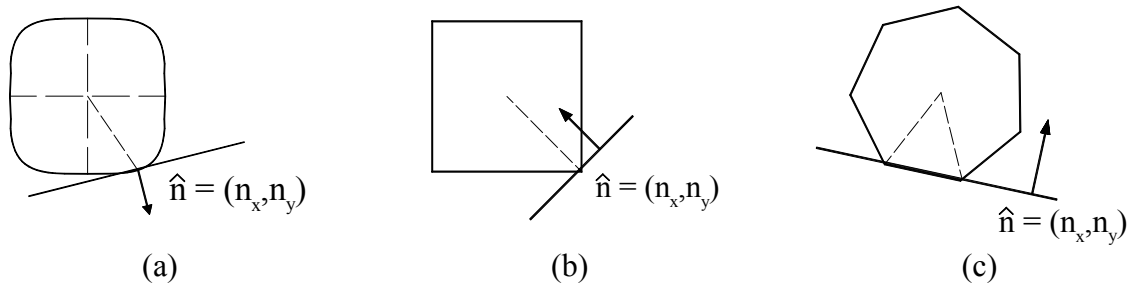


Figure 5.9: Object segment contact points in the object's local coordinate system: (a) Superellipse-segment contact point, (b) polygon-segment corner contact, and (c) polygon-segment side contact when two contact points exist.

Polygon - segment: A polygon may contact a segment in two different ways: side contact or corner contact. Figure 5.9b shows the polygon-segment corner contact which occurs when a corner penetrates into a segment. In Figure 5.9c a polygon is contacting a segment on a side, which occurs with the penetration of two nodes into a segment. In this case an object contacts a surface at a relatively low angle; however, this situation occurs rarely, especially using the time refinement procedure. For the sake of completion, the option of side contact in the case of one corner contact when the side has a low angle is also provided, Figure 5.10a.

5.3.2.4 Object-corner contact

There are a lot of difficulties in finding the object-corner contact point and calculating the normal vector. Actual slopes do not have sharp corners, usually there is a gradual variation from one surface inclination to another. Defining a curvilinear approximation, instead of using sharp corners, results in smoother variation in the rebound parameters; however, this is not defined in this simulation as it is less conservative and, besides, it is computationally more expensive.

Corner contact occurs for the ellipsoidal group of shapes, shown in Figure 5.10b, when one of the segment nodes lays inside the object, which results in $F(x_c, y_c) < 0$, where F is the

function defined by Equation (5.3.1). In this case, the contact normal vector for superellipses is the object gradient vector, $\hat{n} = \nabla F(x_c, y_c)$, where $P_c = (x_c, y_c)$ is the corner coordinate.

Figure 5.10c depicts corner contact for polygonal shapes in flat side contact and simple corner contact situations. The normal vector is always perpendicular to polygon side.

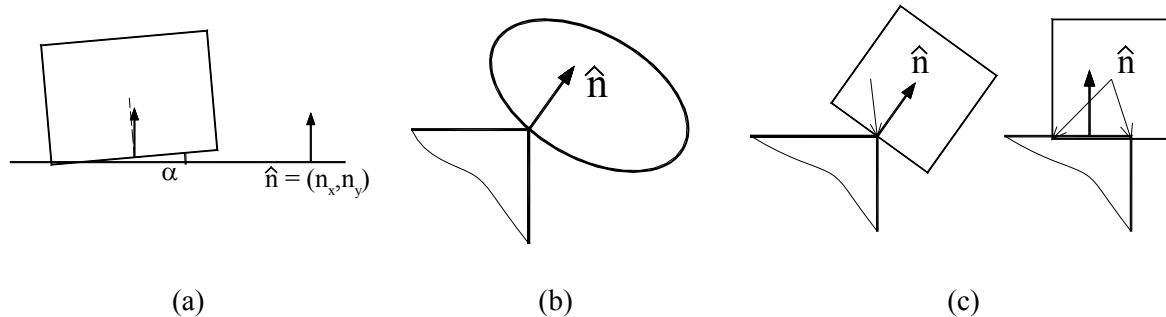


Figure 5.10: (a) Polygon side contact happening at low angle of impact, (b) object-corner contact for superellipses, (c) object-corner contact for polygons.

5.3.2.5 Back transformation

The local contact point will be transferred back to the global coordinate system using reverse transformations, by an opposite succession of matrix multiplications: $P = T_S(a, b)T_R(\theta)T_T(x_0, y_0)P'$. The transformation matrices (T_S , T_R , T_T) are defined by Equations (5.3.2) and a , b , θ , x_0 , and y_0 are defined in Section 5.3.2.2.

5.4 MISCELLANEOUS SIMULATION ASSUMPTIONS

In the following sections some miscellaneous assumptions performed in *GeoRFS* are reviewed.

5.4.1 Time domain formulation

A suitable time domain integration method is needed to integrate the differential equations of motion. In the rolling-sliding mode, the object is in continuous contact with the surface and the acceleration vector varies continuously. Using trapezoidal time integration makes the

calculation stable, permits having a larger time step, and prevents the object from increasingly penetrating into the surface, following the impenetrability condition more rigorously. By deriving the translational and rotational acceleration from the equation of motion, the velocities and translations can be defined using Equation (5.4.1).

$$\begin{aligned}
 v_i^{t+\Delta t} &= v_i^t + \Delta t (a_i^t + a_i^{t+\Delta t}) / 2 \\
 \omega_2^{t+\Delta t} &= \omega_2^t + \Delta t (\alpha_2^t + \alpha_2^{t+\Delta t}) / 2 \\
 x_i^{t+\Delta t} &= x_i^t + v_i^t \Delta t + \Delta t^2 (a_i^{t+\Delta t} + a_i^t) / 4 \\
 \theta_2^{t+\Delta t} &= \theta_2^t + \omega_2^{t+\Delta t} \Delta t + \Delta t^2 (\alpha_2^{t+\Delta t} + \alpha_2^t) / 4
 \end{aligned} \tag{5.4.1}$$

where $i=1, 3$ refers to the perpendicular axes in the Cartesian coordinate system, v_i and ω are translational and rotational velocities, a_i and α are translational and rotational accelerations, x_i is the object's position, θ is the orientation angle, and Δt is the timestep. The superscript, t , refers to the time step at which the integration is being performed.

Unlike discrete or continuum models, in rigid body impact mechanics, the collision occurs in infinitesimal time. As a result the collision time is considered zero and the rebound velocities are calculated explicitly. Freefall motion is modeled using a simplified version of Equation (5.4.1).

5.4.2 Multiple contacts manipulation

There are situations when an object collides with the impact surface at more than one contact point, as shown in Figure 5.11a; however, this does not commonly occur, as the time step in which the impact occurs is small and the impact configurations are not usually symmetric. In contrast, the impact of a rolling or sliding object with another surface occurs regularly, as shown in Figure 5.11b. Since the utilized impact models are developed for a single impact point, some ad-hoc rules are invented which can manipulate multiple contacts. The two common cases are: an object having multiple impacts, and a rolling object impacting a second surface.

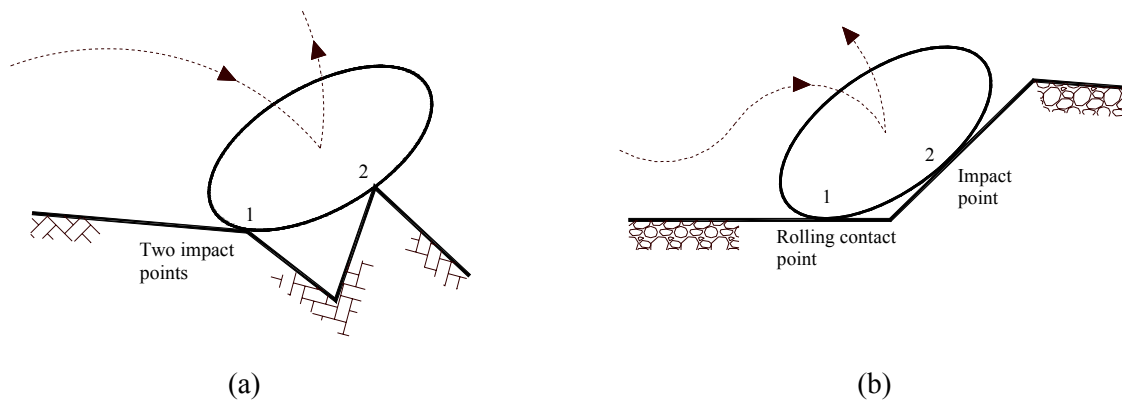


Figure 5.11: Multiple contact points in one time step: (a) multiple impact points, and (b) one rolling contact point and one impact contact point.

5.4.2.1 Multiple contacts: all impact modes

Figure 5.11a shows a rock impacting a contact surface at two impact points; here two corners. Since in real rock surface modeling this scenario is not very realistic, as the rock always hits one corner earlier, the simulation randomly chooses one of the contact points as the target contact point.

5.4.2.2 Multiple contacts: rolling with impact

Figure 5.11b plots the impact of a rock which was originally rolling on a rigid half surface. By convention, the effective mode of contact in this case is the impact mode, since the rock is in equilibrium during the rolling period. As a result, the rebound velocities are calculated based on the impact contact point(s).

5.4.3 Defining contact mode: impact mode versus rolling-sliding mode

When the contact normal velocity, $v_{c,n}$, approaches zero, the contact mode transfers from impact to the rolling-sliding mode. Numerically, defining a threshold velocity, defined by the modeler, is necessary. This velocity can be:

$$v_{c,n} < v_{roll,tr} \Rightarrow \text{rolling-sliding mode initiates} \quad (5.4.2)$$

where $v_{roll,tr}$ is the rolling threshold velocity and is recommended to be chosen between 0.1 to 0.5 m/s.

5.4.4 Overlap treatment in impact mode

In this simulation, a contact occurs when an object intersects a surface, as shown in Figure 5.9. In other words, in addition to the contact point, some parts of the object penetrate into the impact surface. In low normal contact rebound velocities, the contact may not be terminated by the rebound velocities, thus the object stays in contact with the surface. In this case, the normal velocity is also greater than the rolling threshold velocity required to enter the rolling mode. This situation occurs when:

$$\hat{v}_{c,n} \cdot \hat{n} < (\hat{g} \cdot \hat{n}) \cdot \Delta t \quad (5.4.3)$$

where $v_{c,n}$ is the contact normal velocity, \hat{n} is the contact normal vector, \hat{g} is the gravity vector, and Δt is the timestep. To eliminate the overlap numerical problem, the object is moved in a direction opposite to the contact normal vector. Assuming the timestep is very small, the energy violation, as a result of an increase in potential energy, can usually be ignored.

5.4.5 Critical timestep criteria

In discrete or explicit computational methods, the stability of the model is based on the timestep, and the solution produced by the governing equations will remain stable only if the timestep does not exceed a critical timestep, which is related to the minimum natural frequency of the total system. In contrast, the stability in the simulation proposed in this work is independent of the timestep as the equations defining the rebound velocities are time-independent and are a function of the contact impulse. However, the timestep affects the accuracy by perturbing the accurate contact position; consequently, a larger timestep leads to unsatisfactory rock trajectory prediction.

In this work, it is important to define the timestep accurately. Hence, the object-surface overlap or penetration should be decreased to a definite critical value. This overlap depends on several parameters, including: the maximum rock dimension, the translational and rotational velocities of the rock, and the slope complexity. The maximum timestep, Δt_{\max} , for

an object, with maximum dimension, D_{max} , and translational and rotational velocities equal to V and ω , is suggested to be:

$$\Delta t_{max} = f \frac{D_{max} / \beta_{dfn}}{|V| + |r\omega|} n_{fractions} \quad (5.4.4)$$

where β_{dfn} is the diameter fraction number which results in the maximum acceptable overlap, suggested to be 100, resulting in a maximum overlap equal to 1% of the diameter; $n_{fractions}$ is the number of secondary timestep refinements; and f is the safety factor, usually between 0.7 and 0.8 as also recommended in *PFC^{2D}* manual.

5.4.6 Arrest (termination) criteria

The arrest terminology was originally used by Descouedres et al. (1987) to indicate a termination or stop in the rockfall simulation where the rock shape allows a stable static equilibrium. This state of equilibrium can be reached only for polygonal objects when an object has the ability of resting on one edge, in contrast to ellipsoidal objects where the arrest mode always occurs with oscillation around the contact point. In rigid body modeling, the sources of energy dissipation are: plastic deformation at the impact point which is integrated in the energy COR, e_* ; frictional dissipation which results from the opposing force during sliding; frictional dissipation in rolling-sliding mode; and the rolling-friction dissipation resulting from the eccentricity of the normal contact force. Hybrid models like CRSP[®] or RocFall[®] identify the stop point based on a low velocity criterion in sliding mode, which is defined by users.

In this work, arrest is used to indicate that the object has lost a considerable portion of its energy, definable by the modeler, while kinetically the object can not accelerate. This state depends on the object's geometry, its translational and rotational velocities, the inclination of the contacted surface, and the contact material frictional properties. The model must arrest the moving object accurately, otherwise the object is terminated in the model while, in reality, it can roll out significantly further. The arrest usually occurs during rolling-sliding mode, as a result, mathematically, the arrest criteria can be written as follows:

$$\left\{ \begin{array}{l} (V_t^2 + V_n^2) + k_r^2 \omega^2 < V_{arrest}^2 \\ \alpha < 0 \\ \gamma_{slope} < \tan^{-1}(\mu) \end{array} \right. \quad (5.4.5)$$

where V_t and V_n are the tangential and normal object velocities, k_r is the polar radius of gyration, ω is the rotational velocity, V_{arrest} is the threshold cut-off velocity, suggested to be between 0.5 to 1.0 m/s (also recommended by Stevens (1998)); α is the angular rotational velocity defined in Section 4.1; γ_{slope} is the slope inclination; and μ is the contact friction coefficient.

5.4.7 Modeling pseudo-code

A simplified version of the pseudo-code, applied in the *GeoRFS* simulator, is presented in Table 5.3. This pseudo-code is based on the time-driven methodology and traces the rock trajectory from the creation instance to the arrest.

Table 5.3: The simulation pseudo-code applied in the *GeoRFS* engine

generate a rock and a slope based on the settings and the statistical distribution
define the optimum time step
iterate through timestep
iterate through walls and barriers
perform contact search
create a contact object with the configurations
create the local coordinate system, vectors and trajectories
set contact mode (impact, rolling)
randomly generate the material property from the statistical distribution
add the contact to the contact list
treat contacts penetrations
loop over contacts and choose the effective contact
compute rigid body rebound velocities
map velocities and accelerations back to global coordinate system
roll or move the object
check truncation (arrest)
stop

5.4.8 Programming language used

The simulation program *GeoRFS* is written using the C++ language in Visual Studio .NET 2003[®], using Object Oriented Programming (OOP) techniques. The graphical user interface (GUI) is designed using .NET Form Menu facilities. A series of windows set the rock initial parameters and the simulation initial settings. As an example, the sample window for superellipse properties is shown in Figure 5.12a. Each rock shape is given a unique window. The output picture-box plots the rock geometry, which results from the path of the rock, in addition to the slope trajectory, which is read from an input file. The rebound velocities and energies are shown in an output text-box. This is useful in order to check the energy and velocity values after certain impacts. Figure 5.12b shows the trajectory of a rock and the different rock energies.

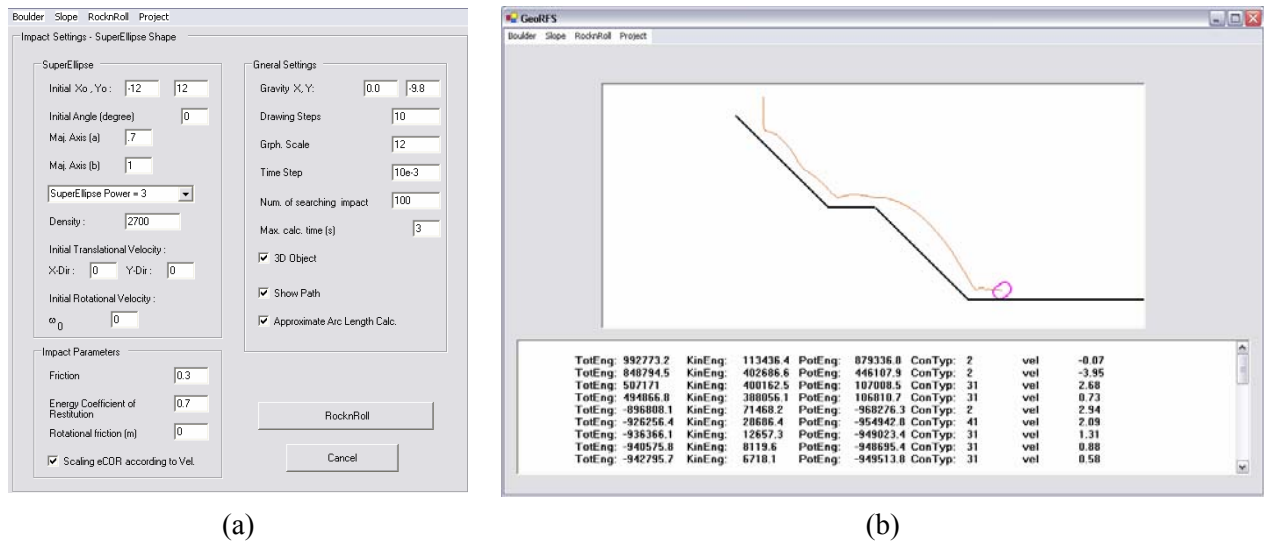


Figure 5.12: *GeoRFS* graphical user interface (GUI): (a) typical input menu for a superellipsoid, and (b) typical output window showing the impact of the rock with a typical slope.

5.4.9 UML diagram of the simulation implementation

Objects in the real world share two characteristics: state and behavior. In OOP, the classes are the main unit of programming, describing a set of objects with common attributes, operations, semantics, associations, and interactions. As a result, an object, as an instance of a class, contains both the attributes and operations representing state and behavior. Using

objects in a program may provide a lot of facilities including: encapsulation, data hiding, inheritance, code reuse, plug-ability, debugging ease, and polymorphism (Deitel et al. (2001)).

In order to show the classes and their interactions in *GeoRFS*, a powerful diagrammatic tool called the Unified Modeling Language (UML) is used. These models represent the main classes and the interactions among them (Bennett (2002) and Peters (2002)), as shown in Figure 5.13. As the classes in the model are complicated and contain many attributes and operations, only the class names are presented here.

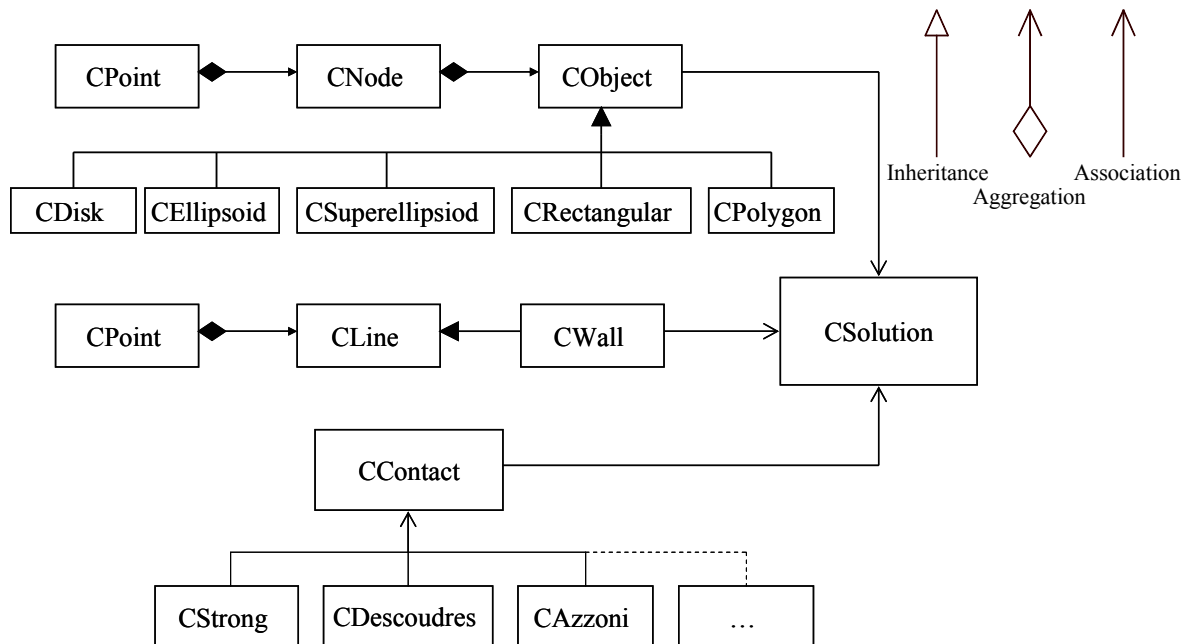


Figure 5.13: UML representation of the main simulation classes used in *GeoRFS* in addition to the class relationship legend.

The most important classes included in this simulation are: *CObject*, *CWall*, *CContact*, and *CSolution*. In *CObject*, the main attributes and methods for all of the objects are provided. All the geometries, used as rock representations, are inherited from this main class. *CLine* is the class which defines the geometries of a segment and is a parent class to *CWall*, which defines the slope segments with the material behavior. A *CContact* object instantiates when an object intersects with a wall or a wall corner. At this time, two pointers are introduced pointing to the intersecting objects, with the *CContact* object borrowing the contact

characteristics from these objects. Different impact models can be associated with the *CContact* by introducing them as definite classes. Here, the three impact models introduced in Chapter 4 (Stronge (1994a), Descouedres (1987), Azzoni (1995)) are defined as three different classes. *CSolution* performs the interactions and message transfers between the classes in addition to other essential operations including: contact search, arrest check, contact mode setting, overlap manipulation, and defining the local coordinate system and vectors.

5.5 IMPLEMENTATION OF *GeoRFS* IN RocFall[®] RESEARCH VERSION

The Object-Oriented engine of *GeoRFS* is implemented, with the author's help in both the implementation and debugging stages, in the research version of RocFall[®] by Rocscience[®]. RocFall[®] benefits from a robust OOP design in addition to a redesigned graphical user interface. The new interface provides several facilities including: easy geometry definition, either by a drawing tool or by data entry; various probabilistic seeder definitions; straightforward barrier and data collector design tools; robust probabilistic material definition; sophisticated probabilistic rock shape editor; descriptive animation control boxes; and powerful output data graphs and charts in addition to the output data files. Figure 5.14 shows the RocFall[®] graphical user interface while modeling a highway passing through a mountainous area.

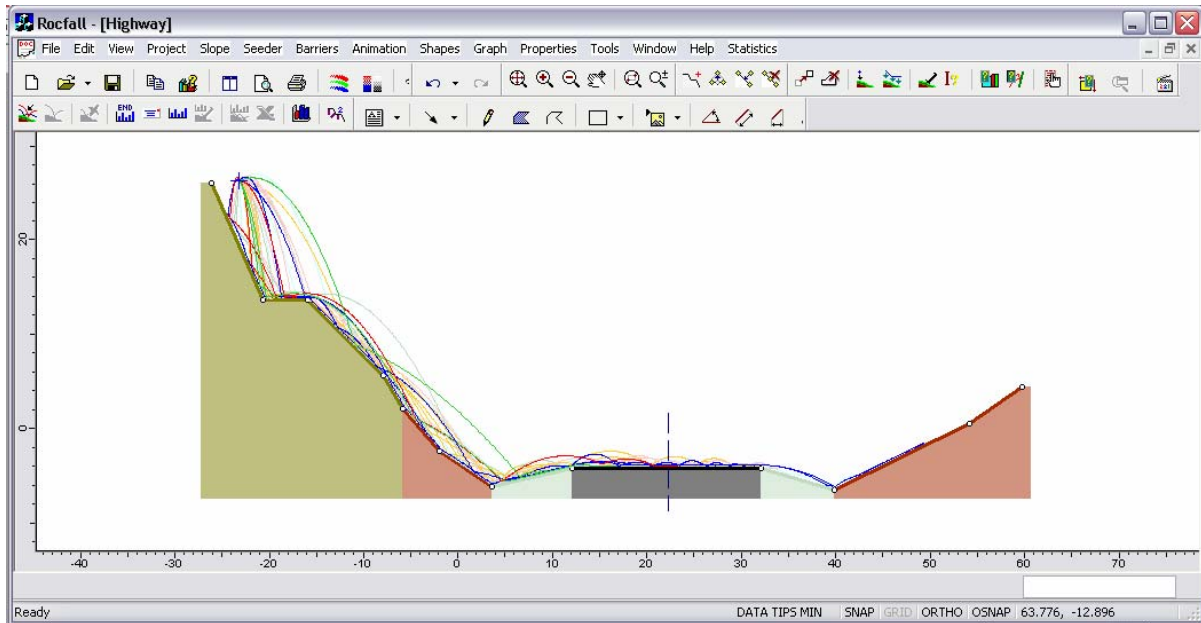


Figure 5.14: The RocFall[®] research version graphical user interface simulating a highway slope.

Three different input menus in RocFall[®], directly affected by the *GeoRFS* and its geometrical innovations, are reviewed in the following sections. These key windows are: seeder property, material property, and rock geometry editor.

5.5.1 Seeder Properties Window

In the Seeder Properties Window, in addition to the location, the user has control over several parameters. The properties which complete the features of *GeoRFS* are: probabilistic distribution for the initial vertical, horizontal, and rotational velocities; and probabilistic distribution for the rock initial orientation, as shown in Figure 5.15. Moreover, this window enables the user to choose the rock geometries. In the project settings, it is also possible to choose the number of random rock generations either per rock geometry or per a collection of different rocks. By using the mentioned facilities, the study of rockfalls of either a single rock shape or as a collection of different rock geometries becomes feasible. Such studies are performed in Chapter 6.

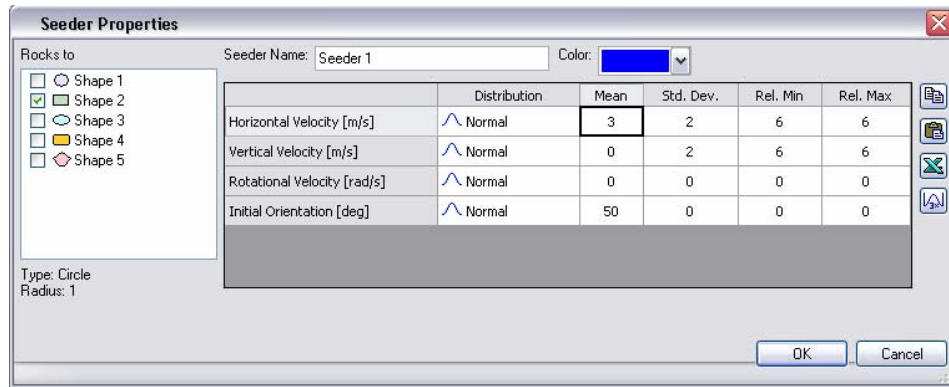


Figure 5.15: The seeder property window in RocFall® research version.

5.5.2 Material Property Window

In the Material Properties Window, multiple material tabs are provided which enable the introduction of several materials to the model, this is shown in Figure 5.16. For each material type, there are several list boxes which allow the definition of a statistical distribution model for the different properties. For each distribution, the mean, standard deviation, and relative maximum and minimum are definable based on the distribution type.

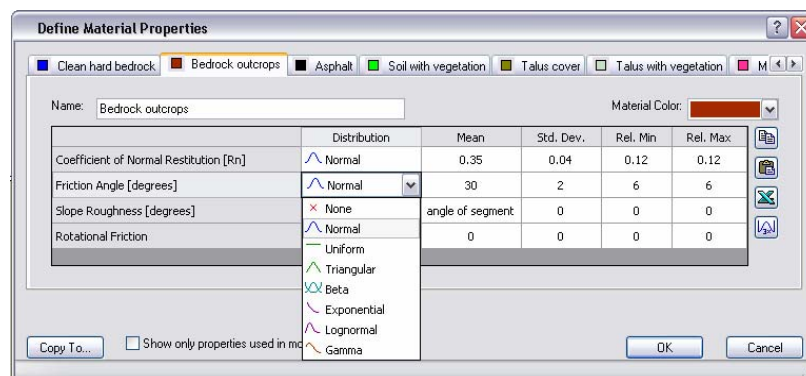


Figure 5.16: The Material Property Window in RocFall® research version.

5.5.3 Rock Shape Editor Window

The Shape Editor Window, as shown in Figure 5.17, provides the ability to edit the rock geometry that is specified for a seeder. The following shape categories may be chosen in this window: circular, ellipsoidal, superellipsoidal, uniform polygonal and random polygonal. The major and minor dimensions of these shapes, using different distribution models, must

be defined. In addition, superellipsoids' power and the number of sides for polygons can be set. The variation of rock mass density can usually be ignored when compared to other variables; therefore it is considered constant, and not adjustable by the application.

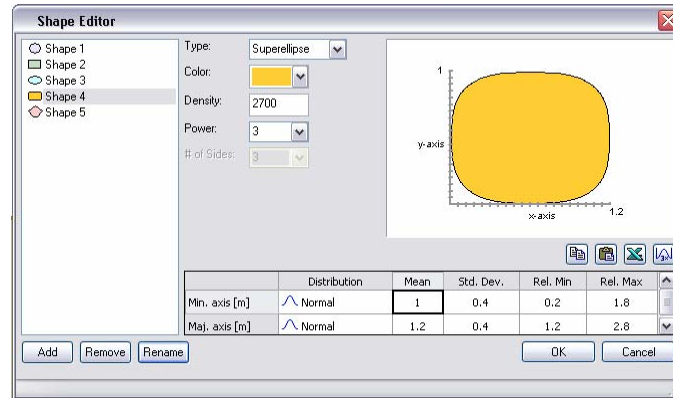


Figure 5.17: The shape editor window in RocFall® research version showing the superellipse case.

There is a feature which allows random polygon generation, requiring two initial settings: first, the total mass of the rock, and second, rock side numbers. Based on these two characteristics, the simulation produces a convex polygonal rock with definable thickness and with the specified mass and side numbers.

5.6 SUMMARY

- In this Chapter, a computer program, *GeoRFS*, which can successfully simulate rockfall phenomenon is described. This program is based on rigid body mechanics (RBIM).
- The modeling of complicated rock geometries in *GeoRFS* is limited mainly by the ability to find the point of contact of the falling rock with the slope.
- Although RBIM is the primary impact model used in *GeoRFS*, the other impact models by Descouedres et al. (1987) and Azzoni (1995) are also implemented in the program.
- The geometric transformation contact search procedure in *GeoRFS* demonstrated a robust performance in defining the contact points.

- Despite the fact that only simple optimization procedures were used in *GeoRFS*, running time of the application was quite satisfactory for use in practical engineering applications. This is in contrast to Discrete Element Modeling (DEM) programs, which are dramatically slower.

CHAPTER 6

RIGID BODY IMPACT MECHANICS IN ROCKFALL ANALYSIS: APPLICATION AND VERIFICATION

6.1 INTRODUCTION

In this chapter the application of rigid body impact mechanics (RBIM) to rockfall analysis is investigated. Both the *GeoRFS* and RocFall[®] research version simulations are used based on the facilities provided in their output data manipulations. The RocFall[®] research version is highly sophisticated in that it uses probabilistic analysis to provide different charts and figures, while *GeoRFS* uses deterministic analysis to provide easy output data files. Using these simulation programs, the effects of multiple impacts on rebound parameters and the object trajectory for rocks with different geometries on horizontal and inclined surfaces are investigated. These rebound parameters can be listed as: roll-out distances, height of bounces, retrieved energies, and rotational and translational velocities. The field observations provided by Pierson et al. (2001) (Oregon Department of Transportation (ODOT)) are modeled using RocFall[®] research version and rebound parameters are compared with the simulation output data.

6.2 EFFECT OF ROCK GEOMETRY ON MULTIPLE IMPACTS

In Chapter 4, the rebound parameters of a single impact of a rock with a rigid half space were studied. In this section, the time parameter is added into the analysis, providing the possibility of studying the effects of multiple impacts of a rock on energy dissipation, roll-out distance, and bounce height. Formerly, it was shown that in addition to the material properties, the rock shape, impact angle, and the mass distribution around the contact point have a dramatic effect on the rebound energies and velocities. These studies must be extended with additional studies which investigate the effect of the mentioned properties on the rebound parameters during multiple impacts.

In the literature, it is common to model complicated slopes. Researchers are accustomed to comparing the model output results with field observations without attempting to address the effect of rock geometries or impact configurations on the model results. In this work, several numerical experiments are executed in order to investigate the effect of these parameters on the rock trajectories through multiple impacts. The experiments are performed ordered from the simpler tests to more complicated situations, based on the number of impacts, slope inclination, the material properties, and the rock slenderness.

6.2.1 Equivalent object convention

Objects which have equal cross sectional area or volume (weight) are assumed to be equivalent. All of the numerical investigations which follow are performed on the rebound parameters of a group of equivalent objects. In this work, all the rock geometries with different aspect ratios have the same volume as a sphere with radius of 1 m. These dimensions are illustrated in Table 6.1.

Table 6.1: The dimensions for different equivalent geometrical shapes

<i>Ratio</i>	<i>Ellipsoid power 2</i>		<i>Ellipsoid power 4</i>		<i>Prism with a rectangular cross section</i>	
	<i>a</i>	<i>b</i>	<i>a</i>	<i>b</i>	<i>a</i>	<i>b</i>
<i>1:1</i>	1	1	0.866	0.866	0.806	0.806
<i>1.2:1</i>	1.129	0.941	0.978	0.815	0.910	0.758
<i>1.5:1</i>	1.310	0.874	1.134	0.756	1.056	0.704
<i>2:1</i>	1.587	0.794	1.374	0.687	1.279	0.640
<i>3:1</i>	2.080	0.693	1.801	0.600	1.677	0.559

6.2.2 Double-impact numerical test

Numerical impact tests, as defined in Figure 6.1, are used to study the rebound parameters resulting from the impact of an object on horizontal and inclined rigid half spaces. For material parameters, in order to be consistent with the tests performed in Chapter 4, e_* is chosen to be 0.5 and the friction coefficient is chosen to be $\tan(30^\circ) = 0.58$. These values represent typical material properties for rock impact. The tests are run under gravitational forces, therefore the rock initial position is important in the final results. As a result, the rock center is located at a vertical distance of 3.0 m from the surface and is projected at a vertical velocity of -10 m/s, while the tangential velocity is variable, equal to either 0 or 10 m/s.

In Chapter 4, it was shown that the object orientation and impact angle strongly affects the rebound parameters. As shown in Figure 4.9, the definitions of low, intermediate, and high impact angles are not only a function of the ratio of tangential to normal contact velocities but also a function of variation of rock mass distribution around the contact point, or initial orientation. For dimensionless objects, the rock orientation does not affect the rebound velocities, while in geometrical modeling it can dramatically change the rebound velocities; therefore, we focus our attention to the rock orientation on the contact as the main variable. For all the results, kinetic energy is replaced with total energy. The object velocities at the contact point during different orientations are variable, and therefore the kinetic energies are also variable. As a result, to compare energies during successive impacts, total energies are used instead of kinetic energies.

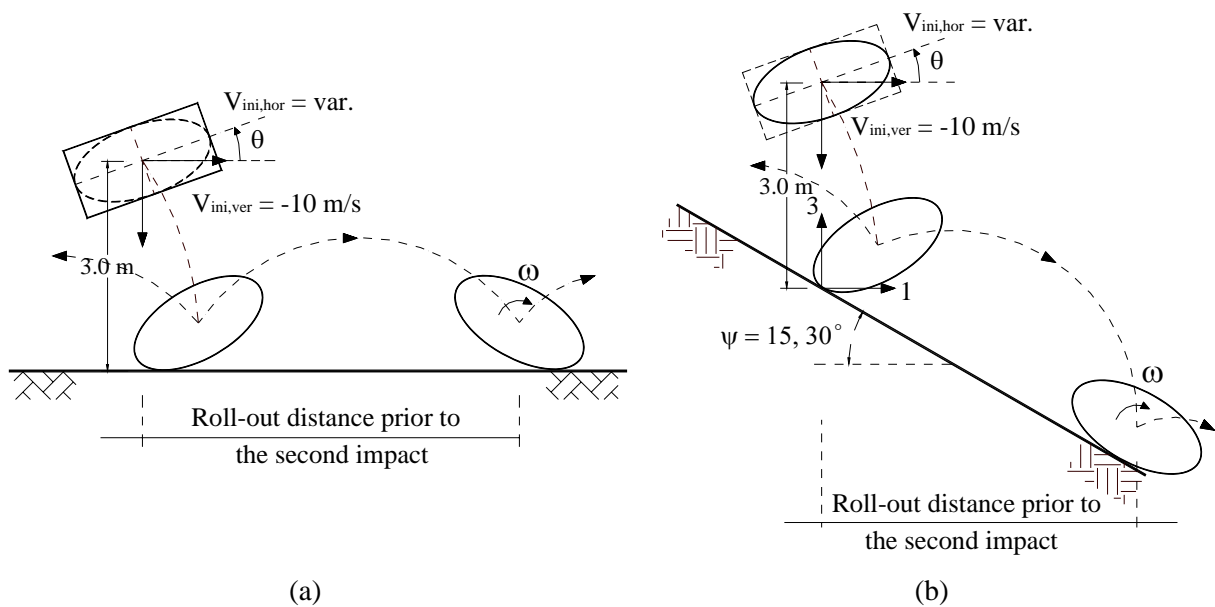


Figure 6.1: Double impact of different geometrical objects on a rigid half space at different orientations with $V_{ini,ver} = -10$ m/s located at a vertical distance equal to 3.0 m on: (a) horizontal plane, and (b) inclined plane, here 15° and 30° .

It should be mentioned that in this chapter a *rectangle* means a prism with a rectangular cross section and *ellipsoid-2* and *superellipsoid-4* means an ellipsoid with power 2 or 4 with the closed-form Equation (5.2.1).

6.2.2.1 Double impacts on a horizontal plane – 0° impact

Figure 6.2 plots the variation of the rebound parameters versus initial orientation with the initial settings of Figure 6.1a for ellipsoidal objects with powers of 2 and 4 and a prismatic object with a rectangular cross section. All these objects have an aspect ratio of 2:1 and are projected with an initial horizontal velocity of zero. Therefore, all these objects have the same initial total energy.

Figure 6.2a depicts the variations of the ratio of retrieved total energies to the initial total energy after the second impact. This figure shows that the trends of variations of the retrieved total energies for the three objects are approximately similar. As shown in Figure 4.16, the rectangular object has the highest retrieved energy after the first impact for the orientation angles between 0 and 25° , and 165 to 180° . However, this figure shows that after the second impact rectangular objects lose more energy in comparison to ellipsoidal objects. In addition,

it can be seen that ellipsoid-4 has the highest average ratio of retrieved energy of 0.34, while a rectangle has the lowest average ratio of 0.29. This is in contrast to the case of the first impact, where a rectangle had the highest average retrieved energy, underlining the importance of considering a chain of impacts rather than a single impact.

Figure 6.2b plots the variation of the ratio of normal velocity after the second impact to the initial normal velocity. Ellipsoid-4 has the highest rebound velocity followed by the rectangle. However, on average, ellipsoid-2 has the highest average, equal to 0.29, when compared to the rectangle, equal to 0.25. Rectangle and ellipsoid-4 still have negative normal velocities at some initial orientation angles, showing the possibility of a third successive impact.

Figure 6.2c plots the variation of roll-out distances for the three objects. The rectangle and ellipsoid-4 have a relatively small amount of roll-out distance for small and large orientation angles, as they experience an immediate second impact. In contrast, at these orientations, ellipsoid-2 experiences a large amount of roll-out distance with the values up to 3.2 m to the left or right. Between the orientations of 60° and 90° , the ellipsoids are moving in the positive direction, while the rectangular object is projected to the left (the negative direction), emphasizing a different trend of displacement variation for the three objects which results from the presence of corners in the rectangular object. Generally, the displacements experienced by ellipsoid-4 are between the displacements experienced by the two other objects. Figure 6.2c also shows that the maximum amount of roll-out distance is the same for all three objects, although occurring at different orientations.

Figure 6.2d plots the maximum heights of bounces for the objects between the first and second impact. The maximum height for all three objects occurs when the impact is centric at 90° . Ellipsoid-2 has the highest maximum bounce height as it has larger dimensions, as shown in Table 6.1; however, the rectangular cross section has the highest average, equal to 2.06 m, in comparison to the ellipsoid-2 bounce height equal to 1.98 m. These values, in addition to the shape of the variations, show that the heights of the bounces have approximately the same trend of variation as each other, while the shape of the variation is a function of the objects' geometry.

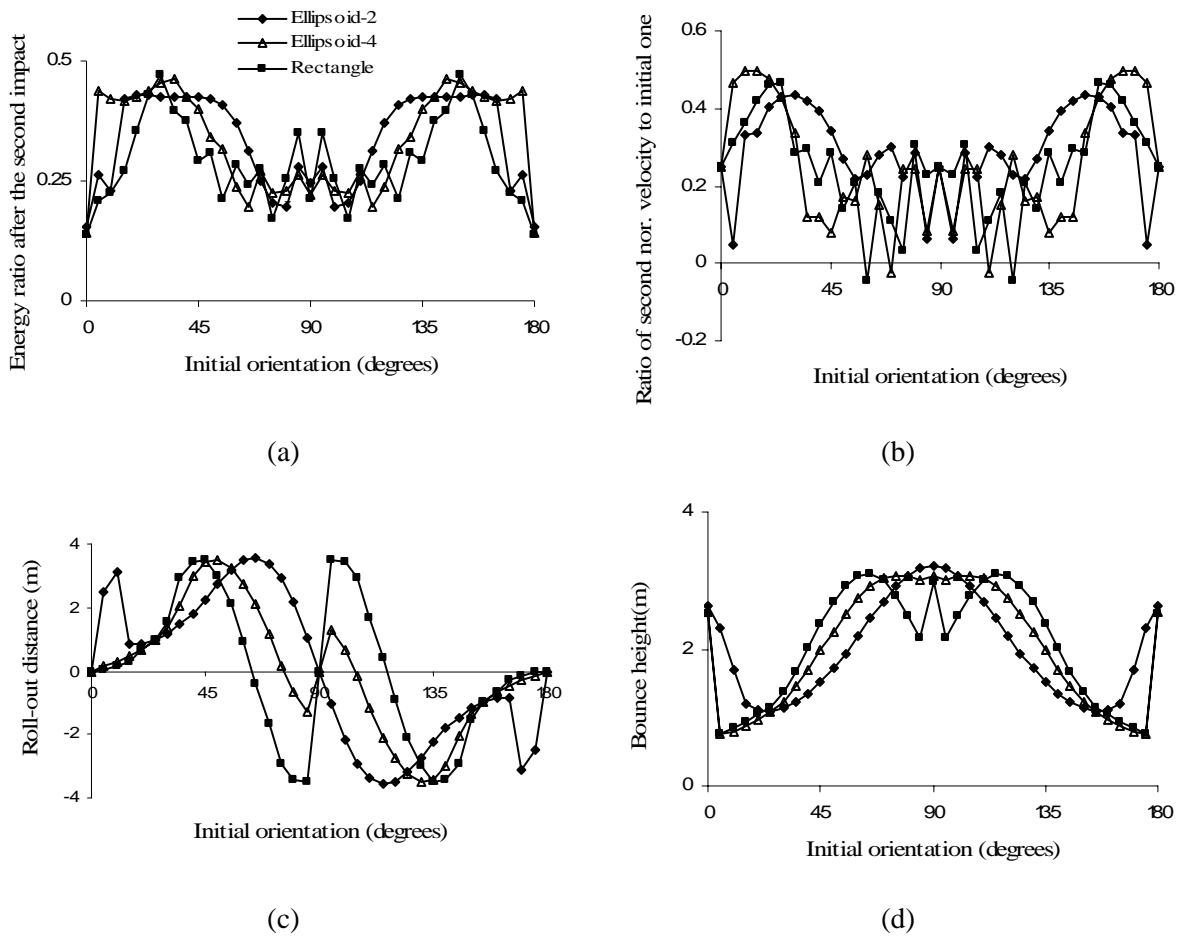


Figure 6.2: Variation of the rebound parameters versus object initial orientation for planar impact of different geometrical objects with the configuration of Figure 6.1a and horizontal velocity equal to zero (impact angle of 0°): (a) ratio of the retrieved total energy to the initial total energy after the second impact, (b) ratio of the second normal rebound velocity to the initial normal velocity, (c) roll-out distances of object up to the second impact, and (d) maximum height of bounce after the first impact.

6.2.2.2 Double impacts on a horizontal plane – 45° impact

Figure 6.3 plots the variation of the rebound parameters versus initial orientation for objects thrown at an angle of 45° . These experiments have the same configurations as the experiments described in Figure 6.1a. The objects used are ellipsoids with powers of 2 and 4 and a prism with a rectangular cross section. All the objects have an aspect ratio of 2:1 where the dimensions are defined in Table 6.1, and are projected with the initial horizontal velocity equal to 10 m/s and with equal initial total energy.

Figure 6.3a plots the variation of the ratio of retrieved energies after the second impact to the initial energy for different objects. The rectangle has the highest retrieved energy among all objects; however, the rectangle's maximum ratio is very close to the maximum value derived for ellipsoid-2. On average, ellipsoid-2 has the highest ratio of retrieved energy after the second impact, with the value equal to 0.35, in comparison to the rectangular section with a value of 0.30 after the second impact, while ellipsoid-4 has an average ratio equal to 0.33. In Figure 4.17, it is shown that the rectangle has the highest retrieved energy after the first impact; however, this figure shows that because of the second immediate impact, the rectangular prism loses a considerable amount of its energy.

Figure 6.3b plots the ratio of the objects' normal velocities after the second impact to the initial normal velocity. The ellipsoid-2 has the highest ratio while, on average, ellipsoid-4 has the highest value, equal to 0.41. The ellipsoid-4 also has an average ratio equal to 0.40 and the rectangle has the lowest value of 0.36. This figure shows that, for lower initial orientation angles, the objects' negative normal rebound velocity changes to a positive value after the second impact.

Figure 6.3c illustrates the variation of horizontal roll-out distances for the three objects. At low orientation angles, all three objects experience the second impact immediately after the first impact; therefore, they do not experience significant displacement. At medium orientations, from 45° to 60° , the rectangle has the highest roll-out distance and ellipsoid-2 has the lowest. The average of the 36 orientation angles shows that the ellipsoid-4 object has the highest average roll-out distance, with a value of 5.6 m, while the ellipsoid-2 object has an average roll-out distance equal to 4.6 m. On average the rectangle rolls out 5.2 m, higher than the ellipsoid-2.

Figure 6.3d depicts the maximum bounce height for objects between the first and second impact. The ellipsoid-2 has the maximum bounce height and the largest average bounce height; however, the differences between the values of bounce heights for the objects are not significant. Generally, the three objects have the same trend of variation, except for the effects of corners, which are apparent around the orientations of 0° and 90° .

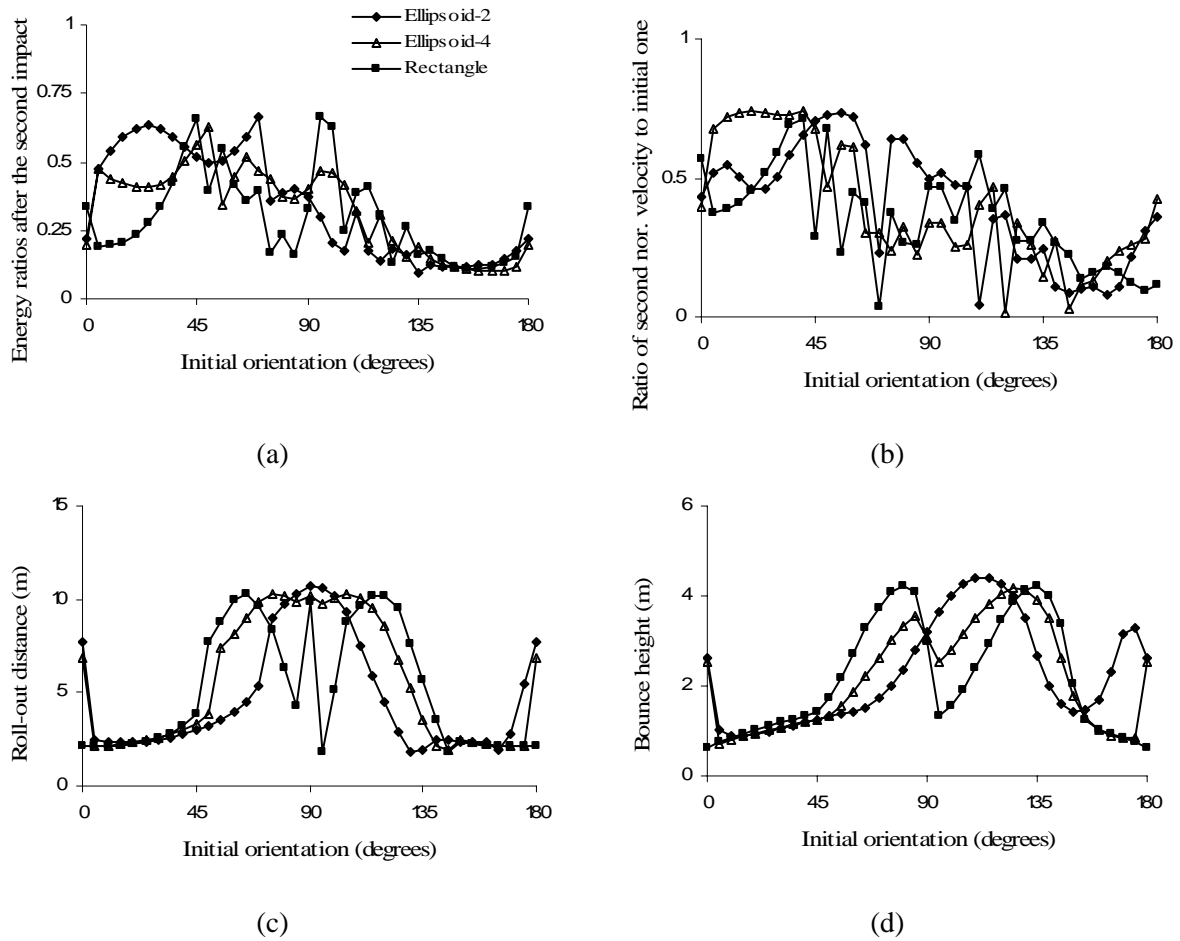


Figure 6.3: Variation of the rebound energies and displacements versus object initial orientation for planar impact of different objects at the impact angle of 45° with the configuration of Figure 6.1: (a) ratio of the retrieved energy to the initial energy after the second impact, (b) ratio of the second normal rebound velocity to the initial normal velocity, (c) horizontal displacement of object until the second impact, and (d) maximum height of bounce after first impact.

6.2.2.3 Double impacts on an inclined plane – 0° impact angle

To produce the first examples of impacts on an inclined surface, in this section the rebound parameters of the double impacts of three objects are examined. These impacts use the objects and configurations of Figure 6.1b. The rebound parameters for these experiments are plotted in Figure 6.4. The horizontal velocity is set to zero and the object is shot 36 times, varying each time by 5° , at a surface with an inclination of 30° . All the objects have an aspect ratio of 2:1 and have dimensions as defined in Table 6.1.

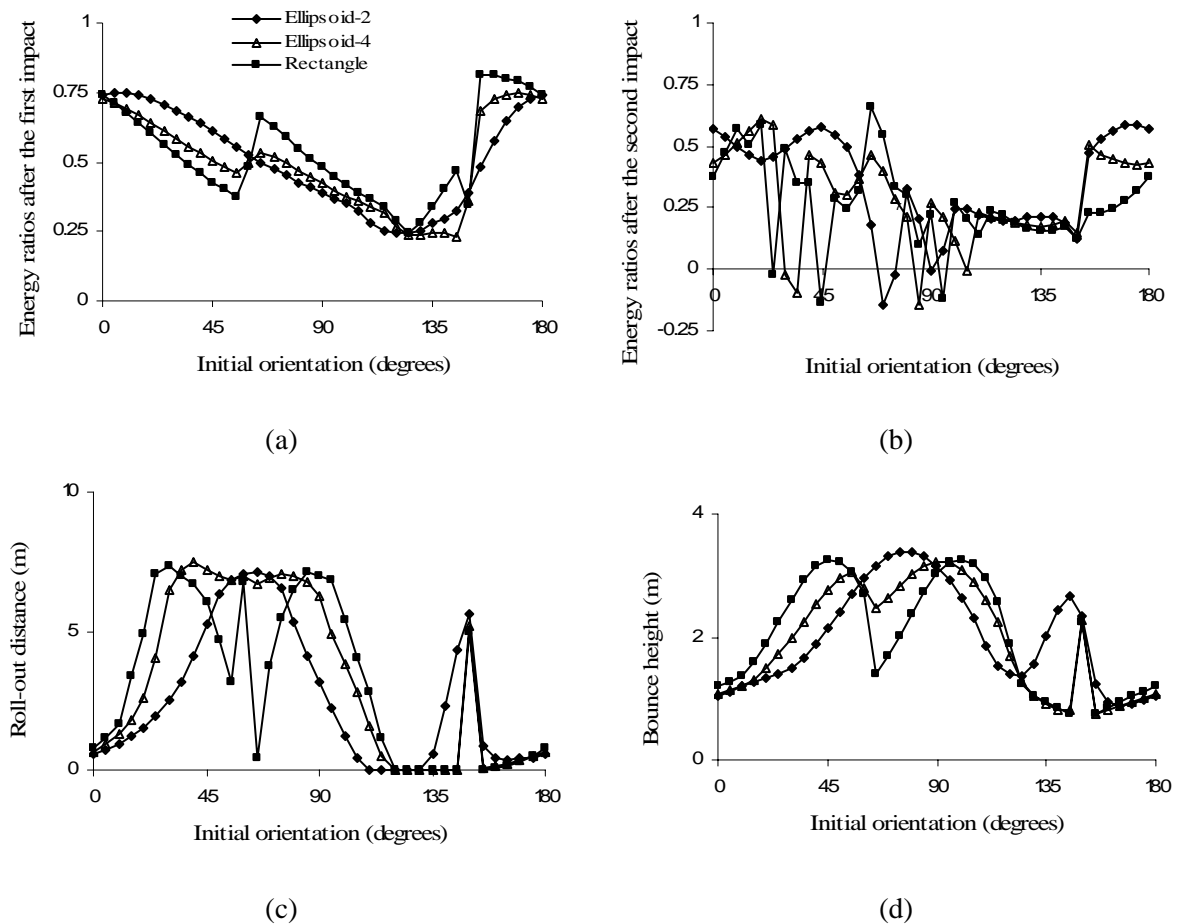


Figure 6.4: Variation of the rebound energies and displacements versus object initial orientation for planar impacts of different objects at the impact angle of 0° ($V_{ini,hor} = 0$ m/s) at a surface with an inclination angle of 30° with the configuration of Figure 6.1b: (a) ratio of the retrieved energies to the initial energy after the first impact, (b) ratio of the retrieved energies to the initial energy after the second impact, (c) horizontal displacements prior to the second impact, and (d) maximum height of bounce after the first impact (normal distance to the plane).

Figures 6.4a and 6.4b plot the variation of retrieved total energies versus orientation after the first and second impacts for different objects. The largest retrieved energies after the first and second impacts belong to the rectangle. On average, after the first impact, the rectangle has the highest ratio of retrieved energy (0.52) when compared to the ellipsoid-2 (0.50). After the second impact, the ellipsoid-2 has the highest ratio equal to 0.34 while the rectangle has the lowest ratio, equal to 0.27. This shows that the rectangle loses a considerable portion of its energy after the second impact, in contrast to the ellipsoid-2, which retains more of its energy.

Figure 6.4c depicts the roll-out distances prior to the second impact for the different objects versus initial orientation. The ellipsoid-4 has the highest roll-out distance, equal to 7.45 m, followed by the rectangle, equal to 7.35 m. In addition, the ellipsoid-4 has an average roll-out distance of 3.4 m higher than the average of 3.2 m for the rectangle and 2.6 m for the ellipsoid-2.

Figure 6.4d shows the variation of maximum bounce height versus the object's initial orientation after the first impact for the three tested objects. The maximum bounce height for ellipsoid-2 is slightly higher than the other objects; however, the average bounce heights of all objects are generally similar, near 2 m.

6.2.2.4 Double impacts on an inclined plane – 45° impact

In this section the rebound parameters for the impact of the three objects on an inclined surface, are investigated. The initial conditions are set according to the configuration of Figure 6.1b. The objects are projected 36 times with different orientations and with a horizontal velocity of 10 m/s, representing an impact angle of 45°. To follow the experiments performed in the previous chapters, the objects are chosen to be consistent with the definitions contained in Table 6.1 and with an aspect ratio of 2:1. Figure 6.5 illustrates the rebound energies and displacements occurring after two impacts versus initial orientation. The means, maximums, and standard deviations for the three objects are summarized in Table 6.2.

Figures 6.5a and 6.5b plot the variation of the ratio of retrieved energies to the initial energy versus the initial orientation after the first and second impacts. As the object's initial tangential velocity is not equal to zero, the energy ratios are higher for the first and second impacts in comparison to the values in the last section (case of 0° impact angle). Table 6.2 shows that the averages and maximums of the ratios of the retrieved energies are higher for the rectangle than for the ellipsoids.

Figure 6.5c shows the variation of roll-out distances prior to the second impact versus the initial orientation. The average and maximum roll-out distances for the ellipsoid-2 are higher than the other two objects, as indicated in Table 6.2. Considering the other cases of two

impact tests, performed in Section 6.2.2, the differences between the statistical values of roll-out distance for the ellipsoid-2 and the other two objects are considerable.

Figure 6.5d depicts the variation of bounce height versus the object's initial orientation after the first impact for the three tested objects. The highest maximum bounce height occurs for the ellipsoid-2. This value is 16% higher than the value for rectangle. On average, the bounce heights for the three objects are approximately the same.

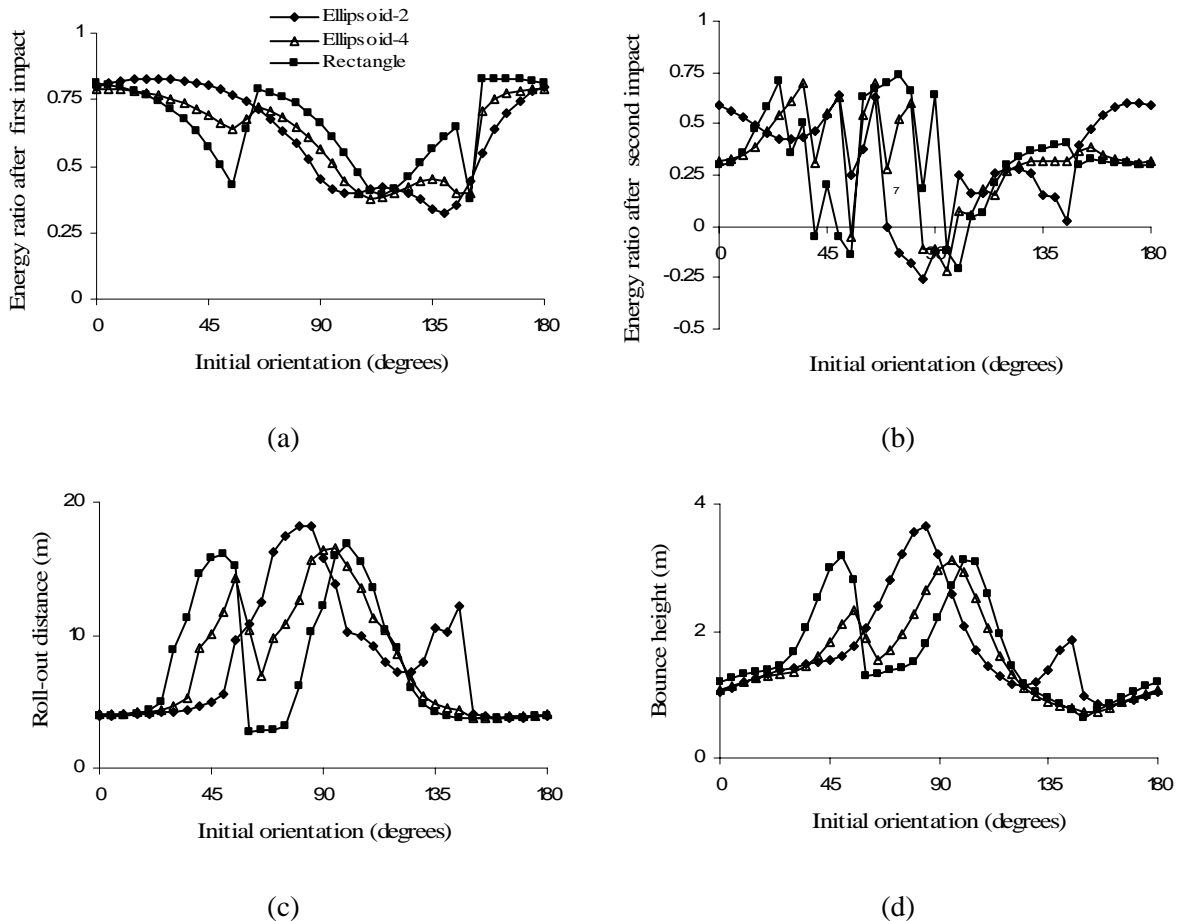


Figure 6.5: Variation of the rebound energies and displacements versus object initial orientation for a planar impact of different objects at an impact angle of 45° ($V_{ini, hor} = 10$ m/s) on a 30° inclined surface with the configuration of Figure 6.1b: (a) ratio of the retrieved energies to the initial energy after the first impact, (b) ratio of the retrieved energies to the initial energy after the second impact, (c) central horizontal displacements prior to the second impact, and (d) maximum height of bounce after the first impact (normal distance to the plane).

Generally, comparing the rebound parameters of ellipsoids and the prism with a rectangular cross section indicates that the trend of variation for the ellipsoid-4 is between the ellipsoid-2 and the rectangle. The rectangle has the lowest energy decrease after two impacts, while the roll-out distances and height of bounces are the largest for the ellipsoid-2. In general, the rebound parameters for the three objects do not differ dramatically from each other after two impacts; however, the trend of variations between the objects is completely different. Because of the sharp corners in the rectangles, the trends of variation for these objects are discontinuous. A similar behavior can be observed for ellipsoid-4. It can be predicted that ellipsoids with higher orders, and therefore higher values of n in Equation 5.2.1, also experience such discontinuities.

Table 6.2: Variation in the rebound energies and roll-out distances for rocks with variable orientations and different geometries on a 30° inclined surface with an initial angle of 45°

	<i>Ellipsoid with power 2</i>			<i>Prismatic with a rectangular cross section</i>			<i>Ellipsoid with power 4</i>		
	mean	max	S.D.	mean	max	S.D.	mean	max	S.D.
<i>Ratio of rebound total energy to initial energy after the first impact</i>	0.62	0.83	0.19	0.65	0.83	0.15	0.62	0.79	0.15
<i>Ratio of rebound total energy to initial energy after the second impact</i>	0.31	0.64	0.26	0.32	0.73	0.25	0.33	0.70	0.22
<i>Roll-out distance</i>	8.2	18.2	3.8	7.6	16.8	2.7	8.0	16.6	3.8
<i>Bounce height*</i>	1.7	3.7	0.8	1.6	3.2	0.6	1.6	3.1	0.7

* This value is measured based on the normal distance between an object center and the impact plane

6.2.3 Five-impact numerical test

It is observed that most of an object's kinetic energy is dissipated after 4 or 5 impacts, when the object has a tendency to start rolling. To confirm these observations, the rebound parameters of different objects subjected to 5 impacts, are studied in this section. The initial configurations are the same as is used in the experiment described in Figure 6.1 and the objects are ellipsoids power 2 and 4 and a prism with a rectangular cross section. The numerical tests are performed using two impact angles of 0° and 45° . The variation of the

rebound total energies, roll-out distances, and height of bounces are studied in the following sections.

6.2.3.1 5 impacts on a horizontal plane – 0° impact angle

Figure 6.6 plots the variation of the ratio of rebound total energies to the initial total energy as well as the roll-out distances versus initial orientation for the three objects with zero horizontal velocity and the same configurations as used in Figure 6.1a. All the objects' dimensions follow the convention introduced in Table 6.1 which have an aspect ratio of 2:1. The objects are projected 36 times on a flat surface with the energies and roll-out distances recorded as presented in the Figure 6.6.

Figures 6.6a and 6.6b plot the variation of the ratio of total retrieved energies to the initial energy and roll-out distances versus initial object orientation for five successive impacts for the ellipsoid-2. This figure shows that the ellipsoid-2, when having an initial orientation between 60° to 70° (also between 110° and 120°), maintains a considerable portion of its energy after 5 impacts. Also, considering that at these initial orientation angles, the object has a small variation in roll-out distances after second impact, it can be concluded that the ellipsoid has a tendency to start rolling with a high energy. For most of the impact angles the ellipsoid does not lose a significant amount of energy after the fourth impact, which confirms that the object starts to roll. This observation is supported by the variation of roll-out distances, showing that the object does not roll out drastically after the fourth impact.

Figures 6.6c and 6.6d plot the variation of the ratio of total retrieved energies to initial total energy and the roll-out distance for five successive impacts of the prism with a rectangular cross section. Figure 6.6c shows that the object loses a major portion of its energy at all initial orientation angles with a maximum of 23% and average of 14% of the initial total energy. The variation of roll-out distances in Figure 6.6d illustrates that the roll-out distances for the fourth and fifth impacts are converging. This figure shows that for initial orientations from 0° to 15°, when the larger dimension of the rectangular object impacts the surface, not only does the object lose its energy quickly but also, because of the immediate successive impacts, it does not roll out considerably. This is in contrast to situations where the object impacts the surface at the corners, when it is impacting at a low angle between the surface

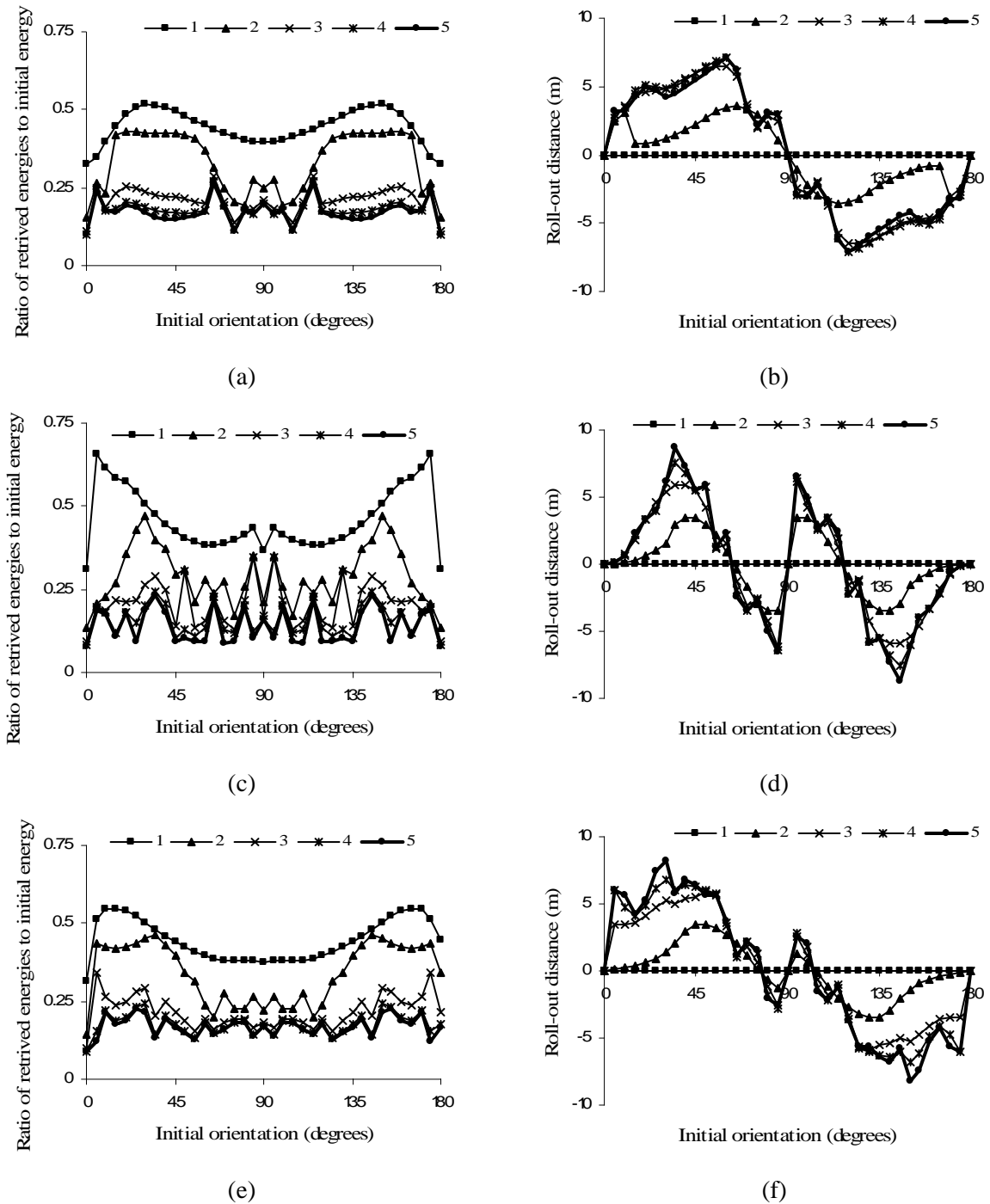


Figure 6.6: Variation of the rebound energies and roll-out distances versus object initial orientation occurring during five successive planar impacts of different objects (with an aspect ratio of 2:1) at an impact angle of 0° ($V_{ini,hor} = 0$) on a horizontal surface with the same configuration as in Figure 6.1a: (a) retrieved energies for the ellipsoid, (b) roll-out distances for the ellipsoid, (c) retrieved energies for the rectangle, (d) roll-out distances for the rectangle, (e) retrieved energies for ellipsoid-4, and (f) roll-out distances for ellipsoid-4.

and object's smaller side. In this case, around the orientation of 80° to 100° the object experiences one of the highest roll-out distances, when compared with other orientations.

Figures 6.6e and 6.6f depict the variation of the ratio of total retrieved energies to initial total energy and the roll-out distance for five successive impacts of an ellipsoid-4. The highest retrieved energy ratio after five impacts is 23% and the average ratio is 17% of the initial total energy. While the maximum ratio is equal to the maximum ratio of a rectangle, but on average the ellipsoid-4 retains more in energy than the rectangle which retains 14% of its initial energy. These figures show that the trend of energy variations is similar to the variations for the rectangle, while the trend of variation for the roll-out distances is similar to the trend of an ellipsoid-2.

When comparing the energy figures, Figures 6.6a, 6.6e, and 6.6e, after 5 impacts it can be seen that the ellipsoid-2 has the highest maximum and average ratio of retrieved total energies, equal to 0.26 and 0.17, respectively. The rectangle retains the least energy among the three objects. However, for roll-out distances the order reverses. The Rectangle has the highest roll-out distance, equal to 8.8 m, in comparison to the ellipsoid-4 and 2 with the values equal to 8.3 and 7.1 m. For the ellipsoid-2 the roll-out distance will increase significantly undergoing the rolling mode as the object has conserved 26% of its initial energy. This is in contrast to the other objects which have lost a large portion of their energy.

6.2.3.2 5 impacts on a horizontal plane – 45° impact angle

Figure 6.7 plots the variation of the ratio of rebound total energies to the initial total energy and roll-out distances versus initial orientation for the three objects. These tests use a horizontal velocity of 10 m/s and the same configurations as used in Figure 6.1a and the objects are ellipsoids power 2 and 4 and a prism with a rectangular cross section. The dimensions of the objects are chosen based on the convention of Table 6.1 having an aspect ratio of 2:1. The tests are performed 36 times with different initial orientations and with impact occurring on a flat surface. The rebound parameters are recorded successively for the 5 successive impacts.

Figure 6.7a plots the variation of the ratio of total energies to the initial energy versus initial object orientation for five successive impacts for an ellipsoid-2. At initial orientations around 70° the object maintains up to 50% of its initial total energy after 5 impacts. In these initial orientation angles, the ellipsoid-2 does not roll out further than the distance of the third impact, as is shown in Figure 6.7b, indicating that it undergoes rolling after the third impact. After five impacts, on average, the ellipsoid-2 retains 18% of its initial energy.

Figure 6.7b plots the variation of roll-out distances for the ellipsoid-2 versus the initial orientation angle for 5 successive impacts. For initial orientations between 135° to 170° the object hits the surface collinearly, resulting in small roll-out distances; at the same time, the object loses a considerable portion of its energy. At an impact angle of 130° the object experiences a negative roll-out distance. Negative roll-out distances can not be derived in lumped-mass models in a 45° impact. Figure 6.7b also indicates the presence of another type of impact behavior, double impact, which also is referred by Azzoni et al. (1995). This occurs between initial orientations of 5° and 70° where the object experiences two simultaneous impacts. Despite the situation when the impact is almost collinear, in this situation, the object significantly rolls out after the second impact. Between initial orientations of 70° and 125° the object bounces from the impact surface after the first impact.

Figures 6.7c and 6.7d plot the variation of the ratio of the retrieved total energies to the initial total energy and roll-out distances for a rectangle. The object uniformly loses its energy at the end of the fifth impact with a maximum value of 22% and an average of 11% of the initial total energy. As the object dramatically loses a considerable portion of its energy, it does not roll out significantly further, and the roll-out after this point mainly occurs as sliding. The roll-out distances between the fourth and fifth impacts are notably similar, confirming that the sliding process started and the object can not roll out significantly further after these number of impacts. The maximum value of the roll-out distance for the rectangle is 23.9 m, which is greater than the ellipsoid-2 value; however, in average it rolls out 10.6 m which is less than the value for ellipsoid-2 equal to 11.0 m. Similar to the ellipsoid-2 between 5° and 45° of the initial orientation angles, the impact is succeeded by a second impact and between 135° and 175° , the impact is almost collinear, resulting in small roll-out distances.

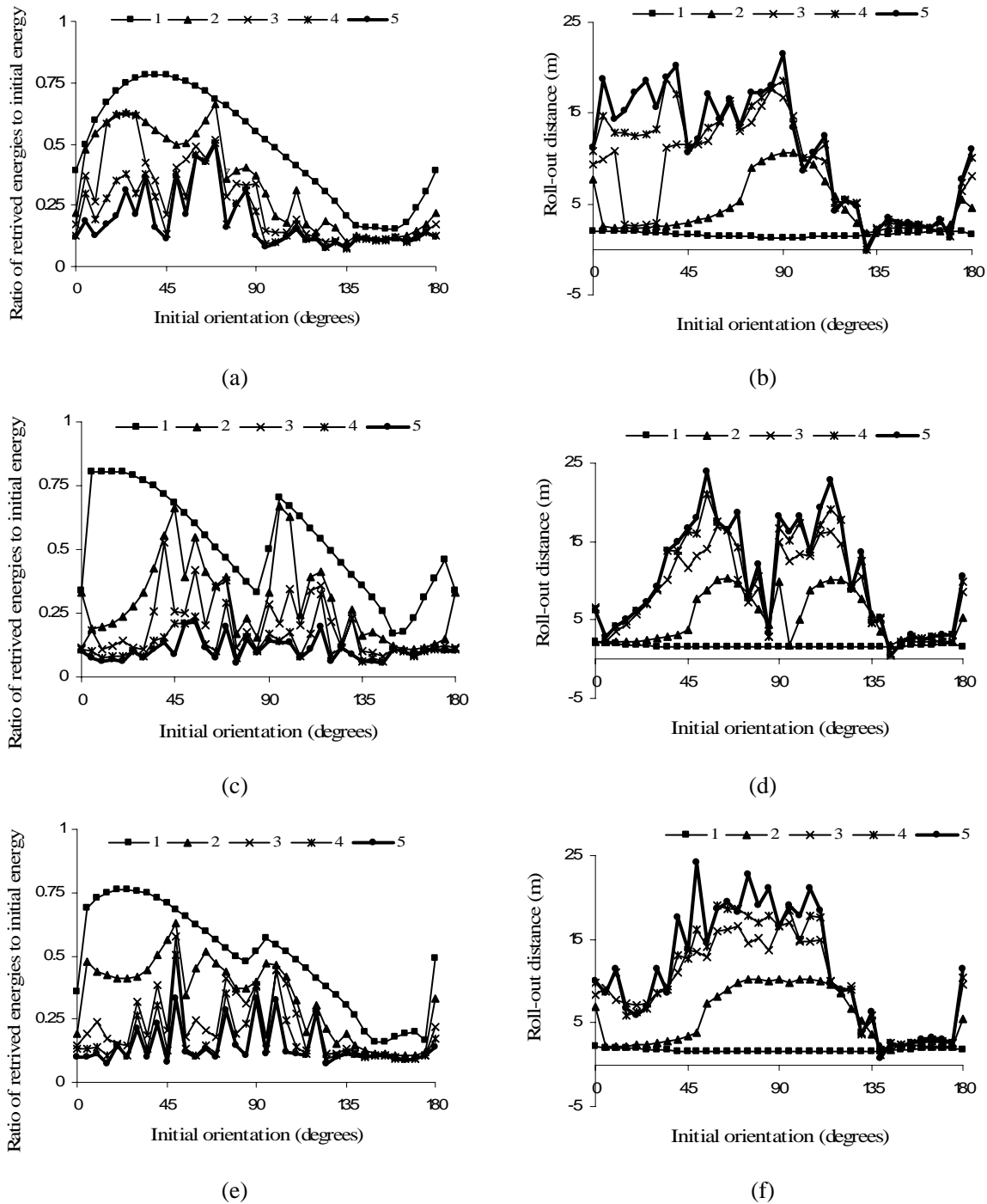


Figure 6.7: Variation of the rebound energies and roll-out distances versus object initial orientation occurred during five successive planar impacts of different objects (with an aspect ratio of 2:1) at an impact angle of 45° ($V_{ini,hor} = 10$ m/s) on a horizontal surface using the configuration of Figure 6.1a: (a) ratio of retrieved energies to initial energy for the ellipsoid, (b) roll-out distances for the ellipsoid, (c) ratio of retrieved energies to initial energy for the rectangle, (d) roll-out distances for the rectangle, (e) ratio of retrieved energies to initial energy for the ellipsoid-4, and (f) roll-out distances for the ellipsoid-4.

Figures 6.7c and 6.7d plot the variation of the ratio of the total retrieved energies to initial total energy and roll-out distances for an ellipsoid-4. Like the rectangular object, the ellipsoid-4 loses its initial energy independent of orientation angle after the fifth impact and the variation curves for the fourth and fifth impacts are similar, indicating that the object is transferring to rolling mode. The ellipsoid-4 object, on average, maintains 14% of its initial energy with a maximum of 33%. Generally, the variations of energy and roll-out curves of the ellipsoid-4 are between the roll-out and energy variation curves of the ellipsoid-2 and the rectangle, as is expected from the object's geometry. Similar to the other two objects, when the ellipsoid-4 has an initial orientation between 135° and 175° , the object does not roll out significantly, as the first impact is centric. The ellipsoid-4 has the highest average and maximum roll-out distances after five impacts among the three objects equal to 11.4 and 24.3 m. However, as, on average the ellipsoid-4 has significantly less energy than the ellipsoid-2, the ellipsoid-2 will eventually roll out the furthest.

Figures 6.8a to 6.8c plot the variations of bounce heights for the ellipsoid-2, the rectangle, and the ellipsoid-4 using the configurations of Figure 6.1a and an initial velocity of 10 m/s. The maximum bounce heights for the three objects are roughly similar, equal to 4.7 m, and occurring after the second impact. On average, the ellipsoid-4 has the largest bounce height occurring after the second impact and equal to 2.5 m, while this value for the ellipsoid-2 and the rectangle is 2.4 m and 2.2 m, respectively, as described in Table 6.3. These values indicate that the rocks experience the highest bounce height after the first or second impacts. However, in some cases, even if the rocks experience the maximum bounce height after the second impact, the rock has not moved very far, as shown in Figure 6.7. These second immediate impacts occur when the rock initial orientations are between 0° and 45° .

Table 6.3: The averages of height of bounces for different objects during the five impacts

	<i>Impact 1</i>	<i>Impact 2</i>	<i>Impact 3</i>	<i>Impact 4</i>	<i>Impact 5</i>	<i>Average</i>
Ellipsoid power 2	2.3	2.4	1.7	1.5	1.3	1.85
Rectangular section	2.2	2.2	1.6	1.3	1.1	1.68
Ellipsoid power 4	2.2	2.5	1.7	1.5	1.4	1.85

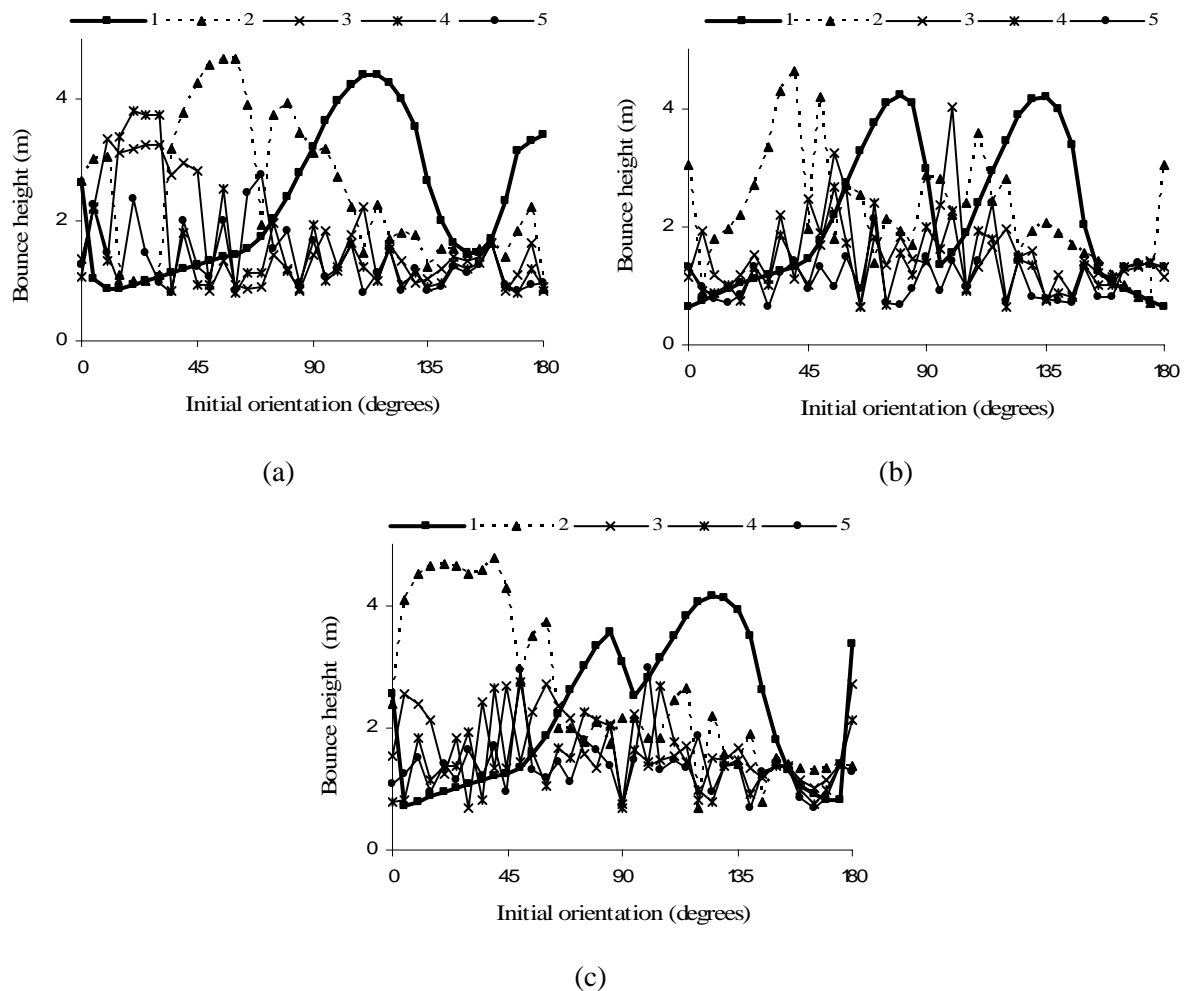


Figure 6.8: Variation of bounce height versus object initial orientation occurring during five successive planar impacts of different objects (with ratio of 2:1) at an impact angle equal to 45° ($V_{ini,hor} = 10$ m/s) on a horizontal surface with the configuration as used in Figure 6.1a: (a) the ellipsoid-2, (b) the rectangle, and (c) the ellipsoid-4.

6.2.3.3 Shape effect on roll-out distances on a plane with 15° of inclination – 45° impact angle

Figure 6.9 plots the variation of roll-out distance and bounce heights after the fifth impact for the three objects with the same configurations as used in Figure 6.1b and an initial horizontal velocity of 10 m/s. Similar to previous sections, these objects are an ellipsoid-2, a rectangle, and an ellipsoid-4. The tests are performed 36 times using different initial orientations, with the objects hitting an inclined surface with an inclination angle of 15° . The rebound parameters are recorded at every 5° change of initial orientation.

Figure 6.9a plots the variation of the roll-out distance for the three objects after five impacts versus the objects' initial orientation. This figure shows that the maximum roll-out distance for the rectangle and ellipsoid-4 are approximately equal to 46 m, while this value for ellipsoid-2 is equal to 44 m. However, on average, all objects have approximately the same average roll-out distance, equal to 23.0 m. It should be mentioned that these values are derived for only first five impacts and that their energy levels determine which object can displace the furthest before arrest.

Figure 6.9b shows the envelope curves for the maximum bounce height occurring during five impacts for the three objects. The envelope curve is derived based on the maximum bounce heights after the five impacts for each initial orientation angle. The rectangle has the largest bounce height among the three objects; however, on average the two ellipsoidal objects experience a bounce height equal to 4.1 m, compared to an average of 3.3 for the rectangle.

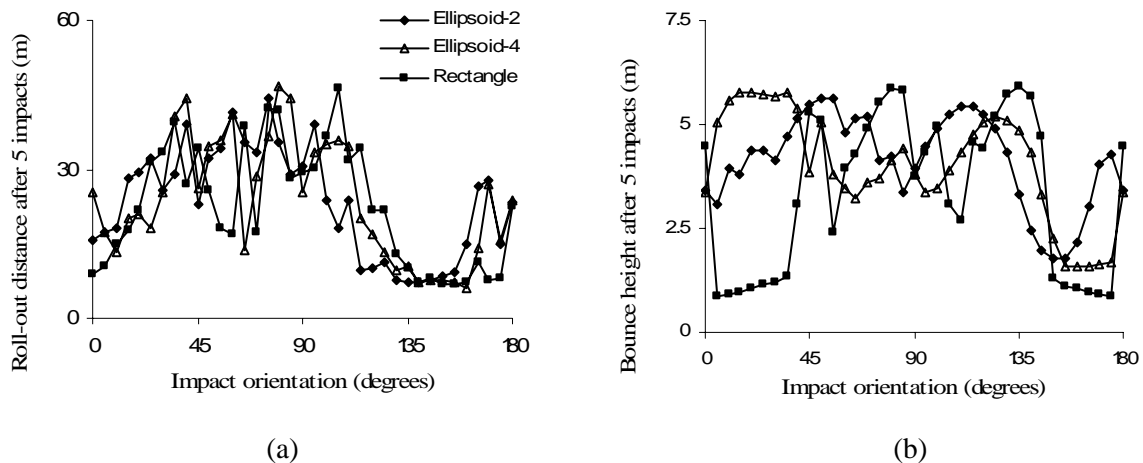


Figure 6.9: Variation of the rebound parameters versus object initial orientation occurring during five successive planar impacts for different objects (with ratio of 2:1) at an impact angle of 45° ($V_{ini,hor} = 10$ m/s) on a surface with 15° of inclination and the configuration of Figure 6.1a: (a) roll-out distances after five impacts, and (b) bounce height envelope curve for five impacts.

6.2.3.4 Aspect ratio effect on roll-out distances and total energies

To investigate the effect of an object's aspect ratio or slenderness on the rebound velocities and energies after several impacts, the numerical setup applied in Figure 6.1 is utilized. In this test the object is projected at an initial horizontal velocity, $V_{ini,hor} = 10$ m/s, which results

in an impact angle of 45° . The objects' dimensions follow the convention introduced in Table 6.1. For each aspect ratio, the rock is projected a total number of 90 times against a rigid half space, varying the orientation angle by 2° for each shot. To capture the variation of rebound parameters more accurately, especially after successive impacts, the total number of impacts in this test is increased from 36 to 90, and therefore the orientation intervals are decreased from 5° to 2° . After the fifth impact, Equation (6.2.1) is used to derive the average values of the roll-out distance and maximum bounce height using the 90 impact results. The variations are presented in Figure 6.10 for the three tested objects. In this example, a flat surface is preferred to an inclined surface, as the last stages of rockfall next to infrastructures usually occur in horizontal planes adjacent to the talus of the slopes where the rocks undergo multiple impacts.

$$\bar{D} = \frac{\sum_{\alpha=0}^{180} D}{90} \quad \bar{R}_E = \frac{\sum_{\alpha=0}^{180} R_E}{90} \quad (6.2.1)$$

Figure 6.10a plots the variation of the maximum roll-out distance results for the impacts of the three objects versus the aspect ratio in the above mentioned configurations. For aspect ratios smaller than 1.5, the rectangle and the ellipsoid-4 have the highest roll-out distance; however, for aspect ratios greater than this value, the maximums for the three objects are approximately equal. The maximum roll-out distance decreases for the rectangle and ellipsoid-4 when the aspect ratio increases. For the ellipsoid-2 the maximum roll-out distance occurs for the aspect ratio of 1.5.

The variations of the average roll-out distances versus the object aspect ratio are plotted in Figure 6.10b for the three analyzed objects. The ellipsoid-2 has the largest average roll-out distance for aspect ratios smaller than 2.0. The average roll-out distance for the rectangle is almost independent of the aspect ratio for aspect ratios smaller than 2.0. In contrast for the ellipsoidal objects the average roll-out distance dramatically decreases with respect to increasing rock slenderness. It may be observed that for aspect ratios greater than 2.0, both the maximum and average roll-out distances are very similar.

Figure 6.10c depicts the variation of the maximum ratio of retrieved total energies to initial total energy versus object initial orientation after five impacts. Other than for aspect ratios lower than 1.3, the ellipsoid-2 has the highest maximum retrieved energies. The ellipsoid-2 has the lowest because the impacts for ellipsoid-2 become mainly centric with a steady energy dissipation trend, while for the other objects, the variations of retrieved energy are dispersed. At an aspect ratio equal to 1.0, the ellipsoid-4 has the highest maximum retrieved energy, showing that corner abrasion dramatically increases energy retention ratio of rectangles from 0.37 to 0.57. Generally, these curves show that a rock can maintain up to 63% of its initial energy after five successive impacts on a typical rock material surface.

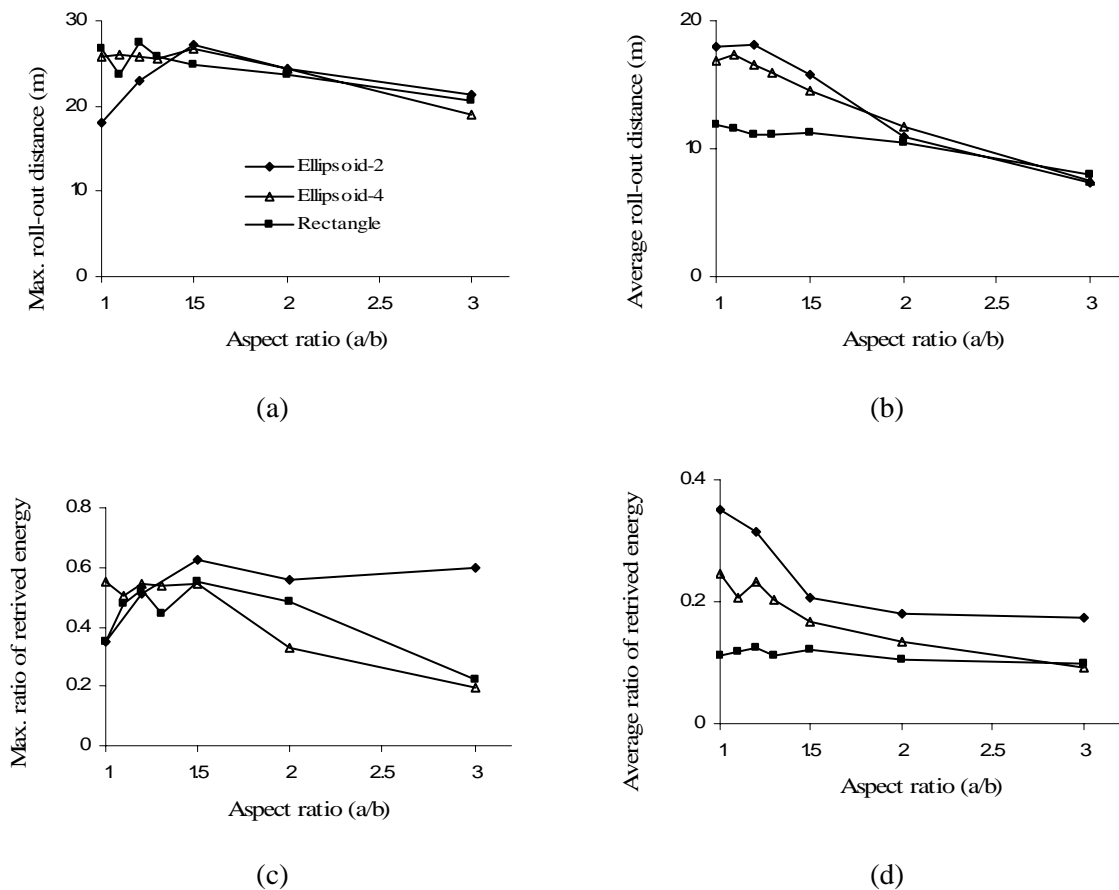


Figure 6.10: Average and maximum rebound parameters for different objects versus aspect ratio after five successive impacts at an impact angle of 45° ($V_{ini,hor} = 10$ m/s) on a horizontal surface with the configuration used in Figure 6.1a: (a) maximum roll-out distances, (b) average roll-out distances, (c) maximum retrieved energies, and (d) average retrieved energies.

Figure 6.10d shows the variation of the average ratio of retrieved total energies to the initial total energy versus aspect ratio after five impacts. On average, the ellipsoid-2 has the highest retrieved energy ratio with a decreasing variation trend from 0.35 to 0.18. This high energy ratio is very significant, as it shows that ellipsoidal rocks with low slenderness maintain their energy before starting the rolling phase. From Figure 6.10b, it may also be concluded that the ellipsoid-2 has the highest average roll-out distance. As a result, ellipsoidal rocks with a low aspect ratio have the highest roll-out distance value, before entering the rolling phase. The ratio of average retrieved energy to initial energy is almost constant for the rectangle, having a value of 0.12. This low ratio shows that the motion of these types of objects may be terminated after this number of impacts. The ellipsoid-4 has an energy retention ratio between the other two geometrical shapes, varying from 0.24 to 0.10.

6.2.3.5 Effect of friction and energy COR on rebound parameters of an ellipsoid

In order to study the effect of material parameters, e_* and μ , on successive impact rebound parameters, the numerical test setup of Figure 6.1a is used for five successive impacts. The initial impact angle is assumed constant, at an angle of 45° , with an initial horizontal velocity of 10 m/s ($V_{ini,hor} = 10$ m/s). The object's aspect ratio is assumed constant equal to 1.5:1. In this numerical test, this aspect ratio is chosen instead of a ratio of 2:1. According to Figure 6.10b, ellipsoidal objects with this ratio have the largest roll-out. In this case the objects are shot 90 times, varying the object orientation every 2° with every shot. The results are presented for the ellipsoid-2 and the rectangle objects, in Figures 6.11 and 6.12. The rebound parameters are restricted to: roll-out distance, bounce height, and the ratio of retrieved total energy to initial total energy.

Figure 6.11a plots the variation of average roll-out distances after five impacts of the ellipsoid-2 for different energy COR versus the friction coefficient. Generally, the roll-out distances reduce significantly with the reduction of the energy COR. The friction coefficient has a major effect when the values for energy COR are greater than 0.5. For typical rockfall COR, which are usually smaller than 0.6, Figure 6.11a shows that friction has a minor effect on average roll-out distances. The variation of the maximum roll-out distance is similar to the variation of the average values, as shown in Figure 6.10b. The maximum roll-out distance is

dramatically affected by energy COR; however, the friction coefficient has only a minor effect.

Figure 6.11c depicts the variation of average maximum bounce height versus friction coefficient for different energy COR during five impacts of the ellipsoid-2. Bounce heights reduce significantly with a reduction in energy COR, and increase slightly with an increase in friction coefficients for friction values less than 0.5. This slight increase occurs due to an increase in normal COR, as a result of an increase in the friction coefficient demonstrated in Figure 4.11a. This trend of variation can be also observed in the variation of the maximum height of bounce as is shown in Figure 6.11d.

Figure 6.11e shows the variation of the ratio of average retrieved total energy to the initial energy for the ellipsoid-2 after five impacts. Generally, for friction coefficients lower than 0.3, the average ratio of retrieved energy decreases as the friction coefficient increases. At energy COR equal to 1.0, the average ratio of retrieved energy increases for friction coefficients greater than 0.2 and stays constant at the ratio of 0.87. This increasing trend can be explained by observing that, due to a lack of energy dissipation in the normal direction, the sliding process is terminated in early stages by a high friction coefficient, changing the sliding mode to stick mode. This early sliding termination decreases the total energy dissipation. The average retrieved energy decreases for energy CORs smaller than 1.0; however, this decreasing trend stops for friction coefficients higher than 0.3.

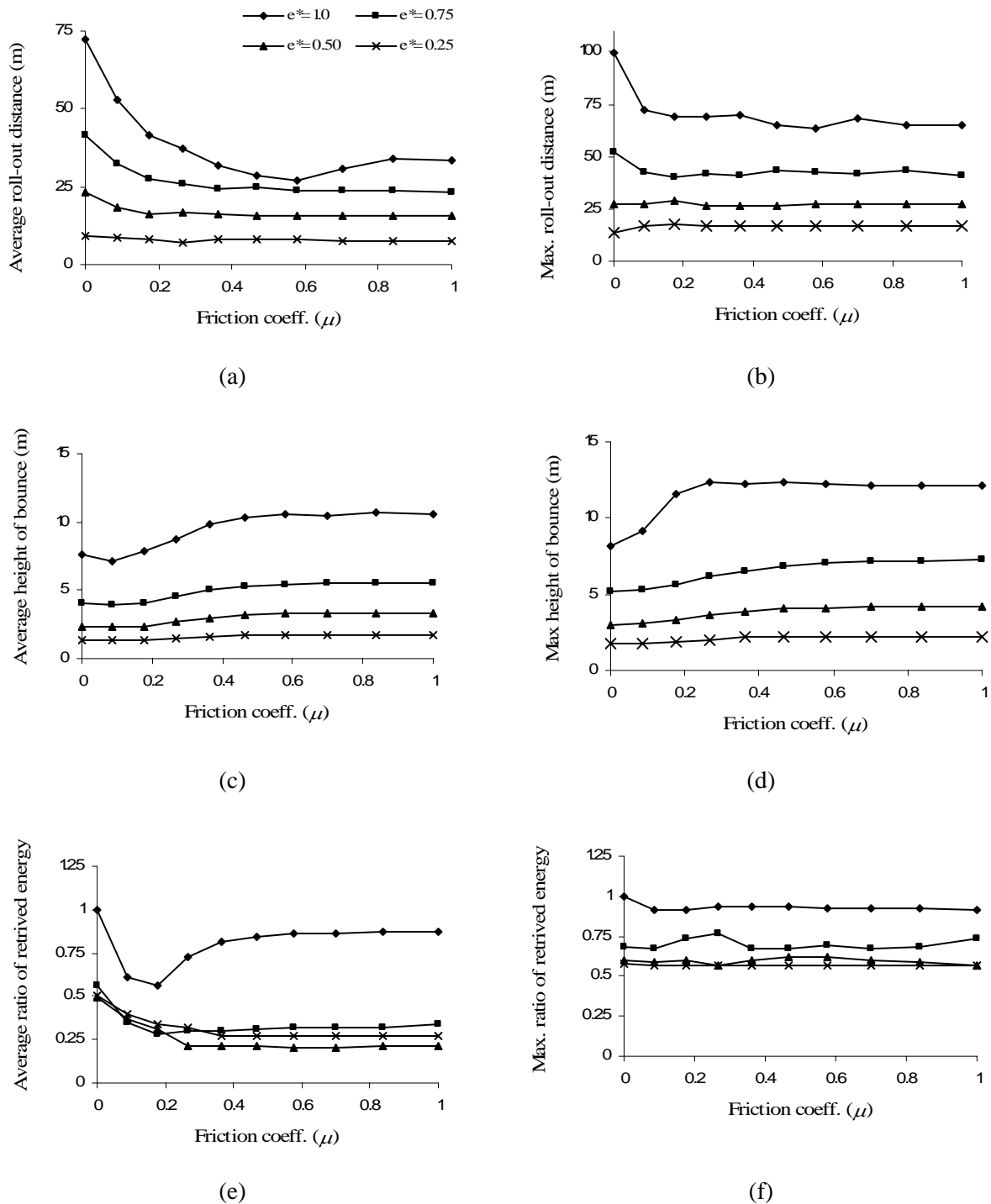


Figure 6.11: Variation of the average and maximum rebound parameters for ellipsoid-2 versus the friction coefficient for different energy COR after five successive impacts occurring with an impact angle of 45° ($V_{ini,hor} = 10$ m/s) on a horizontal surface with the same configuration as used in Figure 6.1a: (a) maximum roll-out distance, (b) the average roll-out distance, (c) maximum bounce height, (d) the average bounce height, (e) maximum ratio of retrieved total energy to initial total energy, and (f) the average ratio of total retrieved energy to initial total energy.

In Figure 6.11e, it can be noticed that the average ratio of retrieved energy, for the energy COR equal to 0.25, is higher than the values derived when the coefficient is 0.5. This unexpected increase in the ratio of retrieved energy is due to a mode change at the impacts with small energy COR that changes the object's impact mode to sliding mode. Furthermore, when the variations in impact configurations are small, multiple successive impacts dissipate only a small amount of energy. Further reasons for this low energy dissipation can be gathered by looking at Figures 6.11a and 6.11c. In these figures, curves showing the average roll-out distance and the average bounce height illustrate that the object stays in close contact with the surface, resulting in a negligible variation in contact configurations. Figure 6.11f plots the variation of maximum ratio of retrieved total energies to the initial energy occurring at the end of five impacts, and shows a decreasing trend with energy COR. Figure 6.11f shows that the friction coefficient has no meaningful effect on the maximum retrieved energy.

6.2.3.6 Effect of friction and energy COR on rebound parameters of a prism with a rectangular cross section

In order to observe the effects of corners on rebound parameters, all of the numerical tests performed in the last section for the ellipsoid-2 are repeated here for a prism with a rectangular cross section with an aspect ratio of 1.5:1. The rectangle's dimensions are defined in Table 6.1. The results for the variation in the average values are presented in Figure 6.12.

Figure 6.12a plots the variation of average roll-out distances versus the friction coefficient for different energy COR after five impacts for the rectangle. Generally, the roll-out distance decreases dramatically when the energy COR decreases; however, this is not true for energy COR equal to 1.0 and friction coefficients greater than 0.5. At high friction coefficients and when energy COR is equal to 1.0, in many initial orientations, the rectangle moves in negative direction after the first impact. Thus opposite roll-out is observed much more than for the ellipsoid-2, as shown in Figure 6.11a. Figure 6.12a shows that the roll-out distances decrease when the friction coefficient increases; however, for energy COR equal to 0.25, the average roll-out distances after five impacts are almost independent of friction coefficient.

On average, the effect of the friction coefficient on the average roll-out distances is more tangible for the rectangle than for the ellipsoid-2.

Figure 6.12b shows the variation of average maximum bounce height versus the friction coefficient for the rectangle for different energy COR during five impacts. On average, the bounce height decreases when the energy COR decreases, as the energy dissipation increases and consequently the normal COR decreases. The average bounce height increases when the friction coefficient increases. Thus, with higher friction coefficients, the tangential impact process changes from pure slip or slip-reversal to slip-stick, resulting in a higher normal COR and higher rebound bounce height.

Figure 6.12c depicts the average ratio of retrieved total energy to initial total energy for different energy COR versus the friction coefficient for the rectangle after 5 impacts. At an energy COR equal to 1.0, the ratio of retrieved energy decreases from 1.0 at a friction coefficient value of 0 to 0.41, at a friction coefficient of 0.27, and then increases to 0.87 at a friction coefficient of 1.0. This variation of the ratio of retrieved energy may appear to be inconsistent; however, it is not. As was explained in the last section, at energy COR equal to 1.0, the only source of energy dissipation is due to friction force; consequently, at higher friction coefficients, the sliding mode changes to sliding-stick, which results in less dissipation. This effect can be also noticed for energy COR equal to 0.75; however it is not substantial. For other values of energy COR, the average retrieved energy decreases as the friction coefficient increases before staying at a constant value for friction coefficients greater than 0.57.

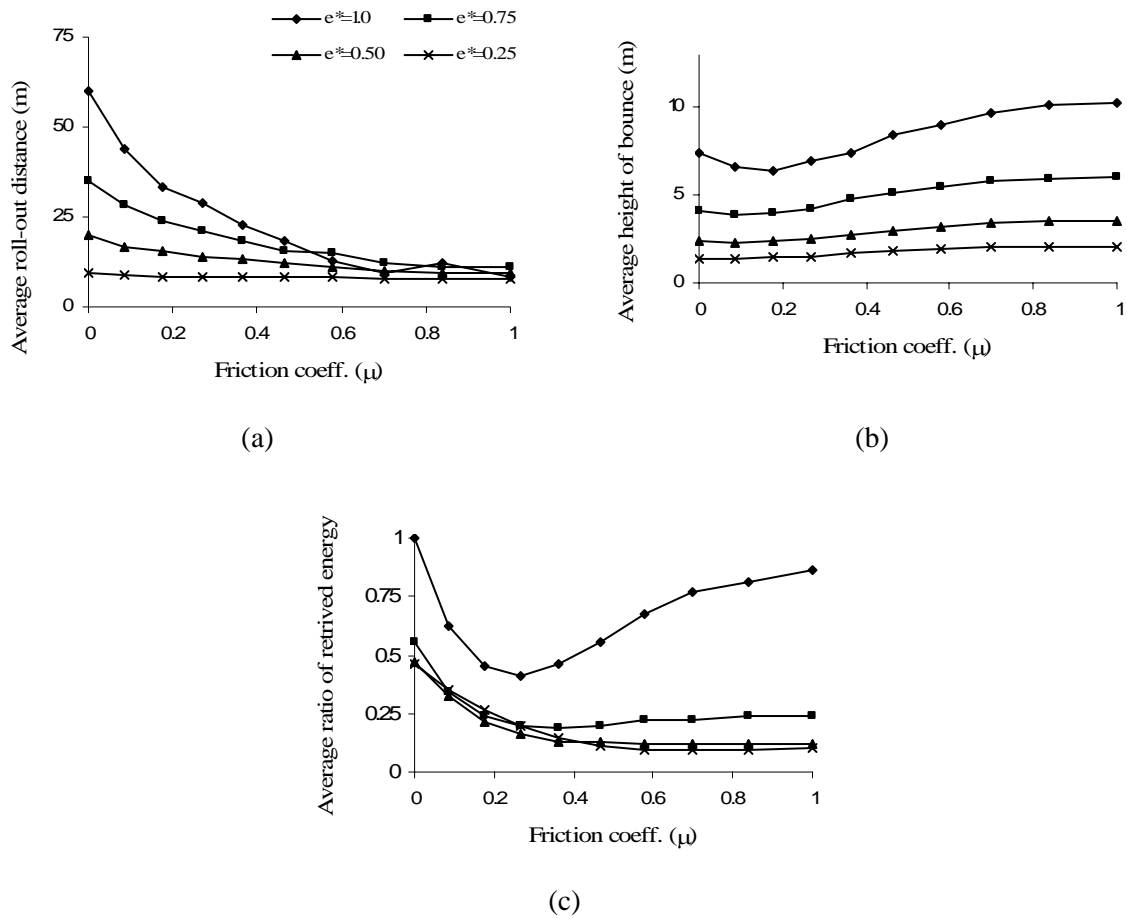


Figure 6.12: Variation of the average rebound parameters for a rectangle versus the friction coefficient for different energy COR after five successive impacts occurring with an impact angle of 45° ($V_{ini,hor} = 10$ m/s) on a horizontal surface with the same configuration as used in Figure 6.1a: (a) the average of roll-out distances, (b) the average of bounce height, and (c) the average of the ratio of retrieved total energy to initial total energy.

Comparing Figure 6.12 with the similar graphs in Figure 6.11 emphasizes the observation that the influence of the friction coefficient is more perceptible when rebound parameters are varied for rectangles. This is further supported by the variation curves of the coefficients of restitution discussed in Section 4.4.3.

6.2.4 Multiple impact studies using random object generation

Several parameters affect the rebound parameters in the numerical tests defined in Figure 6.1. All the numerical tests performed in the previous chapters consider some of the variables

constant including: impact angle, material parameters, geometrical shape and aspect ratio. In this section, the numerical test defined in Figure 6.1 is repeated using the research version of RocFall[®] and its random object generation capabilities. In order to be consistent with the numerical tests performed in previous chapters, the mean for the material impact parameters is chosen to be 0.50 for energy COR and a value of $\tan(30^\circ)$ is chosen for the friction coefficient. The statistical values and the applied distributions are presented in Tables 6.4. This table illustrates that the normal distribution is chosen for material parameters while the uniform distribution is preferred for initial orientation and initial horizontal velocity. The values set for horizontal velocity indicate that the initial impact angle varies from 26° to 56° . In every set of experiments, the rock geometry is considered constant and all the geometries follow the convention of equivalent objects defined in Table 6.1. For each scenario, 250 rocks are generated randomly and are projected on the rigid surface.

Table 6.4: The model parameters used to randomly generate objects

<i>Parameter</i>	<i>Mean</i>	<i>St. Dev.</i>	<i>Min</i>	<i>Max</i>	<i>Distribution</i>
<i>Energy COR</i>	0.50	0.05	0.40	0.6	normal
<i>Friction angle</i>	30°	5°	25°	35°	normal
<i>Initial orientation</i>	90°	-	0°	180°	uniform
<i>Hor. velocity (m/s)</i>	10	-	5	15	uniform
<i>Vert. velocity (m/s)</i>	-10	-	-	-	-

6.2.4.1 Effect of aspect ratio on trajectories during five impacts on a horizontal plane

In this section the ellipsoid-2, the rectangle, and the ellipsoid-4 are tested with different aspect ratios. The aspect ratios considered in these series of numerical tests are: 1:1.05, 1:1.5, 1:2.0 and 1:3.0. Figure 6.13 demonstrates the rocks trajectories during five impacts for different objects and the parameter distributions described in Table 6.4.

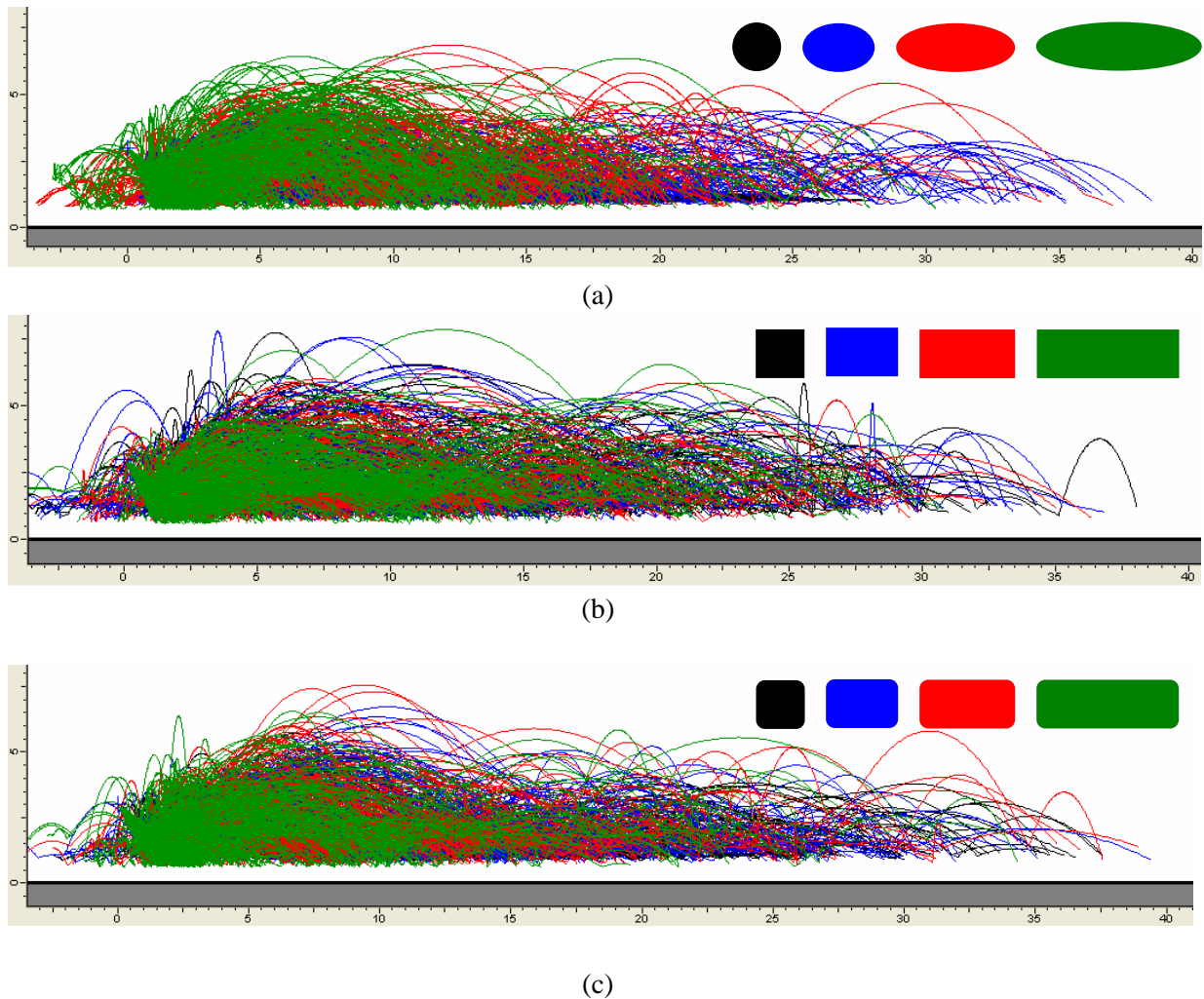


Figure 6.13: Rock trajectories during five successive impacts for different geometries and the configurations used in Figure 6.1a and the settings of Table 6.4 for rock aspect ratios of 1:1.05, 1:1.5, 1:2.0, 1:3.0: (a) ellipsoid-2, (b) prism with rectangular cross section, and (c) ellipsoid-4.

Figure 6.13a shows the trajectories resulting from the five successive impacts of the ellipsoids on a flat surface with the previously described setup and aspect ratios. This figure shows that the maximum roll-out distance belongs to the ellipsoid with the ratio of 1:1.5. Figure 6.13b shows the trajectories resulting from the impacts of rectangles at different aspect ratios. This figure shows that the rectangle with the aspect ratio of 1:1.05 has the maximum roll-out distance; however, this distance is closely followed by the rocks with the ratios of 1:1.5 and 1:2.0. It shows also that the rectangular rock possesses a higher height of bounce than the other shapes. Figure 6.14c plots the trajectories resulting from the impacts of

ellipsoids-4 with different aspect ratios. This figure shows that ellipsoids-4 with ratios of 1:1.5 and 1:2.0 have the highest roll-out distances.

The Figure 6.13 confirms that the results derived in Figure 6.10 capture the main elements of random object generation. This is achieved by comparing the maximums of roll-out distances and height of bounces between the two figures.

6.2.4.2 Effect of rock shape on trajectories for the objects with a 1:2 aspect ratio

To define the effect of rock geometry on the roll-out distances further than five impacts, the proposed numerical experiment on Figure 6.1a is expanded to include 5 and 10 impacts. The applied geometries are ellipsoids power 2 and 4, and a rectangle. To further investigate the effect of rolling, a situation where the rocks either arrest or roll for more than 10 seconds is also tested. In each case, 250 rocks are generated for each of the three assumed geometries and are projected at the flat surface. The initial impact settings are derived based on the random object generation from the data presented in Table 6.4 and with aspect ratios of 2:1 and the conventions of Table 6.1. The trajectories for individual rocks are presented in Appendix 3.

Figure 6.14a shows the rock path trajectories resulting from the five impacts of the three rocks on a flat surface. It can be observed from this figure that the three rocks experience approximately the same roll-out distance. The maximum height of bounce in this case belongs to the rectangle. Figure 6.14b depicts the trajectories resulting from 10 successive impacts of the proposed rock geometries. It can be observed that the ellipsoid-4 has the highest bounce height and highest roll-out distance after 10 impacts. The rectangle also has a maximum roll-out distance higher than ellipsoid-2. These are all in contrast to the case of 5 impacts where all the rocks with an aspect ratio of 2:1 have the approximately the same maximum and average roll-out distance.

Figure 6.14c depicts the rock path trajectories resulting from the impacts and rolling of the three rocks with the initial random object generation mentioned above for a time equal to 10 seconds. In this test the rolling friction coefficient is set to zero. This figure illustrates that the rolling mode for ellipsoidal objects is a significant mode of motion; however, this mode does

not occur for prismatic rocks. This figure shows that, on average, the ellipsoid roll-out distance is dramatically higher than the prismatic rock; although in some situations, the rectangle may experience a significant roll-out distance, resulting from the impact mode.

As observed in the last sections, the maximum bounce height for the three objects are approximately the same. It can be observed from Figure 6.14 that the maximum height of bounce may occur for all three objects.

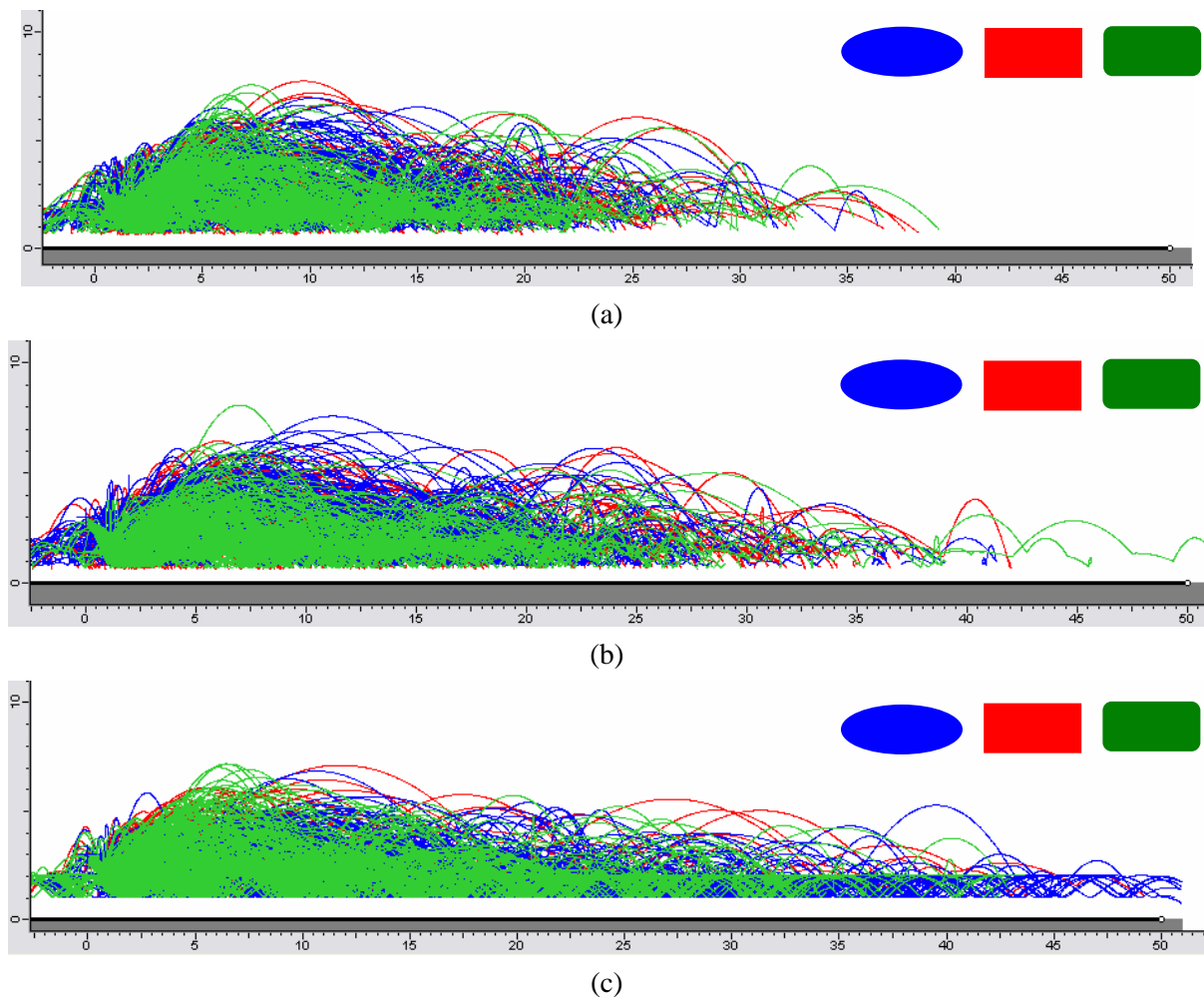


Figure 6.14: Rock trajectories during several successive impacts for rock geometries including: ellipsoids 2 and 4 and a rectangle with the configurations of Figure 6.1a and settings of Figure 6.4 for a rock aspect ratio equal to 2:1: (a) 5 impacts, (b) 10 impacts, and (c) time limit of 10 seconds.

6.2.4.3 Effect of rock shape on trajectories for the unit objects

The effect of rock geometry on rock path trajectories of unit shape geometries is shown in Figure 6.15. In this figure, successive impacts of sphere (an ellipsoid with aspect ratio of 1:1.05), an ellipsoid-4, a square, and a five and a six-sided polygon are depicted. The initial settings are randomly generated using the definitions of Table 6.4, with constant horizontal velocity, $V_{ini,hor} = 10$ m/s. For each shape, 250 rocks are generated and the impact trajectories are presented in Figure 6.15.

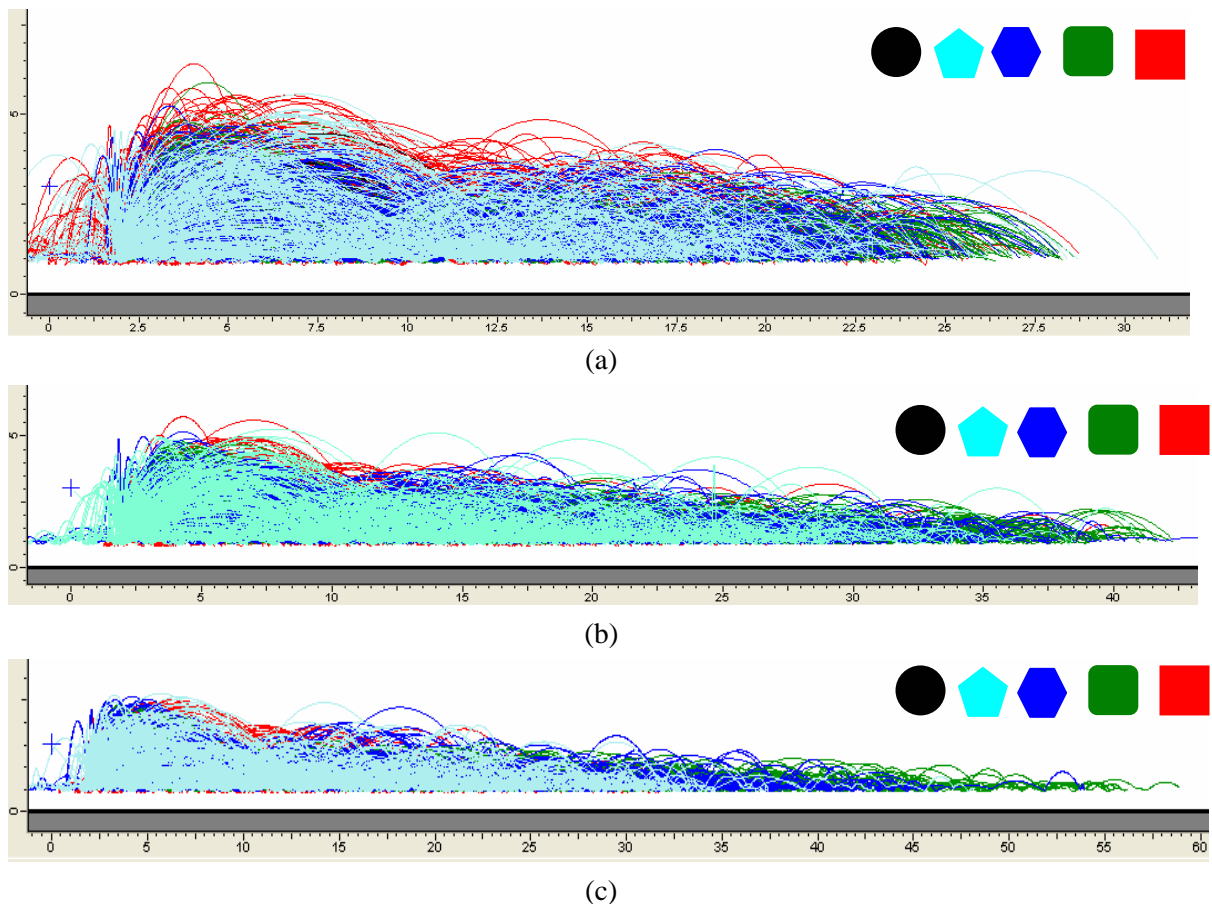


Figure 6.15: Rock trajectories during successive impacts for rock geometries of a near sphere (ellipsoid with aspect ratio of 1:1.05) and prisms with square and polygon five and six-sided cross sections using the configurations of Figure 6.1a and the settings of Figure 6.4 for rock aspect ratio equal to 1:1: (a) 5 impacts, (b) 10 impacts, and (c) 10 seconds.

Figure 6.15a depicts the roll-out trajectories of spherical, cubical, ellipsoid-4 rocks during 5 impacts. It can be observed that all the objects have a similar highest roll-out distance;

however, Figure 6.10 states that on average the sphere has the highest average roll-out distance. Figure 6.15b shows the trajectories for 10 impacts of the prismatic rock with polygonal cross sections (five and six-sided) and the near sphere (ellipsoid 1:1.05). It can be observed that the ellipsoid-4 and six-sided polygon have the highest roll-out distance.

Figure 6.15c shows the trajectory of the five unit objects after 10 seconds and the previously described initial settings. This figure illustrates that the ellipsoid-4 has the highest roll-out distance followed by the six-sided polygon section. The prism with a five-sided polygon has a higher maximum roll-out distance than the rectangle. In this case the sphere has the smallest maximum roll-out distance.

6.3 ROCKFALL CASE STUDY

Pierson et al. (2001) performed a series of rockfall field tests to develop design charts for dimensioning rockfall catchment areas adjacent to highways. These tests were originally initiated by Oregon Department of Transportation (ODOT) in collaboration with six other US states. The tested slopes consisted of: three main heights, 12, 18, and 24 m; five inclinations, vertical, 0.25H:1V, 0.5H:1V, 0.75H:1V, and 1H:1V; and catchment areas with three different inclinations, flat, 6H:1V, and 4H:1V. A total number of 11,250 rocks were rolled off the slope, where every slope with a different combination of slope inclination and catchment received a standard suite of tests containing a total of 250 rocks, with 100 rocks having a diameter of 0.30 m, 75 having a diameter of 0.60, and 75 having a diameter of 0.90 m. Figure 6.16 shows a photo of a sample slope and rockfall in-situ test, performed by Pierson et al. (2001). The gathered data was evaluated using statistical and graphical methods. In addition, the authors suggested a series of “practitioner-friendly” charts that can be used to dimension the catchment areas subjected to specific slope and catchment inclination which satisfy the catching/retention requirements.

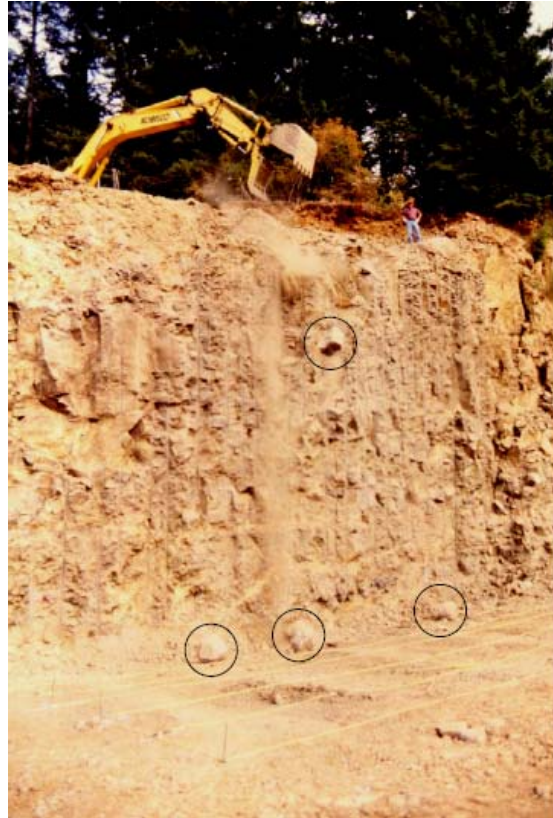


Figure 6.16: Typical rockfall test performed by Pierson et al. (2001) where the slope height is 12.0 m and the circles denote the rocks.

Pierson et al. used the Colorado Rockfall Simulation Program (CRSP), developed originally by Pfeiffer et al. (1990), to replicate the rockfall test observations for specific slopes with inclination of 0.25H:1V. Unfortunately, there is not enough information on the coefficients and/or distributions used as input in the computer program. This information could be used to produce the coefficients which are used in the applied simulation programs of this work. In this section, the roll-out outputs from the CRSP simulation are presented alongside the field observations and the outputs of RocFall[®] research version. Generally, Pierson et al. were satisfied with the results derived from the CRSP simulation; however, it is reported that the program underestimates the roll-out distances for the 24 m slope, while it overestimates the same distances for 12 m slopes.

The number of rock samples and the slope configuration were chosen by Pierson et al. (2001) and in this work it is intended to replicate the configurations of rockfall tests and to compare the simulation outputs with field observations. Unfortunately, there is no detailed report on

the rock sample shapes used in Pierson et al.'s simulations; therefore, as a substitute, most of the geometries provided in the research version of the RocFall[®] simulation code are tested and the rockfall rebound parameters are compared with in-situ observations, mainly roll-out distances.

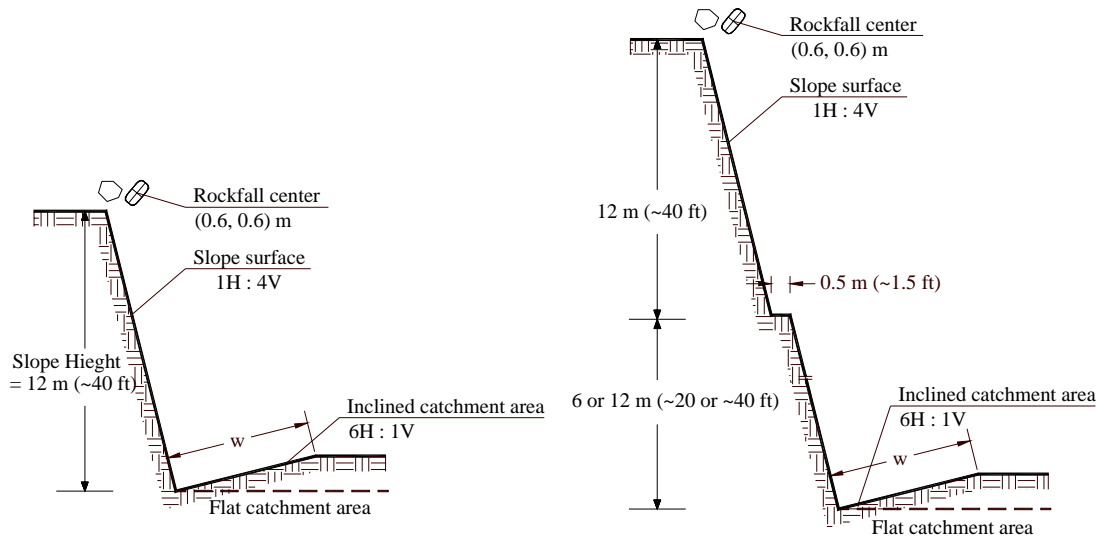


Figure 6.17: Slope configurations used in numerical tests with inclination of 1H:4V and catchment areas of flat and 6H:1V.

As the output results using the program CRSP were provided for 0.25H:1V slopes, this work also uses this inclination for all three tested slope heights, 12, 18, and 24 m, in combination with two catchment areas, flat and 6H:1V. The typical slopes with the corresponding catchment areas are presented in Figure 6.17. For the 18 and 24 m slopes, there is a 0.5 m offset for presplit drilling, 12 m from the crest of the slope.

The ODOT report does not refer to the material properties resulting from performing single impact tests, or to the coefficients of restitution used in the CRSP simulation. By sensitivity analysis and by referring to relevant literature, the mean energy COR is chosen to be 0.35, the mean friction coefficient is chosen to be 0.25, and their variations were chosen to follow a normal distribution. The rock seeder is located at a distance of 0.6 m (2 feet) horizontally and vertically from the rock crest with uniform variation for rock orientation and initial horizontal velocity. The rock mean dimensions are set to 0.30 m, with uniform distribution, in each direction and not having a diameter greater than 0.45 or smaller than 0.15. Table 6.5

summarizes these assumptions. In the simulations, the rock normal and rotational initial velocities are assumed constant, equal to 0.0 m/s and the maximum rock aspect ratio is set to 1.5. Furthermore, the objects are considered three-dimensional, meaning that the rocks mass and radius of gyration are calculated based on three-dimensional shapes, as indicated in Table 5.2, while their motion is planar.

Table 6.5: RocFall[®] research version parameters used in simulating the Oregon catchment field test

<i>Parameter</i>	<i>Mean</i>	<i>St. Dev.</i>	<i>Min</i>	<i>Max</i>	<i>Distribution</i>
<i>Energy COR, e_*</i>	0.35	0.05	0.30	0.40	normal
<i>Friction, μ</i>	0.25	0.05	0.20	0.30	normal
<i>Rot. Friction, μ_r</i>	0.40	0.05	0.35	0.45	normal
<i>Rock dimension (m)</i>	0.30	-	0.15	0.45	uniform
<i>Initial orientation</i>	90°	-	0°	180°	uniform
<i>Hor. velocity (m/s)</i>	0.5	-	0.5	1.5	uniform

6.3.1 Output data analysis

Rebound parameters of six different objects are tested in the RocFall[®] research version and the results are compared with the in-situ test output data and CRSP simulation performed by Pierson et al. (2001). 200 rock samples were thrown for each geometrical shape and the results are presented in Figure 6.18. Roll-out histograms for both the CRSP simulation and field observation showed that only a small percentage of the rocks travel large distances from the slope. As a result, to discard the effect of these stranded rocks, the output roll-out figures are prepared for the roll-out of the nearest 90% of the rocks in addition to the average and standard deviation figures. This is similar to the procedure followed by Pierson et al. (2001).

Figure 6.18a plots the 90% roll-out distances versus slope height for different geometrical shapes resulted from the RocFall[®] research version simulation, in addition to the data from the field observations and from the program CRSP[®]. Among the different geometries, the prisms with a rectangular cross section and the five-sided polygonal shapes give the best prediction for 90% roll-out distances. Simulations using spherical rocks can only correctly predict the roll-out distances for a 12 m slope while they underestimate the value for the slopes with higher heights. The ellipsoid-2 has the largest roll-out distances and after it, the

ellipsoid-4 has the highest roll-out distance. The prism with a cross section of a six-sided polygon produces the highest roll-out distance after the ellipsoidal objects. In-situ tests show that the difference between the roll-out distances for the slopes with the height of 12 and 18 m are significantly larger than the difference between the roll-out distances between the slopes with the height of 18 and 24 m. The main reason for this phenomenon is the presence of the 0.5 m presplit berm for the heights of 18 and 24 m as shown in Figure 6.17. The new model offered in this work, which is shape-inclusive, can catch the slope corner effect that causes extra roll-out distance. In contrast CRSP, as a hybrid model with the contact search based on the contact of a dimensionless lumped-mass model, is not capable of modeling the corners. Therefore its roll-out distance estimation varies almost linearly as a function of slope height.

In the Figure 6.18b, the variation of 90% roll-out distances of rocks versus the slope height is plotted for different geometrical shapes using the inclined 6H:1V catchment area. The simulations using the spherical object underestimate the roll-out distance while simulations with the other geometries over-estimate the roll-out distances. Similar to the flat catchment area, simulations with the prisms with a rectangular or five-sided polygonal cross section object predict roll-out distances very close to in-situ observations, while the roll-out distances of simulations with ellipsoids power 2 and 4 overestimate them. The linear variation of CRSP highly overestimates the roll-out distances for the 12 m slope, while it underestimates the distances for the slopes with a 24 height.

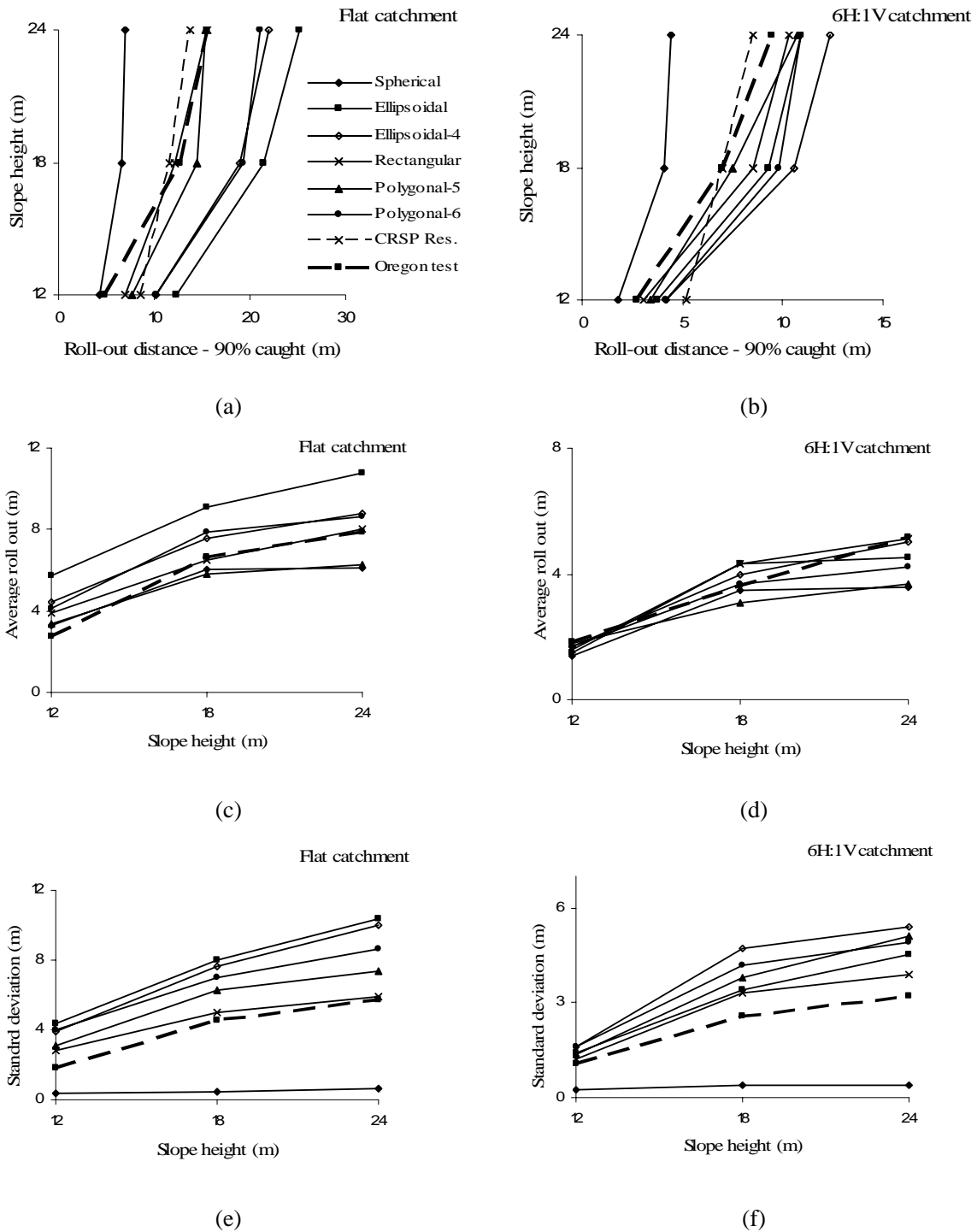


Figure 6.18: Variation of roll-out parameters versus slope height for different geometrical shapes and for the slopes with the same configuration as used in Figure 6.17 and the setup of Table 6.4: (a) roll-out distance for 90% caught, flat catchment area, (b) roll-out distance for 90% caught, 6H:1V catchment area, (c) average roll-out distance, flat catchment area, (d) average roll-out distance, 6H:1V catchment area, (e) roll-out standard deviation, flat catchment area, and (f) roll-out standard deviation, 6H:1V catchment area.

Figures 6.18c and 6.18d plot the average roll-out distances for the flat and inclined modeled catchments areas for different geometrical shapes using the slopes in Figure 6.17. It is apparent that the stop points are much more restricted by the inclined catchment for both the field and numerical tests. The new simulation can predict the average roll-out distances which are much closer to the field data when compared to the values predicted by RocFall® research version for the 90% roll-out distances. The results for the 6H:1V catchment area are even closer to the values observed in the field tests than the flat catchment. Similar to 90% roll-out distance curves, prisms with rectangular or polygonal five-sided cross sections give the best results. The Figure 6.18d illustrates that the predictions for roll-out distances for the 12 and 18 m slopes are closer to the field observations when compared to the values predicted for the 24 m slope.

Figures 6.18e and 6.18f show the standard deviation derived for the fall of the different rock geometries used and the in-situ test for the slopes shown in Figure 6.17. As it was concluded from the 90% and average roll-out distances, the derived standard deviations are greater than the standard deviations derived from the field observations. This may be a result of the lack of data on in-situ test configurations including: the rock shapes, the material properties, the slope roughness, etc.

To derive the roll-out histograms, the stop points for different geometries are derived and plotted in Figure 6.19. These histograms are compared with the histograms derived from in-situ distributions.

Figures 6.19a through 6.19d show the frequency diagram for the six objects used in the 24 m slope with flat catchment area. It is observed that the roll-out distance variation for the ellipsoid-2 and the prism with a rectangular cross section has the same shape as the histograms close to the lognormal distribution. However, the ellipsoidal shapes roll out much further with a larger average roll-out distance and standard variation. The histograms for the prisms with five- and six-sided polygonal shape and the ellipsoid-4 objects are close to the gamma distribution.

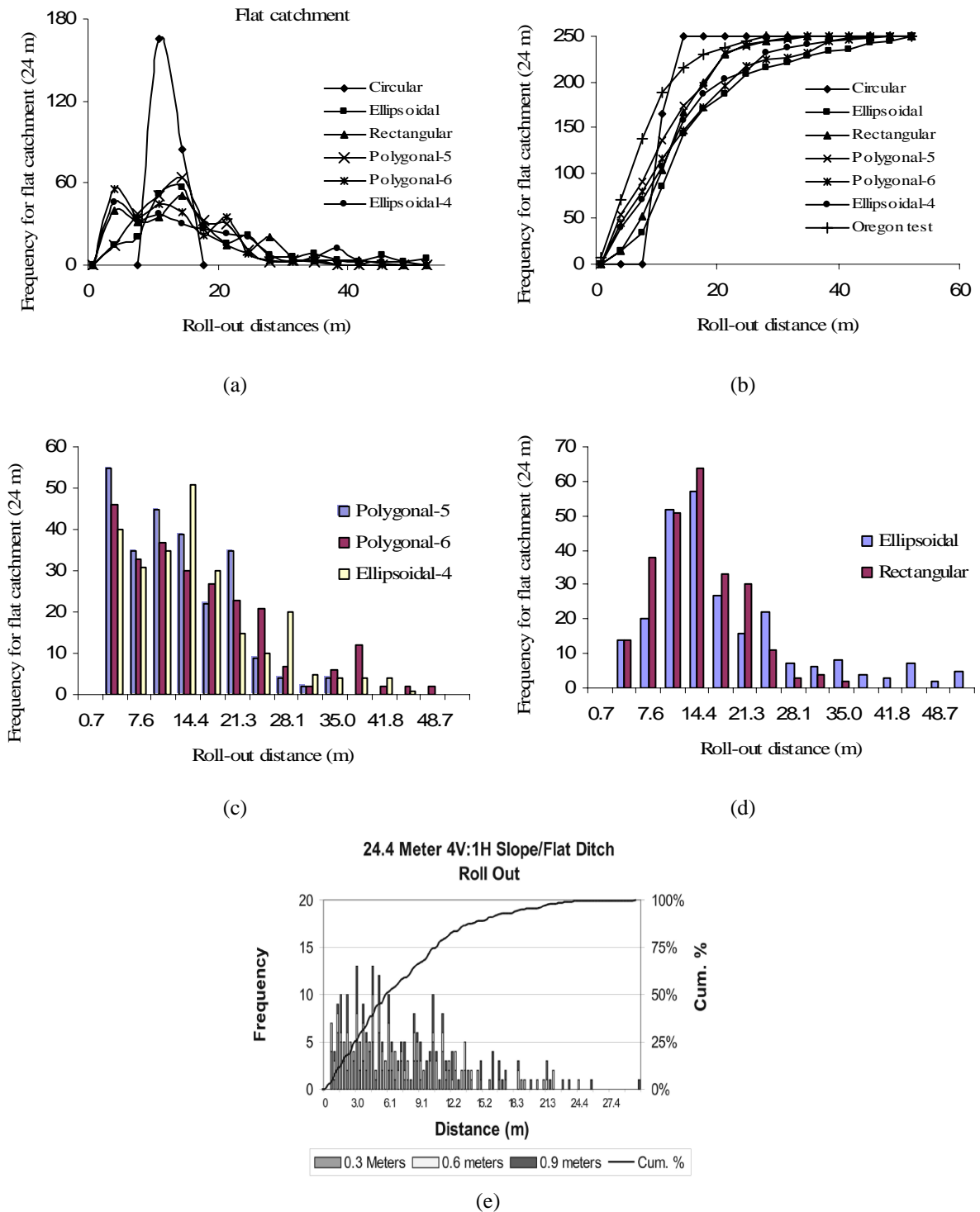


Figure 6.19: Rockfall roll-out distance histograms for different geometrical shapes and for the 24 m slope using the configuration of Figure 6.17 and flat catchment area: (a) frequency curve for different geometries, (b) cumulative frequencies for different geometries, (c) frequency for five and six-sided polygonal shapes, (d) frequency for ellipsoidal and prism with a rectangular cross section, and (e) frequency and cumulative histogram for field observation after Pierson et al. (2001).

Figure 6.19e presents the histogram for the in-situ test results which shows that the stop-point distribution curve is a lognormal curve. The cumulative curve is similar to the histograms of the roll-out distances for prismatic objects shown in Figure 6.19d, but it can be observed that the roll-out distances derived from the simulation are generally larger than the observed values. Larger maximum roll-out distances are also reflected in the 90% stop-point values as shown in Figure 6.18a.

6.4 SUMMARY

Multiple impacts:

- In the application of RBIM to successive impact modeling, it is shown that after the second impact, all the ratios of retrieved energy to the initial energy for different rock geometries have a similar trend of variation. This is in contrast to the first impact, where the rectangular rock had the highest ratio.
- After 5 successive impacts of different objects on a horizontal plane, it was shown that the ellipsoidal rock has both the highest average and the highest maximum ratio of retrieved energy to the initial energy. This shows that the ellipsoidal rock tends to maintain a larger portion of its energy, in comparison to the rectangular rock. Ellipsoidal rocks transfer reserved energy to the rotational mode.
- On average, ellipsoidal (including spherical) objects have the highest roll-out distance in comparison to rectangular and ellipsoid-4 rocks up to an aspect ratio of 2.0.
- When testing using conventional slope materials, it was shown that the energy COR dramatically effects the roll-out distances of ellipsoidal rocks. The friction coefficient, on the other hand, has no significant effect on the roll-out distances.
- The studies performed on multiple impacts shows that it is important to study a chain of impacts rather than a single impact. It is strongly recommended that this type of analyses

should be repeated, taking into account specific slope geometry while considering the variation of rock geometry and material properties.

Case study:

- The different derived curves suggest that the new shape-inclusive simulation program can satisfactorily model the roll-out distances performed by Pierson et al. (2001).
- Prisms with a rectangular or pentagonal cross section replicate the in-situ results adequately, while ellipsoidal and prismatic shapes with a six-sided polygonal cross section overestimate the distances. However, generally the standard deviation derived from the simulation is greater than the field observed values resulting in more dispersed stop-points in comparison to the field observations.
- The provided rock photos in the reports of Pierson et al. confirm that the rock cross section is polygonal.
- The roll-out results are generally conservative. However, it is expected that a two-dimensional model would overestimate the roll-out distances as the energy dissipation is restricted to planar impacts, while in reality a rock tumbles out of a plane causing extra energy dissipation. This out of plane displacement is not measured or reported in two-dimension models, even though it is certainly occurring in the field, as either the rock or the slope is not ideally symmetric.

CHAPTER 7

CONCLUSIONS AND FUTURE WORK

7.1 CONCLUSIONS

Within the framework of this thesis, the application of two different theories in rockfall simulation was investigated using a wide range of geometrical shapes to represent the falling rock. The two applied theories were: discrete element modeling (DEM), and rigid body mechanics. Two simulation programs were developed by the author to assist in investigating the rock behavior in single impacts or during successive multiple collisions.

Application of discrete element modeling in rockfall modeling:

Using discrete element modeling, it was proposed to substitute the linear normal dashpot with a nonlinear viscous module, where the damping force is a function of the impact velocity and the contact indentation. It was shown that in this system of nonlinear viscosity, the normal energy dissipation, or, in other words, the normal coefficient of restitution (COR), is velocity dependent. This nonlinearity eliminates the impact forces at the initiation and termination of the contact. A closed-form solution was derived for the coefficients of restitution using the nonlinear dashpots. A practical method for the calibration of the normal viscosity coefficient for the application in rockfall modeling was offered.

It was shown that a single particle in DEM is similar to a single particle in discrete compliant model (DCM), as offered by Stronge (1994b). Using these models, Maw et al. (1976) showed that for most of the range of angles of incidence, spanning from low to medium, the velocity at the time of termination is in an opposite direction to the initial sliding direction. The rebound velocities predicted by these two models are similar to the elastic solutions, as described by Jonson (1985), and also similar to the experimental results of the impact of an elastic rubber sphere with a Poisson ratio of 0.5. These models are not suitable for modeling impacts with low tangential compliance force, as described by Brach (1988), as the direction of tangential force reverses. These ideas led to the introduction of a mono-direction unit in the tangential direction of DEM model which modifies this behavior and releases the strain energy at the time of tangential reverse. Because it has been observed that the tangential dashpot has a minor effect in mobilizing the tangential force in comparison to the tangential spring, this dashpot is eliminated from the modified discrete element model (MDEM), which is offered in this work. This decreased the total number of parameters in MDEM to four.

To verify the performance of the new module, several numerical tests were carried out using DEM and MDEM. A series of spheres were projected on a horizontal rigid half space with constant normal and variable tangential velocity, resulting in variable angles of impact. The variations of the tangential contact velocities and contact forces for the two models were presented, categorized by low, medium and high angles of impact. There were some perturbations in tangential forces and velocities due to the variations in the indentation. In another numerical test, where the successive impacts of a sphere on a tangential plane were tested, the variations of the sphere's tangential velocity versus time for different friction coefficients were calculated. The mono-direction module successfully eliminated inconsistent variations in the tangential velocity after each impact. These rebound tangential velocities had approximately 1% difference with the values predicted by other rigid body models, for example the model offered by Brach (1984).

To further investigate the application of MDEM, different rock geometries were modeled using rigid body clumps, and rebound velocities were derived for the vertical impact of these objects at variable orientation angles. The rebound velocities were compared with the velocities predicted by the impact of equivalent geometries in the application of the rigid

body impact mechanics (RBIM) proposed by Stronge (1994a). The rebound velocities for a three-particle clump, representing an ellipsoid, were generally far from the RBIM predictions. For the five-particle clump, the velocities approached the values predicted by RBIM, suggesting that the deficiencies were due to poor geometrical representation, not faults contained within the model. For a rectangle with aspect ratio of 2.0, represented by eight particles, the rebound velocities were in agreement with the results produced by RBIM. In the case of four particles, representing a square, the trend of variation of the rebound velocities was between the variation of a square and the variation of a unit superellipse-4. This result is compatible with expectations, as the clump geometry can be considered as an approximation of both the square and the power 4 superellipse. These results strongly suggest that if shape geometries can be sufficiently approximated by the clumps, the proposed MDEM can replicate the rebound velocities that are predicted by the application of rigid body impact mechanics.

In the last modification of DEM, a rotational module needed to be added in the rotational direction for energy dissipation in the rolling mode. This module consisted of two members: the rotational spring, and a slider for representing the rolling friction.

Application of rigid body mechanics in rockfall modeling:

In the framework of Chapters 4 through 6, the application of rigid body mechanics in rockfall studies was investigated. The focus of this thesis was mainly on the application of rigid body impact mechanics (RBIM), introduced by Stronge (1994a), in rockfall studies. In this work, a practical method for defining the tangential slip process was offered, based on the proposal of definitions for critical impulses. These critical impulses halt or terminate the tangential and normal velocities assuming that the tangential and normal impulses vary independently. A table for defining the impact rebound parameters, which were originally offered by Strong (2000), was completed to consider all modes and circumstances in planar impacts. This table, based on the tangential slipping process, defines the critical impulses and rebound velocities. As most classical rockfall models consider rock geometry as spherical or discoidal shapes, collinear impacts were studied as an important type of impact. The definition of critical friction was used to define the lowest tangential COR for different rock geometries in centric

impacts. It was shown that these minimum tangential coefficients of restitution are in strong agreement with the minimum observed values for tangential coefficients of restitution.

In this work, RBIM was compared with some other rigid body and hybrid models available in the rockfall literature. These models were proposed by Azzoni et al. (1995), Pfeiffer et al. (1989) and Descouedres et al. (1987) and the advantages and limitations of each model were discussed. A closed-form solution was developed by the author for the impact model offered by Descouedres et al. (1987) for planar impacts. Proposing several numerical tests, it was shown that an object's coefficients of restitution are strongly affected by its geometry and configuration at the instant of impact. A series of numerical tests were suggested to show that several parameters and settings affect the rebound values, or, in other words, coefficients of restitution. These parameters are as follows: the impact model, the impact material parameters, the rock geometry and its aspect ratio, the impact angle (or the ratio of tangential to normal contact velocities), and the object orientation at the instance of contact (or mass distribution around the contact point).

It was shown that rock geometry dramatically affects the coefficients of restitution, emphasizing that they can not be considered as material properties. In an impact angle of 45° for ellipsoidal rocks, it was shown that the normal COR decreases significantly when there is a decrease in energy COR, while this value increases when there is an increase in the friction coefficient. Tangential COR decreases versus an increase in the friction coefficient while energy COR does not affect this value significantly. In vertical impact numerical tests, the range of variation of COR for rocks with a rectangular cross section is much wider than the range of variation for ellipsoidal objects. Rock slenderness also changes the COR by dispersing the rebound velocities. This makes field investigation of the shape of the rocks a vital step in the estimation of mitigation distances. Infrastructure might be in the safe zone for the fall of spherical rocks but in the danger zone for the fall of ellipsoidal rocks.

Rolling equations of motion in rigid body mechanics were also derived for both general shapes and discoidal objects in two-dimensional space. These equations were implemented in the simulation programs as the equations of motion in rolling mode.

Introducing the Geometrical Rockfall Simulation program (*GeoRFS*)

GeoRFS is a two-dimensional time-domain rigid body rockfall simulation program developed in the framework of this work. The code considers the rock motion in two different modes: freefall or contact, where in the contact mode, impact, rolling-sliding, or arrest may occur. The contact normal velocity separates the rolling-sliding mode from the impact mode and the low energy level defines simulation termination, also called arrest. This simulation uses the rigid body impact mechanics (RBIM) as the main impact model; however, other recognized rockfall impact models are also implemented in the program including those developed by Descouedres et al. (1987) and Azzoni et al. (1995). This simulation considers different shapes for rock geometries, from ellipsoidal to superellipsoidal shapes and from prisms with uniform polygonal cross sections to randomly generated polygons. Surface roughness can be incorporated into the simulation by generating slopes with a rotated surface.

In *GeoRFS*, contact search procedures are performed based on the geometrical transformation method, where the system geometry transforms to the object's local coordinate system. To decrease the computational cost, several optimization procedures are used, such as: circumscribing objects by a circle or a rectangle, time refinements using a relatively large time step, and using the performing grid cell method. Since, in this simulation, the contact forces are not calculated and the rebound velocities are defined explicitly, all exceptional circumstances should be predicted in advance and handled, including: corner impacts, multiple impacts, overlap treatment, and arrest for different geometries at different contact configurations.

The *GeoRFS* engine was finally transferred into RocFall[®], where it benefits from a powerful graphical user interface and probabilistic data generation. Several tests proved that the programs were working correctly, as is discussed in the following section.

Application of rigid body impact mechanics in rockfall simulation:

In Chapter 6, the effect of multiple rock impacts on several parameters and for different rock geometries were investigated, including: energy dissipation, roll-out distance, and bounce

height. To pursue this investigation, several numerical tests were proposed for rock impacts at angles of 0 and 45° on horizontal and inclined planes. The rock geometries used for these studies were: ellipsoid, ellipsoid with power 4 and prism with a rectangular section. Typical material parameters were assumed to be: energy COR = 0.5 and $\mu = 0.57$.

In vertical impacts on horizontal planes, after the second impact, all the ratios of retrieved energy to the initial energy for different rock geometries had a similar trend of variation. This was in contrast to results collected after the first impact, where the rectangular rock had the highest ratio energy amongst all other geometries. After the second impact, the rectangular section had the highest ratio of retrieved energy to initial energy, while the ellipsoidal rock had the highest average value. The trends for the energy ratios repeat for impacts with an initial impact angle of 45°, with the average ratio of retrieved energy being significantly higher for ellipsoidal rocks. The average roll-out distance prior to the second impact, for ellipsoidal power 4 rocks, was greater than for rectangular rocks, and on average both of these rocks roll-out a larger distance in comparison to ellipsoidal rocks.

In the next test, the previously described numerical investigation was repeated for five successive impacts for the three objects and for 0° and 45° impact angles. It was shown that the ellipsoidal rock has both the highest average and the highest maximum ratio of retrieved energy to the initial energy. This shows that the ellipsoidal rock tends to reserve a larger portion of its energy in comparison to the rectangular rock. This tendency is much more visible at an impact angle equal to 45°. An ellipsoidal rock can reserve up to 50% of its initial energy at some initial configurations, while for rectangular rocks this ratio is less than 22%. The high ratio of retrieved energy for ellipsoidal rocks illustrated that the rock has started to roll in some initial orientations; however, the rectangular rock can roll out at a larger distance in comparison to the ellipsoidal rock at the end of five impacts. The energy ratio and roll-out distance for ellipsoids power 4 are between the values for the other two objects.

In order to investigate the effect of rock geometry and aspect ratio on roll-out distances and the ratio of retrieved energy to initial energy, the three different objects were used in a numerical test for impact at an initial angle of 45°. After five impacts, for the objects with an aspect ratio of 1.0, spheres have the lowest maximum roll-out distance, while the square and

ellipsoid power 4 have the highest maximum. On average, ellipsoidal objects have the highest roll-out distance up to an aspect ratio of 2.0. The studies suggest that, when the aspect ratios increase, all the objects have a similar roll-out distance value. From the energy point of view, an ellipsoidal rock may reserve up to 60% of its initial energy, even after five impacts, for some certain initial configurations. On average, ellipsoidal rocks have a higher retrieval rate for their kinetic energy than rectangular rocks; however, the ratio of retrieved energy to initial energy dramatically decreases with an increase in aspect ratio. The average ratio of retrieved energy for rectangular rocks versus the aspect ratio is almost constant. Ellipsoids power 4 show a behavior which is between the behavior of the rectangular and ellipsoidal rocks, highlighting the importance of considering the abrasion of rock corners.

The effect of slope material parameters on the rockfall trajectories and energies was investigated performing a set of 5 successive impact tests with rectangular and ellipsoidal rocks on a horizontal plane. When testing using conventional slope materials, the energy COR dramatically effects the roll-out distances of ellipsoidal rocks. The friction coefficient, on the other hand, has no significant effect on the roll-out distances. Increasing the friction coefficient slightly increases the bounce height for the friction values smaller than 0.5 and the height bounce stays constant for the friction values greater than 0.5. The same trend of variation was observed for the variation of the ratio of retrieved energy to initial energy: the friction coefficient decreases the energy ratio only for low values, smaller than 0.3.

The results for average roll-out distances for rectangular objects showed that the energy COR mainly effects trajectory parameters; however, for rectangular objects, the effect of the friction coefficient is more significant in comparison to ellipsoids. An increase in the friction coefficient decreases the roll-out distance and increases the bounce height. The friction coefficient decreases the average ratio of retrieved energy for rectangular rocks up to friction values of 0.4. These results demonstrated that, due to geometrical shape, the variation of material properties has different effects on rockfall trajectories.

Another series of numerical tests were carried out using research version of RocFall[®], using random object generation. Performing these tests, several initial settings could be generated randomly, including: slope material properties, initial impact angle, and object initial

orientation. The results were in strong agreement with the results from previous sections, where only the initial orientation varied. The observations illustrated that in five impact tests, all three geometries, ellipsoid, rectangular section and ellipsoid-4, have a near equal maximum roll-out distance. However, in ten impact tests, the rectangular section and ellipsoid-4 roll out much further than the ellipsoid. Extending the time of calculation to 10 seconds and ignoring frictional rolling, the figures showed that the ellipsoids started rolling while the rectangular objects reached arrest. The ellipsoid-4 inherits from the characteristics of both the ellipsoid-2 and rectangle as the ellipsoid-4 can be considered a corner-abraded rectangle. As a result, after impact, the ellipsoid-4 has the tendency either to displace significantly after impacts or to start rolling.

Rockfall case study:

In this work the in-situ experiments of Pierson et al. (2001) were modeled using the research version of RocFall[®]. These tests were originally performed to develop design charts for dimensioning rockfall catchment areas adjacent to highways. An attempt was made to replicate the initial test settings; however, not all the necessary information was available including: slope material properties, and rock sample maximum aspect ratios. The simulation results suggest that the shape-inclusive simulation program developed in this work can satisfactorily model the performed rockfall in-situ tests using RBIM. In the simulations, prisms with rectangular and pentagonal cross sections replicate the in-situ results robustly, while ellipsoids and prisms with hexagonal cross sections have predictions for larger roll-out distances in comparison to the field observations. Generally, the standard deviations derived from the simulation were greater than the field-observed values, resulting in more dispersed stop-points compared to the field observations. The predicted roll-out distances were generally more conservative, which is consistent with the expectations from a two-dimensional model. Lower energy dissipation in two-dimensional space is because no energy dissipation occurs in the third dimension due to asymmetries in rock and slope geometry.

7.2 FUTURE WORK

Hoek (2007) states that slope geometry is the most important factor in influencing the rockfall trajectory. It is generally accepted that two-dimensional (2D) rockfall simulations involve major simplifying assumption on the slope geometry in comparison to three-dimensional (3D) modeling. Therefore, a significant improvement to the present rockfall simulator would be to extend the model to full 3D space.

The effect of rock fragmentation in rockfall simulation is considered by a few researchers, such as Fornaro et al. (1990), based mainly on empirical observations. However, most researchers ignore rock fragmentation, as they believe the rock translational energies are more conservative due to higher kinetic energy (Bozzolo et al. (1986) and Azzoni et al. (1995)). This may not be always true, as kinetic energy is proportional to the multiplication of rock mass and the square of rock velocity. Moreover, smaller rock pieces resulting from the fragmentation may roll out further. To resolve this problem, further experimental and numerical investigations are needed.

The application of rigid body impact mechanics is limited to the impact of rigid rocks and rigid slopes, where the deformations of the rocks and slopes are negligible in comparison to the rock dimensions, as explained in Chapter 4. In the case of soft-material slopes, due to large deformations, different constitutive models are needed for defining the rebound velocities.

7.2.1 Three-dimensional simulation

In the real world, rocks travel in 3D space, since neither the rocks nor the slopes are symmetric. Constraining the rock path into two dimensional space results in approximations when determining the rock trajectory and roll-out distances. Theoretically, in 3D models, there is no difficulty in defining the rebound velocities using rigid body mechanics; however, the computational expense of the simulation increases dramatically on three levels: slope modeling, contact search procedures, and the iterative solution of the impact equations. It is the author's opinion that with the recent progress in the speed of processors, optimization

procedures, and utilization of parallel processing, rockfall simulation will tend towards the 3D modeling. In the following sections the 3D impact of rough rigid bodies for the centric and eccentric cases using RBIM are reviewed.

7.2.1.1 3D eccentric collision of objects on rough half space

During the 3D collision of rough bodies, the magnitudes of the velocity components change three dimensionally, provided that the collision is eccentric and the initial direction of sliding is not in-plane with two of the three principal axes of inertia for each body, as is stated by Stronge (2000). The presence of the dry friction force, which is represented by Coulomb's law, results in a curvilinear path in the plan. This variation, in turn, results in variation of the sliding direction in the initial phase of contact in an eccentric contact configuration, shown in Figure 7.1a.

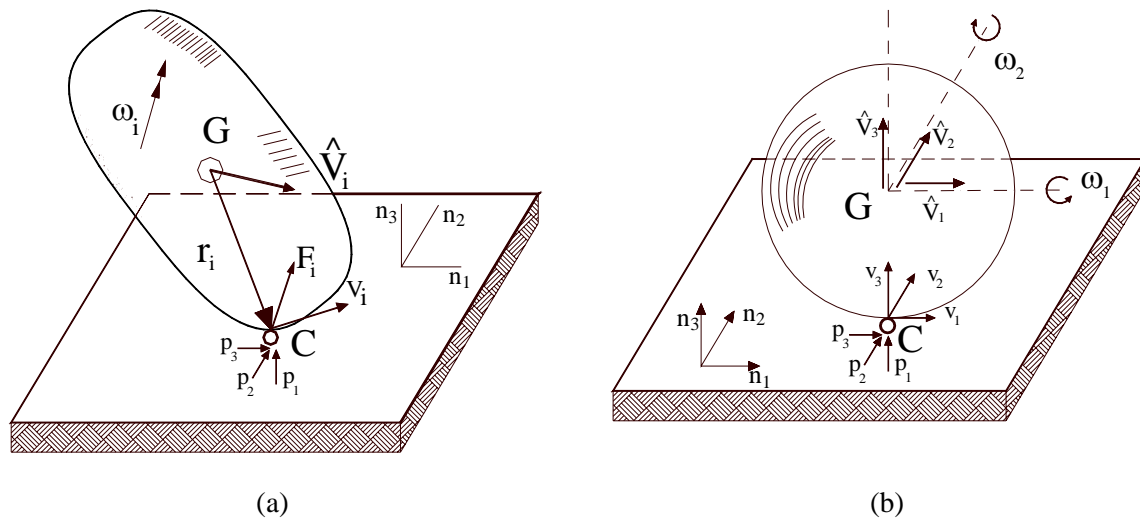


Figure 7.1: 3D rigid body collision on a rigid half space: (a) eccentric impact of an arbitrary object, and (b) collinear impact of a sphere.

Considering the object velocity, \hat{V}_i , the trajectories of the contact velocity are derived by the following equation:

$$v_i = \hat{V}_i + \varepsilon_{ijk} \omega_j r_k \quad (7.2.1)$$

where v_i is the velocity vector at the contact point, ω_i is the rotational velocity vector, r_k is the contact vector and ε_{ijk} is the permutation tensor. Stronge (2000) defines the equation of motion for changes in relative contact velocity as follows:

$$dv_i = m_{ij} dp_j \quad (7.2.2)$$

In the Equation (7.2.2), p_i is the component of impulse at the contact point and $dp_i = F_i dt$, where F_i is the contact force component, t is the time, and dp_i is the variation of impulse components. In Equation (7.2.2), m_{ij}^{-1} is the inverse of the inertia matrix and is defined as:

$$m_{ij}^{-1} \equiv 1/M \delta_{ij} + \varepsilon_{ikm} \varepsilon_{jln} I_{kl}^{-1} r_m r_n \quad (7.2.3)$$

where M is the object's mass and I_{kl} is the inertia tensor passing through the center of gravity. Amontons-Coulomb law of sliding friction (Johnson, 1986) relates the tangential to the normal component of the impulse by introducing the coefficient of limiting friction, μ . This friction force would be active when sliding occurs at the contact point, i.e. $\sqrt{v_1^2 + v_2^2} > 0$, where v_1 and v_2 are the planar trajectories of the velocity. The friction law can be expressed as the following:

$$\begin{aligned} \sqrt{(dp_1)^2 + (dp_2)^2} &< \mu dp & \text{if } v_1^2 + v_2^2 &= 0 \\ dp_1 &= -\frac{\mu v_1}{\sqrt{v_1^2 + v_2^2}} dp, \quad dp_2 = -\frac{\mu v_2}{\sqrt{v_1^2 + v_2^2}} dp & \text{if } v_1^2 + v_2^2 &> 0 \end{aligned} \quad (7.2.4)$$

The sliding direction, ϕ , is defined as the angle between the direction of the sliding vector, s , and the direction of n_l . These two values can be defined as follows:

$$\begin{aligned} \phi &\equiv \tan^{-1}(v_2/v_1) \\ s &= \sqrt{v_1^2 + v_2^2} \end{aligned} \quad (7.2.5)$$

Consequently, the components of tangential velocity can be stated as:

$$v_1 = s \cos \phi \quad v_2 = s \sin \phi \quad (7.2.6)$$

Stronge (2000) showed that the variation of the components of tangential velocity can be defined as a function of the rate of change of the impulse for the normal component of the reaction. The equation of motion for sliding in the direction of $\phi(p)$ can be derived as a function of the variation of the normal impulse, as in the following:

$$\begin{aligned} dv_1 / dp &= -\mu m_{11}^{-1} \cos \phi - \mu m_{12}^{-1} \sin \phi + m_{13}^{-1} \\ dv_2 / dp &= -\mu m_{21}^{-1} \cos \phi - \mu m_{22}^{-1} \sin \phi + m_{23}^{-1} \\ dv_3 / dp &= -\mu m_{31}^{-1} \cos \phi - \mu m_{32}^{-1} \sin \phi + m_{33}^{-1} \end{aligned} \quad (7.2.7)$$

These equations of motion are not separable into independent equations, except in two situations: when the impact condition is centric and the contact vector passes through the center of gravity, or when impact occurs in the smooth condition, in other words, when $\mu = 0$. As these conditions are not usually satisfied, the rates of change for the components of the tangential velocity are usually different from each other, as a result the direction of slip varies, while $s > 0$.

7.2.1.2 3D centric collision of objects on rough half space

Figure 7.1b shows the case of centric impact for a sphere including the object's velocity trajectories at the center of gravity, and the contact point. Strong (1994a) and (2000) defined the object's rebound velocities at the termination impulse, p_f , as follows:

$$\frac{\hat{V}_i(p_f)}{\hat{V}_3(0)} = \begin{cases} \begin{cases} \frac{\hat{V}_i(0)}{\hat{V}_3(0)} - \frac{2}{7} \frac{v_i(0)}{\hat{V}_3(0)} & \text{if } \left| \frac{s(0)}{\hat{V}_3(0)} \right| < 3.5\mu(1+e_*) \\ \frac{\hat{V}_i(0)}{\hat{V}_3(0)} + \mu(1+e_*) \cos \tilde{\phi}_i(0) & \text{if } \left| \frac{s(0)}{\hat{V}_3(0)} \right| > 3.5\mu(1+e_*) \end{cases} \\ -e_* \end{cases} \quad (7.2.8)$$

In these equations v_i is the contact point velocity as defined in Equation (7.2.1), e_* is the energy coefficient of restitution illustrated in Section 4.2.2 and $\hat{\phi}_i$ is:

$$\hat{\phi}_i = \begin{cases} \phi, & i = 1 \\ \pi/2 - \phi & i = 2 \end{cases} \quad (7.2.9)$$

Equation (7.2.8) shows that the variation in the object's velocity can be as large as 2/7th of the velocity at the contact point. A complete discussion of the lowest values of tangential velocity for different geometries in collinear impacts is provided in Section 4.2.4.

7.2.2 Application of RBIM in hybrid modeling

It was shown in Section 5.1.1 that utilizing hybrid rockfall models incorporates inaccuracies into rockfall simulations. It is also illustrated in Chapter 4, using rigid body models, that the domain of variation for the coefficients of restitution is much wider than the traditional definitions of the COR provided in lumped-mass models (Ashayer and Curran (2007)). Many researchers, such as Bozzolo (1986), Pfeiffer (1989), Azzoni (1995), Stevens (1998) and Jones et al. (2000), use hybrid models and introduce simplified mathematical models which have either mechanical or geometrical approximations in comparison to rigid body models. Any hybrid modeling utilizing RBIM will dramatically improve the accuracy of the simulation as RBIM thoroughly accounts for the sliding mechanisms.

As a result, we suggest a new hybrid model using RBIM (or any other rigid body model), which applies the following steps:

1. Define the rock geometry and dimensions based on field observations and an appropriate statistical distribution.
2. Calculate the intersection of the rock path parabola and the slope segment (refer to Figures 5.1 and 5.2). The ratio of velocities at the instance of impact determines the impact angle. Define the material properties, energy COR, and friction coefficient, from the statistical distribution of the material properties.
3. At the time of contact, rock orientation or mass distribution around the contact point dramatically affects the coefficients of restitution (COR). There are two practical approaches to estimating the CORs: randomly defining them using the distribution of the

coefficients, or randomly choosing the impact orientation. When the impact orientation is chosen randomly, the rebound velocities can be determined based on geometrical mapping. This geometrical mapping results from the impact of the object and a horizontal plane where the impact velocities are mapped to the transformed geometry. This method seems to be more practical as the variations of CORs do not always follow a definite statistical distribution. Figure 7.2 shows the histogram of variation of the coefficients of restitution during the impact of an ellipsoid on a horizontal half space with an impact angle of 45° , where the numerical test is described in Figure 4.8.

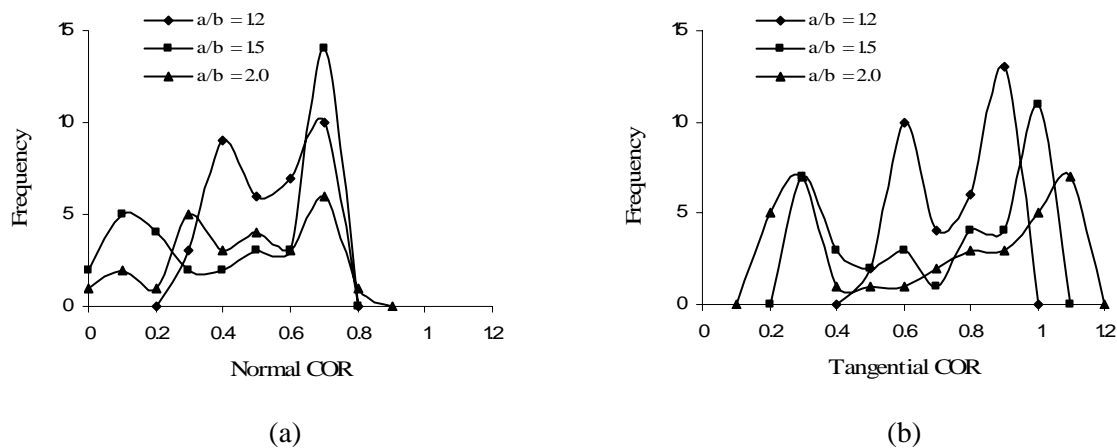


Figure 7.2: Histogram of the variation of the coefficients of restitution for an ellipsoid with different aspect ratios for an impact angle of 45° and the settings of Figure 4.8: (a) tangential COR, and (b) normal COR.

7.2.3 Complementing the application of modified DEM in 2D and 3D rockfall modeling

In Chapter 3, the Voigt-Kelvin system of springs and dashpots, which is the most well-known and widely-used contact constitutive model, was modified to model low-compliant impacts. It was shown that this model can accurately replicate the rigid body impact of a group of particles, known as clumps. The application of this modified version of DEM (MDEM) can be used to model complicated rock geometries. Some of the rockfall features like fragmentation can be only captured by models like DEM, while rigid body impact mechanics are not capable of capturing these features.

Potyondy et al. (2004) used contact bonds to successfully capture the elastic moduli of rocks, consisting of a deformable assembly of particles glued together; however, it was shown that the spring and dashpot cannot model low-compliant impacts. It is our opinion that MDEM can replace the classical spring-dashpot modules used as contact constitutive models in most discrete element models. Once the new model been thoroughly tested and verified against other models and in-situ and laboratory rockfall experiments, it may also be able to model soft impacts and rock fragmentations.

7.2.4 Extending the application of *GeoRFS* to soft-soil slopes

Several rockfall impact constitutive models are proposed to capture soft-soil impacts including: Heidenreich (2004), Azimi et al. (1977), and Ushiro et al. (2000). Each of these models is offered for certain rock geometries, mainly spherical or cylindrical. In section 5.4.9, it was explained that *GeoRFS* is implemented in an object-oriented paradigm. Already, in addition to RBIM, two other impact constitutive models offered by Descouedres et al. (1987) and Azzoni et al. (1995) are implemented in the program. The application of soft-ground slope materials can be implemented into *GeoRFS* which by nature is a geometrical model and considers the rock shape. Then, this application can be expanded to hybrid modeling using the hybrid concept introduced in Section 7.2.2. This way, complicated soft-impact constitutive models which predict rock trajectory can be applied and studied.

APPENDIX 1

VALUES OF RESTITUTION, FRICTION, AND ROLLING FRICTION COEFFICIENTS

Table A.1.1: Values of COR in the literature defined by various researchers as well as different types of coefficient and for different materials after Heidenreich (2004) and RocFall[®] 4.0 (2002)

Reference	Values for R_n	Values for R_t	Values for R_E	Values for R_{TE}	Values for R_{Kin}	Values for μ	Values for μ_{rot}	Remarks
Habib 1977	0.75-0.80							Based on experience in Italy
	0.5-0.6							Based on experience in Norway
Piteau and Claton 1977	0.8-0.9	0.65-0.75						Solid rock
	0.5-0.8	0.45-0.65						Detrital material mixed with large rock boulders
	0.4-0.5	0.35-0.45						Compact detrital material mixed with small boulders
	0.2-0.4	0.2-0.3						Grass covered slopes
Wu 1985	0.2-0.8	0.5-0.75						Rock on rock or wood platform
Heierli 1985	0.95		0.9					Rock
	0.55		0.3					Gravel layer (35 cm)
	0.45		0.2					Gravel layer (70 cm)
	0.45		0.2					Debris
Bozzolo & Pamini 1986				0.7				Rock at a slope angle of 44°
				0.55				Debris at a slope angle of 57°
Descouedres & Zimmermann 1987					0.4	0.5		Vineyard slopes
					0.85	0.5		Rock slopes
Hoek 1987	0.53	0.99						Clean hard bedrock
	0.4	0.9						Asphalt roadway
	0.35	0.85						Bedrock outcrops with hard surface, large boulders
	0.32	0.82						Talus cover
	0.32	0.8						Talus cover with vegetation
	0.3	0.8						Soft soil, some vegetation

Table A.1.1 (continued):

Reference	Values for R_n	Values for R_t	Values for R_E	Values for R_{TE}	Values for R_{kin}	Values for μ	Values for μ_{rot}		Remarks
Urciuoli 1988	0.05-0.35	0.5-1	0.02-1						Rock block impacting limestone
	~0	0.24							Debris fan
Gerber 1995	0.17-0.43	0.45-0.88							Rock (limestone)
Ushiro & al. 2000	0.1-0.4	0.71							?
Pfeiffer & Bowen 1989 (older versions of program CRSP)	0.37-0.42	0.87-0.92							Smooth, hard surface as paving rock
	0.33-0.37	0.83-0.87							Bedrock or boulders with little soil or vegetation
	0.30-0.33	0.83-0.87							Talus with little vegetation
	0.3-0.33	0.80-0.83							Talus with some vegetation
	0.28-0.32	0.80-0.83							Soft soil slope with little vegetation
	0.28-0.32	0.78-0.82							Vegetated soil slope
Giani 1992, Barbieri & al. 1988	0.5	0.95							Bedrock
	0.35	0.85							Bedrock covered by large blocks
	0.3	0.7							Debris formed by uniform distributed elements
	0.25	0.55							Soil covered by vegetation
Azzoni & al. 1995							0.3 m ³	1.2 m ³	
					0.75-0.90		0.4-0.45	0.4	Rock (limestone)
					0.55-0.6		0.5-0.6	0.4	Fine angular debris and earth (compacted)
					0.35-0.45		0.7-0.8	0.6-0.7	Fine angular debris and earth (soft)
					0.45-0.5		0.6-0.7	0.5-0.6	Medium angular debris with angular rock fragments
					0.4-0.5		0.70-1.00		Medium angular debris with scattered trees
					0.55-0.7		0.65-1.20	0.60-0.80	Coarse angular debris with angular rock fragments
					0.5-0.6		0.55-0.65	0.45-0.50	Earth with grass and some vegetation
					<0.2		0.85		Ditch with mud
					0.5-0.65		0.50-0.65		Flat surface of artificially compacted ground
				0.75		0.40-0.45		Road	
Kamijo 2000	0.1-0.35								Vertical impact of a 220kg rock on hard surface
	0.1								Vertical impact of a 800kg rock on hard surface

Table A.1.1 (continued):

Reference	Values for R_n	Values for R_t	Values for R_E	Values for R_{TE}	Values for R_{Kin}	Values for μ	Values for μ_{rot}	Remarks
Jones & al. 2000 (Values gathered by program calibration for CRSP 4.0)	0.6-1.0	0.9-1.0						Smooth hard surface and paving
	0.15-0.3	0.75-0.95						Bedrock and boulder fields
	0.12-0.2	0.65-0.95						Talus and firm soil slopes
	0.1-0.2	0.5-0.8						Soft soil slopes
Budetta & Santo 1994 (evaluated by program calibration)	0.2	0.53						Rock
Kobayashi et al. 1990							0.64	Rock slope also covered with trees
							0.38	Rock
							0.53	Scattered sagebrush, grass, few other boulders
							0.33	Rock
Hungry, O. and Evans, S.G. 1988	0.5	0.8						Sparsely forested slope covered by a veneer of very fine weathered talus derived from weak schistose
	0.5	0.8						Limestone on bare uniform talus slope formed of basalt fragments
	0.7	0.9						Rectangular boulder of metamorphosed tuff on bare rock and a steep snow covered shelf
Robotham et al.	0.32	0.71						Limestone face
	0.3	0.62						Partially vegetated limestone scree
	0.32	0.71						Uncovered limestone blast pile
	0.25	0.49						Vegetated covered limestone pile
	0.28	0.84						Chalk face
	0.27	0.60						Vegetated chalk scree

APPENDIX 2

DEFINING RIGID BODY IMPACT MECHANICS (RBIM) PARAMETERS USING EXPERIMENTAL METHODS

One of the most important advantages of rigid body impact mechanics is that the two model parameters, e_* and μ , are experimentally measurable. As described in Chapter 4, to apply rigid body mechanics, another parameter, rolling friction, μ_r , needs to be defined. There are several methods which can be used; however, only the simplest methods are reviewed in this Appendix.

Normal coefficient of restitution, e_* :

Ideally, an object should be dropped vertically when the impact configuration is collinear. In this case the definition of the energy coefficient of restitution is the same as the kinetic and the kinematic coefficients of restitution. The square root of the ratio of the rebound height, h_1 , to the initial height, h_0 , defines the energy coefficient of restitution, e_* , or simply the normal coefficient of restitution, R_n , as shown in Figure A.2.1. It is also possible to use the second measured rebound heights, h_2 , or the third, h_3 , to define this coefficient as described by Equation (A.2.1). It is recommended to use circular shapes or shapes with a curvilinear side as the rebound height for these objects are less sensitive to small tilting if when the impact configuration is not completely collinear.

$$e_* = \sqrt{h_1/h_0} = \sqrt[4]{h_2/h_0} = \sqrt[6]{h_3/h_0} \quad (\text{A.2.1})$$

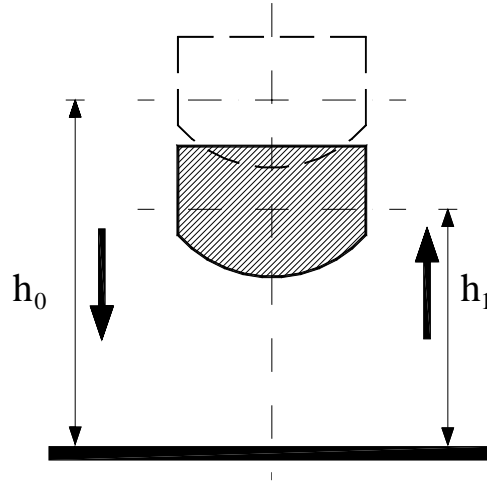


Figure A.2.1: Defining rebound height, h_r , using the collinear drop test.

Friction coefficient, μ :

The sliding experiment can be used to calculate the friction coefficient between two objects, as shown in Figure A.2.2a. In this case, the velocity of the sliding object at two different times, t_0 and t_1 , should be recorded. Using Equation (A.2.2), the friction coefficient can be defined as follows:

$$\mu = \tan(\phi) - \frac{[V_x^2(t_1) - V_x^2(t_0)]}{2g \cos(\phi)[X(t_1) - X(t_0)]} \quad (\text{A.2.2})$$

where $V_x(t_1)$ and $V_x(t_0)$ are the velocities parallel to the sliding surface; $X(t_1)$ and $X(t_0)$ are the object locations at times t_1 and t_0 , respectively; and g is the gravitational acceleration. It should be mentioned that if the object slides with a constant velocity, then: $\mu = \tan(\phi)$.

Rolling friction coefficient, μ_r :

Figure A.2.2b shows the rolling of a circular object on an inclined surface which can be used to define the rolling friction coefficient. If the object's velocities at the two different times t_1 and t_0 are recorded, Equation (A.2.3) can be used to calculate μ_r , as defined by Azzoni et al. (1995).

$$\mu_r = \tan(\phi_r) - \frac{[V_x^2(t_1) - V_x^2(t_0)]}{2\left(\frac{1}{1+k_r^2}\right)g \cos(\phi_r)[X(t_1) - X(t_0)]} \quad (\text{A.2.3})$$

In the above equation, k_r is polar radius of gyration as defined in Section 5.2.3, and the other parameters are the same as defined in Equation (A.2.2). Similar to the sliding experiment, if the object rolls with a constant velocity, then: $\mu_r = \tan(\phi_r)$.

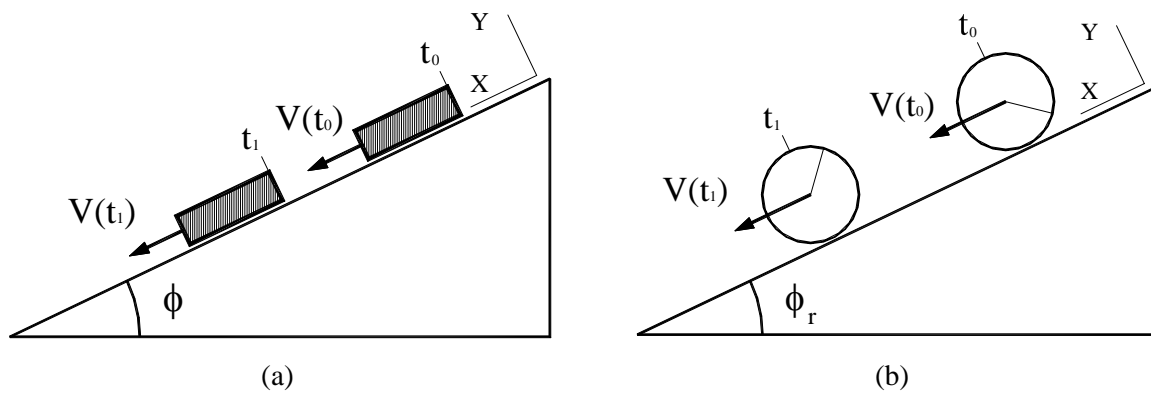


Figure A.2.2: Calculating the friction coefficients: (a) using the sliding test on an inclined surface for the friction coefficient, μ , and (b) using rolling test on an inclined surface to define the rolling friction coefficient, μ_r .

APPENDIX 3

EFFECT OF ROCK SHAPE ON ROCK TRAJECTORIES PERFORMING RANDOM OBJECT GENERATION

In this Appendix, the numerical experiments performed in Section 6.2.4.2 are presented, with the trajectories for each object given in a separate figure. This separation helps to follow each rock geometry more easily in comparison to the case when all of them are shown in one figure. The applied geometries are ellipsoids power 2 and 4, and a rectangle. In each case, 250 rocks are generated for each of the three assumed geometries, and are projected at the flat surface. The initial impact settings are derived based on the random object generation procedure where the data settings are presented in Table 6.4 and with aspect ratios of 2:1 and the conventions used Table 6.1.

Figure A.3.1 depicts the rock path trajectories resulting from five impacts of the three rocks on a flat surface. Figures A.3.1a to A.3.1.c show the trajectories for each individual rock and Figure A.3.1 shows the trajectories resulting from the impact of three rocks from another rock generation. It can be observed from these figures that the three rocks experience approximately the same roll-out distance.

Figure A.3.2 depicts the trajectories resulting from 10 successive impacts of the proposed rock geometries. From Figures A.3.2a to A.3.2.c, it can be observed that the ellipsoid-4 has the highest roll-out distance after 10 impacts. Following the ellipsoid-4, the rectangle has the next greatest maximum roll-out distance, followed by the ellipsoid-2. It can be observed that

ellipsoids-2 roll out much less than the other two shapes, both in average and in maximum value.

Figure A.3.3 shows the rock path trajectories resulting from the impacts and rolling of the three randomly generated rocks for a time equal to 10 seconds when the rolling friction coefficient is set to zero. Figures A.3.3a and A.3.3b illustrate that the rolling mode for ellipsoidal objects is a significant mode of motion; however, this mode occurs more often for ellipsoid-2 in comparison to ellipsoid-4. Figure A.3.3c shows that the rectangular rocks lose their energy during the simulation period and reach arrest. It can be seen that, no significant displacements occur for rectangular rock during rolling-sliding mode of motion.

According to Hoek (2007), the slope geometry is the most significant factor in controlling the roll-out distances. It is recommended to test all the rock geometries with the proposed slope and to find the maximum roll-out distances for each rock under the different modes of motion, either impact or rolling-sliding.

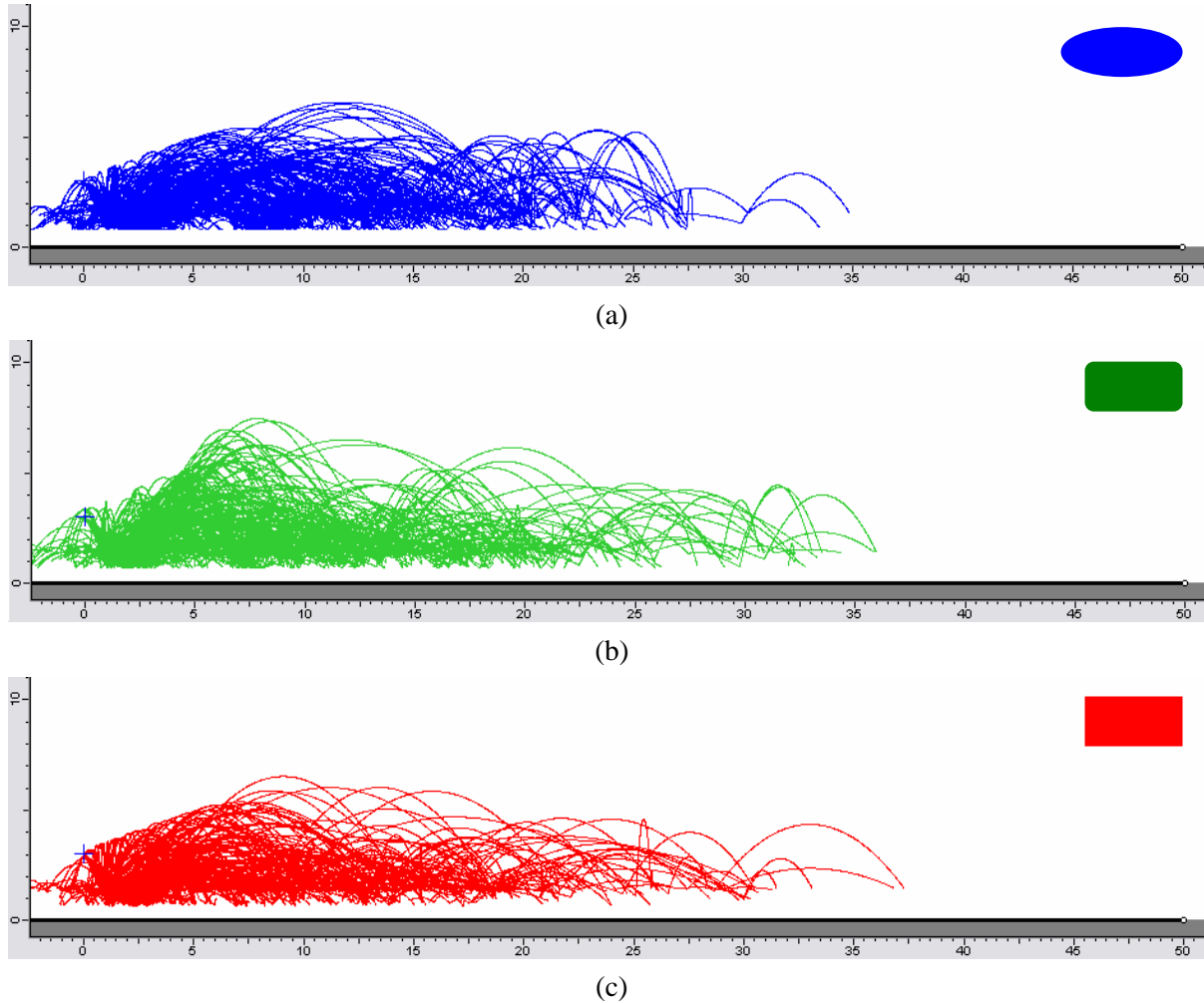


Figure A.3.1: Rock trajectories during successive impacts for rock geometries with the configurations of Figure 6.1a and settings of Figure 6.4 for different rock geometries with aspect ratio equal to 2:1 after 5 impacts: (a) an ellipsoid-2, (b) an ellipsoid-4, and (c) a rectangle.

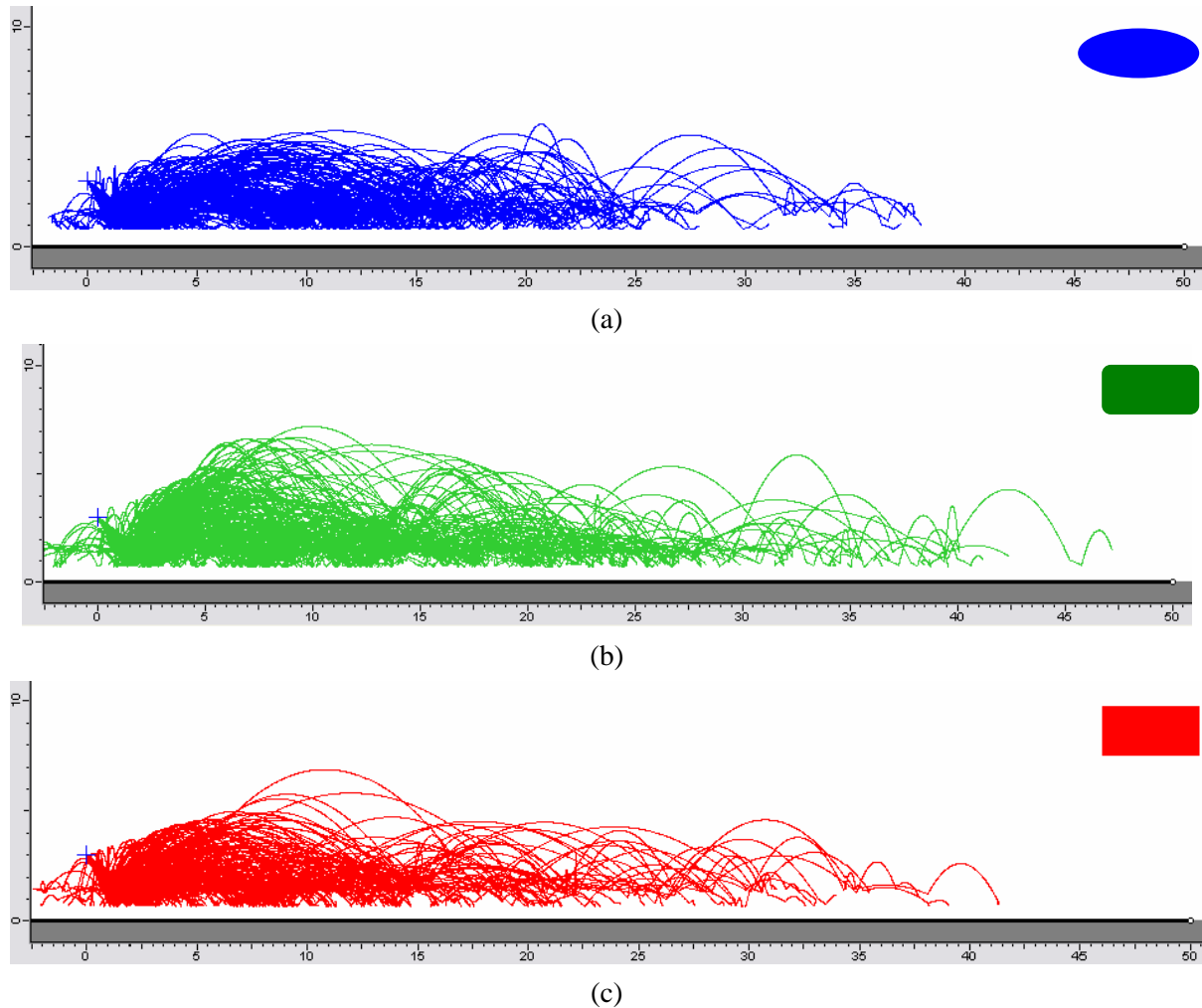


Figure A.3.2: Rock trajectories during successive impacts for rock geometries with the configurations of Figure 6.1a and settings of Figure 6.4 for different rock geometries with aspect ratio equal to 2:1 after 10 impacts: (a) an ellipsoid-2, (b) an ellipsoid-4, and (c) a rectangle.

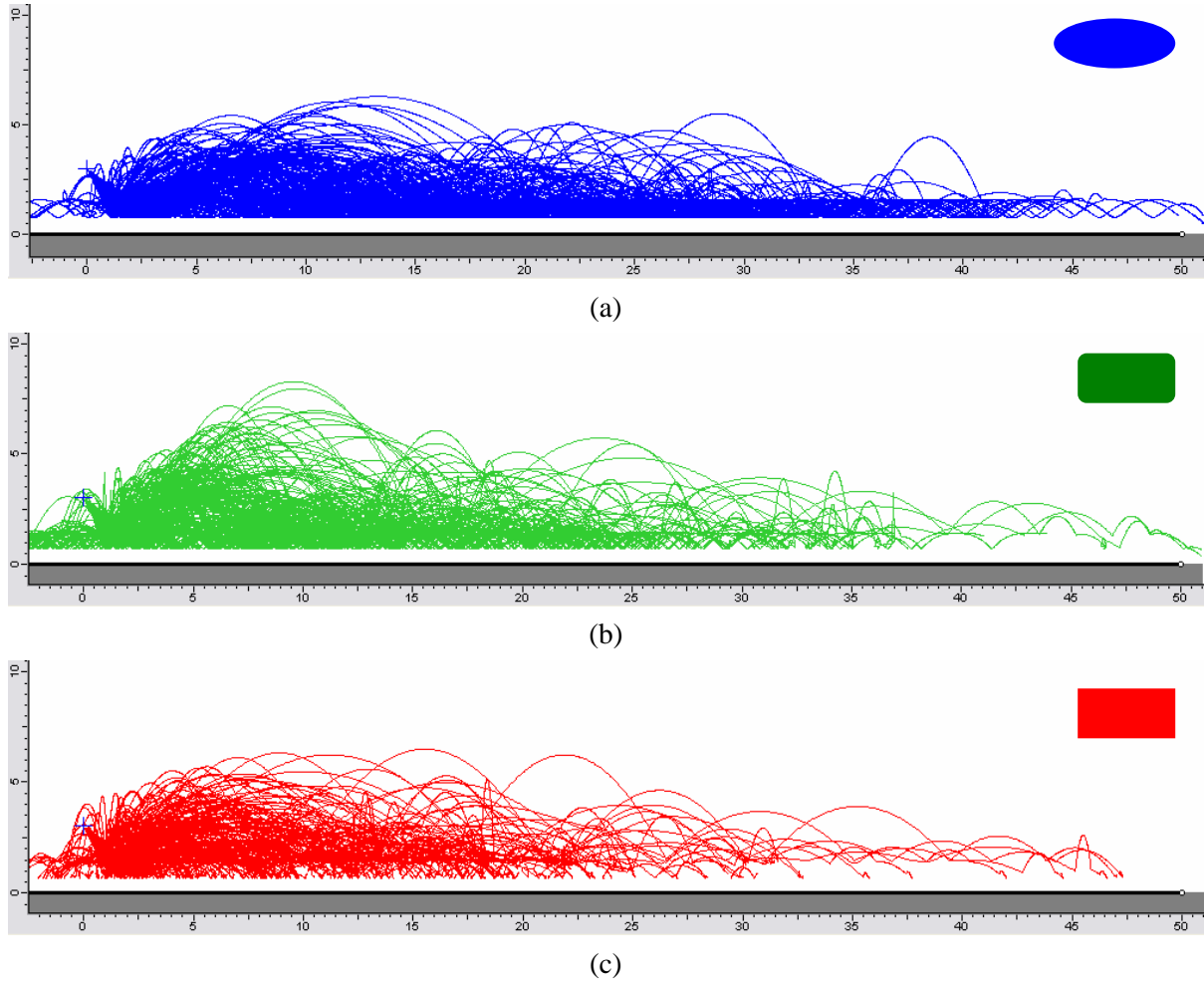


Figure A.3.3: Rock trajectories during successive impacts for rock geometries with the configurations of Figure 6.1a and settings of Figure 6.4 for different rock geometries with aspect ratio equal to 2:1 after 10 seconds: (a) an ellipsoid-2, (b) an ellipsoid-4, and (c) a rectangle.

References

- Ashayer P. and Curran J.H., 2007: Coefficients of restitution in the application of rigid body impact mechanics in rockfall analysis, *SME 2007 annual meeting and Colorado Mining Association 109th National Western Mining Conference*, Denver, 116-121
- Azimi C. and Desvarreux, P., 1988: Les paravalanches: ouvrages de protection contre les avalanches et les chutes de pierres. *Direction de la formation continue et de l'action internationale*, Chambéry, 8-10 mars 1988, Paris
- Azzoni A., Barbera G.L. and Zaninetti A., 1995: Analysis and prediction of rockfalls using a mathematical model. *International Journal of Rock Mechanics and Mining Science & Geomechanics*, 32(7), 709-724
- Azzoni A. and Freitas M.H., 1995: Experimentally Gained Parameters, Decisive for Rock Fall Analysis. *Rock Mechanics and Rock Engineering*, 28(2), 111-124
- Bardet J.P., 1994: Observations on the effect of particle rotations on the failure of idealized granular materials. *Mech. Mat.*, 18, 159-182
- Bennett S., McRobb S. and Farmer R., 2002: *Object-oriented systems analysis and design using UML* (2nd ed. ed.). Toronto: McGraw-Hill
- Belytschko T., 2000: In Liu W. K., Moran B., *Nonlinear finite elements for continua and structures*, New York: John Wiley
- Bozzolo D. and Pamini R., 1986: Simulation of rock falls down a valley side. *Acta Mechanica*, 63(1-4), 113-130
- Bozzolo D., Pamini R. and Hutter K. 1988: Rockfall analysis – A mathematical and its test with field data. *Landslides, Proceedings of the fifth international symposium on landslides*, 10-15 July, 1, 555-560, Lausanne
- Brach R.M., 1984: Friction, restitution, and energy loss in planar collisions. *Transactions of the ASME Journal of Applied Mechanics*, 51, 164-170
- Brach R.M., 1988: Impact dynamics with applications to solid particle erosion. *International Journal Impact Engineering*, 7 (1), 37-53
- Brach R. M., 1991: *Mechanical impact dynamics: rigid body collisions*. John Wiley
- Chatterjee A. 1997: Rigid body collisions: some general considerations, new collision laws and some experimental data, *PhD Dissertation*, Cornell Uni., Ithaca, NY, USA
- Chau K.T., Wong R.H.C. and Wu. J.J. 2002: Coefficient of restitution and rotational motions of rockfall impacts. *International Journal Rock Mechanics Mining Science*, 39, 69–77

- Cundall P.A. and Strack O.D.L., 1979: A discrete numerical model for granular assemblies, *Geotechnique*, 29(1), 47-65
- Cundall P.A. and Hart R.D., 1992: Numerical modeling of discontinua. *Engineering Computations*, 9(2), 101-113
- Deitel H.M. and Deitel P.J., (2001): *C++ how to program* (3rd ed.), Upper Saddle River, NJ: Prentice Hall.
- Descouedres F. and Zimmermann T., 1987: Three-dimensional dynamic calculation of rockfalls. *Proceedings of the 6th International Congress on Rock Mechanics*, Montreal, 337-342
- Evans S.G. and Hunger O., 1993: The assessment of rockfall hazard at the base of talus slopes. *Canadian geotechnical journal*, 30, 620-636
- Fornaro M., Peila D. and Nebbia M., 1990: Block falls on rock slopes - application of a numerical simulation program to some real cases, *Proceedings of the 6th International Congress IAEG*, Rotterdam, NL., 2173-2180
- Giani G.P., Giacomini A., Migliazza M. and Segalini A., 2004: Experimental and theoretical studies to improve rock fall analysis and protection work design. *Rock Mechanics and Rock Engineering*, 37 (5), 369-389
- Guzzetti F., Crosta G., Detti R. and Agliardi F., 2002: STONE: a computer program for the three-dimensional simulation of rock-falls, *Computer & Geosciences*, 28, 1079-1093
- Giani G.P., 1992: Rock slope stability analysis. Balkema, Rotterdam
- Habib P., 1976: Note Sur Le Rebondissement Des Blocs Rocheux, Istituto Speromente Modolli E Structure. In Meeting on Rockfall Dynamics and Protective Works, Bergamo, Italia, 123-125
- Herbert R.G. and McWhannell D.C., 1977: Shape and frequency composition of pulse from an impact pair. *Journal of Engineering for Industry*, August, 513-518
- Heidenreich B., 2004: Small- and half-scale experimental studies of rockfall impacts on sandy slopes, *PhD Dissertation*, Ecole polytechnique federale de Lausanne
- Hill F.S. 2001: Computer graphics: Using OpenGL (2nd ed.). *Upper Saddle River*, N.J.: Prentice Hall
- Hoek E., 1986: Rockfall - a program in Basic for the analysis of rockfalls from the slopes. Golder Associates/University of Toronto, *Unpublished notes*
- Hoek E., 2007 (new edition): Practical rock engineering, course notes, University of Toronto
- Hunt K.H., and Crossley, F.R.E. 1975: Coefficient of restitution interpreted as damping in vibroimpact. *Transactions of the ASME, Series E*, 42(2), 440-445
- Iwashita K. and Oda M., 1998: Rolling resistance at contacts in simulation of shear band development by DEM. *Journal Engineering Mechanics*, 124(3), 285-292

- Jaklič A., Leonardis A. and Solina F., 2000: Segmentation and recovery of superquadrics. Boston, Mass.: Kluwer Academic Publishers
- Johnson K.L., 1985: *Contact mechanics*. Cambridge UK, Cambridge University Press
- Jones C.L., Higgins J.D. and Andrew R.D., 2000: Colorado Rockfall Simulation Program Version 4.0. Colorado Geological Survey, Colorado
- Keller J.B., 1986: Impact with friction. *Journal of Applied Mechanics, ASME*, 53(1), 1-4
- Kobayashi Y., Harp E.L. and Kagawa T., 1990: Simulation of rockfall triggered by earthquakes. *Rock Mechanics and Rock Engineering*, 23: 1-20
- Maw N., Barber J.R. and Fawcett J.N., 1977: The rebound of elastic bodies in oblique impact. *Mechanics Research Communications*, 4, 17-22
- Maw N., Barber J.R. and Fawcett J.N., 1976: The oblique impact of elastic spheres. *Wear*, 38, 101-114
- Meriam J.L. and Kraige L.G., 1987: *Engineering Mechanics – Dynamics*. John Wiley
- Munjiza A. and Andrews K.R.F., 1998: NBS contact detection algorithm for bodies of similar size. *International Journal for Numerical Methods in Engineering*, 43(1), 131
- Munjiza A., 2004: The combined finite-discrete element method. Hoboken, NJ: Wiley
- PFC^{2D} theory and background, Ver. 3.0, 2002, Itasca Consulting Group, Inc.
- Peters B. and Dziugys A., 2002: Numerical simulation of the motion of granular material using object-oriented techniques. *Computer Methods in Applied Mechanics and Engineering*, 191(17-18), 1983-2007
- Pfeiffer T.J. and Bowen T.D., 1989: Computer simulations of rockfalls, *Bulletin of the association of Engineering Geologists*, 26(1): 135-146
- Pierson L.A, Gullixson F.C and Chassie R.G. 2001: Rockfall catchment area design guide, Final report, SPR-3(302), Oregon Department of Transportation, USA
- Poisson S.D, 1811: *Traite de Mecanique*, Courier, Paris
- Potyondy D.O. and Cundall P.A., 2004: A bonded-particle model for rock. *International Journal of Rock Mechanics and Mining Sciences*, 41, 1329-1364
- Press W.H., Teukolsky S.A., Vetterling W.T. and Flannery B.P., 2002: Numerical recipes in C : The art of scientific computing (2nd ed.). New York, NY, USA: Cambridge University Press
- Ritchie A.M. 1963: Evaluation of rockfall and its control. *Highway research record 17*, Washington, USA
- RocFall[®] Verification manual, 2002: Rocscience Inc.

- Shi G.H. and Goodman R.E., 1985: Two-dimensional discontinuous deformation analysis. *International Journal for Numerical and Analytical Methods in Geomechanics*, 9(6), 541-556
- Spang R.M. and Rautenstrauch R.W., 1988: Empirical and mathematical approaches to rockfall protection and their practical applications. *Proceedings of the Fifth International Symposium on Landslides*, Lausanne , 2, 1237-1243
- Spang R.M. and Sönser Th., 1995: Optimized rockfall protection by 'rockfall'. *Proceedings of the 8th International Congress in Rock Mechanics*, Tokyo, Japan, 1233-1242
- Stevens W., 1998: Rockfall: a tool for probabilistic analysis, design of remedial measures and prediction of rockfalls, *M.A.Sc. Thesis*, Department of Civil Engineering, University of Toronto, Ontario, Canada
- Stoianovici D. and Hurmuzlu Y., 1996: A critical study of the applicability of rigid-body collision theory, *Journal of Applied Mechanics*, 63, 307-316
- Stronge W.J., 1990: Rigid body collisions with friction. *Proceedings of the Royal Society London*, A431, 169-181
- Stronge W.J., 1991: Friction in collisions: resolution of a paradox. *Journal of Applied Physics*, 69(2), 610-612
- Stronge W.J., 1994a: Swerve during three-dimensional impact of rough rigid bodies. *Journal of Applied Mechanics*, 61, 605-611
- Stronge W.J., 1994b: Planar impact of rough compliant bodies, *International Journal of Impact Engineering*, 15(4), 435-450
- Stronge W.J., 2000: *Impact Mechanics*. Cambridge University Press
- Ting J.M., 1991: An ellipse-based micromechanical model for angular granular materials. *proceedings ASCE engineering mechanics specialty conference on mechanics computing in 1990's and beyond*, Columbus, Ohio, 2, 1214-1218
- Ting J.M., 1992: A robust algorithm for ellipse-based discrete element modeling of granular materials. *Computers and Geotechnics*, 13(3), 175-186
- Ting J.M. and Corkum B.T., 1992: Computational laboratory for discrete element geomechanics. *Journal of Computing in Civil Engineering*, 6(2), 129(18)-147
- UDEC (Universal Distinct Element Code) theory and background, 2000, Itasca Consulting Group, Inc.
- Walton O.R., 1992: Granular solids flow project, Report UCID-20297-88-1, Lawrence Livermore National Laboratory
- Wriggers P., 2002: *Computational contact mechanics*. Hoboken, NJ: John Wiley & Sons
- Wu S.S., 1985: Rockfall evaluation by computer simulation. *Transportation Research Record* 1031, 1-5, Washington, USA